

## **Copyright Warning & Restrictions**

The copyright law of the United States (Title 17, United States Code) governs the making of photocopies or other reproductions of copyrighted material.

Under certain conditions specified in the law, libraries and archives are authorized to furnish a photocopy or other reproduction. One of these specified conditions is that the photocopy or reproduction is not to be “used for any purpose other than private study, scholarship, or research.” If a user makes a request for, or later uses, a photocopy or reproduction for purposes in excess of “fair use” that user may be liable for copyright infringement,

This institution reserves the right to refuse to accept a copying order if, in its judgment, fulfillment of the order would involve violation of copyright law.

**Please Note: The author retains the copyright while the New Jersey Institute of Technology reserves the right to distribute this thesis or dissertation**

Printing note: If you do not wish to print this page, then select “Pages from: first page # to: last page #” on the print dialog screen

The Van Houten library has removed some of the personal information and all signatures from the approval page and biographical sketches of theses and dissertations in order to protect the identity of NJIT graduates and faculty.

## **ABSTRACT**

### **THE STABILITY OF NANOBUBBLES AND ITS APPLICATION IN CONTAMINATED SEDIMENT TREATMENT**

**by  
Shaini Dilsha Aluthgun Hewage**

This dissertation consists of two sections. First, nanobubbles' stability and behavior are studied using experimental and theoretical approaches. Second, nanobubbles application combined with ultrasound to remediate contaminated sediments is discussed.

The stability study consists of four sections. (i). Laboratory investigation to determine bubble size distributions and zeta potentials for different gases, pH levels, temperatures, and salt conditions. (ii). A theoretical study based on the diffused double layer theory to explain nanobubbles' behavior in different NaCl concentrations. (iii). Nanobubbles' stability in electrolyte solutions under different ion valencies using deionized water, NaCl, Na<sub>2</sub>SO<sub>4</sub>, Na<sub>3</sub>PO<sub>4</sub>, CaCl<sub>2</sub>, and FeCl<sub>3</sub>. (iv). The molecular dynamic simulation to evaluate the O<sub>2</sub> gas nanobubbles' properties and behavior.

Test results show that the average bubble size depends on the gas solubility in water. The zeta potential depends on the gas's ability to generate OH<sup>-</sup> ions at the gas-liquid interface. Bubbles with high negative zeta potentials can be generated in high pH solutions, low temperatures, and low salt concentrations. High pH solutions produce smaller but stable nanobubbles. With time, the zeta potential of bubbles decreases while the bubble size increases. Although bubble sizes are expected to decrease with time due to gas diffusion, the increased bubble sizes are attributed to the possible bubble coalescence.

With increase NaCl concentration, bubble size, surface charge density, and the number of negative charges on the bubble surface increases. In contrast, the magnitude of

zeta/surface potential, double layer thickness, internal pressure, and electrostatic repulsion force decreases. The total net energy for 0.001 M NaCl solution had a  $6.99 \times 10^{-20}$  J energy barrier, which prevents bubble coalescence. In different valency salts solutions, size and zeta potential depend on solution pH and cation valency. The cation concentration at the bubble surface is higher than that of bulk, confirming the bubbles are negatively charged. The high valency cations could neutralize or completely reverse the bubble charge. There is no significant energy barrier to overcome the attractive van der Waals forces for all the solutions, questioning the validity of the used Hamaker constant in calculations as that nanobubble may contain exceptional interfacial properties.

High inner density O<sub>2</sub> gas nanobubble is simulated using LAMMPS molecular dynamics code. Bubble size is stable for the simulated length 5ns. After 3ns, the diffusion coefficient is small, and the gas diffusion rate becomes nearly constant. The calculation shows that the inside pressure and surface tension at the bubble surface decrease, and the external gas partial pressure increases with time. Thereby, the bubble is metastable with high inner gas density and the supersaturate condition with slow diffusion.

An in-situ sediment remediation method is studied using ultrasound and ozone nanobubbles to remediate contaminated sediments. Two experimental setups are conducted (i). remediation of organic contaminant (p-terphenyl), (ii). remediate both organic (p-terphenyl) and inorganic (chromium) chemicals in contaminated sediments. Experiments are conducted with ultrasound and ozone nanobubbles under different operating conditions. For organic contaminant treatment, the maximum treatment efficiency of 91.50%, and the combined contaminant treatment, the average removal efficiencies of 71% for chromium and 64% for p-terphenyl are recorded.



**THE STABILITY OF NANOBUBBLES AND ITS APPLICATION IN  
CONTAMINATED SEDIMENT TREATMENT**

**by  
Shaini Dilsha Aluthgun Hewage**

**A Dissertation  
Submitted to the Faculty of  
New Jersey Institute of Technology  
in Partial Fulfillment of the Requirements for the Degree of  
Doctor of Philosophy in Civil Engineering**

**John A. Reif, Jr. Department of Civil and Environmental Engineering**

**December 2020**

Copyright © 2020 by Shaini Dilsha Aluthgun Hewage

ALL RIGHTS RESERVED

**APPROVAL PAGE**

**THE STABILITY OF NANOBUBBLES AND ITS APPLICATION IN  
CONTAMINATED SEDIMENT TREATMENT**

**Shaini Dilsha Aluthgun Hewage**

---

Dr. Jay N. Meegoda, Dissertation Advisor Date  
Professor of Civil and Environmental Engineering, NJIT

---

Dr. Wen Zhang, Committee Member Date  
Associate Professor of Civil and Environmental Engineering, NJIT

---

Dr. Taha F. Marhaba, Committee Member Date  
Professor of Civil and Environmental Engineering, NJIT

---

Dr. Bruno Gonçalves da Silva, Committee Member Date  
Assistant Professor of Civil and Environmental Engineering, NJIT

---

Dr. Dibakar Datta, Committee Member Date  
Assistant Professor of Mechanical and Industrial Engineering, NJIT

---

Dr. David W. Washington, Committee Member Date  
Associate Professor of Engineering Technology, NJIT

## BIOGRAPHICAL SKETCH

**Author:** Shaini Dilsha Aluthgun Hewage

**Degree:** Doctor of Philosophy

**Date:** December 2020

### **Undergraduate and Graduate Education:**

- Doctor of Philosophy in Civil Engineering, New Jersey Institute of Technology, Newark, NJ, 2020
- Master of Science in Geotechnical and Earth Resources Engineering, Asian Institute of Technology, Pathum Thani, Thailand, 2015
- Bachelor of Science in Civil and Infrastructure Engineering, Asian Institute of Technology, Pathum Thani, Thailand, 2013

**Major:** Civil Engineering

### **Presentations and Publications:**

Aluthgun Hewage, S., & Meegoda, J. N. Molecular Dynamic Simulation of Oxygen Gas Bulk Nanobubble. [Manuscript preparation for publication]

Aluthgun Hewage, S., Batagoda, J. H., & Meegoda, J. N. Remediation of Contaminated Sediments Containing Both Organic and Inorganic Chemicals Using Ultrasound and Ozone Nanobubbles. [Manuscript submitted for publication]

Aluthgun Hewage, S., Kewalramani, J., & Meegoda, J. N. (2020). Stability of Nanobubbles In Different Salts Solutions. *Colloids and Surfaces A: Physicochemical and Engineering Aspects*, 125669.

Aluthgun Hewage, S., Batagoda, J. H., & Meegoda, J. N. (2020). In Situ Remediation of Sediments Contaminated with Organic Pollutants Using Ultrasound and Ozone Nanobubbles. *Environmental Engineering Science*, 37(8), 521-534.

Meegoda, J. N., Aluthgun Hewage, S., & Batagoda, J. H. (2019). Application of the Diffused Double Layer Theory to Nanobubbles. *Langmuir*, 35(37), 12100-12112.

Batagoda, J. H., Aluthgun Hewage, S., & Meegoda, J. N. (2019). Remediation of Heavy Metal Contaminated Sediments In USA Using Ultrasound and Ozone Nanobubbles. *Journal of Environmental Engineering and Science*, 14(2), 130-138.

- Batagoda, J. H., Aluthgun Hewage, S., & Meegoda, J. N. (2018). Nano-ozone Bubbles for Drinking Water Treatment. *Journal of Environmental Engineering and Science*, 14(2), 57-66.
- Meegoda, J. N., Aluthgun Hewage, S., & Batagoda, J. H. (2018). Stability of Nanobubbles. *Environmental Engineering Science*, 35(11), 1216-1227.
- Batagoda, J. H., Meegoda, J. N., & Aluthgun Hewage, S. (2018). In Situ Remediation of Passaic River Sediments Using Ultrasound and Ozone Nanobubbles. In *World Environmental and Water Resources Congress 2018: Groundwater, Sustainability, And Hydro-Climate/Climate Change* (pp. 49-63). Reston, VA: American Society of Civil Engineers.
- Meegoda, J. N., Batagoda, J. H., & Aluthgun Hewage, S. (2017). Briefing: In Situ Decontamination of Sediments Using Ozone Nanobubbles and Ultrasound. *Journal of Environmental Engineering and Science*, 12(1), 1-3.
- Meegoda, J. N., Batagoda, J. H., Aluthgun Hewage, S., (2017). Decontaminate Passaic River Sediments Using Ultrasound with Ozone Nano Bubbles. *Proceedings of the 19<sup>th</sup> International Conference on Soil Mechanics and Geotechnical Engineering*, Seoul, South Korea.

*This dissertation is dedicated to my dearest mother, father, and brother  
For their endless love, support, and encouragement  
I love you so much*

## ACKNOWLEDGMENT

The past five-years of my Ph.D. studies were one of the happiest and fruitful times that I experienced as a student. In this journey, there were many individuals who, in different ways, make this possible and memorable. I would like to take this opportunity to acknowledge those individuals with all respect.

Firstly, I want to express my sincere gratitude to my advisor, Dr. Jay Meegoda, for his constant and precious guidance and support all-time provide me over the years. He always advises and guides me to develop my career, expand my knowledge and experience. He was not only just a mentor; he was very caring and kind towards us, always wanted to see our success, always understood my career goals, and supported and guided me to achieve them. Words are certainly not enough to express my gratitude to my advisor, and I am honored and pleased to work under his guidance.

I would also like to extend my deepest gratitude to my dissertation committee members, Dr. Wen Zhang, Dr. Taha F. Marhaba, Dr. Bruno Gonçalves da Silva, Dr. Dibakar Datta, and Dr. David W. Washington, for all of their guidance and valuable advice. I am incredibly thankful to Dr. Zhang and Dr. Marhaba for providing lab access and lab equipment for the experiments, and Dr. Datta for teaching me the Molecular Dynamic simulation.

I would like to acknowledge the Civil and Environmental Engineering Department, NJIT, and US National Science Foundation Award #1634857 for providing funding for my Ph.D. studies. I like to acknowledge above support made this dissertation possible.

Special thanks go to Mr. Stephen George and Mr. Nasser Channaoui for their kind help and support for my research and laboratory work. I appreciate Dr. Larisa Krishtopa

and Dr. Jeong Seop Shim for their kind guidance and support at the York Center, NJIT, with chemical analysis experiments and equipment learning.

I would like to extend my sincere thanks to all the professors that I worked as a TA for their flexibility, understanding, and guidance. I would like to especially mention Mr. Andrew Ciancia, Dr. Vatsal Shah, Dr. Danial Esmaili, Dr. Bruno Gonçalves da Silva, Dr. Fadi Karaa, and Dr. Matthew Riegel. I am also grateful to Dr. Methi Wecharatana and Dr. Matthew Bandelt for their advice and direction to fulfill my graduation requirements.

I would also like to acknowledge the assistance from the Civil and Environmental Engineering Department administration for all their support. I especially like to mention the department chair, Dr. Taha F. Marhaba, and the staff, Ms. Heidi Young, Ms. Dallas Link, Ms. Sylvana Brito, and Ms. Diana Ochoa Urgiles.

Also, I am thankful to all the professors under whom I took courses and the administrative staff at NJIT for their all-time support, especially Ms. Gonzalez-Lenahan and Dr. Ziavras, for reviewing my dissertation. I like to mention Dr. John Schuring, a great and sincere professor who gave me the first opportunity to see outside the campus by organizing the field trips to explore the NJ geology, a great experience.

NJIT became a happy place, mainly because of my friends. I am giving my kind regards to all of you, my Civil and Environmental Engineering Department friends. I am very thankful to Janitha, Zou, and Lucas, the first three friends I met here, who welcomed me and helped me adjust to the new place. I specially thankful to Janitha and Jitendra for being very supportive co-workers and great friends. I am also very much pleased to all the undergraduate and high school students who helped me with the experimental work; here, I notably thank Brian Mcglew and Natan Herzog for their contribution. Also, Wanyi Fu,



Likun Hua, Xiaonan Shi, and Jatin Kashyap for their kind help with research work. I am also thankful to my friends, Gayani, Anuruddha, Caterina, Bruno, Di, Mandeep, Jin, Ehsan, Hasan, and all my other friends, for your friendship and support.

I am forever grateful to my loving parents, mother Ayoma Pushparani, father Premalal Kumarasiri, and brother Asela Rajamanthri for their unconditional love, patience, and endless support.

## TABLE OF CONTENTS

<b>Chapter</b>	<b>Page</b>
1 INTRODUCTION .....	1
1.1 Background Information .....	1
1.2 Problem Statement .....	2
1.3 Objectives .....	3
2 LITERATURE REVIEW .....	5
2.1 Introduction to Fine Bubbles .....	5
2.2 General Behavior of Fine Bubbles .....	7
2.3 Detection Techniques for Fine Bubbles .....	8
2.3.1 Dynamic light scattering method .....	9
2.3.2 Laser diffraction scattering method .....	10
2.3.3 Particle tracking analysis method .....	12
2.3.4 Electrical sensing zone method .....	12
2.3.5 Resonance mass measurement method .....	13
2.3.6 Zeta-potential measurement method .....	14
2.4 Nanobubbles Generation Techniques .....	15
2.4.1 Hydrodynamic cavitation .....	16
2.4.2 Acoustic cavitation .....	20
2.4.3 Optical cavitation .....	21
2.4.4 Particle cavitation .....	22
2.5 Industrial Application of Nanobubbles .....	22

**TABLE OF CONTENTS**  
**(Continued)**

<b>Chapter</b>	<b>Page</b>
2.6 Characteristics of Ultrafine Bubbles or Nanobubbles .....	24
2.6.1 Smaller size and high surface area .....	24
2.6.2 Low buoyancy and low rising velocity .....	25
2.6.3 Electrically charged gas-liquid interface .....	30
2.6.4 Thermodynamic properties of nanobubbles .....	32
2.6.5 Diffusion barrier .....	34
2.6.6 Hydrogen bonds .....	35
2.6.7 Gas saturation .....	36
2.6.8 Clusters .....	37
2.6.9 Radical .....	37
3 STABILITY OF NANOBUBBLES .....	39
3.1 Introduction .....	39
3.2 Applications of Nanobubbles .....	40
3.3 Experimental Methods .....	43
3.3.1 Generation of nanobubbles .....	43
3.3.2 Measurement of size distribution and zeta potential .....	44
3.3.3 Test procedure .....	44
3.4 Results and Discussion .....	45
3.4.1 Different gas types .....	45
3.4.2 Variations in solution pH .....	49

**TABLE OF CONTENTS**  
**(Continued)**

<b>Chapter</b>	<b>Page</b>
3.4.3 Impact of salt concentration .....	53
3.4.4 Impact of solution temperature .....	55
3.4.5 Stability of nanobubbles .....	57
Summary and Conclusions .....	60
<b>4 APPLICATION OF THE DIFFUSED DOUBLE LAYER THEORY TO NANOBUBBLES .....</b>	<b>62</b>
4.1 Introduction .....	62
4.2 Derivation of Equations .....	63
4.2.1 Derivation of modified Young Laplace equations .....	63
4.2.2 The formation of the diffuse double layer around nanobubbles .....	65
4.2.3 Derivation of surface charge density equations .....	69
4.2.4 Interfacial forces .....	74
4.3 Materials and Methods .....	78
4.4 Results and Discussion .....	80
4.5 Conclusions .....	95
<b>5 STABILITY OF NANOBUBBLES IN DIFFERENT SALTS SOLUTIONS .....</b>	<b>97</b>
5.1 Introduction .....	97
5.2 Formation of Electric Double-Layer Around Nanobubbles .....	99
5.3 The Bubbles Interaction Force and Energy .....	100
5.3.1 Equations for modeling .....	101

**TABLE OF CONTENTS**  
**(Continued)**

<b>Chapter</b>	<b>Page</b>
5.4 Experimental Procedure .....	105
5.4.1 Materials .....	105
5.4.2 Preparation of nanobubble .....	106
5.4.3 Measurement of zeta-potential and nanobubble size .....	106
5.5 Results and Discussion .....	107
5.6 Summary and Conclusions .....	124
<b>6 MOLECULAR DYNAMICS SIMULATION OF BULK NANOBUBBLES .....</b>	<b>129</b>
6.1 Background Information .....	129
6.1.1 Literature survey of molecular dynamic simulations of bulk nanobubbles	130
6.2 Model and Simulation Details .....	132
6.2.1 Methodology .....	132
6.3 Theory .....	133
6.3.1 Pressure and surface tension .....	133
6.3.2 The diffusion of oxygen from the bubble .....	135
6.4 Simulation Results and Discussion .....	136
6.5 Summary and Conclusions .....	145
<b>7 IN-SITU REMEDIATION OF SEDIMENTS CONTAMINATED WITH ORGANIC POLLUTANTS USING ULTRASOUND AND OZONE NANOBUBBLES .....</b>	<b>148</b>
7.1 Introduction .....	148

**TABLE OF CONTENTS**  
**(Continued)**

<b>Chapter</b>	<b>Page</b>
7.1.1 Background .....	148
7.1.2 Research objectives .....	149
7.2 Remediation Method .....	150
7.2.1 Ultrasound and ozone nanobubbles for remediation of sediments .....	151
7.2.2 Proposed in-situ remediation technology .....	155
7.3 Materials and Methods .....	157
7.3.1 Sediment sample preparation .....	157
7.3.2 Sediment contamination .....	157
7.3.3 Ozone nanobubble generation .....	158
7.3.4 Ultrasound generation .....	158
7.3.5 Sediment remediation .....	159
7.3.6 Chemical analysis .....	160
7.3.7 Other measurements .....	161
7.4 Results and Discussion .....	161
7.4.1 Ozone nanobubbles .....	161
7.4.2 Impact of ultrasound on solution properties .....	164
7.4.3 Change in the particle size distribution of sediments due to sonication ...	166
7.4.4 Remediation of sediment using ultrasound and ozone nanobubbles .....	167
7.5 Summary and Conclusions .....	172

**TABLE OF CONTENTS**  
**(Continued)**

<b>Chapter</b>	<b>Page</b>
8 REMEDIATION OF CONTAMINATED SEDIMENTS CONTAINING BOTH ORGANIC AND INORGANIC CHEMICALS USING ULTRASOUND AND OZONE NANOBUBBLES .....	177
8.1 Introduction .....	177
8.1.1 Background .....	177
8.1.2 Hypothesis .....	178
8.1.3 Research objectives .....	179
8.2 The Development of The Treatment Method .....	179
8.2.1 In-situ treatment technologies .....	179
8.3 Materials and Methods .....	183
8.3.1 Soil preparation and contamination .....	183
8.3.2 Preparation of contaminated sediments .....	185
8.4 Experimental Setup .....	186
8.4.1 Generation of ozone nanobubbles .....	187
8.4.2 Treatment of sediments using ozone nanobubbles and ultrasound .....	187
8.4.3 Chemical analysis .....	189
8.5 Results and Discussion .....	190
8.5.1 Size of ozone nanobubbles, zeta potential, and dissolved gas concentration .....	190
8.5.2 Treatment efficiencies of contaminated sediments .....	191
8.6 Summary and Conclusions .....	203

**TABLE OF CONTENTS**  
**(Continued)**

<b>Chapter</b>	<b>Page</b>
9 SUMMARY, CONCLUSIONS, AND FUTURE RECOMMENDATIONS .....	205
9.1 Summary and Conclusions .....	205
9.1.1 Experimental investigation: nanobubble stability based on infilled gas type and effect of solution chemistry .....	205
9.1.2 Application of the diffused double layer theory to nanobubbles .....	206
9.1.3 The stability of nanobubbles in different electrolyte solutions .....	207
9.1.4 Molecular dynamic simulation of oxygen gas nanobubble .....	208
9.1.5 Application of ozone nanobubbles coupled with ultrasound to treat contaminated sediments .....	210
9.2 Future Recommendations .....	212
9.2.1 Experimental and theoretical study on nanobubble stability .....	212
9.2.2 Molecular dynamic simulation .....	212
9.2.3 Application of nanobubbles for sediment treatment .....	213
APPENDIX A SYNTHETIC SEDIMENT COMPOSITION .....	214
APPENDIX B DETAILS FOR THE TEST OF DISSOLVED OZONE CONCENTRATION USING A REGULAR DIFFUSE .....	215
APPENDIX C GS/MS ANALYSIS DATA .....	216
APPENDIX D COMPARISON OF PROPERTIES OF P-TERPHENYL WITH 16 US-EPA PAHS .....	218
REFERENCES .....	224



## LIST OF TABLES

<b>Table</b>	<b>Page</b>
2.1 Terminal Velocity of Oxygen Nanobubbles .....	26
4.1 NaCl Solution Concentration with Average Size, Average Zeta Potential, the Calculated Double Layer Thickness, Surface Charge Density, Surface Potential, Number of Electrons, and the Pressure Difference Across the Fluid Interface ....	84
5.1 Solution Properties and Parameters .....	113
5.2 Nanobubbles Measured and Calculated Parameters .....	113
5.3 Summary of Findings for the Nanobubbles In Multivalent Electrolytes from the Published Literature .....	126
6.1 LJ Simulation Parameters .....	132
6.2 Calculation of Possible Values for Internal Pressures and Surface Tension .....	147
7.1 Impact of Ultrasound Power and Ozone Delivery Method on Treatment Efficiency .....	168
7.2 Removal Efficiency of P-Terphenyl by Varying the Treatment Duration .....	169
7.3 Review of Different Research Findings: Ultrasound to Remediate Organic Pollutants in Sediment .....	174
8.1 Summary of Results .....	194
A.1 Composition of Synthetic Dredge Sediment .....	214
D.1 Comparison of Properties of P-Terphenyl with 16 US-EPA PAHs .....	219
D.2 Comparison of Laboratory Chemical Safety of P-Terphenyl with 16 US-EPA PAHs .....	222

## LIST OF FIGURES

<b>Figure</b>	<b>Page</b>
2.1 Timeline of a brief selection of significant publications in the field of surface and bulk nanobubbles. ....	6
2.2 Bubble characterization based on size. ....	6
2.3 Bubble classification based on visibility. ....	7
2.4 Bubble behavior with time. ....	8
2.5 Different measurement methods. ....	9
2.6 Schematic showing the instrumentation of DLS. ....	11
2.7 Laser diffraction scattering method. ....	11
2.8 Particle tracking analysis. ....	12
2.9 Principle of the electrical sensing zone method. ....	13
2.1 Resonance mass measurement method. ....	14
2.11 Particle tracking/dynamic light scattering method. ....	15
2.12 Four main cavitation mechanisms. ....	16
2.13 Sketch of the water phase diagram. boiling is the phase change from liquid to a gas by temperature increase, whereas cavitation is the phase change by pressure decrease. ....	17
2.14 OHR laboratory corporation (a) vertical section view (b) cross-section view. ....	18
2.15 Spiral liquid flow generation method. ....	19
2.16 Schematic diagram of the cavitation venturi tube. ....	20
2.17 Growth and collapse of bubbles in acoustic cavitation. ....	21
2.18 Application of fine bubbles. ....	23
2.19 Comparison between the surface area of microbubble and nanobubble at the same volume. ....	24

**LIST OF FIGURES**  
**(Continued)**

<b>Figure</b>	<b>Page</b>
2.20 Increase in the specific area of bubbles with decreased bubble size. ....	25
2.21 Force balance of a bubble and terminal velocity. ....	27
2.22 Terminal velocity of oxygen nanobubbles. ....	27
2.23 Rising velocities of the MBs according to size (data points show a single bubble)..	29
2.24 The measured rising velocity of 500nm size bubble. ....	29
2.25 The ion distribution around the nanobubble and the zeta potential. ....	31
3.1 Experimental setup. (The figure shows the ozone nanobubbles generation setup, for other gas bubbles, the gas inlet is directly connected to the gas cylinder instead of the ozone generator). ....	43
3.2 Relationship between (a) bubble diameter and gas types of the nanobubbles and (b) Zeta potential and the gas types of the nanobubbles. ....	49
3.3 Relationship between (a) zeta potential and pH, and (b) bubble diameter and pH, for oxygen nanobubble solution at 20°C. ....	50
3.4 Relationship between (a) zeta potential variation with time and (b) bubble size variation with time, for oxygen nanobubble, prepared with different pH at 20°C.	52
3.5 Relationship between (a) zeta potential and the NaCl concentrations and (b) bubble diameter and NaCl concentrations for ozone nanobubbles at 25°C. ....	54
3.6 Relationship between (a) bubble diameter and NaCl concentrations, (b) zeta potential and NaCl concentrations for oxygen nanobubbles at 20°C and pH≈7. ....	57
3.7 Relationship between (a) zeta potential and temperature and (b) bubble diameter and temperature for oxygen nano-bubbles solution generated in DI water. ....	58
3.8 The fate of macro, micro, and nanobubbles in liquids with time. ....	59

**LIST OF FIGURES**  
**(Continued)**

<b>Figure</b>	<b>Page</b>
4.1 A schematic of the bubble interactions between two bubbles. ....	76
4.2 The Electric double layer and Van der Waals interactions between two bubbles.	77
4.3 Relationship between NaCl concentration and (a) bubble diameter, (b) zeta potential, for oxygen nanobubbles at 20°C and pH≈7. ....	81
4.4 Variation with time: a) diameter b) zeta potential, for oxygen nanobubbles in NaCl solution at 20°C and pH≈7. ....	82
4.5 Surface charge density for oxygen nanobubbles in NaCl solution at 20°C and pH≈7. ....	85
4.6 Variation of electrical potential with distance for oxygen nanobubbles in NaCl solutions of varying concentrations (20°C and pH≈7). ....	86
4.7 The variation of the electric double layer thickness and number of electrons with NaCl concentration for oxygen nanobubbles at 20°C and pH≈7. ....	87
4.8 The pressure difference across the fluid interface (based on the Young- Laplace equation and modified Young-Laplace equation). ....	89
4.9 Van der Waals, electrostatic and total energy and forces vs. separation distances for nanobubbles in NaCl solutions for varying concentrations (20°C and pH≈7).	91
5.1 The bubble size and zeta potential variation (a) bubble size at week 0, (b) bubble size, and percentage change in size after 1 week, (c) zeta potential and pH of the solution in week 0, (d) zeta potential and percentage change in zeta potential after 1 week, for air bubbles at 25°C. ....	108
5.2 Surface charge density, zeta potential, and surface potential at week 0 and week 1. ....	114
5.3 Ionic concentration at the bubble surface for different salts (a) cation (b) anions.	114
5.4 The variation of ion concentration with distance. ....	117

**LIST OF FIGURES**  
**(Continued)**

<b>Figure</b>	<b>Page</b>
5.5 The attractive, repulsive, and total interacting forces/energy diagrams for five electrolyte bubble solutions. ....	123
5.6 Comparison of results of salts solutions with similar Debye lengths (a) $1/K = 4.54\text{nm}$ $\text{Na}_2\text{SO}_4$ and $\text{CaCl}_2$ , (b) $1/K = 2.57\text{nm}$ $\text{Na}_3\text{PO}_4$ and $\text{FeCl}_3$ . ....	124
6.1 Simulation configuration. ....	133
6.2 The systematic diagram of the bulk nanobubble and gas-concentration profile. ...	135
6.3 Snapshots of the bubble with time. ....	137
6.4 Gas and liquid density profile. ....	138
6.5 The total gas density distribution. ....	138
6.6 Dissolved gas concentration with time (outside distance $r = 60 \text{ \AA}$ ). ....	139
6.7 The rate of change of dissolved gas concentration with time (outsider = $60 \text{ \AA}$ ). ...	139
6.8 The variation of the calculated diffusion coefficient base on Equation (6.5) with time. ....	141
6.9 The variation of the mean square displacement with time. ....	141
6.10 The total pressure distribution is calculated by stress/atom data obtained from MD simulation output data (A) 3ns, (B) 4ns, and (C) 5ns. ....	143
7.1 A sketch of the containment chamber was used for the proposed remediation. ...	156
7.2 Experimental setup (a) nanobubble generation setup, (b) the sediment treatment chamber. ....	160
7.3 Variation (a) diameter/bubble size distribution and (b) zeta potential for ozone nanobubbles with the temperature at $\text{pH} \approx 7$ , and (c) ozone concentration with time for regular bubbles and nanobubbles at different temperatures and $\text{pH} \approx 7$ (a) $10^\circ\text{C}$ , (b) $15^\circ\text{C}$ , and (c) $20^\circ\text{C}$ . ....	163
7.4 Temperature variation in water to different ultrasonic power. ....	165

**LIST OF FIGURES**  
**(Continued)**

<b>Figure</b>	<b>Page</b>
7.5 Ozone concentration variation with time for different sonication power levels. ...	165
7.6 The particle size distribution of sediments with and without sonication. ....	167
7.7 Variation of removal efficiency for different ultrasound power levels. ....	168
7.8 Removal efficiency of p-terphenyl by varying the treatment duration. ....	169
8.1 Sketch of the sediment treatment chamber for field implementation. ....	183
8.2 Schematic flow diagram of the experimental procedure. ....	187
8.3 Contaminated sediment treatment chamber. ....	188
8.4 Characteristics of ozone nanobubbles generated at 20°C and pH 7. ....	193
8.5 Summary of the calculated values for each test performed (a) Part A, (b) Part B.	199
8.6 Test results for similar contamination concentration (Cr: 4211mg/kg and p-terphenyl: 1875 mg/kg). ....	200
8.7 Effect of the initial concentration of contaminants. ....	200
B.1 Diffuser used for ozonation and the constant temperature baths. ....	215
C.1 Formation of esters from broken p-terphenyl benzene rings. ....	216
C.2 GC/MS chromatogram and a mass spectrum for wastewater. ....	217

# CHAPTER 1

## INTRODUCTION

### 1.1 Background Information

In recent years, the industrial application of nano-bubbles/ultrafine bubbles has increased due to their unique characteristics and behavior. Nanobubbles can mainly classify into two categories based on their presence in an aqueous solution: surface and bulk nanobubbles. The industrial application of bulk nanobubbles is more recent than surface nanobubbles [1]. This research investigates the stability of bulk nanobubbles. The gas-filled cavities suspended in an aqueous solution are referred to as bulk bubbles. In general, bubbles are characterized based on their size; macro-bubbles ( $>100\mu\text{m}$ ), micro-bubbles ( $1\mu\text{m}$  to  $100\mu\text{m}$ ), nano-bubbles ( $<1\mu\text{m}$ ) [2]. However, based on the literature and various applications, most nanobubbles explored were less than 200nm in diameter [2–4]. The industrial application of nanobubble technology has exponentially increased over the past two decades due to their long-term stability and reactivity [5,6]. Due to their extra small size, high specific area, and long stagnation times, they have increased mass transport efficiencies, physical absorptions, and chemical reactions at the gas-liquid interfaces when compared to the ordinary and microbubbles [7]. These nanobubbles are also very important due to their long residence time in solutions and electrically charged interfaces [8]. Nanobubbles have many industrial applications due to these unique properties, including manufacturing functional materials, soil and sediment decontamination, pharmaceutical delivery, and food disinfection [9].

After generation, nanobubbles are found to exist in aqueous solutions for several weeks. Azevedo et al. [10] reported that bubbles of radii 150-200nm were in a solution for two weeks. The electrically charged liquid-gas interface of nanobubbles creates repulsive forces that prevent bubble coalescence. Also, higher bubble densities creating higher dissolved gas concentration in water and preventing the gas diffusion from the bubble due to smaller concentration gradient [6]. The stability of nano-bubbles increases due to low rising velocity because of smaller size and smaller buoyancy force. Seung-Uk, [11] the measured rising velocity and reported to be as small as  $4.58 \times 10^{-7}$  m/s for 500nm bubbles. Other than these reasons, nanobubbles are considered stable by a mutual shielding against the diffusive outflow of gases, which can be achieved if bubbles are sufficiently close together or gathered as clusters [12].

As of now, the presence of stable nanobubbles have been experimentally confirmed, but a consistent theoretical basis has not been established to explain their long-term stability. Hence, for practical and functional use of these bubbles, a consistent theoretical basis of their properties and behavior are quite important. Thus, further study is required to understand nanobubbles' stability, impacted by generation techniques, coalescence, and free radical generation. The factors that influence nanobubbles' stability are temperature, pressure, pH, salt concentration, ion strength, and the presence of organic matter and surfactants. This research investigates the bulk nano-bubbles with experimental, analytical, numerical, and molecular dynamics simulation methods.

## **1.2 Problem Statement**

Even though nanobubbles' long-term existence was experimentally confirmed, a consistent theoretical basis has not yet been established to explain their long-term stability. Therefore,



this research will explore nanobubbles' long-term stability using experimental, theoretical, and numerical investigation.

### 1.3 Objectives

This study proposes to develop an accurate theoretical understanding of bulk nanobubbles' properties and stability. The objectives of this study as follows:

1. Experimental study: Generate nanobubbles under various conditions and measure their sizes and zeta potential values immediately and 1 week after the generation. The following variations were considered:
  - 1.1 Different type of gases (air, oxygen, nitrogen, and ozone in deionized water)
  - 1.2 Different pH conditions (DI water with NaOH and HCl to produce solutions with different pH values 4, 7, and 10)
  - 1.3 Different temperatures (DI water with 15<sup>0</sup>C, 20<sup>0</sup>C, and 30<sup>0</sup>C solution temperatures by heating or using a chiller)
  - 1.4 Different salt concentrations (DI water with NaCl to prepare different solution concentrations 0M, 0.001M, 0.01M and 0.1M solutions)
2. Theoretical study: Develop an explanation based on diffuse double layer theory for the stability of nanobubbles. The different salt solutions were prepared and tested for size and zeta potential to evaluate the stability of nanobubbles. Then the electric double layer theory was applied to bulk nanobubbles to explain their stability. Hence, two series of experiments were conducted.
  - 2.1 Nanobubbles were generated in different concentration of NaCl solutions (0M, 0.001M, 0.01M and 0.1M solutions)
  - 2.2 Nanobubbles were generated in different valency of salts solutions with 0.001M concentration (NaCl, CaCl<sub>2</sub>, FeCl<sub>3</sub>, Na<sub>2</sub>SO<sub>4</sub>, and Na<sub>2</sub>PO<sub>4</sub>)

3. Computational study: Apply the Molecular Dynamic (MD) simulations to understand the stability of nano-bubbles and diffusion of gas into bulk fluid using LAMMPS software.
  - 3.1 A 10nm diameter, high inner gas density single oxygen gas bulk nanobubble was simulated for 5ns with NVT ensemble using LJ interaction parameters to evaluate stability and related parameters (i.e., surface tension, gas solubility, and gas diffusion)
  
4. The application of ozone nanobubbles combined ultrasound to remediate contaminated sediments. In this content of work, two different experimental series were presented.
  - 4.1 Treatment of sediments contaminated with organics contaminants (p-terphenyl)
  - 4.2 Treatment of sediments contaminated with both organic (p-terphenyl) and inorganic (chromium) contaminants

## CHAPTER 2

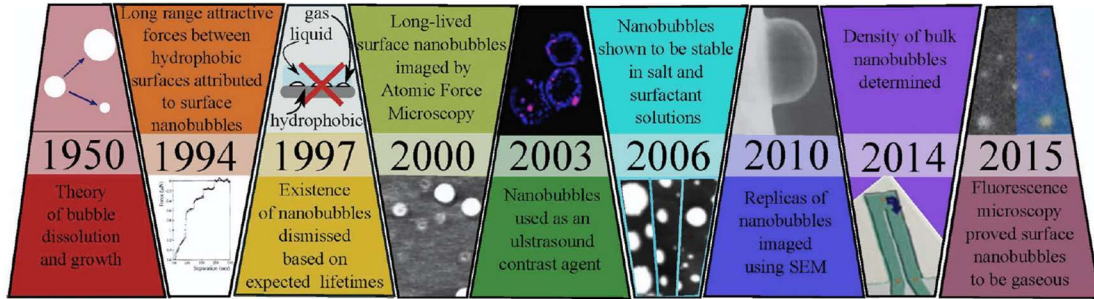
### LITERATURE REVIEW

#### 2.1 Introduction to Fine Bubbles

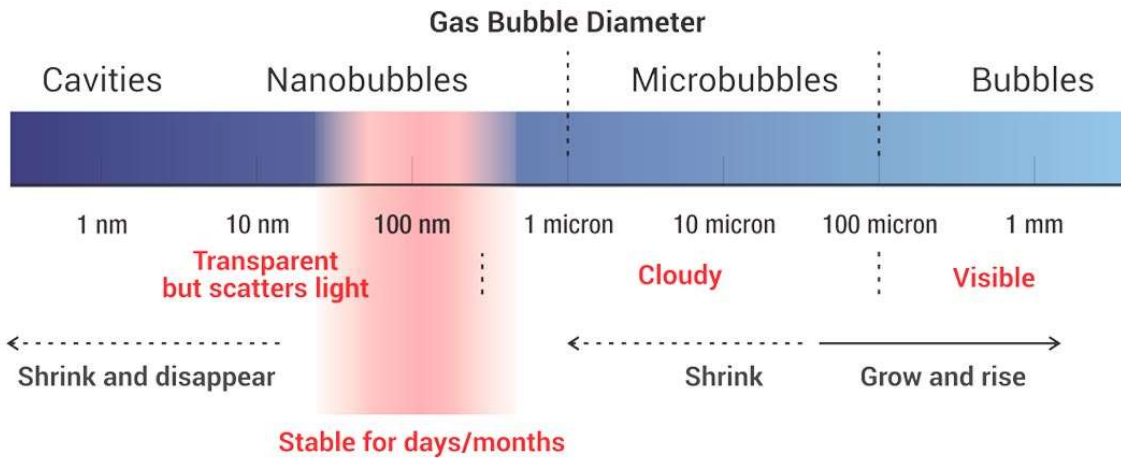
During the past two decades, the use of fine bubble technologies has increased steadily. International Organization for Standardization (ISO) has reported that, according to the initial market research conducted by the Fine Bubble Industries Association (FBIA) of Japan, the total fine bubble market, including management, facilities, and related operations, was USD 20 million in 2010. It was estimated to increase to USD 4.3 billion in 2020 and USD 8.5 billion in 2030 [13].

The interest in studying fine bubbles is not new [14]. Many researchers performed bubble studies from 1950 (Figure 2.1). They used the Epstein–Plesset theory to predict a single bubble's lifetime as a function of the bubble radius and saturation. According to this theory, a nanobubble in a saturated solution should dissolve within a few milliseconds [15]. In 1994, Parker et al. showed the existence of surface nanobubbles as a possible explanation for hydrophobic attraction. In 2000, The first images of surface nanobubbles were recorded using atomic force microscopy (AFM) [16,17]. The application of bulk nanobubbles is newer than surface nanobubbles. The study of bulk micro/nanobubbles started in 2005. Takahashi reported that under the wide range of pH values, the bubbles were negatively charged, and under the strongly acidic conditions, the surface charge can be positive. He also proposed that OH<sup>-</sup> and H<sup>+</sup> are the reasons for the gas-water interface charges, while other anions and cations have secondary contributions [18]. Ohgaki et al. reported the presence of small nitrogen, methane, and argon bulk nanobubbles of radius

50nm that were stable for up to 2 weeks [19]. Also, Ushikubo et al. presented the existence of stable oxygen nanobubbles for days through a dynamic light scattering method [6].



**Figure 2.1** Timeline of a brief selection of significant publications in the field of surface and bulk nanobubbles.  
Source: Alheshibri et al.[14].




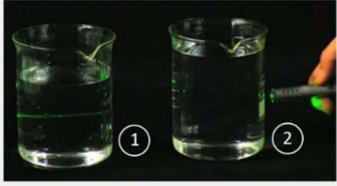


**Figure 2.2** Bubble characterization based on size.  
Source: Chaplin [2].

Since this research is on bulk nanobubbles, all discussion will be limited to the bulk nanobubbles. The bulk nanobubbles are gas-filled cavities suspended in an aqueous solution. In general, bubbles are characterized based on their size; micro-bubbles/regular bubbles ( $>100\mu\text{m}$ ), micro-bubbles/fine bubbles ( $1\mu\text{m}$  to  $100\mu\text{m}$ ), nano-bubbles/ ultrafine

bubbles ( $<1\mu\text{m}$ ) [2]. The summary of the bubble categorization based on the size is presented in Figure 2.2.

The bubble classification can be explained by bubble visibility in liquids. Regular bubbles are visible to the human eye, and they rapidly rise to the surface and burst. The micro-bubble/fine bubbles appear as milky/cloudy solutions [20]. After a few minutes, these microbubbles disappear. Bubbles smaller than the wavelength (the diffraction limit of the visual ray is 900nm) of light are described as ultrafine bubbles, and they are not visible to the naked eye. Still, these bubbles can be identified using a scatter of a laser beam.

Macro bubble	Microbubbles	Nano bubbles		
Visible to naked eye	Microbubbles are visible as cloudy/milky solution	Nano bubbles are not visible to the naked eye but can be seen by green laser light irradiation		
		 Bubbles are not visible		<ol style="list-style-type: none"> <li>1. Nanobubbles water</li> <li>2. Water without Nanobubbles</li> </ol>

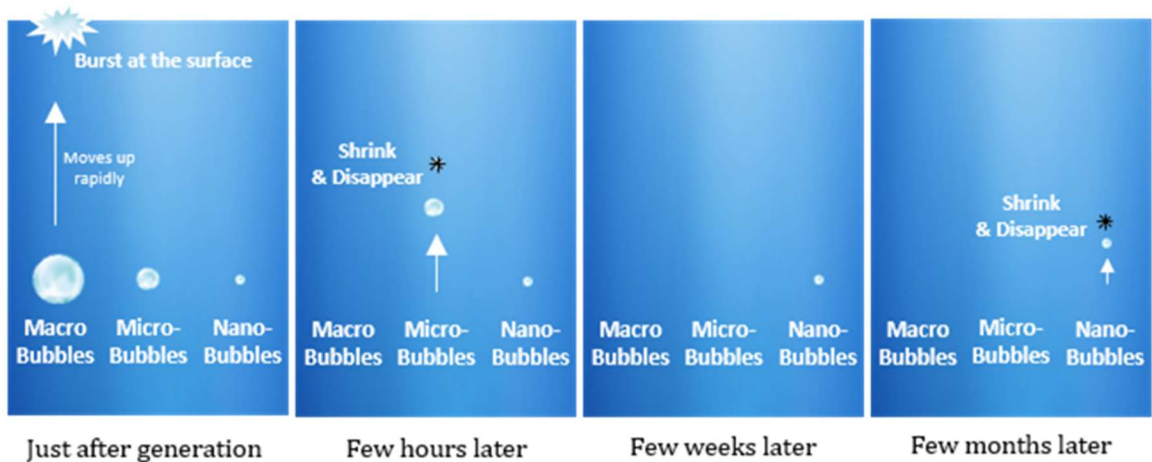
**Figure 2.3** Bubble classification based on visibility.  
Source: Serizawa [21].

## 2.2 General Behavior of Fine Bubbles

One of the main reasons for the interest in nanobubbles/ultrafine bubbles is their long lifetime or long residence time in an aqueous solution [3,6,18,22]. While regular bubbles rapidly rise and burst at the surface, micro/fine bubbles are said to shrink and disappear [23]. However, the mechanism behind the disappearance of nanobubbles with time needs investigation as there are many explanations regarding their fate (existence, stability, lifetime, disappearance, etc.). Fine bubbles are expected to either grow and move to the

surface and burst or shrink and disappear over time. Some experimental results reported microbubbles collapse to form nanobubbles while generating chemical radicals without external stimulation [23,24]. While some authors disagree with the above statement that no radicals are formed due to the dissolution of nanobubbles [25].

Nanobubbles last long in an aqueous solution and are impacted by the Brownian motion [26]. Due to their negligible buoyancy, they do not move to the surface and stay in the solution subjected to the Brownian motion. Most of the time, generated bubbles are not identical in their sizes, and they have different chemical potentials. Hence, the bubbles are governed by the Ostwald ripening. This means the smaller bubble diffuses into a larger bubble, and the smaller bubble will shrink and disappear while the larger bubble grows in size [27].

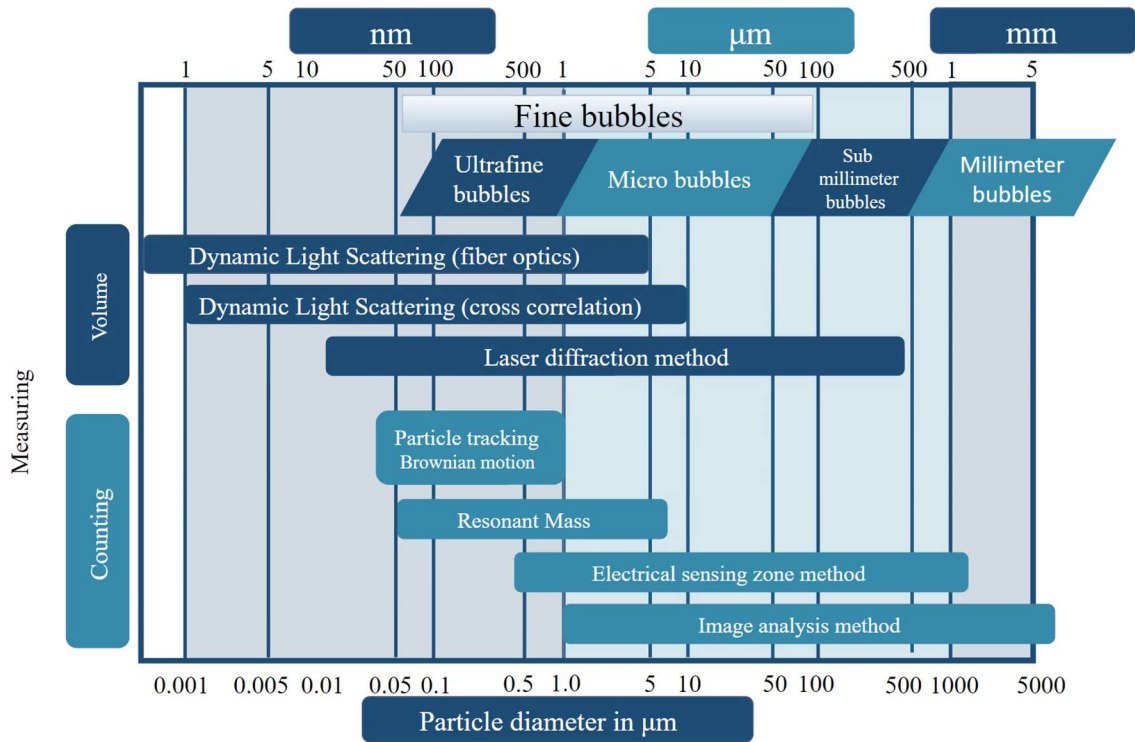


**Figure 2.4** Bubble behavior with time.

### 2.3 Detection Techniques for Fine Bubbles

Nanobubbles/ultrafine bubbles cannot be measured using a regular optical microscope as their diameter is smaller than the wavelength of light. However, with the increased interest in fine bubble technology, various groundbreaking measuring methods of these ultrafine

bubbles have been developed. Such methods are based on tracking the Brownian motion of bubbles, measuring the change in the Brownian motion frequency, analyzing the spectrum of laser backscattered light, and identifying the gas cavities using MEMS resonance devices [28]. Figure 2.5 summarizes the different methods that are used to measure fine bubble properties.



**Figure 2.5** Different measurement methods.  
Source: [www.acniti.com](http://www.acniti.com), accessed on 11/30/2020 [29].

### 2.3.1 Dynamic light scattering method

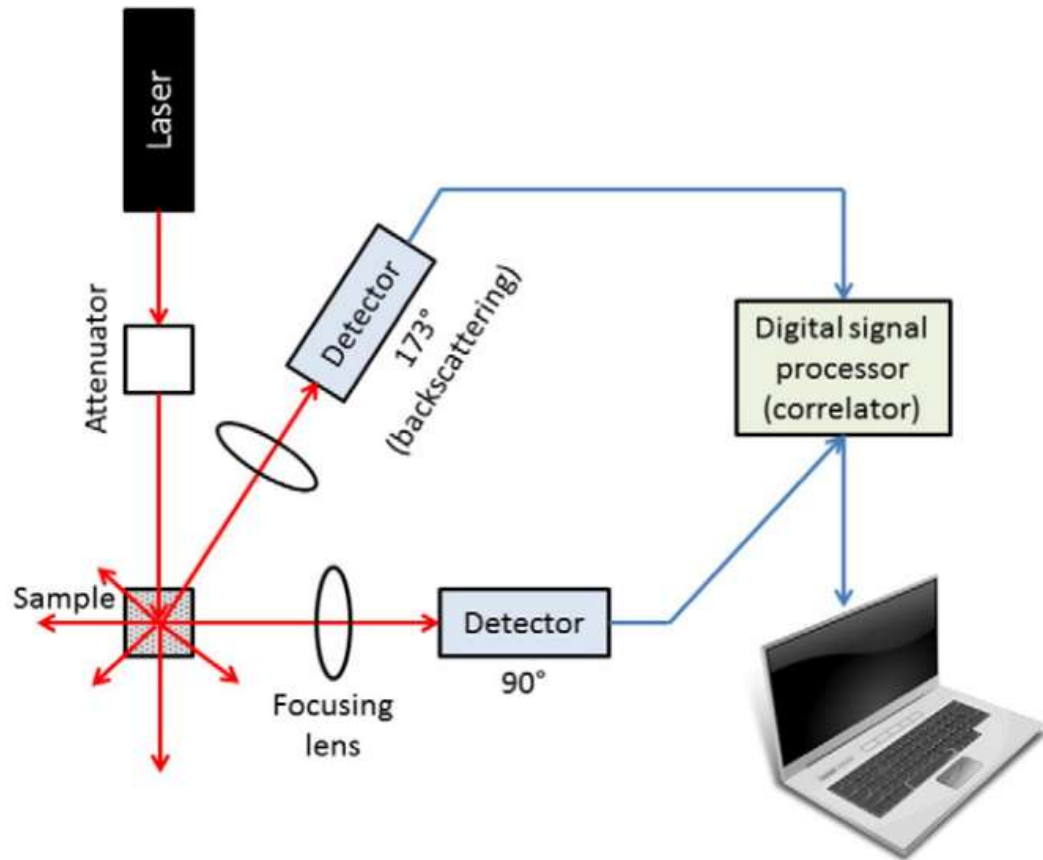
Dynamic light scattering (DLS) (also known as Photon Correlation Spectroscopy or quasi-elastic light scattering) refers to an optical technique used for analyzing dynamic properties and size distribution of a wide variety of physical, chemical, and biological systems composed of several suspended constituents [30]. DLS is one of the most popular light

scattering techniques used to measure fine bubbles as it allows to measure size less than 1 nm diameter. The principle of DLS is that fine particles are in constant random thermal motion, called "Brownian Motion," move at speed related to their size, and smaller particles move faster than larger particles. In the DLS method, the sample is illuminated by a laser beam, and fluctuations of the scattered light are detected at a known scattering angle  $\theta$  by a fast photon detector. The scattering intensity at a specific angle will fluctuate with time, and this is detected using a sensitive avalanche photodiode (APD). Since the speed of Brownian motion depends on the temperature, maintaining a constant temperature is very important to obtain accurate size measurements. The intensity changes are analyzed with a digital autocorrelator, which generates a correlation function. This curve can be analyzed to give the size and size distribution.

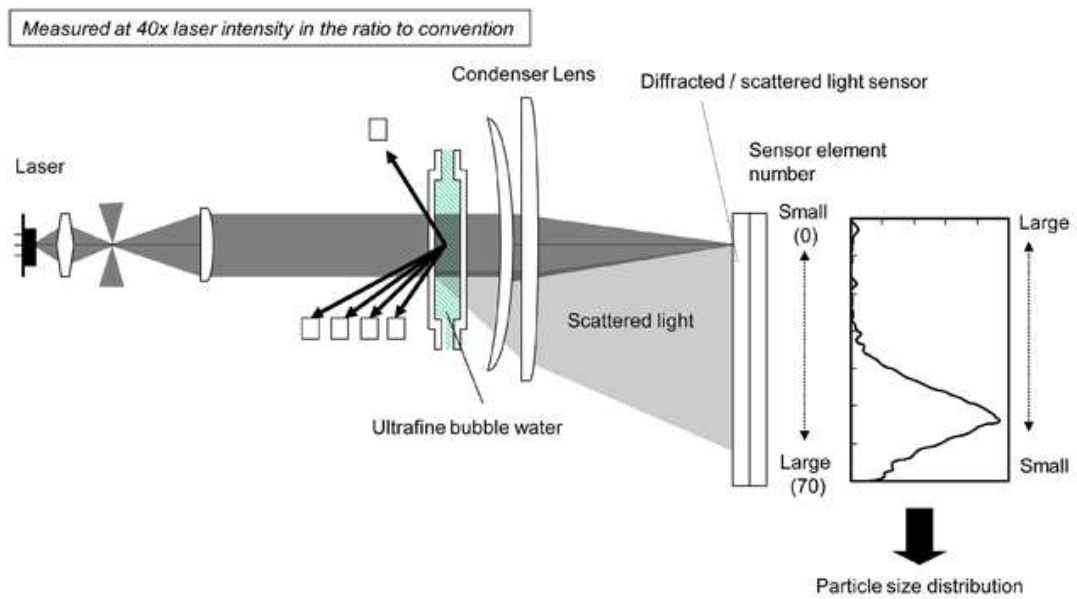
### **2.3.2. Laser diffraction scattering method**

When a light beam hits a particle in the laser diffraction scattering method, the light is either diffracted or scattered. The intensity pattern of diffraction/scattering depends on the particle size. Depending on the diffraction/scattering angle, the intensity pattern (intensity distribution) varies. Based on the intensity pattern, particle size distribution can be measured with the Fraunhofer diffraction equation and/or Mie scattering theory.





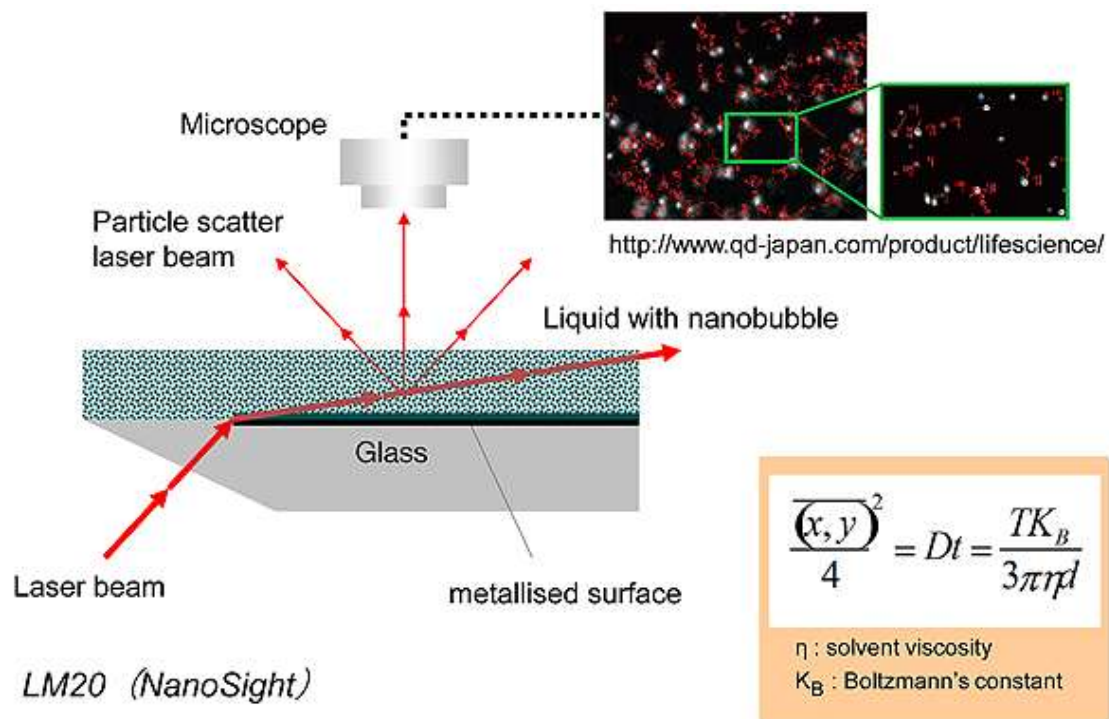
**Figure 2.6** Schematic showing the instrumentation of DLS.  
 Source: Bhattacharjee [31].



**Figure 2.7** Laser diffraction scattering method.  
 Source: www.idec.com, accessed on 11/30/2020 [32].

### 2.3.3 Particle tracking analysis method (Brownian motion tracking analysis method)

The particle tracking analysis method (i.e., NTA, Nano Tracking Analysis) utilizes both properties of light scattering and Brownian motion to determine the particle size distribution and the number particle distribution in liquid in real-time (Figure 2.8). The Brownian motion can determine the particle size distribution as the particle size's speed depends on the particle size.



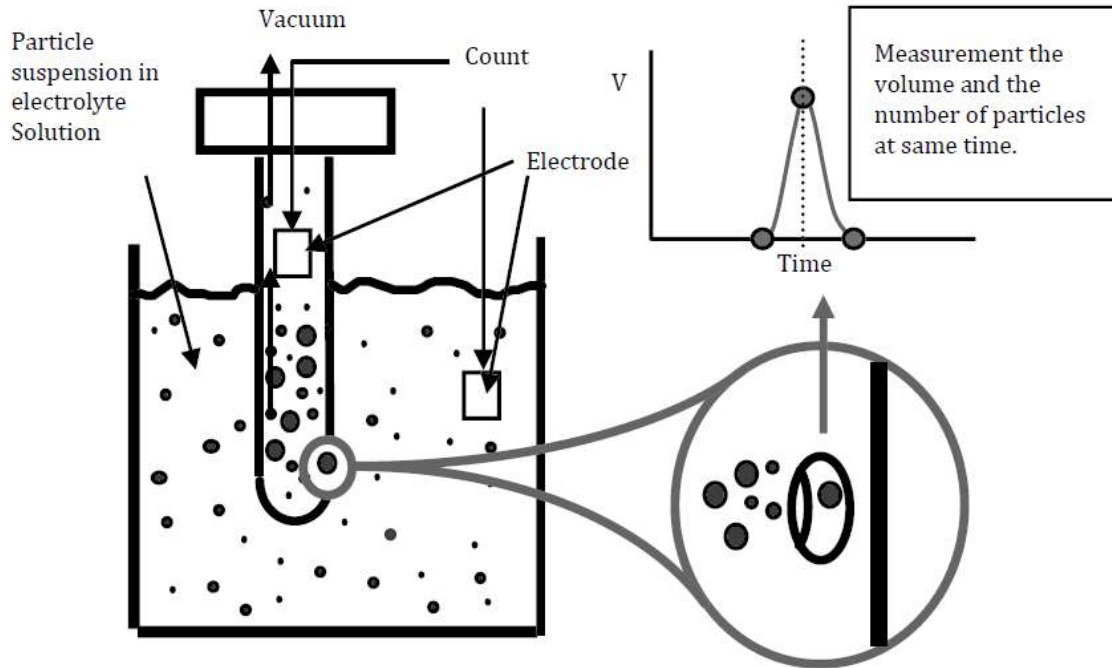
**Figure 2.8** Particle tracking analysis method.

Source: [www.idec.com](http://www.idec.com), accessed on 11/30/2020 [32].

### 2.3.4 Electrical sensing zone method

The electrical sensing zone (ESZ) method, also known as the Coulter principle, is based on increased electric resistance by particles in an electrical field passing an aperture or pore between two electrodes. The electrical resistance is proportional to the volume of particles passing through a pore. Because the volume of sample suspension passing through the

pores is known, the volume, diameter, and concentration of particles can be measured with a high degree of accuracy. Hence, it is possible to measure the particle distribution at ultra-high resolution and the concentration (number) of coarse particles (foreign particles and aggregated substance) (Figure 2.9).

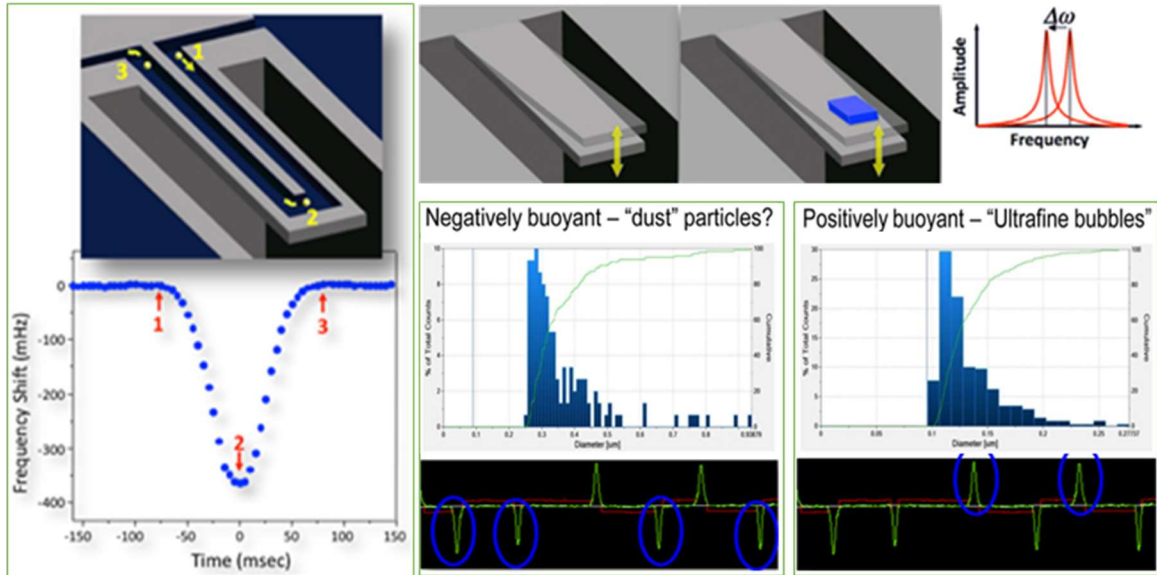


**Figure 2.9** Principle of the electrical sensing zone method.  
Source: Tusge [33].

### 2.3.5 Resonance mass measurement method

The resonance mass measurement method is an advanced innovative method (Figure 2.10) developed to detect and count the subvisible and submicron particle suspension in a liquid that can provide the size, weight, and distribution profiles [34]. At the center of the measuring device, the Micro-Electro-Mechanical Systems (MEMS) sensor is located with a resonant cantilever embedded with a micro-fluid channel. When a particle diameter of

50nm to 5 $\mu$ m passes through the fluid channel, the resonating frequency will be changed, allowing determine the suspended particle's weight, dry weight, and particle diameter.



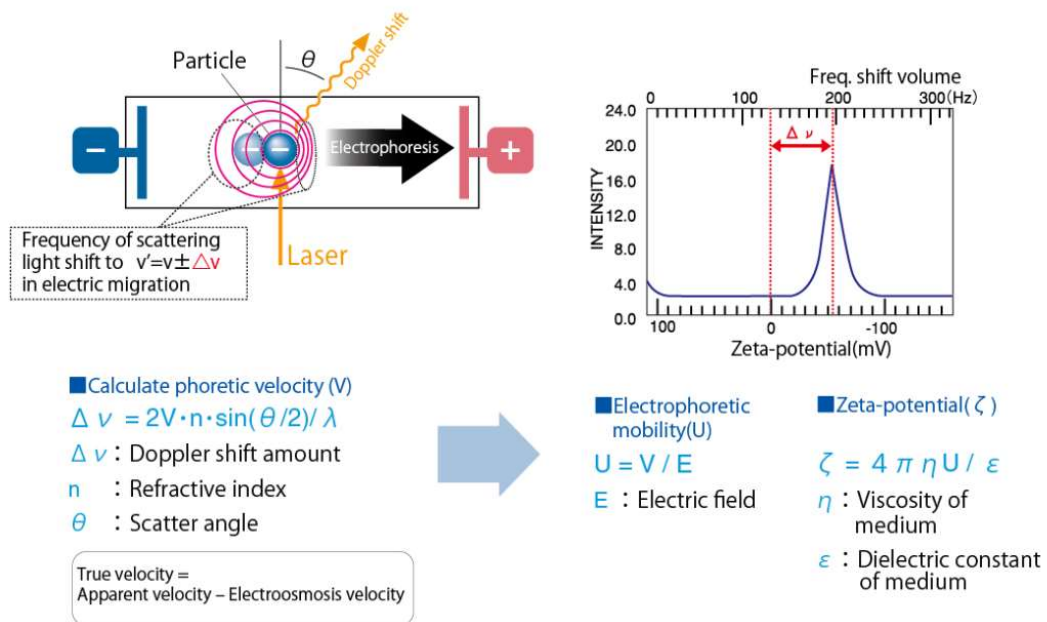
**Figure 2.10** Resonance mass measurement method.

Source: [www.idec.com](http://www.idec.com) [32].

### 2.3.6 Zeta-potential measurement method (particle tracking/dynamic light scattering)

A suspension's behavior depends on the surface interactions controlled by the particle size and surface chemistry. While the particle measurements' size is relevant to the particle size, shape, and porosity, the interface chemistry is related to the surface charge, surface tension, and contact angle. Due to the difficulty of obtaining the direct measurement of surface charges, zeta potential values are used to estimate the surface charge of a colloid system. Zeta potential is the potential at the shear plane. In order to measure the zeta potentials, acoustic techniques using and lights, scattering methods are used. Typical lights scattering methods include Electrophoretic light scattering (ELS), Static Light Scattering (SLS), and Dynamic Light Scattering (DLS) methods. However, Dynamic Light Scattering (DLS)

method (Figure 2.11) is used when the particle motion is related to the Brownian motion. Zeta potential is obtained by applying an electric field and measuring the particle's probe response to the applied field. Then based on the fixed electrode, the particle motion is detected using Doppler shift in scattered light. This method is referred to as Laser Doppler Method, where electrophoretic mobility is determined by the Doppler shift calculations and using the Smoluchovski equation to obtain the zeta potential.

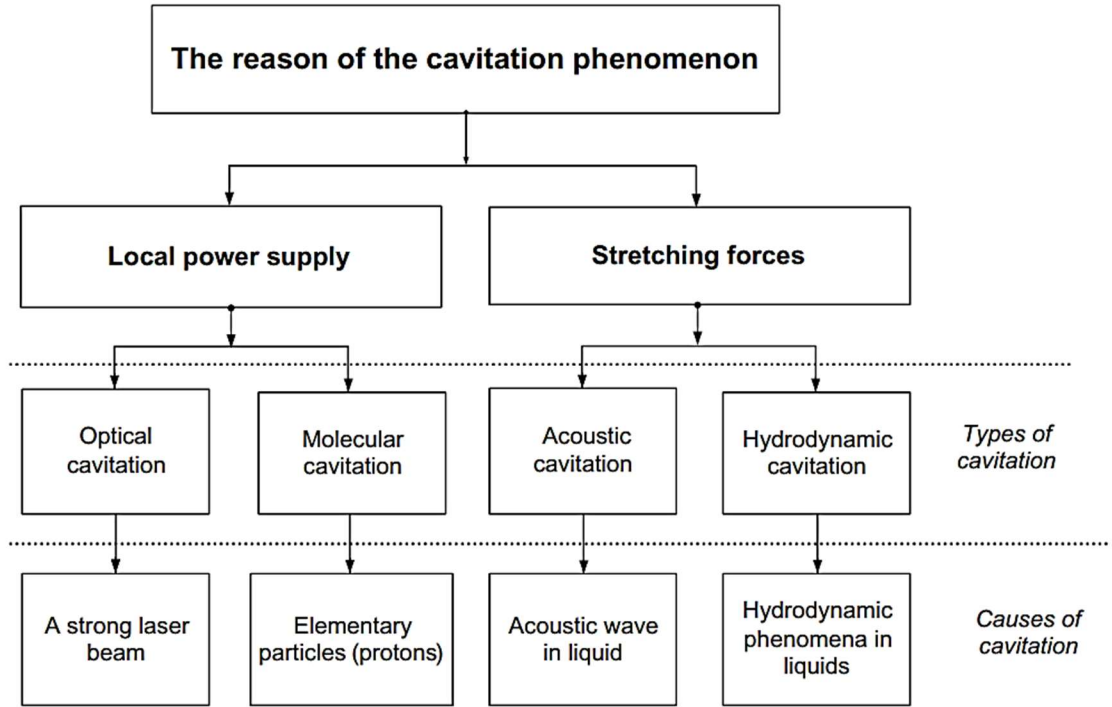


**Figure 2.11** Particle tracking/dynamic light scattering method.  
 Source: www.otsukael.com [35].

## 2.4 Nanobubbles Generation Techniques

There are various methods to generate fine bubbles, and they are mainly classified into the shear flow, nucleation, cavitation, and bubble break down by shockwaves. A combination of these separate mechanisms is possible. Nanobubbles are frequently generated in solutions by creating cavities. Cavitation is caused by a reduction in pressure below a

certain critical value. Based on the pressure reduction mechanism, cavitation mechanisms can be classified into four different types [3,36,37]; Figure 2.12 summarized them.



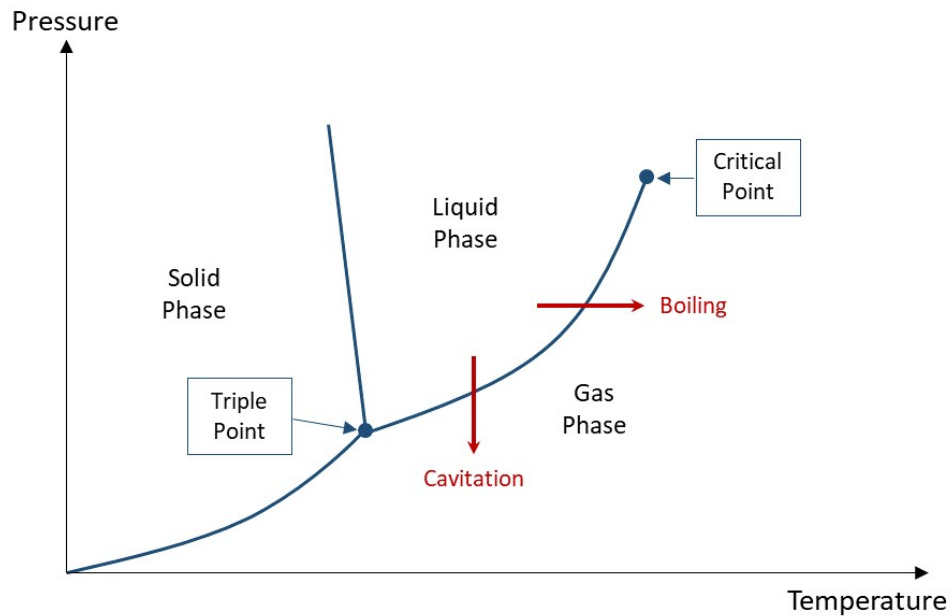
**Figure 2.12** Four main cavitation mechanisms.  
Source: Ozonек [38].

### 2.4.1 Hydrodynamic cavitation

Hydrodynamic cavitation is one of the most frequently used nanobubble generation methods due to its simplicity and low cost. However, one of the significant drawbacks of this method is that it generates a mixture of bubble sizes. In this method, based on the system's geometry, flowing liquid subject to pressure variation and liquid velocity varies locally and, at the point of the highest velocity, causes low-pressure zones, and hence, cavities are formed. Figure 2.13 shows the water phase diagram's sketch to show the gas cavitation occurs when the pressure inside the liquid becomes lower.

Young explained that, as the cavitation appears, to describe the type and stage of the cavitation, the term "incipient cavitation" is used [39]. Also, to explain the cavitation just before it disappears is termed as "desinent cavitation." In general, the boundary or threshold between no cavitation and detectable cavitation are not always identical. The negative pressure of the disappearance of cavitation is considered greater and less variable than that of the negative pressure of bubbles' appearance. In the hydrodynamic method, there is three possible flow cavitation.

1. Traveling cavitation - occurs when cavities or bubbles form in the liquid and travel with the liquid as they expand and subsequently collapse.
2. Fixed cavitation - occurs when a cavity or pocket is attached to the rigid boundary of an immersed body or a flow passage forms and remains fixed in position in an unsteady state.
3. Vortex cavitation - occurs in the cores of vortices which form in regions of high shear, and often occurs on the blade tips of ship's propellers - hence, the name "tip" cavitation.



**Figure 2.13** Sketch of the water phase diagram. Boiling is the phase change from liquid to a gas by temperature increase, whereas cavitation is the phase change by pressure decrease. Source: Batagoda et al. [40].

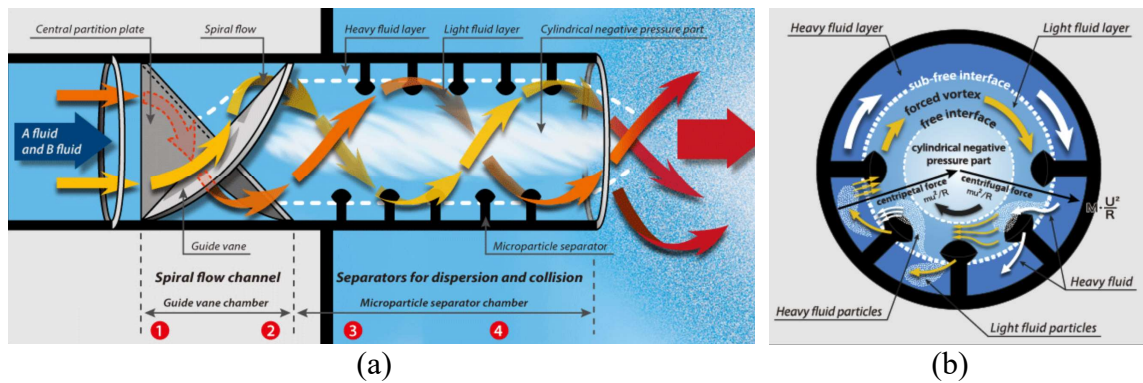


Nanobubbles are usually hydrodynamically generated using the following methods [33].

1. Inject low-pressure gases into liquids to break gas into bubbles by focusing, fluid oscillation, or mechanical vibration. (i.e., static mixer generator, rotational flow method)
2. Full or side streamflow using venturi (i.e., venturi type generator)
3. Dissolve gases in liquids by compressing gas flows in liquids, releasing those mixtures through nano-sized pores (diffusers) to create *nanobubbles*

The following section outlines some of the commercially used methods of bubble generation based on hydrodynamic cavitation.

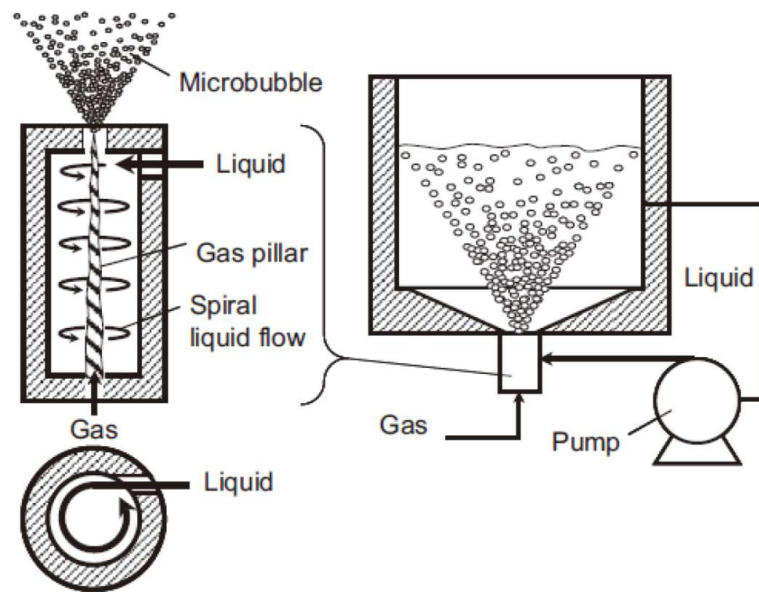
**2.4.1.1 Static mixture generator.** The static mixtures were initially produced for mixing two liquids, and now by mixing a liquid and gases. Figure 2.14 shows the OHR (Original Hydrodynamic Reaction) mixture, a specially designed static mixture. It consists of guide vanes and cutters, which creates high-speed swirl flow along the cylinder's centerline that forms a strong shear field. Nanobubbles will be generated by the combined effect of nucleation, cavitation and shear force and by shockwaves. Usually, a high-pressure pump is used to form smaller sized bubbles.



**Figure 2.14** OHR Laboratory Corporation (a) vertical section view (b) cross-section view. Source:www.ohr-labo.com [41].

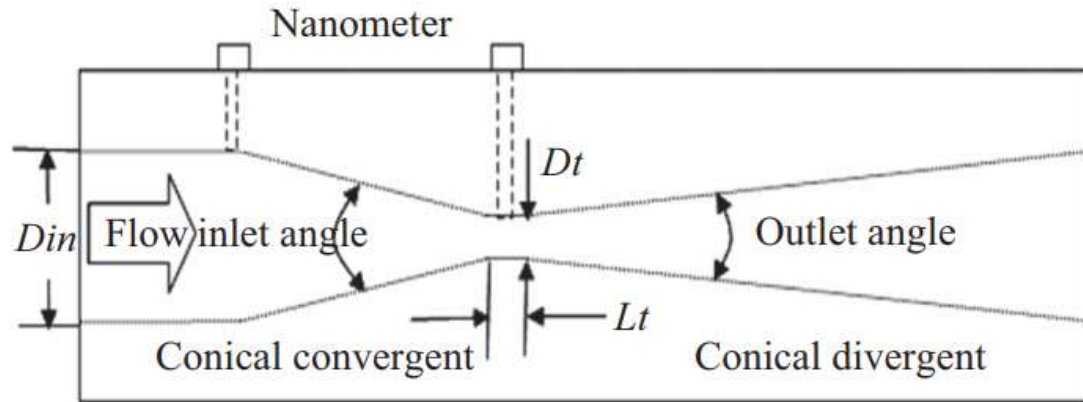


**2.4.1.2 Swirl flow type (shear force).** Water (or water-gas mixture) is allowed into a vessel in a tangential direction to form swirl flow inside the vessel. This swirl flow induces negative pressure along the vessel's centerline, which in turn sucks the air from the top of the vessel to generate rotational fluid flow (Figure 2.15). The Air column is then turned off into fine bubbles by strong shear flows in the vessel's outer region at the bottom or both ends.



**Figure 2.15** Spiral liquid flow generation method.  
Source: Li et al. [42].

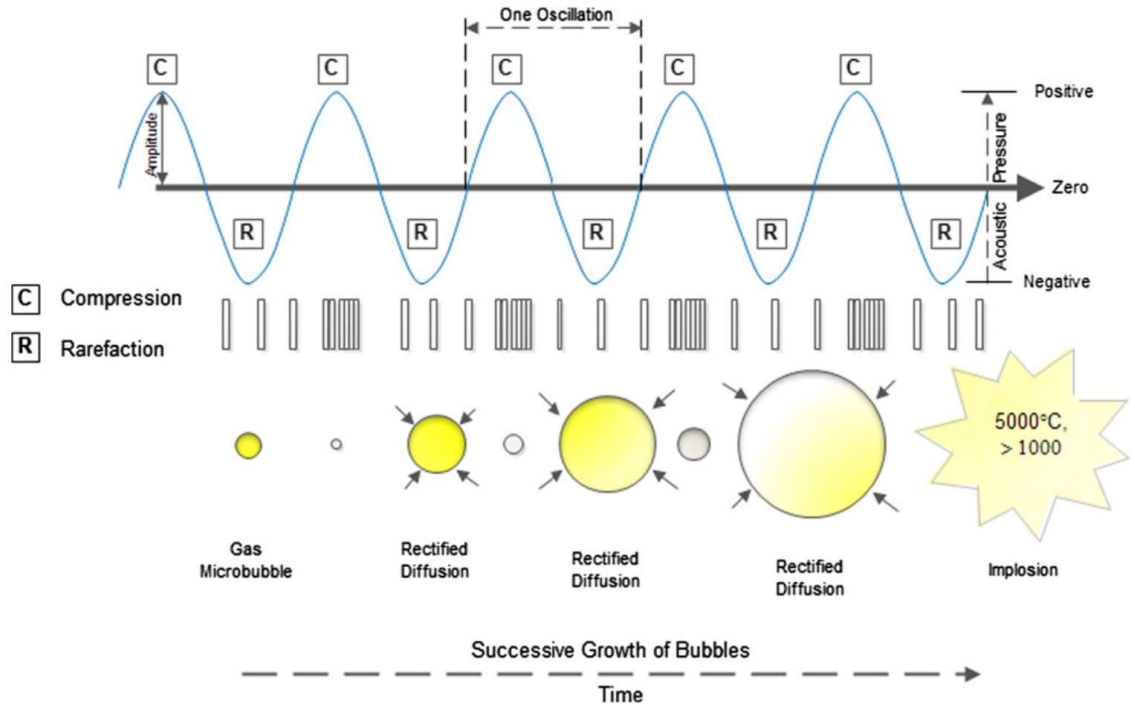
**2.4.1.3 Venturi type.** A liquid stream containing micro-bubbles flows from the inlet of a venturi tube. The two-phase flow is accelerated through the throat of the venturi tube. The pressure changes rapidly, and the nano/microbubbles are formed by reducing the macro-bubbles and/or by cavitation (Figure 2.16).



**Figure 2.16** Schematic diagram of the cavitation venturi tube.  
Source: Xiong et al. [43].

#### 2.4.2 Acoustic cavitation

The sound waves produce acoustic cavitation in a liquid due to pressure variations. In a static liquid system, the ambient pressure can be varied by sending the sound waves through the liquid. Due to applied sound waves, the liquid is subject to a mechanical force creating cycles of high pressure (compression) and low pressure (rarefaction) zones (Figure 2.17). The amplitude of the pressure variation reached or lower than the vapor pressure in the negative part of the sound cycle traversing the liquid will cause cavitation or bubble formation. Two distinct types of bubble motion are possible: Stable cavitation bubbles and Transient cavitation bubbles. Stable cavitation is a bubble that oscillates around their equilibrium position over several successive compression/rarefaction cycles and merges and rises to the surface. The Transient cavitation bubbles are referred to as the bubble grow over a few successive compression and rarefaction cycles until it reaches a critical size and then collapses.



**Figure 2.17** Growth and collapse of bubbles in acoustic cavitation.  
Source: Abbas [44].

In general, this is a non-linear process, and the bubble radius is not proportional to the sound pressure. Also, during these successive growth cycles, the bubble is obtaining an ample amount of potential energy from the sound wave, and therefore, at the collapse, kinetic energy is concentrated. As the bubble collapse, this high energy is concentrated into a very small volume, producing very high pressures and temperatures that can erode solids, initiate chemical reactions, and produce radicals [39].

### 2.4.3 Optical cavitation

Optical cavitation is caused by short-pulsed (high intensity) lasers focused on low absorption coefficient solutions [36,45]. This optical cavitation happens when the large pulses of a Q-switched ruby laser are focused onto a liquid. Under such extreme

environments, the breakdown of the medium occurs, and bubbles are formed. These bubbles formation can capture through a high-speed rotating mirror camera.

#### **2.4.4 Particle cavitation**

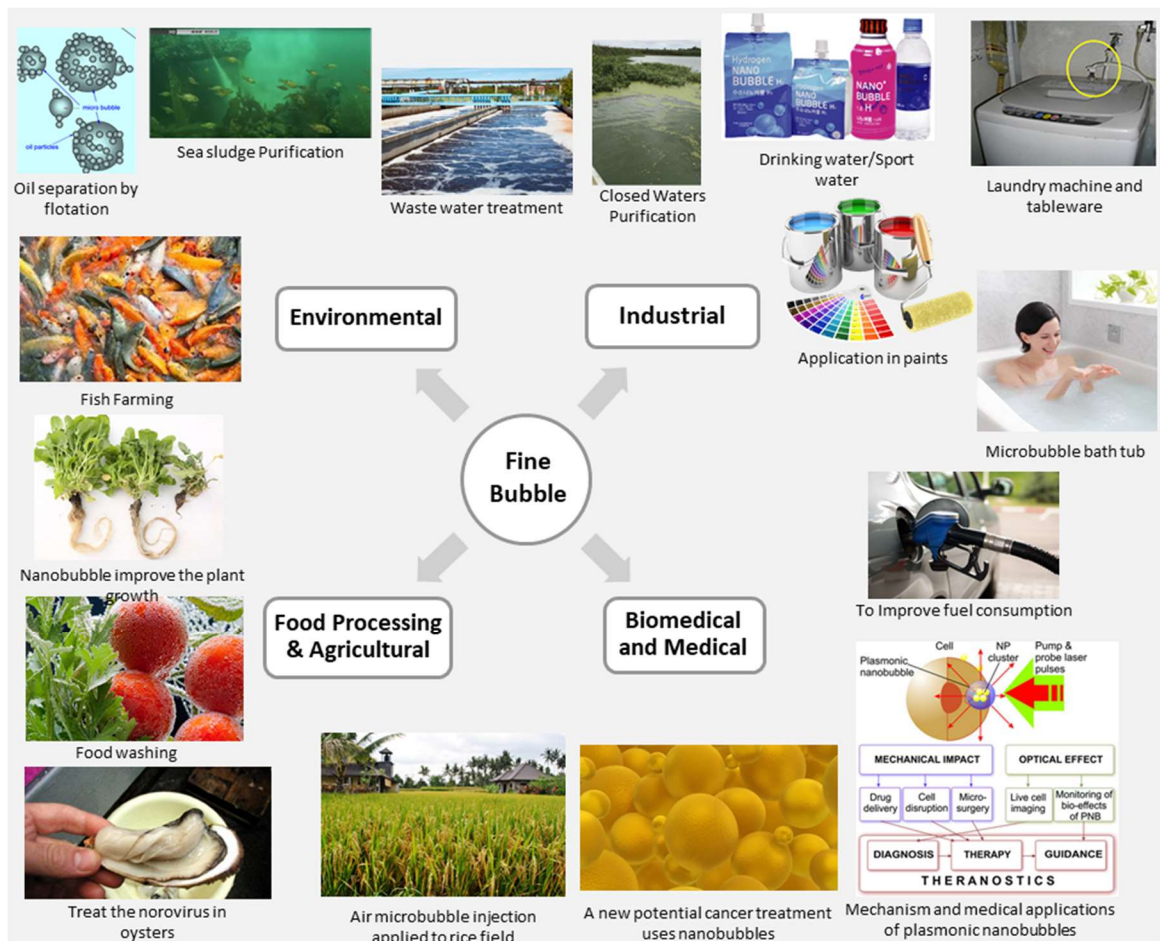
Particle cavitation is caused by passing high-intensity light photons in liquids [46]. Particle cavitation is the result of bubble growth in a superheated liquid. Once the charged particle moves through the fluid, it leaves ionization tracks for a fraction of a second. Those ions' energy can transfer to a few fast electrons, and they can gain 1000 electrons volts of energy in a small volume to generate instantaneous local heating. Therefore, if the liquid subject to superheating by expansion, boiling will cause along the track, and tiny bubbles appear [39].

In summary, hydrodynamic cavitation and acoustic cavitation are created by tension in the liquid, while optic cavitation and particle cavitation are generated by local deposition of energy [38,39]. Unlike hydrodynamic/acoustic cavitation, in particle/optical cavitation, controlled bubble generation can be achieved. Likely, bubble size, their location within the liquid can also be controlled. However, their operation cost is much higher and hence, not widely found in practical applications and only found in laboratory and research studies [38].

### **2.5 Industrial Application of Nanobubbles**

As both measurements and generation technology has progressed, scientific research and the development of industrial application of nanobubbles also have moved forward. Significant success has particularly been achieved in using nanobubbles for cleaning applications. Fine bubbles are currently primarily used for injecting gasses into liquids,

changing the state of fluids, separating particles of waste by flotation, cleaning and sterilization, and medical treatments. The summary of the current application of fine bubbles is shown in Figure 2.18. With the increased improvement of bubble generation technology, industrial applications will be rise rapidly in the near future. Nanobubbles have an extensive range of applications, such as drinking water treatment, wastewater treatment, groundwater treatment, soil and sediment treatment, biomedical engineering, and other industrial applications such as agriculture, fishery, food, cosmetics, emulsified fuel, and cleaning.



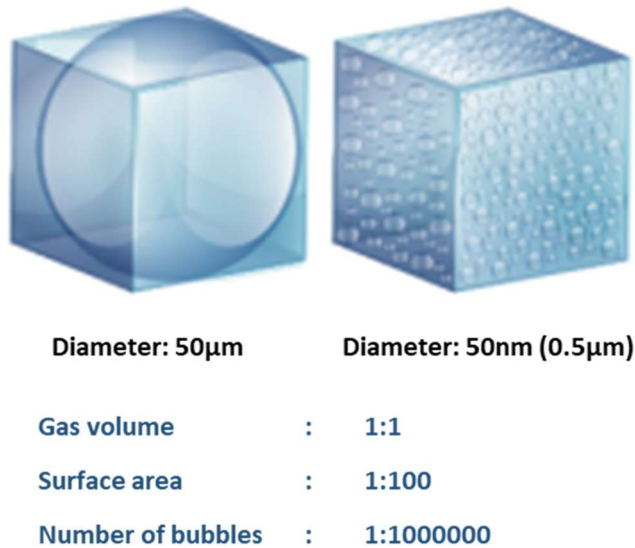
**Figure 2.18** Application of fine bubbles.

## 2.6 Characteristics of Ultrafine Bubbles or Nanobubbles

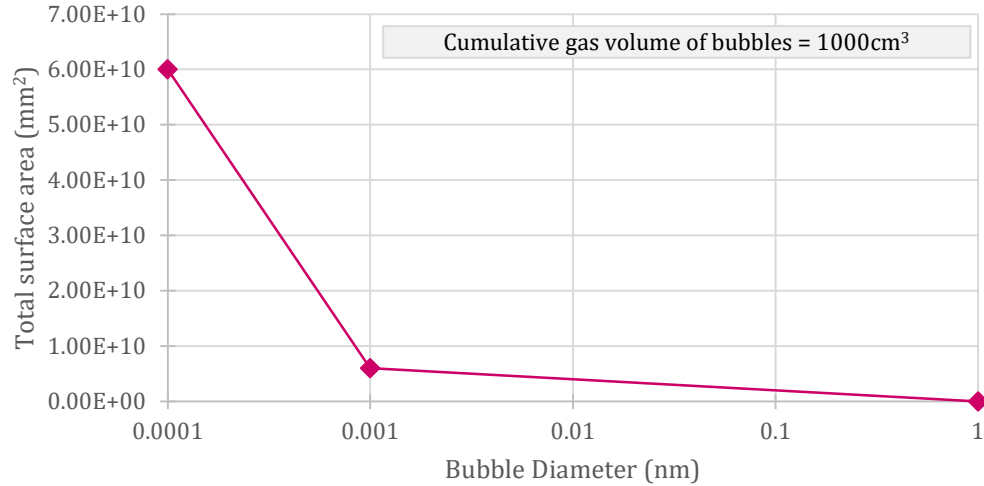
Nanobubbles have had increased industrial applications due to its interfacial properties and their stability in aqueous solutions. The following section will describe their special characteristics and features.

### 2.6.1 Smaller size and high surface area

Nanobubbles are very small in size when compared to regular bubbles. Yet, nanobubbles have a much higher surface area for a fixed volume of gas than the regular bubbles (Figure 2.19) [3,6]. This increased surface area is a crucial factor when considered for industrial applications. With higher specific area or higher contact area will allow higher gas mass transfer rates [6,47].



**Figure 2.19** Comparison between the surface area of microbubble and nanobubble at the same volume.



Bubble Diameter (mm)	Volume (mm <sup>3</sup> )	Surface area of bubble (mm <sup>2</sup> )	Total number of bubbles	Total surface area (m <sup>2</sup> )
1	$5.24 \times 10^{-01}$	$3.14 \times 10^{+00}$	$1.91 \times 10^{+06}$	$6.00 \times 10^{+06}$
0.001	$5.24 \times 10^{-10}$	$3.14 \times 10^{-06}$	$1.91 \times 10^{+15}$	$6.00 \times 10^{+09}$
0.0001	$5.24 \times 10^{-13}$	$3.14 \times 10^{-08}$	$1.91 \times 10^{+18}$	$6.00 \times 10^{+10}$

**Figure 2.20** Increase in the specific area of bubbles with decreased bubble size.

Figure 2.20 shows, using the same amount of gas volume (in here 1000 cm<sup>3</sup>), to form the different sizes of bubbles (diameter 1mm, 0.001mm, 0.0001mm) and then the total number of bubbles can form and the total surface area. Thus, with nanobubbles, an increased amount of bubbles and an increased specific area for the same amount of gas volume are obtained. It will ultimately improve the gas mass transfer efficiencies and reaction capabilities.

### 2.6.2 Low buoyancy and low rising velocity

Smaller nanobubbles have a very small buoyancy force acting on them, resulting in very low rising velocity. The rising velocity of any particle in the solution will depend on two primary forces in the system are gravity and drag (Figure 2.21). The point at which drag force and gravity forces are equal determine the particle's terminal velocity. For the

Laminar flow regime, Stoke's law is applied to calculate the terminal velocity. Stoke's law is given in Equation (2.1) below;

$$v_t = \frac{1}{18} g d^2 \frac{(\rho_m - \rho_b)}{\eta} \quad (2.1)$$

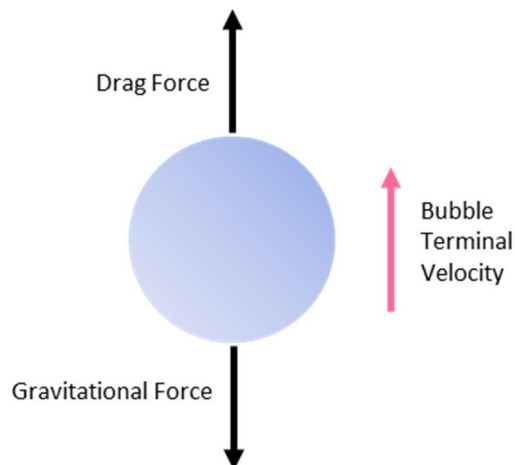
Where,  $v_t$  = terminal velocity of the bubble (m/s),  $g$  = gravitational acceleration ( $m/s^2$ ),  $d$ = diameter of the bubble (m),  $\rho_m$  = density of medium ( $kg/m^3$ ),  $\rho_b$ = density of gas bubble ( $kg/m^3$ ),  $\eta$  = viscosity of medium ( $kg/m/s$ ),  $V_t$  (m/month).

The following Table 2.1 and Figure 2.22 shows the bubble size with the terminal velocity of oxygen nanobubbles, with an assumed gas density of  $\rho_b=1.331kg/m^3$ .

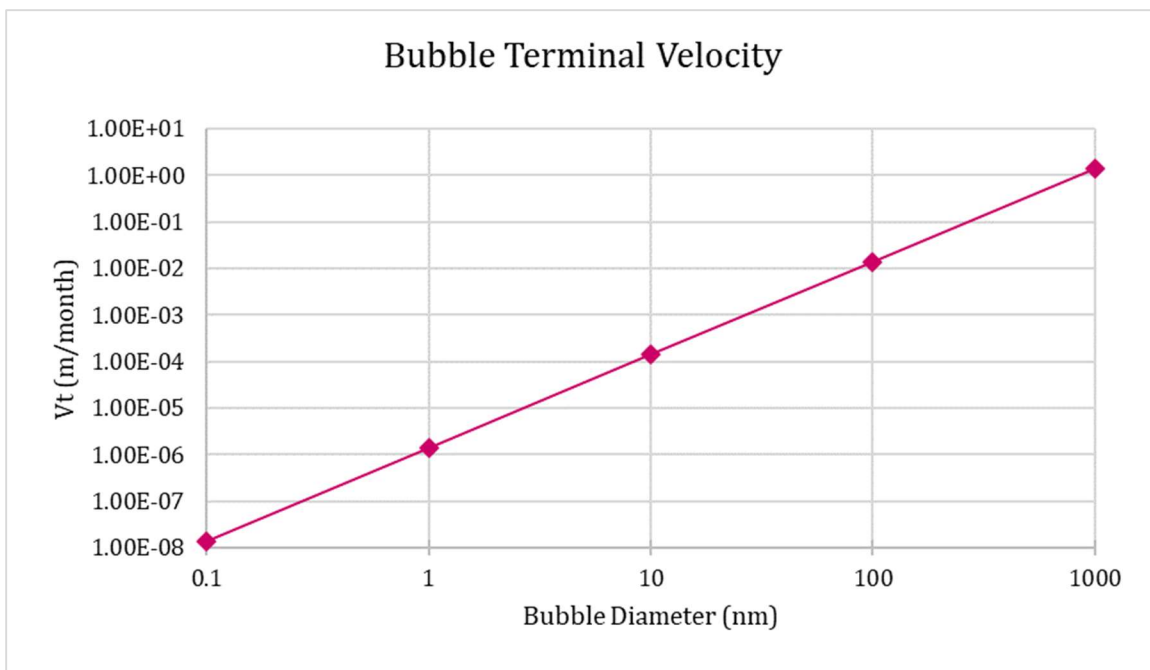
**Table 2.1** Terminal Velocity of Oxygen Nanobubbles

Diameter (nm)	Terminal velocity (m/s)	Terminal Velocity (m/day)	Terminal Velocity (nm/day)	Terminal Velocity (m/month)
0.1	$5.42 \times 10^{-15}$	$4.69 \times 10^{-10}$	$4.69 \times 10^{-01}$	$1.41 \times 10^{-08}$
1	$5.42 \times 10^{-13}$	$4.69 \times 10^{-08}$	$4.69 \times 10^{01}$	$1.41 \times 10^{-06}$
10	$5.42 \times 10^{-11}$	$4.69 \times 10^{-06}$	$4.69 \times 10^{03}$	$1.41 \times 10^{-04}$
100	$5.42 \times 10^{-09}$	$4.69 \times 10^{-04}$	$4.69 \times 10^{05}$	$1.41 \times 10^{-02}$
1000	$5.42 \times 10^{-07}$	$4.69 \times 10^{-02}$	$4.69 \times 10^{07}$	$1.41 \times 10^{-00}$





**Figure 2.21** Force balance of a bubble and terminal velocity.

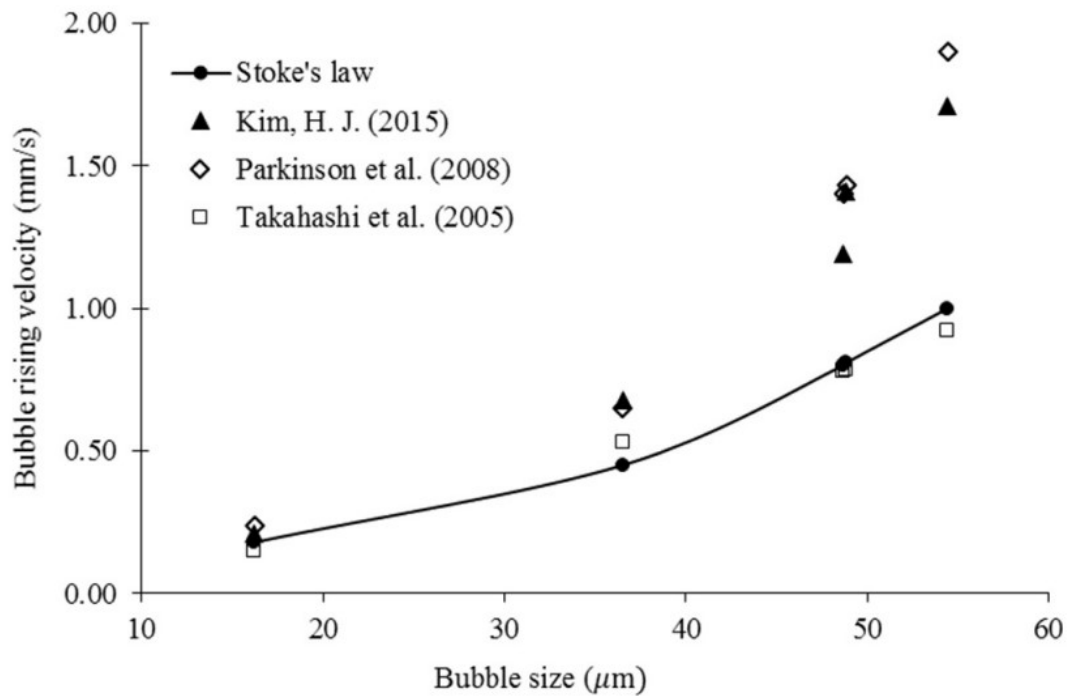


**Figure 2.22** Terminal velocity of oxygen nanobubbles.

The bubble stability can be related to the rising velocity of bubbles as the slower the terminal velocity, the longer it takes a bubble to reach the surface. Based on the calculations, a bubble with a 100nm diameter would just rise around 1.5cm per month.

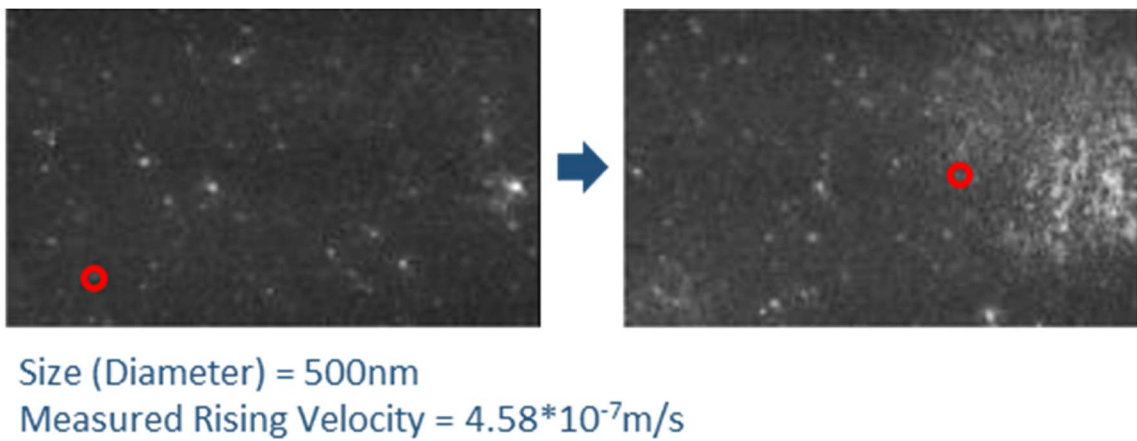
When the bubbles are at the nanoscale, they have a very slow rising velocity; hence, the possibility of longer residence time in the solution. However, the bubble lifetime does not only depend on the rising velocity. Therefore, other factors such as gas diffusion/dissolution should be included to understand the bubble stability. These slow rising velocity bubbles are continually moving through the water because of collisions with the water molecules' Brownian motion.

Takahashi reported the rising speed of 50  $\mu\text{m}$  sized microbubbles is approximately 1 mm/s [18]. Temesgen summarized the rising-velocity measurements of the microbubbles conducted by different researchers [47], and those results also indicated that the rising velocity increases for larger sizes of the bubble (Figure 2.23). The velocity of nanobubbles has been experimentally measured by Seung-Uk, and based on their results, the rising velocity of the 500nm diameter bubble is  $4.58 \times 10^{-7} \text{m/s}$  (Figure 2.24) [11]. Their experimental results also clearly indicate the negligible rising velocity of the nanobubbles.



**Figure 2.23** Rising velocities of the MBs according to size (data points show a single bubble).

Source: Temesgen et al.[47].



**Figure 2.24** The measured rising velocity of 500nm size bubble.

Source: Seung-Uk [11].

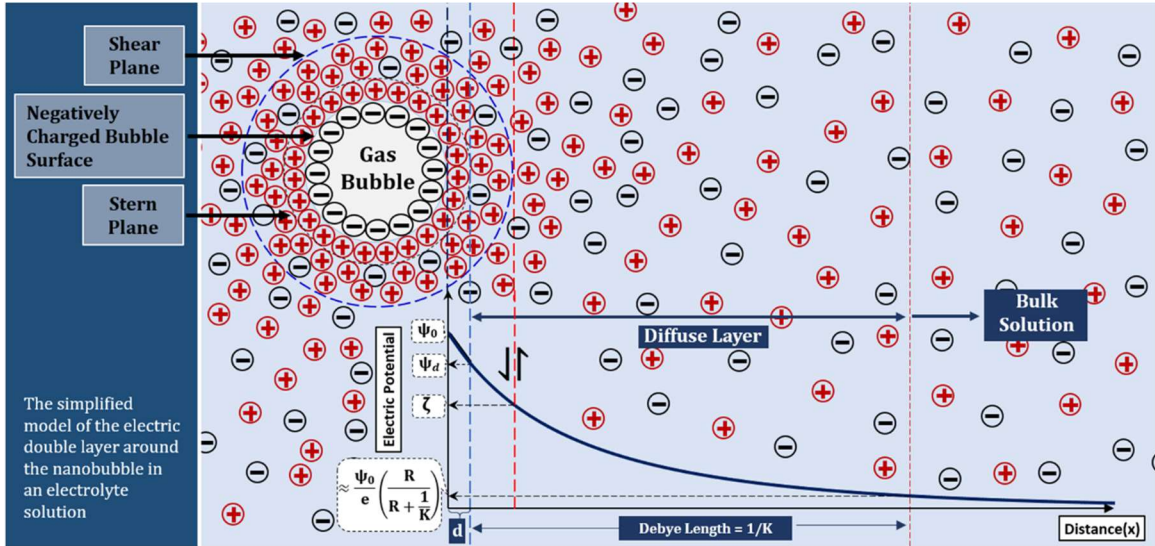
### 2.6.3 Electrically charged gas-liquid interface

Micro/nanobubbles were reported to have an electrically charged interface [18,22,48,49]. The electrical charge on the surface of nanobubbles is one of the main reasons for their wide application. The electrical charge on the bubble plays a vital role in bubble stability and the interfacial property that causes the bubble interactions mechanism. This property is very important in many applications such as bubble-mineral particle interactions, bubble coalescence affecting several industrial processes, mineral flotation, oil sand separation, water, and wastewater treatment [50].

By considering the electrical charge on nanobubbles (surface charge), zeta potential is widely used as they are directly correlated to each other [3]. This is because the direct measurement of surface charge or surface charge density is practically difficult. Even though the zeta potential is not a direct measurement, based on the electrostatic mobility of colloidal particles, surface charge density can be easily determined using the zeta potential. The following section explains the zeta potential and the importance of its measurements towards the bubble's stability.

*Zeta potential.* The presence of an electrical charge on the bubble surface causes the ion distribution around the bubble surface, leading to an electric double layer (EDL) around the bubble. The double-layer is referred to as the two layers where ion distribution contributes. The first layer is referred to as the Stern later, where ions are firmly attached to the charged particle due to electrical attraction. The second layer, called the diffused layer, consists of loosely attached ions attracted to the surface charge due to the Coulomb force. In the diffuse layer, there is an imaginary boundary called the slipping plane. The ions within this boundary move with the bubble, and the ions outside this boundary are not subject to movement with the bubbles (Figure 2.25). The electric potential at this boundary

is defined as the zeta potential [51]. Zeta potential is a critical parameter when discussing the bubble stability and bubble interactions or inter-particle attractions and repulsion. A high absolute  $\zeta$ -potential would create repulsion forces that would avoid bubbles' coalescence and contribute to bubble stability.



**Figure 2.25** The ion distribution around the nanobubble and the zeta potential.

Many researchers have been investigated the surface charge of the nanobubbles and found to be negatively charged under the wide range of pH values [18,47,48,52,53]. Likewise, it was found that the negativity of nanobubbles decreased with increased acidity, and for strong acids ( $\text{pH} < 2$ ), positive zeta potential values were obtained [18,54]. Also, the inorganic electrolytes can decrease the negative surface charge by increasing the counterions at the interface. The negative zeta potential is said to be due to the absorption of  $\text{OH}^-$  ions at the gas-liquid interface and causes due to the difference enthalpies of hydration of  $\text{OH}^-$  and  $\text{H}^+$  ions, the  $\text{H}^+$  ions are likely to remain in the bulk aqueous phase, while the  $\text{OH}^-$  stays at the bubble gas-water interface. [18,47,55,56].

## 2.6.4 Thermodynamic properties of nanobubbles

For the bubble to be in thermodynamic equilibrium, both the mechanical and chemical equilibriums must be obtained. Mechanical equilibrium is related to the balance between opposing mechanical forces or the pressures within the system. Chemical equilibrium refers to the state of balance in the nonmechanical forces that drive specific chemical species from one region to another (i.e., Entropy is an example of a nonmechanical driving force). For nanobubble to be in mechanical equilibrium, the total outward pressure inside the bubble at the gas-liquid interface should be equal to the total inward pressure at the gas-liquid interface. This pressure relationship is given by the Young Laplace equation, which will be discussed below. To bubble system to chemically equilibrium, the partial pressures of each of the gas constituents of the bubble should be equal to their respective pressures in the solution phase determined by Henry's law.

**2.6.4.1 Mechanical equilibrium (based on Young Laplace equation).** Bubble mechanical equilibrium can be expressed by the Young Laplace Equation (2.2). This equation describes the relationship between the pressure difference and the radius of the bubble. [23,48,57].

$$P_{\text{inner}} = P_{\text{outer}} + \frac{2\gamma}{r} \quad (2.2)$$

Where,  $P_{\text{inner}}$  – pressure inside,  $P_{\text{outer}}$  – pressure outside,  $\gamma$  – surface tension, and  $r$  – radius of the bubble.

Based on Equation (2.2), under atmospheric pressure, nanobubble should not exist for a long time. If the justification for the Equation (2.2) would be computed for nanobubbles with radii of 25nm and 100nm, for the surface tension  $\gamma$  with assumed 0.0728N/m, give the internal pressure values of approximately 15atm and 58atm. At these such pressures, nanobubble should be dissolved within milliseconds.

The pressure created by the surface charge can partially balance the pressure created to balance the surface tension, and the Young Laplace equation can be modified, as shown in Equation (2.3), to accommodate the force created by the electrical repulsion from charges on the surface of a nanobubble.

$$P_{inner} = P_{outter} + \frac{2\gamma}{r} - \frac{\sigma^2}{2D\epsilon_0} \quad (2.3)$$

Where,  $P_{inner}$ - pressure inside,  $P_{outter}$  – pressure outside,  $\gamma$ = surface tension,  $r$ =radius of the bubble,  $\sigma$ = charge density,  $D$ =dielectric constant, and  $\epsilon_0$  = permittivity of vacuum.

However, the pressure due to the surface tension is several orders of magnitudes higher than that due to the electrical charge on the surface, and bubbles are still subjected to high internal pressure based on Equation (2.3) for small nanobubbles. Nanobubbles of such high internal pressure should not be at equilibrium with surrounding solutions and dissolve instantaneously [53]. In consequence, the mechanical stability of the nanobubbles itself cannot explain the bubble stability.

**2.6.4.2 Chemical equilibrium (based on Henry's equation).** The bubble will be chemically in equilibrium when partial pressures of each gas type in the bubble is equal to their respective bulk liquid gas pressure determined by Henry's law. However, based on the solution gas saturation (undersaturated, saturated, or supersaturated), bubbles will shrink or grow. Moreover, when hydrodynamics and acoustic cavitation are used to form nanobubbles, a mixture of bubbles is formed of different sizes. This means they are in different sizes; hence, their chemical potentials are not similar. According to Henry's law and the Gibbs-Thomson equation, the smaller bubbles have larger chemical potentials as the gas in the bubble diffuse into the surrounding solution [27]. Thus, a larger bubble grows, and a smaller bubble diffuses into larger bubbles.

Based on the above, the classical thermodynamics theory itself cannot explain the stability of nanobubbles. Therefore, under normal conditions, nanobubbles would not be expected to reach the equilibrium state without reducing the surface tension. So some researchers believe that this is obtained by adjusting the surface properties of the gas-liquid interface with the creation of a diffusion barrier (ion/impurity accumulation) or due to the hydrogen bond structure formed a barrier around the bubble to reduce or prevent gas diffusion.

### **2.6.5 Diffusion barrier**

Based on the thermodynamics theories, nanobubbles' lifetime would be very short due to the induced high internal pressures. In practice, it is believed that the dissolution rates would be reduced due to the diffusion barrier, which means an accumulation of cations or anions (ionic shielding) [27,58,59] and accumulation of impurities, surfactants or small organic molecules [60–62]. Seddon et al., suggested that the electrolytes increase the



lifetime of dispersed nanobubbles due to the ionic shielding effect [58]. Uchida et al. showed the existence of an ion accumulation zone around the bubble surface using the Transmission Electron Microscope (TEM) and concluded that a small amount of NaCl accumulation around the nanobubble increases its stability via the ionic shielding effect [27]. Takahashi reported that with a higher concentration of electrolytes (NaCl and MgCl<sub>2</sub>), the reduction of zeta potential and reduction of their electrostatic repulsion lead to bubble coalescence and instability [18]. Ducker hypothesized an insoluble coat in each nanobubble, reducing the interfacial tension (and Laplace pressure) and providing a barrier to diffusion [61]. Zimmerman et al. explained that the validity of the physical skin model with bulk nanobubbles and illustrated the resistance to the diffusion with the presence of organic or surfactant molecules on the surface [60].

### **2.6.6 Hydrogen bonds**

Based on the literature, nanobubbles should not be thermodynamically stable. However, experimental results confirm nanobubbles' existence for a considerably long period (i.e., two weeks). Ohgaki et al. explained that there should be a reason for high resistance to gas diffusion through the gas-liquid interface [19]. They explained that nanobubbles' interface should consist of hard hydrogen bonds similar to the hydrogen bonds found in ice and gas hydrates [63]. Therefore, Ohgaki et al. concluded that the interfacial film's characteristics strongly influence the superficial stability, and the hard interface made of hydrogen bonds reduces gas diffusion from the nanobubble [19]. They explained the high surface tension (twice the normal values) arising from the hard interface's presence also helps to maintain a kinetic balance against the high pressure.

### 2.6.7 Gas saturation

As with bubble gas diffusion, nanobubble life should decrease. It has been suggested and experimentally shown by several researchers, the supersaturation of gas in the vicinity of the bubble to reduce the gas outflux. In theory, if the bulk liquid medium is supersaturated relative to the bubble, the bubble is expected to grow, and if the bulk medium is an undersaturated bubble is expected to shrink. If all the pressures are in equilibrium in the system, bubble size would remain unchanged and would not cause any mass transfer between the bubble and the surrounding liquid [64]. In such conditions, bubbles are considered to be either thermodynamically stable (globally lowest total free energy) or thermodynamically metastable (at local, but not global, minimum free energy) [64]. These metastable states eventually change to another metastable state or a thermodynamical equilibrium state. Therefore, nanobubble stability would also depend on the gas concentration in the solution.

Based on Uchida et al.'s experimental results, by maintaining high DO concentration than the O<sub>2</sub> saturation, the bubble can maintain at the "semi-stable" state [27]. Uchida et al. concluded that if there are a sufficient number of micro/nanobubble in the solution, the solution remains at saturation, a condition that would reduce the dissolution rate of gas from the bubble (diffusive shielding) [27]. Also, Weijs et al. explained that a locally high concentration of dissolved gas in the water suppresses the diffusive outflux from the bubble, which is defined as the diffusive outflux shield effect [1]. Seddon et al. stated that metastable nanobubbles are possible with a supersaturated solution [58]. When many nanobubbles are available in the solution, the smallest bubbles dissolve and create a supersaturated condition with respect to atmospheric pressure;

therefore, bubbles reach equilibrium with no gas outflux until the gas concentration of the bulk solution is reduced.

### **2.6.8 Clusters**

To explain the nanobubbles stability, many have suggested bubble clustering. However, this concept still needs validation through experiments. Weijs et al. used the molecular dynamic simulation to explain the nucleation and stability of bulk nanobubble clusters [1]. They summarized that if the bubble-bubble interfacing is small, bulk nanobubbles are stable against dissolution, as a cluster of bulk nanobubbles protect each other from dissolution by a shielding. Due to the Brownian motion bubbles coalescence or Ostwald ripening (small bubble drain to the larger bubble), this stability is not expected to last forever. Bunkin et al. showed the existence of the long-living gas nanobubbles and spontaneously formed clusters of nanobubbles in an aqueous salt solution saturated with dissolved gas [65]. Bunkin et al. presented a quantitative theoretical model to describe ions' adsorption at the bubble interface and explained the bubble clustering [59]. The coagulation of identical nanobubbles in an ionic solution should not be attributed to the likely charged bubbles' interaction but opposingly charged compound bubbles.

### **2.6.9 Radical**

Acoustic cavitation causes the formation of OH radicals. The application of a sound wave (mechanical force creating cycles of high pressure or compression and low pressure or rarefaction) to a liquid cause acoustic cavitation. Within the successive sound cycles, bubbles were created to reach a critical size and collapse. With such collapse, the accumulation of energy into a small volume can produce high temperatures and pressures at the moment of collapse and cause chemical reactions and radical formation [25,66].

During the hydrodynamic cavitation and collapse, many OH radicals are produced due to elevated temperatures and pressures inside the bubbles [67,68]. High reactive radical formation opens many valuable applications related to the water disinfection and cleaning/defouling of solid surface, including membrane and many other applications [23].

It was recorded radicals are formed in the absence of a dynamic stimulus. Takahashi and Liu et al. were detected radicals in nanobubbles' bulk solution after stopping nanobubbles' generation (without present dynamic energy) [23,24]. Tada et al. and Yasui et al. showed the opposite, no OH radical generation from dissolving nanobubbles [25,69].

## CHAPTER 3

### STABILITY OF NANOBUBBLES

#### 3.1 Introduction

Nanobubbles or ultrafine bubbles are defined as cavities of gases with a diameter of less than 200nm in aqueous solutions [2]. Nanobubbles' industrial application has exponentially increased over the past two decades due to their reactivity and stability compared with macro and microbubbles. Due to the size, they have high specific surface areas and high stagnation times [7], which increases mass transport efficiencies, physical absorptions, and chemical reactions at the gas-liquid interfaces. Moreover, these ultrafine bubbles are very important because of long residence time in solutions and electrically charged surfaces [8]. Due to the above, nanobubbles have many industrial applications such as manufacturing of functional materials, soil and sediment decontamination, pharmaceutical delivery, and disinfection of food products [9].

After generation, nanobubbles are found to exist in aqueous solutions for several weeks. Azevedo et al. reported that bubbles of radii 150-200nm were in a solution for two weeks [10]. The electrically charged liquid-gas interface of nanobubbles creates repulsive forces that prevent bubble coalescence. Hence, high bubble densities create high dissolved gas concentrations in water, creating smaller concentration gradients between the interface and the bulk liquid [6]. Moreover, bubbles' stability increased by the low rising velocity that is not measurable due to Brownian motion and low buoyancy forces. Other than these reasons, nanobubbles are considered to be stable by a mutual shielding against the diffusive outflow of gases, which can be achieved if bubbles are sufficiently close together or gathered into micrometer-sized clusters [12].

As of now, the presence of stable nanobubbles have been experimentally confirmed, yet a clear theoretical basis has not been established to explain their long term stability. Hence, for effective and functional use of these bubbles, knowing their properties and behavior are quite important. Yet, nanobubble behavior is considered to be complex. Therefore, a further study is required for a proper understanding of the stability of nanobubbles, impacted by generation techniques, coalescence, free radical generation, influencing factors of stability of nanobubbles, such as temperature, pressure, pH, salt concentration, ion strength, presence of organic matters, the origin of the nanobubbles, etc. The following section describes the exponential growth of nanobubbles' application in many fields of science, technology, and industry.

### **3.2 Applications of Nanobubbles**

Nanobubbles have an extensive range of applications such as in drinking water and wastewater treatment, including decontamination of groundwater, decontamination of sediments and soils; biomedical engineering; and other industrial applications such as agriculture, fishery, and food.

The nanobubbles have recently been developed in wastewater and drinking water treatment due to their ability to generate highly reactive free radicals [3]. Hu and Xia showed the feasibility of remediating groundwater using ozone micro-nano-bubbles [70].

Meegoda proposed a new technology to decontaminate sediments using ultrasound with ozone nanobubbles [71]. It uses three innovative technologies, namely, ultrasound, ozone, and nanobubbles, to provide a cost-effective and environmentally sustainable on-site treatment of sediments with a lower total cost over a shorter time span. It also has a minimal adverse impact on the environment and the socio-economic growth of the region.

The ultrasound energy provides agitation and sediment decontamination. The ozone reacts with desorbed contaminants for removal from water. The nanobubbles help the dissolution of ozone gas in water [72–74]. The use of nanobubbles was motivated by their air sparging experiments [75–77].

There are many biomedical applications of nanobubbles. One of them is the delivery of cancer drugs, where nanobubbles are placed in the body and are given the ability to identify tumor cells. The bubbles are blown up when they approach tumor cells, destroying cancer [78]. Nanobubbles have also been used in an emergency procedure, where nano oxygen bubbles are injected directly into the bloodstream allowing people who are suffocating an extra 15 minutes during transportation to hospitals. While this is not a long time, but it does allow for a higher survival rate [79].

There are many industrial applications of nanobubbles. Nanobubbles have shown the ability to create reactive oxygen species that contribute to seed germination. This increase in reactive oxygen species has the same effect as adding  $H_2O_2$ , resulting in higher germination rates [24]. Nanobubbles are also used in sparkling water and sports drinks. With the addition of nanobubbles, the water can potentially keep gases for a longer time period [80]. Nano-bubbles also have application in paints. Due to the presence of nanobubbles, the paint dries faster and also resists mold. Also, there is an increase in brightness due to nanobubbles [81]. Nanobubbles are also used as artificial flotation in water. This is accomplished by altering the ionic equilibria of dissolved ions in solutions and by changing the net charge on particle surfaces [82].

Nanobubbles are also used in the food industry. Nanobubbles are used to regulate pH levels in liquids utilizing  $CO_2$ . This is achieved by adding nano carbon dioxide bubbles

which are suspended in the water for a long time regulating solution pH [83]. Nanobubbles are also used in fish farming. Studies have shown that a decrease of oxygen leads to decreased respiration and feeding activity that slows the fish's growth rate. However, with nano air bubbles, oxygen levels in water are maintained, leading to high fish survival rates [84].

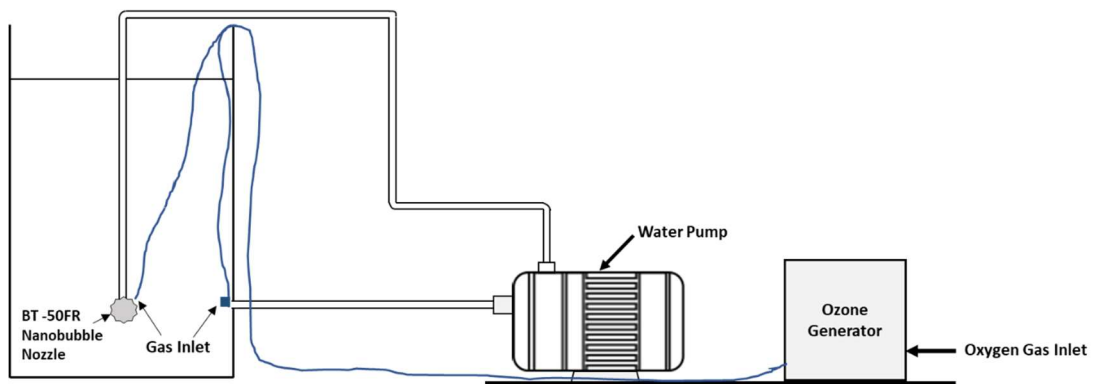
Though there are many nanobubbles applications, as suggested above, there is a limited understanding of the reason for their long-term stability. Therefore, this laboratory study was designed as a comprehensive investigation of nanobubbles based on four different gases. Then further investigated to determine the nanobubble characteristics in an aqueous system under different salt concentrations, pH levels, and temperatures by measuring bubble size distributions and zeta potentials. Measured results were analyzed to develop meaningful conclusions on bubble stability. In this research, bubble size and zeta potential of bubbles made of several gases in different solution environments were measured to study nano-bubbles stability. The size of the bubble is the key parameter that is used to classify the bubble. Another most important parameter of nanobubbles is the electric charge on the bubble surface, as the electric charge can be used to discuss the stability of a colloidal system. Thus, the electric potential of the colloidal system can be expressed in terms of zeta potential, and consequently, zeta potential measurements were used to explain the bubble stability



### 3.3 Experimental Methods

#### 3.3.1 Generation of nanobubbles

In this research, the hydrodynamic cavitation was used to generate nanobubble [3,33,37], where BT-50FR micro-nano sized nozzle was used [9]. This gas-water circulation method generates a flume of micro and nanobubbles in water. First, water is pumped into the nozzle with an eccentricity to create a swirling effect. The swirling water creates a vacuum at the nozzle outlet where the desired gas is injected at a controlled rate. The gas introduced by vacuum into the swirling water will exit from the outlet as a mixture of micro and nanobubbles. The dynamic forces within the vortex will break the injected air into smaller bubbles. The BT-50FR micro-nano-bubble nozzle requires a minimum water pressure of 0.3MPa, a water flow rate of 20 L/min, and an airflow rate of 0.2 – 1.0 L/min. In this research, nanobubbles were generated using a 25L chamber filled with 18L of water and running the gas through nanobubble generating nozzle for 3 minutes. The gas except ozone was supplied from compressed gas cylinders with regulators. An ozone generator was used when generating ozone nanobubbles. Figure 3.1 shows the experimental setup used to generate nanobubbles.



**Figure 3.1** Experimental setup. (The figure shows the ozone nanobubbles generation setup, for other gas bubbles, the gas inlet is directly connected to the gas cylinder instead of the ozone generator).

### **3.3.2 Measurement of size distribution and zeta potential**

The bubble size distribution and zeta potential values were measured using a Malvern Zetasizer Nano ZS. The Zetasizer uses a dynamic light scattering method to analyze the size and the zeta potential of gas bubbles in the water. The Zetasizer is a non-invasive backscatter system, where the laser is directed towards bubbles and detects the backscatter of the laser to determine the sizes of micro and nanobubbles in water. The scatter detector can identify bubble sizes ranging from 0.3nm to 10  $\mu\text{m}$ . The Zetasizer uses the Electrophoretic Light Scattering technology to calculate the zeta potential of the dispersed nanobubbles based on the electrophoretic mobility using a capillary cuvette. Approximately 1 mL sample of the nanobubble saturated water is added to the capillary column, and an electrical field is applied. The net charge on the bubble and the bubble size will dictate the mobility of a bubble within the capillary column. The mobility of a bubble is directly correlated to the zeta potential of that bubble. Bubbles are illuminated with a laser, and the frequency of the scattered light from bubbles is a function of the velocity due to the Doppler shift. The Zetasizer analyzes the original beam and the scattered beam to identify the frequency shift. This frequency shift is related to the velocity of the bubble. The zeta potential is calculated using the Smoluchowski model.

### **3.3.3 Test procedure**

This study's main objective was to investigate the long-term stability of nanobubbles based on factors that influence the generation of nanobubbles. Therefore, nanobubbles were generated under the following four different conditions and tested for their size distributions and zeta potential values. Then, the results were analyzed.

1. **Different type of gases** (test series IA) – air, oxygen, nitrogen, and ozone in DI water
2. **Different pH levels** (test series IIA) – DI water with NaOH and HCl to produce solutions with different pH values (4, 7, and 10)
3. **Different salt concentrations** (test series IIB) – DI water with NaCl to prepare different solution concentrations (0.001M, 0.01M, 0.1M and 1M solutions).
4. **Different temperatures** (test series IIC) – DI water with 15<sup>0</sup>C, 20<sup>0</sup>C, and 30<sup>0</sup>C solution temperatures by heating or using a chiller.

### 3.4 Results and Discussion

#### 3.4.1 Different gas types

The stability and reactivity of nanobubbles should depend on gasses inside cavities. Therefore, to investigate different gas bubble properties, nanobubbles were generated using different gasses, namely, ozone, oxygen, air, and nitrogen. Bubbles were generated in DI water, where the solution's electric conductivity was maintained at 0.3mS/cm by adding NaCl (test series IA).

Figure 3.2(a) shows the variation of the bubble size with the gas type, and recorded average size data are based on six measurements. Ozone gas produced the maximum average bubble size, followed by oxygen, air, and nitrogen, respectively. The trend in Figure 3.2(a) shows that the bubble diameter of relevant gas types can be correlated to their gas solubility in water. The size/diameter results were based on the Number-Distribution data, where the distribution curves' peak values are reported. Among the four types of gases used, ozone has the highest solubility, 13 times more soluble than oxygen [85], and ozone nanobubbles had the largest average diameter. While nitrogen having the lowest solubility in water (normally N<sub>2</sub> is insoluble in water) showed the smallest bubble diameter. The solubility of oxygen, air, and nitrogen in 20<sup>0</sup>C water at 1 atm are 3.10, 1.87, and 1.54 (% v/v), respectively [86]. Figure 3.2(b) shows the zeta potential values for four gases, and the

average results were based on the six measurements. Ozone nanobubbles had the highest zeta potential value, followed by oxygen, air, and nitrogen, respectively. Though, the formed ozone nanobubbles are approximately 5% ozone and 95% oxygen by mass. Several researchers reported zeta potential and bubble sizes for ozone, oxygen, air, and nitrogen [6,49,86–88]. Ushikubo et al. reported a mean diameter of 137nm for oxygen nanobubbles formed in DI water and zeta potential values between -17 to -20mV for air nanobubbles formed in DI water [48]. Ohgaki et al. reported a mean diameter of 50nm for nitrogen nanobubbles in DI water [19]. Zheng et al. reported an average zeta potential value of -22mV for ozone nanobubbles in DI water [88]. The above test results in the literature are within the reported range, as shown in Figure 3.2.

The bubble size should depend on the supplied gas pressure, the energy provided to the system, and the solution's bulk properties. The gas flow rates and gas pressures are major contributors to the bubble size. Nanobubbles are usually generated using two methods. The first method involves a gas to flow into water and allow water with gas bubbles to circulate, causing bubbles to break into smaller sizes. Maintaining high flow rates or energy will produce smaller bubbles. However, both bubble breakage and coalescence occur simultaneously during the water circulation, producing a range of bubble sizes. The other method involves injecting a gas under controlled pressure into the water through a specially designed nozzle with nano-sized pores. By changing the applied pressure or flow rates, bubble size can vary. Smaller size bubbles are achieved by using higher upstream pressure with a lower gas flow rate. Yet, this is very hard to achieve; with increased internal pressures, bubble sizes tend to increase, so that flow rates have to increase or maintain the very smaller bubble size, causing high back pressures, which

required powerful compressors, an expensive proposition. Thus, to obtain optimal bubble sizes, pressures and flow rates should be selected accordingly.

Literature [18,19,47,89] showed that under neutral pH values, the nanobubbles surface is negatively charged, and this negative surface charge is related to the OH<sup>-</sup> ion concentration on the gas/water interfaces of bubbles. Therefore, the bubble properties depend on the surface charge density on the bubble surface, as shown in Equation (3.1). Literature suggested that the Young-Laplace equation is still valid at the nanoscale [90]. It can be considered that pressure difference caused due to surface tension ( $2\gamma/r$ ) can be reduced by the surface charge density ( $\sigma^2/2D\epsilon_0$ ), as shown in Equation (3.1).

$$\Delta P = \frac{2\gamma}{r} - \frac{\sigma^2}{2D\epsilon_0} \quad (3.1)$$

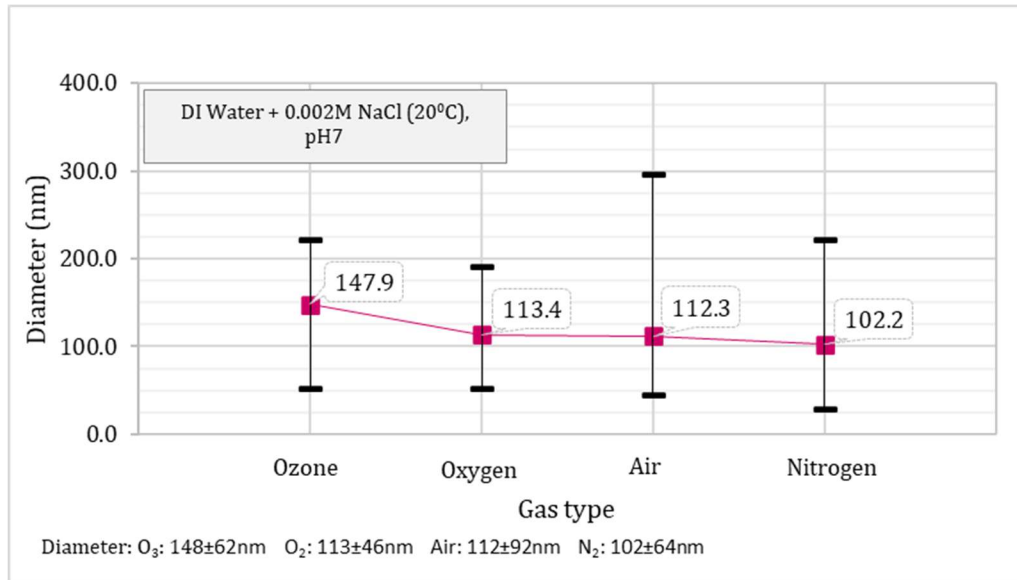
Where  $\gamma$  is the surface tension,  $\sigma$  is charge density, D is dielectric constant,  $\epsilon_0$  is the permittivity of vacuum, and r is bubble radius.

The zeta potential depends on many factors; when keeping all the parameters constant except the gas type, the measured difference in zeta potential must be related to the gas type. This means infilled gas in the bubble should influence the zeta potential. Hence, the negative surface charge on the bubble surface is believed to be due to OH<sup>-</sup> ions' absorption at the gas-water interface. Four gases used should have different levels of contribution to generate negative charges at the bubble surface. The observed differences should be related to the different gas diffusion rates, gas solubility, and the potential contribution to form OH<sup>-</sup> ions at the bubble-water interface. Results indicate that the magnitude of zeta potential is highest for O<sub>3</sub> and followed by O<sub>2</sub>, Air, and N<sub>2</sub>, respectively.

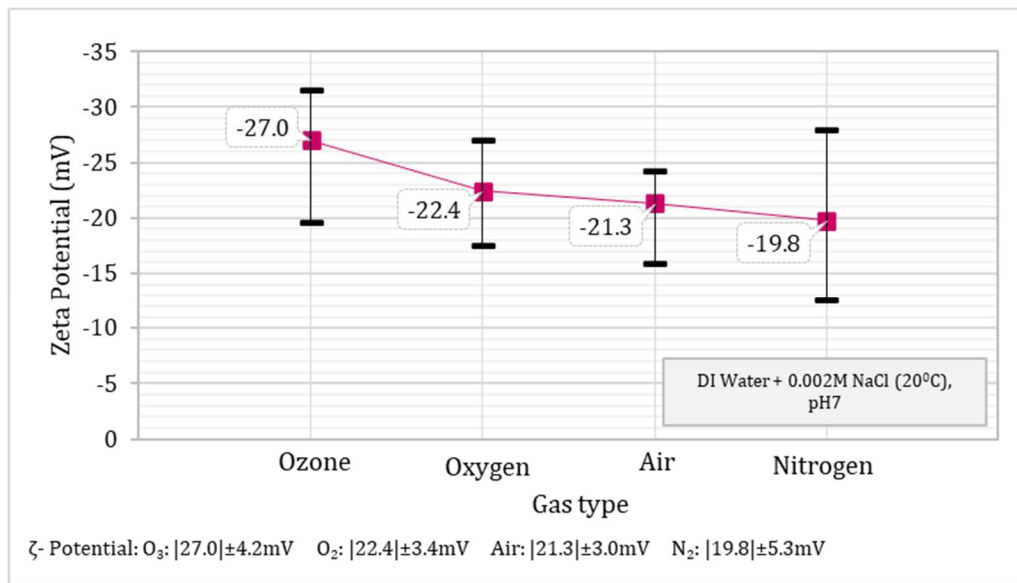
Ozone is a very soluble and very reactive gas, and when it dissolves in water, it tends to generate hydroxyl radicals ( $\text{OH}\cdot$ ),  $\text{O}_2$ , etc. Also, one indirect illustration of ozone molecules in contact with water ( $\text{O}_3 + \text{H}_2\text{O} \rightarrow \text{O}_2 + \text{OH}^- + \text{OH}^-$ ) results in hydroxide ions [91]. The decomposition of  $\text{O}_3$  form  $\text{O}_2$ , thus, increasing the  $\text{O}_2$  concentration in water. According to the many authors, the  $\text{H}^+$  ions are more likely hydrated and tend to stay in the bulk aqueous side, and less hydrated and more polarized anions attract the bubble surface [18,49]. According to the results,  $\text{O}_3$  and  $\text{O}_2$  show higher magnitude zeta potential values or shows higher negative charges on the bubble surface. As such, the diffused  $\text{O}_2$  must be responsible for forming additional  $\text{OH}^-$  ions at the gas-water interface to make more negatively charged bubbles. Based on the results, the next higher zeta potential is related to the Air bubbles, and it can be assumed that air contains some amount of  $\text{O}_2$  compared to the  $\text{N}_2$ . Hence, it contributed to absorb more  $\text{OH}^-$  ions at the bubble interface to form high magnitude zeta potential compared to  $\text{N}_2$  gas bubbles.

Additionally, without assuming the gas reactivity and solubility, the charge density and bubble size should be the same irrespective of the gas type at the time of generation. However, with the high gas solubility, ozone will diffuse into the bulk solution at a much higher mass transfer rate. Which will provide the  $\text{O}_2$  gas to the solution; in other terms, it will form  $\text{OH}^-$  ions at the bubble interface.

When looking into the zeta potential values, it seems, in-filled gas type plays a vital role due to both their solubility and reactivity. Based on test results, it is quite clear that the gas type is a major contributor to zeta potential, and gases that can generate a much higher concentration of  $\text{OH}^-$  ions at the interface will produce higher negative zeta potential values.



(a)



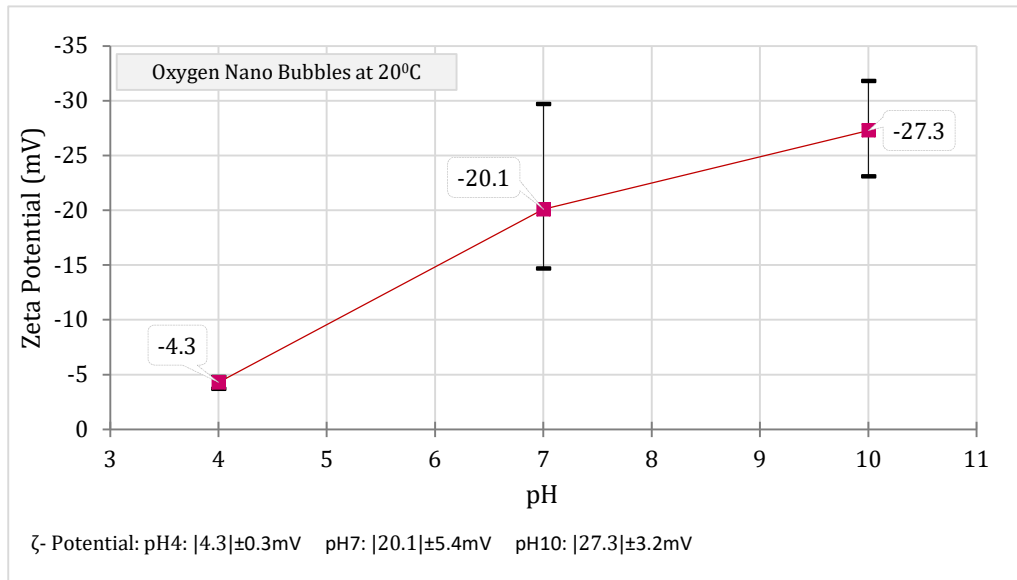
(b)

**Figure 3.2** Relationship between (a) bubble diameter and the gas types of the nano-bubbles and (b) zeta potential and the gas types of the nanobubbles.

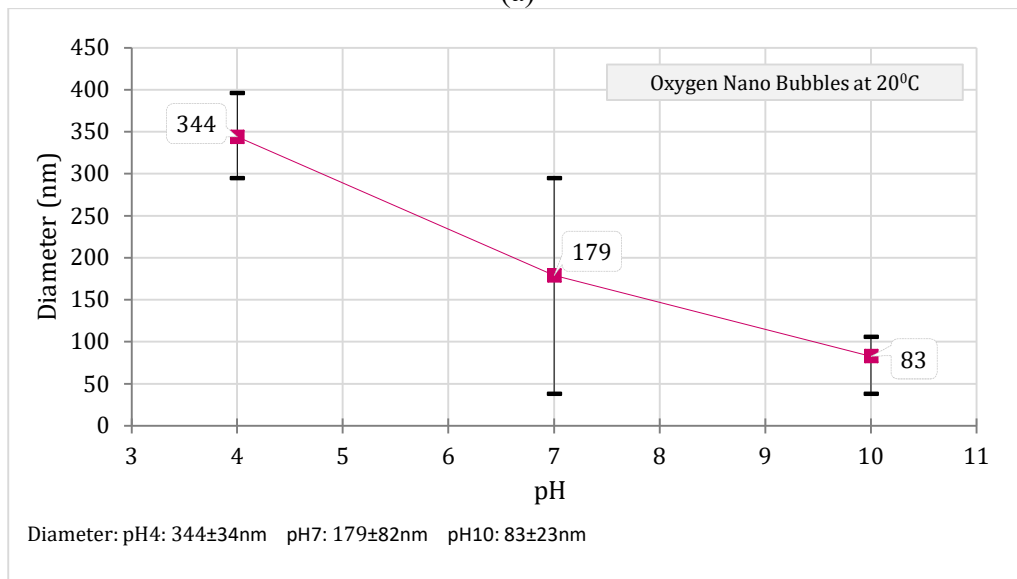
### 3.4.2 Variations in solution pH

Figure 3.3(a) shows the variation in zeta potential values with solution pH values, wherewith increased solution pH, the negativity of zeta potential increases. Figure 3.3(b)

shows the change in bubble size with solution pH values, wherewith higher solution pH values; smaller bubbles are formed. High concentrations of OH<sup>-</sup> ions in the solution created smaller nanobubbles with higher charge density values for a given energy input than at neutral pH solutions.



(a)



(b)

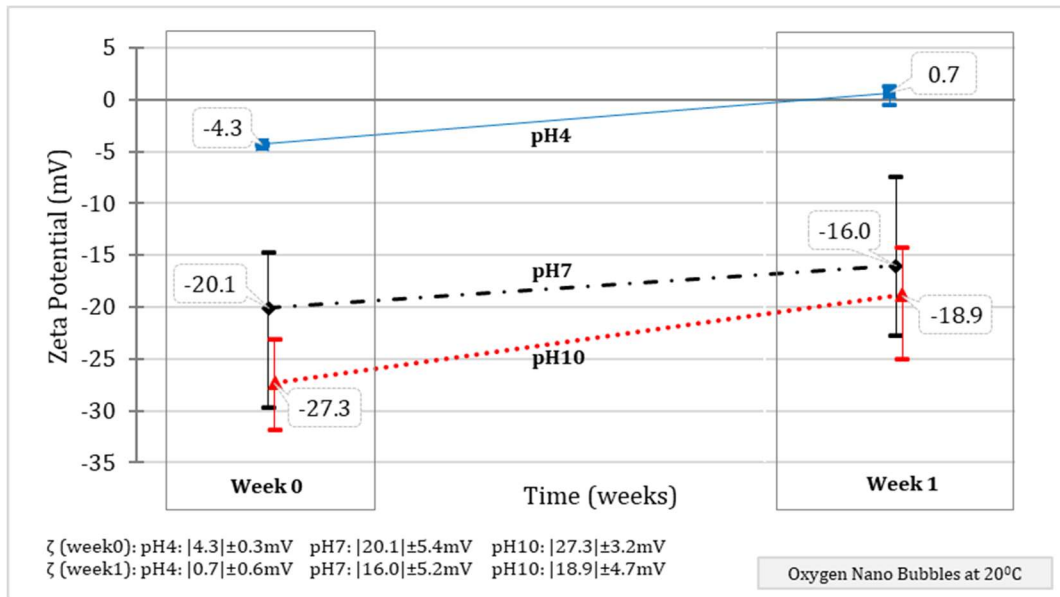
**Figure 3.3** Relationship between (a) zeta potential and pH, and (b) bubble diameter and pH, for oxygen nano-bubble solution at 20<sup>0</sup>C.



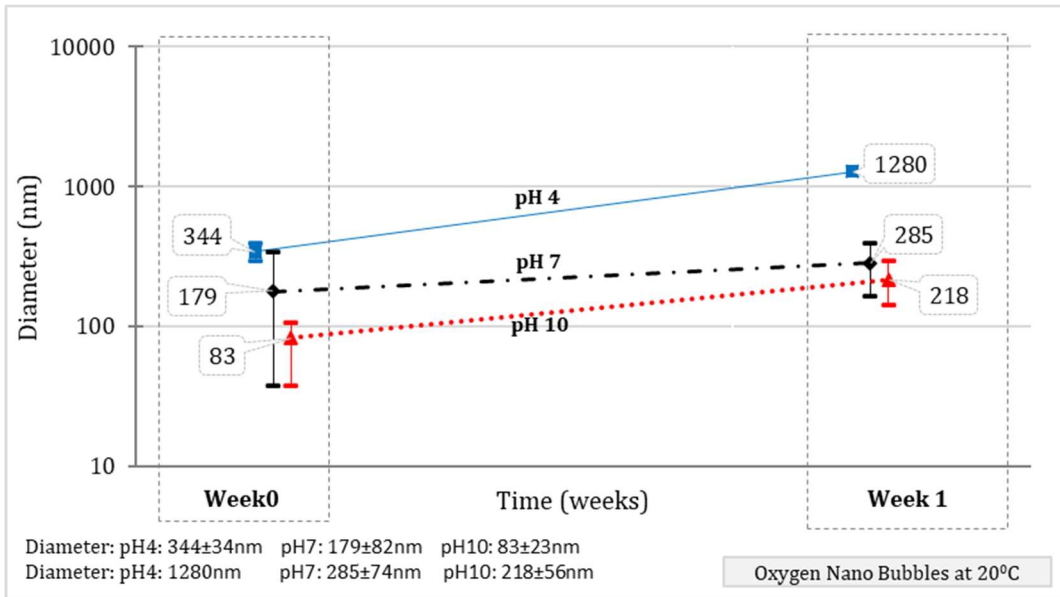
The literature review showed that, under a wide range of solution pH values, nanobubbles' zeta potential was negative, and the magnitude increased with increased solution pH values [18,49,50,89]. Takahashi reported that, with increasing pH, negative zeta potential increased and reached a plateau of approximately -110mV at pH $\approx$ 10, and for acidic solutions with pH below 4.5, zeta potentials values were positive [18]. Calgaroto et al. reported that zeta potential values of nanobubbles showed a sigmoidal behavior between pH 2 (+26 mV) and pH 8.5 (-28 mV) with an isoelectric point (IEP) at pH 4.5 and highest negative zeta potential (-59mV) at pH 10 [50]. When looking at size variation with solution pH, Calgaroto et al. showed that bubble size reached the maximum (720 nm) around an IEP value at pH 4.5, where bubbles were practically uncharged ( $\pm$ 5 mV). Calgaroto et al. concluded that the higher the amount of electrical charge on the bubble resulted in smaller nanobubbles [50]. Also, Kim et al. reported that bubbles created with solution pH of 3 were much larger than those created with solution pH of 12, and effective diameter was reported as 372nm with a pH 3 and 293.4nm solution with a solution of pH 12 [49].

Therefore, increasing the solution pH with a high OH<sup>-</sup> ions concentration would increase the zeta potential. Moreover, this will increase hydrogen bonds around the bubbles and will help to increase the stability of the bubble as well. The experimental data from this research supported the above conclusion that with the highest magnitude of negative zeta potential of -27.3V for nano oxygen in a solution pH of 10. Based on experimental results, the smallest zeta potential value was obtained for a solution pH of 4. The reduction in negative zeta potential can be easily attributed to a high concentration of H<sup>+</sup> ions in the solution or a reduction of OH<sup>-</sup> ion concentration. Figures 3.3(b) and 3.4(b) show that nanobubbles tend to be smaller in size with increased solution pH values. Additionally,

they showed that a solution with a neutral pH and above, bubble size remained smaller in the nano-size range for one week. However, for a solution pH of 4, bubbles were much bigger in the micron size range at the time of generation and very rapidly increased in size. After a week, ZetaSizer could not accurately measure the size (see Figure 3.4(b)).



(a)



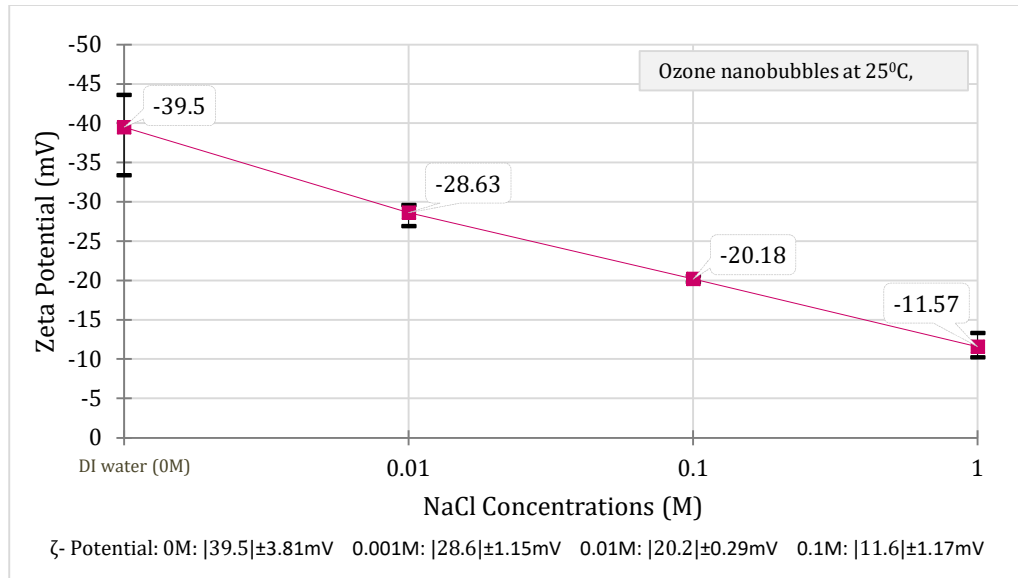
(b)

**Figure 3.4** Relationship between (a) zeta potential variation with time and (b) bubble size variation with time, for oxygen nanobubble, prepared with different pH at 20°C.

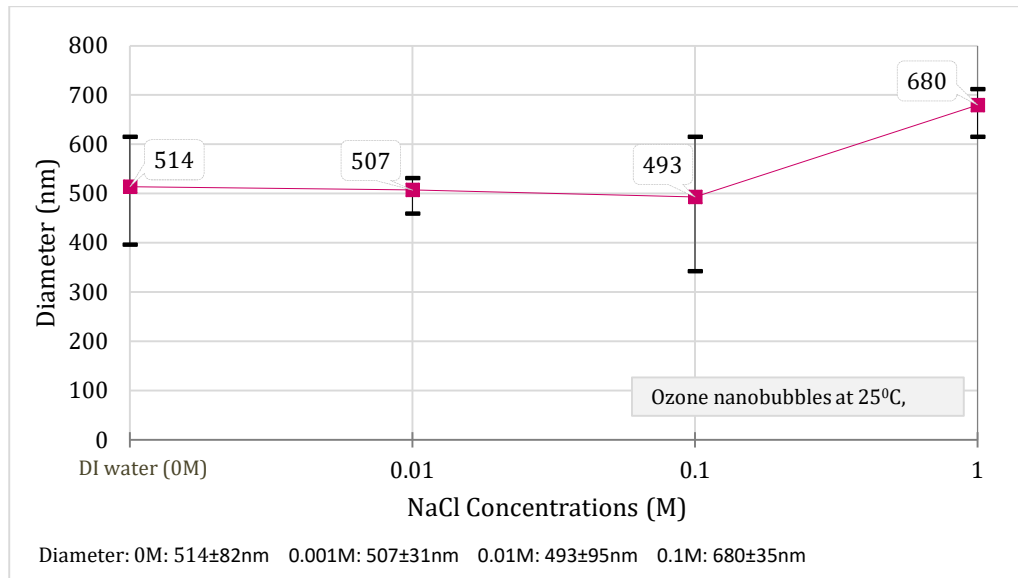
Test results showed that stable bubbles were generated under the neutral solution pH and for solution pH values above 7. Even though nanobubbles in high pH NaOH solutions showed highly negative Zeta Potential value at the time of generation, it rapidly reduced to values close to zeta potential values of nanobubbles produced with neutral solution pH (Figure 3.4(a)). Test results also showed that nanobubbles in acidic solutions were difficult to generate, and those nanobubbles in acidic solutions had positive zeta potential values. This confirms that the surface charge of nanobubbles is strongly related to the OH<sup>-</sup> ion concentration. Hence, it can be concluded that stable nanobubbles are generated under less acidic environments. This can be explained as when nanobubbles are formed in acidic solutions; magnitude zeta potential values are always low when compared to the neutral or alkaline conditions. Those bubbles with low zeta potential have a higher possibility for bubble coalescence and, therefore, creating unstable bubbles.

### **3.4.3 Impact of salt concentration**

Figures 3.5(a) and 3.6(a) show the variation of zeta potential values with NaCl concentration for both ozone and oxygen nanobubbles. In both cases, all the zeta potential values were negative and showed an increase in zeta potential value or reduction in magnitude with increased NaCl concentrations. Figures 5(b) and 6(b) show the bubble size variation with NaCl concentration for both ozone and oxygen nanobubbles. The bubble diameter slightly increased with increasing NaCl concentration for both ozone and oxygen nanobubbles. Literature showed a similar trend, where NaCl concentration reduced negative zeta potential and increased in effective diameter [18,70,92]. To explain this behavior requires the application of diffuse double layer theory to nanobubbles. Authors are developing such a theory and will be presented in a separate future publication.

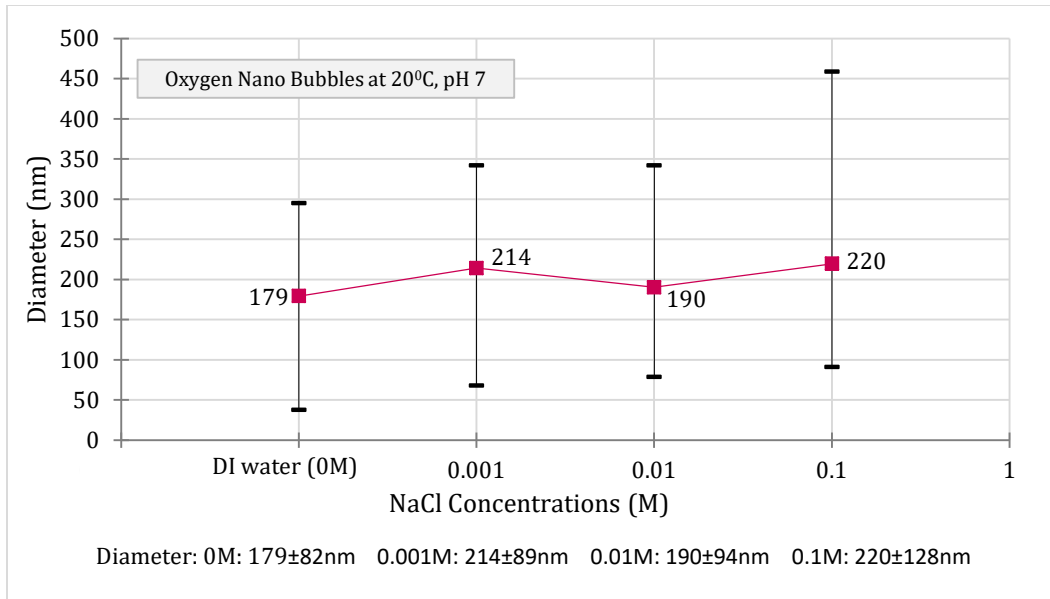


(a)

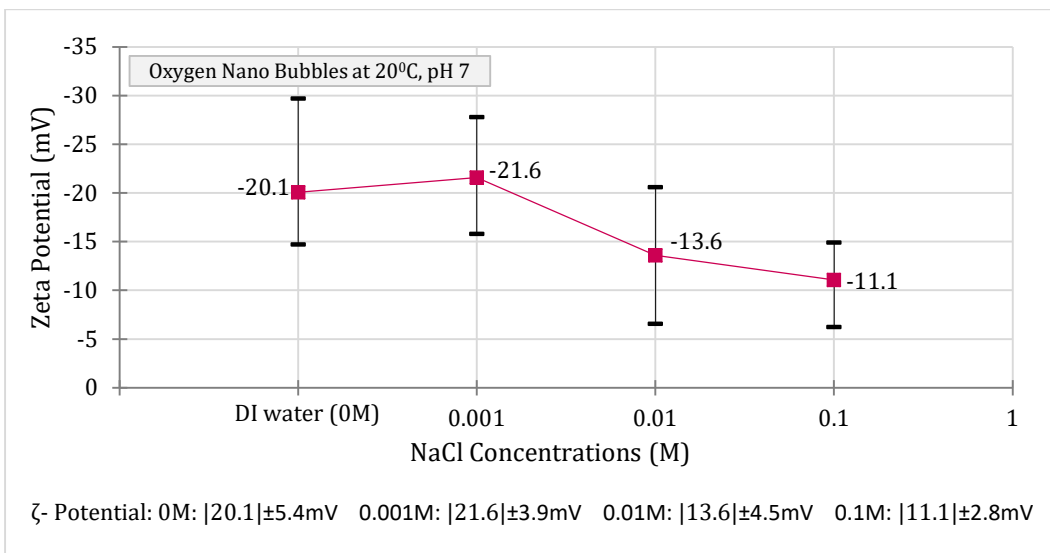


(b)

**Figure 3.5** Relationship between (a) zeta potential and the NaCl concentrations, (b) bubble diameter and NaCl concentrations for ozone nano-bubbles at 25<sup>0</sup>C.



(a)



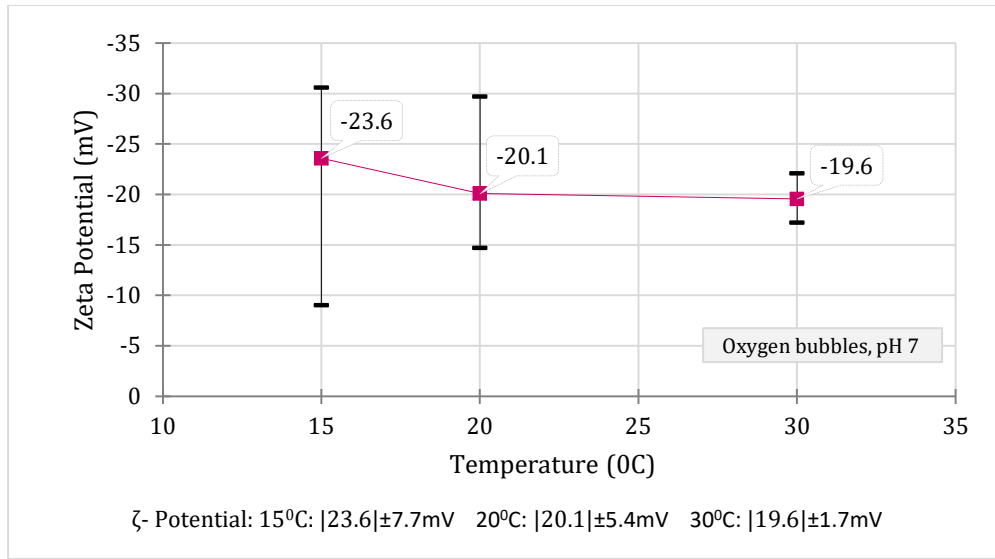
(b)

**Figure 3.6** Relationship between (a) bubble diameter and NaCl concentrations, (b) zeta potential, and the NaCl concentrations for oxygen nanobubbles at 20°C and pH ≈ 7.

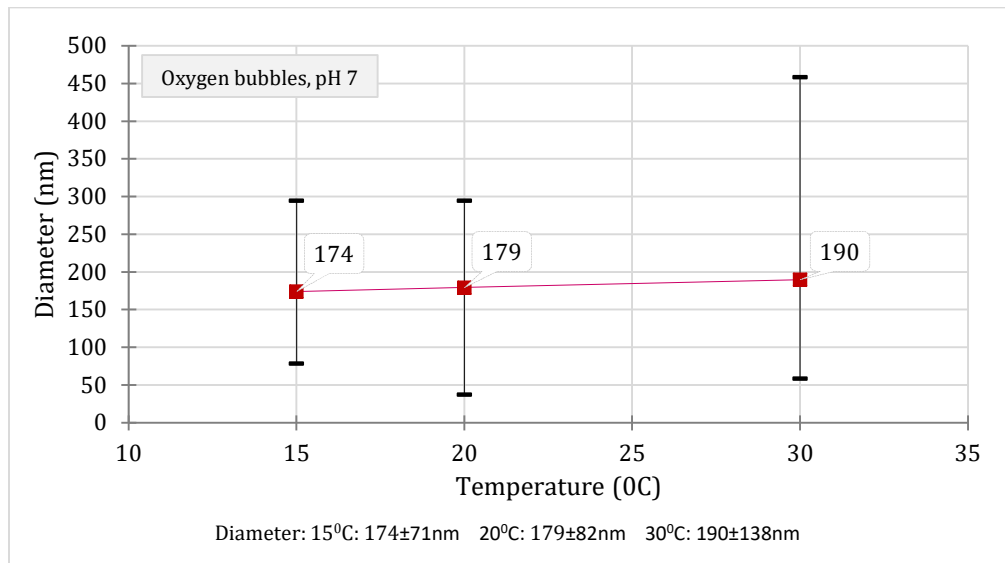
### 3.4.4 Impact of solution temperature

Figure 3.7(a) shows the variation of zeta potential values with solution temperature, and Figure 3.7(b) shows the variation of the bubble diameter with solution temperature for oxygen nanobubbles. Based on test results, it can be concluded that the negativity or

magnitude of the zeta potential increased with a decrease in solution temperature. However, the bubble size did not show a considerable variation. The zeta potential depends on the solution temperature, and having a low solution temperature produced nanobubbles with higher zeta negative potential values. The decreased zeta potential or decreased surface charge density may be due to decreased OH<sup>-</sup> ion concentration on the bubble surface. With increased temperature, the solution's ions are higher and, therefore, decreased OH<sup>-</sup> ion absorption onto the bubble surface. Jia et al. reported similar data showing decreased negative zeta potential values with increasing temperature [89]. Again, an accurate explanation of this behavior requires the application of diffused double layer theory to nanobubbles.



(a)



(b)

**Figure 3.7** Relationship between (a) zeta potential and temperature and (b) bubble diameter and temperature for oxygen nano-bubbles solution generated in DI Water.

### 3.4.5 Stability of nanobubbles

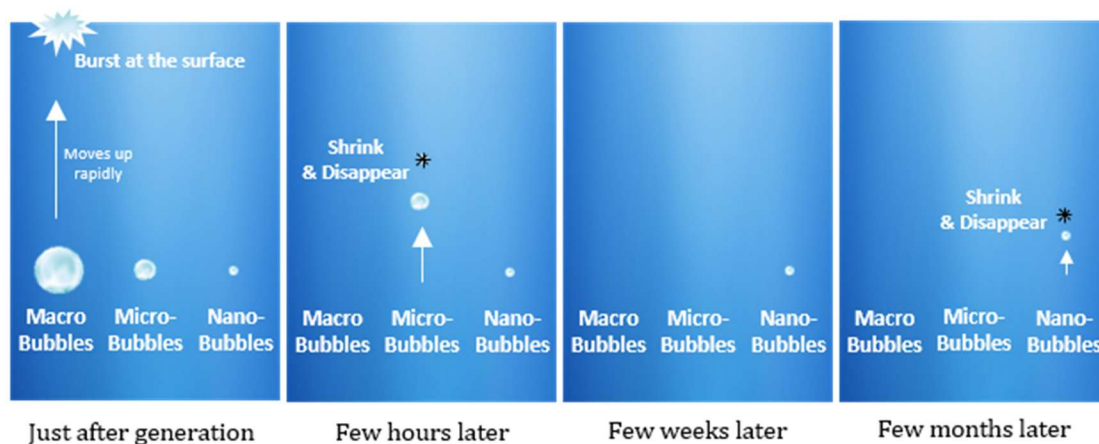
The zeta potential or the surface charge density of nanobubbles would depend on different factors such as viscosity and density of the bulk solution, temperature, pH, type and concentration of solution electrolyte, chemical surfactants, and other contributing factors.

Irrespective of gas type, bubbles can have high zeta potential values by providing sufficient

energy or pressure under controlled gas flow rates. Suppose there is higher gas flow rate with higher bubble concentrations even with high zeta potential values. In that case, there is a high possibility for bubbles to merge to produce larger unstable macro bubbles. The stable nanobubbles are smaller size bubbles with very negligible rising velocity and high-magnitude zeta potential values to reduce the possibility of bubble coalescence. To form high zeta potential values, it must contain high surface charge density. As mentioned before, nanobubbles surface charge is related to the OH<sup>-</sup> ions or less hydrated and more polarized anions at the bubble gas-water interface. By adding surfactants, increasing pH, or using other methods, one can create a favorable environment to generate OH<sup>-</sup> ions/ less hydrated and more polarized anions at the gas-water interface, hence, stable nanobubbles.

The Young-Laplace equation governs the formation of macro and microbubbles. Macro bubbles rise to the surface rapidly, as shown in Figure 3.8, and burst, while the microbubble rises at a slower rate than macro bubbles; because of this extra time, the gas transfer from bubble to liquid is higher. With the substantial loss of gas mass, microbubbles shrink and disappear after a few hours. As shown in Figure 3.8, Micro and Nano-bubbles have different swelling/shrinkage properties from macro bubbles. It is reported that the critical diameter separating bubble swelling and shrinkage is approximately 50–65 $\mu\text{m}$  [42]. Bubbles larger than this critical value will swell, while smaller bubbles will shrink. Microbubbles gradually decrease in size and subsequently disappear due to long stagnation and dissolution of interior gases into the surrounding water, whereas NBs remains in the solution for weeks [18].





**Figure 3.8** The fate of macro, micro, and nanobubbles in liquids with time.

Experimental data from this research showed that smaller bubbles with high zeta potential bubbles are much stable with time. Smaller bubbles tend to stay longer in the solution because their motion is governed by both Brownian motion and the buoyancy force. With this random motion, the gas inside a bubble continuously diffuses and is supposed to decrease in size and eventually disappear. However, the recorded data with time showed that the measured bubble's size increased while the magnitude of zeta potential decreased. This must be due to the bubble merging over time caused bubble sizes to increase while the surface charge density decreases; thus, the zeta potential. Hence, it is hypothesized that with the loss of charges on the surface due to diffusion, eventually, nanobubbles would shrink and disappear, similar to microbubbles' fate. Figure 8 shows the illustration of the fate of macro, micro, and nanobubbles over time. Authors are currently developing a theory to validate the above based on diffused double layer theory and molecular dynamic simulations.

### 3.5 Summary and Conclusions

Different industrial applications of nanobubbles would require the need to understand the properties and behavior of these bubbles. A series of laboratory experiments were conducted to understand the behavior of nanobubbles. First, the impacts of the infilled gas on these bubble properties and behavior were investigated. The test results showed that the size and zeta potential values of nano oxygen, nitrogen, air, and ozone bubbles were the function of the gas type properties, specifically the gas solubility. The nitrogen gas with the least solubility had the smallest bubble diameter, while ozone with the highest gas solubility produced the largest diameter bubbles. The negative zeta potential value of nanobubbles is due to the number of OH<sup>-</sup> ions on the bubble surface. Since all the parameters are identical except the gas type of nanobubbles, it can be concluded that the zeta potential is a function of the gas diffusion rates and gas solubility and would contribute to the generation of OH<sup>-</sup> ions on the bubble surface. Based on test results, ozone had the highest magnitude negative zeta potential value, followed by oxygen, air, and nitrogen.

Then, the bubble properties and behavior under the different bulk properties (pH, temperature, and ion concentration) of the solution were investigated. Test results showed that the negative zeta potential values increased with increased solution pH values. Also, smaller sized bubbles were generated under high solution pH values, and bubbles were bigger and unstable in acidic solutions. These results also supported the hypothesis that the amount of OH<sup>-</sup> ions on the surface governed the nanobubbles' stability. Higher pH levels with a high OH<sup>-</sup> ions concentration generated smaller and stable nanobubbles with higher zeta potential values.

The test results also showed that the zeta potential values decreased with increased solution temperatures. Though, there was no significant change in bubble size with increased solution temperatures. The change in zeta potential value may be due to the change in  $\text{OH}^-$  ion concentration on the bubble surface, and elevated temperatures and increased ion mobility reduced the  $\text{OH}^-$  concentration on the bubble surface.

The experimental results also showed that, with increased NaCl concentrations, zeta potential values decreased, while the bubble diameter increased. This behavior is difficult to explain and would require the application of the diffused double layer theory, which will be presented in a separate publication.

A discussion on the stability of nanobubbles based on experimental data as well as information based on a literature search was presented. Irrespective of gas type, stable bubbles can be generated with high magnitude zeta potentials by providing sufficient energy or pressure under controlled gas flow rates. Also, bubble stability can be increased by providing a favorable environment that can generate higher  $\text{OH}^-$  ions concentration on the bubble surface. However, the bubble density or number of bubbles per unit volume should be considered to avoid the possible merging of bubbles. The bubble clustering needs further investigation to develop a complete picture of bubble stability. Test results also reduced the zeta potential of stable nanobubbles with time and reduced surface charge due to diffusion. Consequently, it is hypothesized that nanobubbles with a reduction in zeta potential and the random movement of bubbles are subject to coalescence, thus, increasing bubble size.

## CHAPTER 4

### APPLICATION OF THE DIFFUSED DOUBLE LAYER THEORY TO NANOBUBBLES

#### 4.1 Introduction

Nano or ultrafine bubbles are defined as gas cavities within aqueous solutions with sizes smaller than 200nm [3,4,93]. In this manuscript, the bubble size refers to the bubble diameter. Nirmalkar et al. experimentally proved that bulk nanobubbles do exist, they are filled with gas, and they survive for a long period of time [93]. The industrial application of nanobubble technology has exponentially increased over the last two decades due to their long-term stability [5,6]. The extra small size, high internal pressure, and electrically charged interface are major reasons for increased industrial applications, where the bulk solution chemistry plays a significant role in nanobubbles' behavior [4]. Also, smaller bubbles with low rising velocities and high zeta potential values prevented bubble coalescence [6,18,94]. Also smaller bubbles with the low buoyancy force and low raising velocities are impacted by the Brownian motion in the water molecules [2,18,95]. The stability of any colloidal system depends on two types of surface forces; electrostatic repulsion and van der Waals attraction. Hence, Derjaguin, Landau, Verwey, and Overbeek (DLVO) theory can be used to explain the colloidal stability. The lifespan of a bubble depends on both the rising velocity [6,18,94] and gas dissolution/diffusion to the bulk solution [96,97]. The gas dissolution/diffusion depends on several factors such as gas solubility, temperature, bubble size, the pressure difference at the gas-liquid interface, interfacial reactions and the gas saturation in the bulk liquid solution.<sup>13</sup> Gases within the bubble dissolve or diffuse to the bulk solution at a faster rate with higher internal pressure

in the bubble [96,97]. Also, bubbles exist as clusters with an increased gas concentration within the solution and slowing the gas diffusion/dissipation from individual bubbles [1].

The Young-Laplace equation is found to be valid at the nanoscale [90]. However, to account for the electrostatic repulsion on the surface of a nanobubble due to surface charge, Bunkin et al. proposed a modification to the Young-Laplace equation. Bunkin et al. showed that the pressure induced by the electric charge ( $P_e$ ) on a nanobubble is based on the "bubstons problem" within the Coulomb model as  $P_e = \frac{2\pi\sigma^2}{D\epsilon_0}$ , and hence, the modified Young-Laplace equation was expressed as shown below [98].

## 4.2 Derivation of Equations

### 4.2.1 Derivation of modified Young Laplace equations

The mechanical equilibrium condition for nanobubble can be explained by the well-known Young Laplace equation as;

$$\Delta P = P_{in} - P_{out} = \frac{2\gamma}{R} \quad (4.1)$$

The Young-Laplace equation should have to be modified in order to accommodate the electrostatic pressure ( $P_e$ ), which act opposite to the surface tension force, and the modified equation can be expressed as below.

$$\Delta P = \frac{2\gamma}{R} - P_e \quad (4.2)$$

This  $P_e$  can be derived based on the general definition of pressure  $P = -\left(\frac{\partial\phi}{\partial V}\right)_T$ , where,  $\phi$  = free energy of the system,  $V$  = volume of the ion cloud around the nanobubble. Consequently, the electrostatic pressure,  $P_e = -\left(\frac{\partial\phi_e}{\partial V}\right)_T$  where  $\phi_e$  is the electrostatic component of the free energy and can be rewritten as;

$$P_e = -\left(\frac{1}{4\pi R^2} \frac{\partial\phi_e}{\partial R}\right)_T \quad (4.3)$$

Bunkin et al. explained that for nanobubbles, in the region of the medium with a radius  $r \geq R$ , the electric field is non-zero, and, inside the bubble, the electric field is zero due to the spherical geometry [98]. Hence, the standard equation for the electrostatic component of free energy,  $\phi_e = \frac{1}{2D\epsilon_0} \int_R^r \frac{Q^2(x)}{x^2} dx$ , where,  $Q(x)$  is the total charge at the distance  $x$  from the center of the bubble. The volume of ion cloud,  $V = \frac{4\pi}{3} (r^3 - R^3)$ .

By simplifying the equations, the electrostatic pressure can be expressed as;  $P_e = \frac{2\pi\sigma^2}{D\epsilon_0}$ , where  $\sigma$  is surface charge density. Therefore, the Modified Young Laplace equation can be expressed as:

$$\Delta P = \frac{2\gamma}{R} - \frac{2\pi\sigma^2}{D\epsilon_0} \quad (4.4)$$

Where  $\gamma$  is the surface tension (N/m),  $\sigma$ = surface charge density (C/m<sup>2</sup>),  $D$ =dielectric constant of the bulk liquid media,  $\epsilon_0$  = permittivity of vacuum (C<sup>2</sup>J<sup>-1</sup>m<sup>-1</sup>) and  $R$ = bubble radius (m).

The accumulated ions around the bubble surface create a thin film, which acts as a diffusion barrier reducing gas dissolution, thereby increasing the nanobubbles' lifespan. This phenomenon is referred to as an ion shielding effect [27,99].

There are many advantages of computing double layer thickness and developing a theory to compute the electrical charges on the bubble surface, as those will provide insights to understand the physical behavior of nanobubbles in an aqueous solution. The bubble solution properties impact the bubble stability, specifically the temperature, pH, ion concentration, and the dielectric constant. Consequently, by changing the bulk solution chemistry, one would be able to calculate the ion distribution within the solution and hence, the properties of nanobubbles.

Therefore, in this manuscript, the diffused double layer theory is applied to nanobubbles in an electrolytic solution using experimental data and theoretical calculations. There are different nanobubbles generation methods: hydrodynamic cavitation, sonication causing acoustic cavitation, electrochemical cavitation, and mechanical agitation [47]. Hydrodynamic cavitation is one of the most frequently used technology. Thus, in this research, hydrodynamic cavitation is used to generate nanobubbles.

#### **4.2.2 The formation of the diffuse double layer around nanobubbles**

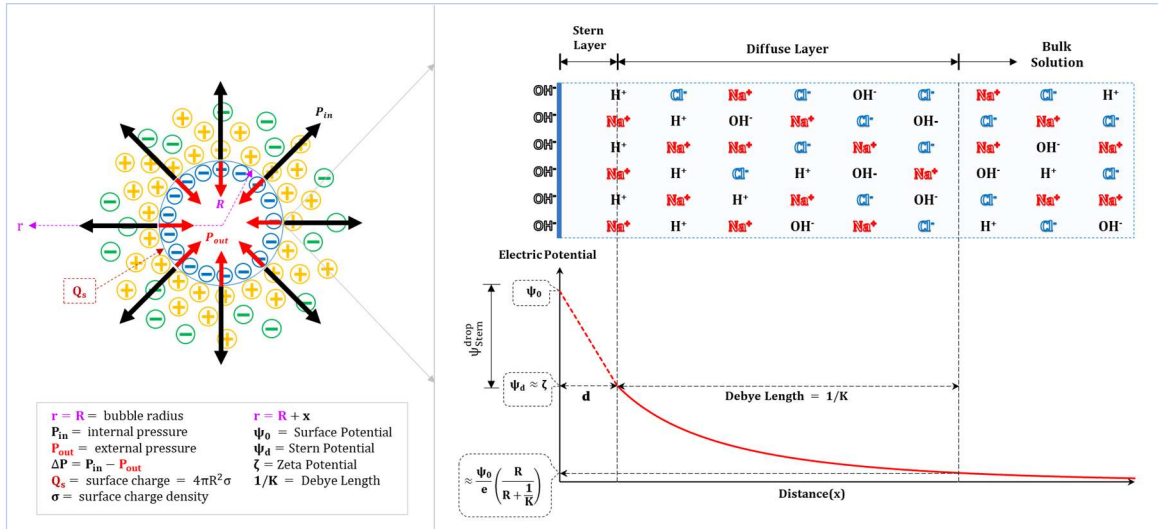
Nanobubbles in aqueous solutions have electrically charge interfaces. This surface charge generates an electrical field that affects the ion distribution in the bulk solution. Adjacent to the bubble surface, there is a high concentration of oppositely charged ions with a diffused distribution of those with the distance from a nanobubble to neutralize the electrical charge on the bubble's surface. Because of the surface charge on bubbles and the

distribution of ions in the liquid adjacent to nanobubbles, a diffused double layer formed, as shown in Figure 4.1. The assumptions made for the calculations of diffuse double layer parameters are discussed below.

The electric double layer consists of two layers, the Stern layer and the diffused layer. The innermost region surrounding the bubble surface is called the Stern layer, and, in this region, ions are strongly attached to the bubble surface. The next region is called the diffused layer, where ions are loosely attached. There is an imaginary boundary in the diffused layer where ions within this boundary move with the bubble, and those ions outside this boundary will not move with the bubble. This boundary is called the slip plane, and the potential at this boundary is known as the zeta potential,  $\zeta$  [51]. However, this shear plane's exact location is not well established, and there is no valid theory to calculate the shear layer thickness [100–103]. On the other hand, the Zeta potential is a very important parameter for real systems, as it is difficult to measure the surface potential. Though zeta potential is not a direct measurement, it is based on the electrostatic mobility of the colloidal particles, and hence, it can be calculated. The zeta potential is commonly used to describe nanobubbles' stability; the strong electrostatic repulsion can prevent the bubble coalescence. The zeta potential depends on the pH of the medium, ionic strength, the concentration of any additives, and temperature. In an electrolyte solution, the double layer thickness is defined as the Debye length  $1/K$  (Equation (4.11)), which is a function of the ionic strength and only depends on the properties of the solution (i.e., ionic valency, temperature, and the ion concentration in the bulk solution) and not on any property of the charged surface. Therefore, solutions with higher ionic strengths would yield a thinner



double layer thickness as well as a lower zeta potential value, which leads to lower repulsion, thus, increased bubble coalescence.



**Figure 4.1** A schematic of the diffused electrical double layer formed around a nanobubble.

The Stern layer is the surface of the region between the surface of the bubbles and the locus of the hydrated counterions at a distance "d" from the bubble surface [104]. The potential, at a distance "d" from the bubble surface, is called the Stern potential  $\psi_d$ ; it is the potential at the beginning of the double layer. The Stern layer thickness of clay, silica, and other colloidal surfaces is reported in the literature, but there is limited information on nanobubbles. Leroy et al. stated that there is no stern layer for nanobubbles [105]. Verwey and Overbeek [106] stated that the Stern layer in the clay-water electrolyte system is approximately 0.5nm [107]. Shang et al. stated that, for the clay-water electrolyte system, the stern layer thickness is two monomolecular layers of adsorbed water, where "d" varies between 0.5-0.6 nm [108]. Sridharan and Satyamurty stated that the stern layer thickness is equal to the hydrated exchangeable cationic radius [109]. Brown et al. showed that the stern layer thickness is always one hydrated cation radius plus one molecule layer of water

(2.1-2.7Å) and concluded that cations are absorbed via nonspecific interactions with silica particles [110]. Herbowski et al. stated that the Stern layer consists mostly of ions; hence, its thickness is of the order of 0.2nm because it depends on ions' diameter [111]. The  $K^+$ ,  $Na^+$  and  $Cl^-$  ions have radii of 0.125nm, 0.183nm, and 0.1206nm, respectively [112,113]. Lim et al. based on the Nernst–Planck–Poisson equations, reported that the Stern layer thickness is equal to 0.5nm (slightly larger than one hydrated ion radius) [113].

Even though there is no experimental evidence on the Stern Layer of nanobubbles, since the bubbles are electrically charged, a diffuse double layer is formed around the bubble surface. In this research, the thickness of the stern layer is assumed as equal to one hydrated ion radius. This is due to no firmly attached water molecule layer, unlike in clay/silica particles.

In this study, the NaCl is used as the electrolyte's solution, the hydrated Na ion radius of 4.7Å (0.47nm) was assumed as the "d" value [114,115]. The zeta potential is equal to or lower than the magnitude of Stern potential ( $|\zeta| \leq |\psi_d|$ ). The difference between  $\psi_d$  and  $\zeta$  is a function of the ionic strength; at low ionic strength, the decay of the potential as a function of distance is small and  $\zeta \cong \psi_d$ ; at high ionic strength, the decay is steeper and  $|\zeta| \leq |\psi_d|$  [111]. As mentioned before, the accurate position of the shear plane is unknown, and over past decades the position of the shear plane has become a subject of great interest for many researchers [101,105]. One of the common general assumptions in the literature is that the shear plane is roughly equal to the stern plane [101,102]. However, a few researchers are of the opinion that the shear plane is located far away from the stern plane but close to the Gouy plane (the Debye–Hückel length,  $1/K$ ) [102]. Liu et al. showed that the position of shear plane depends on the polarization of counterions and concluded

that with ion polarization, there is a higher reduction in the Stern potential than that at the Gouy plane and the thickness of shear plane decreased with increased polarization [100]. In this research, the zeta potential is assumed to equal to the Stern potential ( $\zeta \cong \psi_d$ ). Consequently, the surface potential can be expressed as,

$$\psi_0 = \psi_{Stern}^{drop} + \zeta \quad (4.5)$$

Where the stern layer can be assumed to act as a parallel concentric sphere capacitor [106], and the potential drop assumed to be linear within the stern layer, hence,  $\psi_{Stern}^{drop}$ ;

$$\psi_{Stern}^{drop} = \sigma_0 \left( d_{stern} / \epsilon \epsilon_0 \right) \quad (4.6)$$

By assuming the highest potential value of the diffuse layer potential is equal to the zeta potential, for the electroneutrality of  $\sigma_0 = -\sigma_D$ , where  $\sigma_0$  – surface charge density, and  $\sigma_D$  – the excess charge density in the diffuse layer.

### 4.2.3 Derivation of surface charge density equations

The Poisson-Boltzmann equation was used to describe the distribution of ions around the charged particle. By solving the Poisson-Boltzmann equation, the electric potential,  $\psi(x)$ , around the sphere can be calculated.

Based on the Boltzmann equation for the distribution of ions, the net total charge density is given by (for symmetric electrolytes such as  $\text{Na}^+$  and  $\text{Cl}^-$ ) Equation (4.7);

$$\rho(x) = -2Ze\rho_{\text{bulk}} \text{Sinh}\left(\frac{Ze}{kT}\psi(x)\right) \quad (4.7)$$

Where  $Z$  is ionic valence,  $e$  is an electronic charge ( $1.602 \times 10^{-19} \text{C}$ ),  $\rho_{\text{bulk}}$  is the concentration of ions in the bulk solution ( $\text{ions}/\text{m}^3$ ),  $k$  is Boltzmann constant ( $\text{JK}^{-1}$ ),  $T$  is the temperature ( $^{\circ}\text{K}$ ), and  $\psi(x)$  is the electric potential at a distance  $x$  from the charged surface.

For a sphere of radius " $a$ ", the electric potential,  $\psi(x)$ , is related to the charge density,  $\rho(x)$ , based on Poisson's equation, as shown in Equation (4.8), where  $x$  is the radial distance away from the surface of the sphere. Where  $\epsilon_0$  is the permittivity of the vacuum, and  $D$  is the static dielectric constant.

$$\frac{d^2\psi(x)}{d^2x} + \frac{2}{(a+x)} \frac{d\psi(x)}{dx} = -\frac{\rho(x)}{\epsilon_0 D} \quad (4.8)$$

By combining Equations (4.8) and (4.7), Poisson-Boltzmann equation (PB equation), Equation (4.9) was obtained. The boundary conditions of the PB equation;

- $\psi = \psi_0$  at the surface of the charged particle,  $\psi_0 =$  surface potential
- $\psi = 0$ , and  $\frac{d\psi}{dx} = 0$  at infinitely far from the charged particle

$$\frac{d^2\psi(x)}{d^2x} + \frac{2}{(a+x)} \frac{d\psi(x)}{dx} = -\frac{-2Ze\rho_{\text{bulk}} \text{Sinh}\left(\frac{Ze}{kT}\psi(x)\right)}{\epsilon_0 D} \quad (4.9)$$

Debye and Hückel [116] analytically solved Equation (4.9) for low potentials and found the solution for electric potential around a sphere, Equation (4.10),

$$\psi(x) = \psi_0 \left( \frac{a}{a+x} \right) \exp(-Kx) \quad (4.10)$$

Where  $1/K$  is the Debye length;

$$\frac{1}{K} = \left[ \frac{\epsilon_0 D k T}{2 e^2 Z^2 \rho_{\text{bulk}}} \right]^{1/2} \quad (4.11)$$

Tuinier proposed an accurate equation for potential around a sphere by considering the curvature of the sphere for both low and high surface potentials as well as for small and large spheres [117]. The approximated solution is presented as, shown below, Equation (4.12):

$$\begin{aligned} \psi(x) = & \left( \frac{2a}{a+x} \right) \ln \left( \frac{1 + t_0 \exp(-Kx)}{1 - t_0 \exp(-Kx)} \right) [1 - \exp(-0.3a)] \\ & + 2 \ln \left( \frac{1 + u_0(x) \exp(-Kx)}{1 - u_0(x) \exp(-Kx)} \right) [\exp(-0.3a)] \end{aligned} \quad (4.12)$$

$$\text{Where, } t_0 = \tanh \left( \frac{\psi_0}{4} \right) \text{ and } u_0(x) = \tanh \left( \frac{\psi_0}{4} \frac{a}{a+x} \right)$$

Equations (4.10) and (4.12) describe the electric potential profiles and can be used to determine the charge density on the surface ( $\text{Cm}^{-2}$ ).

Now consider a bubble with radius ' $a$ ' having a surface charge density of  $\sigma$  or the total charge  $Q (=4\pi a^2 \sigma)$  and the net charge density  $\rho(r)$  at a distance  $r$  from the center of the sphere. Therefore, the total surface charge can be calculated, as shown in Equation (4.13), and charge density, as shown in Equation (4.14).

$$Q = 4\pi a^2 \sigma = 4\pi \int_{r=a}^{r=\infty} \rho(r) r^2 dr \quad (4.13)$$

$$\therefore \sigma = \frac{1}{a^2} \int_{r=a}^{r=\infty} \rho(r) r^2 dr \quad (4.14)$$

Now by assuming  $r=x+a$  and by changing the limits of Equation (4.14), Equation (4.15) can be obtained.

$$\therefore \sigma = \frac{1}{a^2} \int_{x=0}^{x=\infty} \rho(x) (a+x)^2 dx \quad (4.15)$$

The double-layer must be electrically neutral; therefore, the total charge on the bubble surface ( $\sigma_0$ ) must be equal and opposite in the sign to the net charge density of the diffused layer ( $\sigma_D$ ). Hence, by combining Equations (4.8), (4.10), and (4.15), the net charge density ( $\sigma_D$ ) for low surface potential is given as Equation (4.16):

$$\begin{aligned} \sigma_D &= \frac{-2Zq\rho_{\text{bulk}}}{a^2} \int_{x=0}^{x=\infty} \text{Sinh} \left( \frac{Zq}{kT} \psi_d \left( \frac{a}{a+x} \right) \exp(-Kx) \right) (a+x)^2 dx \\ &= -\sigma_0 \end{aligned} \quad (4.16)$$

Similarly, by combining Equations (4.8), (4.11), and (4.15), the net charge density ( $\sigma_D$ ) for high surface potential is given as Equation (4.17):

$$\begin{aligned} \sigma_D &= \frac{-2Zq\rho_{\text{bulk}}}{a^2} \int_{x=0}^{x=\infty} \text{Sinh} \left[ \frac{Zq}{kT} \left( \left( \frac{2a}{a+x} \right) \ln \left( \frac{1+t_0 \exp(-Kx)}{1-t_0 \exp(-Kx)} \right) \right) [1 \right. \\ &\quad \left. - \exp(-0.3a)] \right. \\ &\quad \left. + 2 \ln \left( \frac{1+u_0(x) \exp(-Kx)}{1-u_0(x) \exp(-Kx)} \right) [\exp(-0.3a)] \right] (a+x)^2 dx \\ &= -\sigma_0 \end{aligned} \quad (4.17)$$

Equations (4.16) and (4.17) can be numerically integrated to generate tables, which can be easily modified by including input parameters and constants to obtain the surface charge density as output. Numerical integrations are performed using the Trapezoidal Rule and small intervals of distances to generate an accurate solution. The Trapezoidal Rule is presented in Equation (4.18).

$$\int f(x) dx = \frac{\Delta x}{2} \sum_{i=0}^{n-1} [f(x_i) + f(x_{i+1})] \quad (4.18)$$

Although numerical analysis has the ability to provide accurate solutions, approximate analytical solutions are still valuable as they can be conveniently applied with tolerances. Therefore, in this research, two approximate analytical solutions derived by Loeb et al. and Ohshima et al. were also used [118,119]. They used an analytical solution as described below. According to Loeb et al. [119] and Ohshima et al. [118], for 1:1 electrolyte, the surface charge density  $\sigma_0$  of the particle is given by Equation (4.19).

$$\sigma_0 = \frac{D\varepsilon_0 KkT}{e} I = -\sigma_D \quad (4.19)$$

According to Loeb et al. [119], term I is expressed as follows, Equation (4.20);

$$I = 2 \sinh\left(\frac{q\psi_0}{2kT}\right) + \frac{4}{Ka} \tanh\left(\frac{q\psi_0}{4kT}\right) \quad (4.20)$$

Hence, the surface charge density becomes, Equation (4.21):

$$\sigma_0 = \frac{\varepsilon_r \varepsilon_0 KkT}{q} \left[ 2 \sinh\left(\frac{q\psi_0}{2kT}\right) + \frac{4}{Ka} \tanh\left(\frac{q\psi_0}{4kT}\right) \right] \quad (4.21)$$

Also, according to the Ohshima et al. [118] the term I in Equation (4.19) is expressed as follows, Equation (4.22):

$$I = 2 \sinh\left(\frac{q\psi_0}{2kT}\right) * \left[ 1 + \frac{2}{Ka \cosh^2\left(\frac{q\psi_0}{4kT}\right)} + \frac{8 \ln \left[ \cosh\left(\frac{q\psi_0}{4kT}\right) \right]}{(Ka)^2 \sinh^2\left(\frac{q\psi_0}{2kT}\right)} \right]^{1/2} \quad (4.22)$$

Therefore, the surface charge density can be calculated as, Equation (4.23):

$$\sigma_0 = \frac{\epsilon_r \epsilon_0 K k T}{q} \left[ 2 \sinh\left(\frac{q\psi_0}{2kT}\right) * \left[ 1 + \frac{2}{Ka \cosh^2\left(\frac{q\psi_0}{4kT}\right)} + \frac{8 \ln \left[ \cosh\left(\frac{q\psi_0}{4kT}\right) \right]}{(Ka)^2 \sinh^2\left(\frac{q\psi_0}{2kT}\right)} \right]^{1/2} \right] \quad (4.23)$$

#### 4.2.4 Interfacial forces

In 1940 the DLVO theory was separately developed by Derjaguin, Landau, Verwey, and Overbeek to explain the stability of colloids by considering the balance between the attractive, short-range van der Waals forces and the repulsive electric double layer forces [120,121].

In the case of nanobubbles, with the electrically charged interface, the overlap of the interacting double layers produces electrostatic repulsion due to the increased counterions between the bubbles (i.e., consider interacting bubbles with the similar charges (sign negative/positive)). Also, with similar size bubbles, there is an attractive force due to the dipole-dipole interactions, known as van der Waals forces.

The bubble-bubble interaction can be considered in two ways. First by considering stability due to force equilibrium and the second by computing the potential for bubble



collision. In order to explore the bubble stability (the possibility of coalescence, repulsion or no net force), the repulsive and attractive forces were calculated using experimental data (i.e., size, and zeta potential). Here an assumption is made that the calculated surface potentials remain constant for all bubble separation distances. Then the resultant force is calculated for different solution concentrations. Here a quantitative analysis of the bubble dynamics was not performed (i.e., the bubble approaching speed/collision rate), which is the second approach, the bubble collision. Such computation is complex and requires the consideration of bubble deformation, the ions regulation phenomenon (ion rearrangement and nonuniform surface charge densities) as bubbles approach each other, size of the bubble, the change in of bubble size over time due to the gas diffusion, as well as the induce bubble movement due to the Brownian motion.

For droplet coalescence calculations, the droplet deformation and the thin liquid film between droplets are accounted [122,123]. However, for nanobubbles with high internal pressures, bubbles are rigid with limited deformation, and hence, they maintain a spherical shape. Chen et al. stated that the deformation of micro-scale droplets could be safely disregarded for oil droplets smaller than  $10\mu\text{m}$  [124]. Thus, in this study, for the calculation of both the van der Waals forces and the electrostatic repulsive forces, nanobubbles are assumed as perfect spheres for all separation distances. Moreover, until the moment of bubble collision, the assumption of the spherical shape should not introduce errors to the calculations. Accordingly, the resultant net energy ( $W(D)$ ), and net force ( $F = dW/dD$ ), as well as van der Waals attractive energy/force and double layer repulsive energy/force versus separation distances ( $D$ ) can be plotted for two identical spherical

nanobubbles. The classical equations used in this research were obtained from the literature and described as follows:

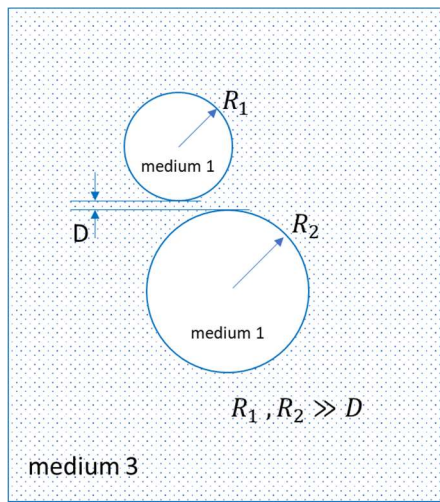
**4.2.4.1 Electrical repulsive interaction energy/force.** When two likely charged bubbles are close enough to overlap, the diffuse double layer produces the repulsive force. The forces between the two charged surfaces can be calculated with the consideration of the non-linear Poisson-Boltzmann equation. Figure 4.2 shows the sketch diagrams of the two spherical surfaces with the separation distance  $D$  ( $D \ll R$ ). The Equations (4.24-4.26) show the electric double-layer interaction of two bubbles [125].

$$\text{Energy, } W \quad \left( \frac{R_1 R_2}{R_1 + R_2} \right) Z e^{-kD} \quad (4.24)$$

$$\text{Force} = -dW/dD \quad K \left( \frac{R_1 R_2}{R_1 + R_2} \right) Z e^{-kD} \quad (4.25)$$

Where  $Z$  is interaction constant,

$$Z = 64\pi\epsilon_0\epsilon(kT/e)^2 \tanh^2(ze\psi_0/4kT) \quad (4.26)$$



**Figure 4.2** A schematic of the bubble interactions between two bubbles.

**4.2.4.2 The Van der Waals interaction.** The van der Waals interaction energy,  $W(D)$ , between two spherical particles for the all separation distance is firstly derived by the Hamaker [126] and expressed as follows, and then the interaction force can be calculated by  $F(D) = -dW/dD$ .

$$W(D) = -\frac{A}{6} \left\{ \frac{2R_1R_2}{(2R_1 + 2R_2 + D)D} + \frac{2R_1R_2}{(2R_1 + D)(2R_2 + D)} + \ln \frac{(2R_1 + 2R_2 + D)D}{(2R_1 + D)(2R_2 + D)} \right\} \quad (4.27)$$

Where,  $A$  - Hamaker constant;  $R_1$  and  $R_2$  the radius of each spherical particle whose interacts each other;  $D$  - separation distance.

For the small separation distances ( $D \ll R$ ), the van der Waals interaction energy/forces can be expressed as shown in Equation (4.28) and (4.29) [125].

$$\text{Energy, } W \quad \frac{-A}{6D} \left( \frac{R_1R_2}{R_1 + R_2} \right) \quad (4.28)$$

$$\text{Force} = -dW/dD \quad \frac{-A}{6D^2} \left( \frac{R_1R_2}{R_1 + R_2} \right) \quad (4.29)$$

Lifshitz (1959) derived the Hamaker constant with the consideration of the effects of many-body effects of an intervening liquid medium and retardation effects for large distances. The Hamaker constant for two identical phases of interaction medium 1 across medium 3 (immersion medium) (see Figure 4.2) can be expressed as bellow [127].

$$A \cong \frac{3}{4} k_B T \left( \frac{\epsilon_1 - \epsilon_3}{\epsilon_1 + \epsilon_3} \right)^2 + \frac{3h\nu_e}{16\sqrt{2}} \frac{(n_1^2 - n_3^2)^2}{(n_1^2 + n_3^2)^{3/2}} \quad (4.30)$$

Where,  $k_B$  is the Boltzmann constant ( $1.381 \times 10^{-23} \text{ JK}^{-1}$ ),  $T$  is the temperature, static and frequency-dependent dielectric constants,  $\epsilon_1$ ,  $\epsilon_3$  and refractive index,  $n_1$ ,  $n_3$ ,  $h$  is the Planck constant ( $6.626 \times 10^{-34} \text{ Js}$ ),  $\nu_e$  The absorption frequency (s<sup>-1</sup>), and for simplicity normally, is considered similar for all mediums. To calculate the Hamaker constant, the following parameters were used.  $T=20^\circ\text{C}$ ,  $C=293.15\text{K}$ ,  $k_B=1.381 \times 10^{-23} \text{ JK}^{-1}$ ,  $h=6.626 \times 10^{-34} \text{ Js}$ ,  $\nu_e=3.29 \times 10^{15} \text{ s}^{-1}$ ,  $n_1=1.00$ ,  $n_3=1.333$ ,  $\epsilon_1=1.00$ ,  $\epsilon_3$ , (for  $c=0.001\text{M}$ ,  $\epsilon_3=79.98$ ; for  $c=0.01\text{M}$ ,  $\epsilon_3=79.84$ ; for  $c=0.1\text{M}$ ,  $\epsilon_3=78.48$ ) [128], therefore, the calculated Hamaker Constant  $A = 4.05 \times 10^{-20} \text{ J}$ .

For the small separation distance ( $D \ll R$ ), the total energy is given by,

$$W(D) = \frac{-A}{6D} \left( \frac{R_1 R_2}{R_1 + R_2} \right) + K \left( \frac{R_1 R_2}{R_1 + R_2} \right) Z e^{-kD} \quad (4.31)$$

### 4.3 Materials and Methods

To generate nanobubbles, a 25-liter container was used and filled up to 18 liters. Nanobubbles were generated using the hydrodynamic cavitation method [3,9,33,37]. A BT-50FR micro-nano-sized nozzle [9,73,74] with a 55psi capacity water pump was used to generate nanobubbles. To generate nanobubbles, water was allowed to flow through the nanobubbles, generating a nozzle for 3 minutes while supplying oxygen gas. In this experiment, oxygen nanobubbles were generated using compressed oxygen in a cylinder with a regulator.

After the generation of nanobubbles, samples were collected and tested to obtain bubble size distribution and zeta potential values of using the Malvern Zetasizer Nano Z.S.52-54 The Zetasizer measures the size of the particles using the technique called

Dynamic Light Scattering (DLS), which measures the Brownian motion of the particles and relates this to the size of the particles using the Stokes-Einstein equation. Brownian motion is measured by illuminating the particles with a laser and analyzing the fluctuation in scattering intensity. Zetasizer is based on the Non-Invasive Back-Scatter (NIBS) system, which increases the accuracy of the measurements compared to conventional optics. The Zetasizer analyzes the zeta potential by determining the electrophoretic mobility of the particles and then applying the Henry's equation based on the Smoluchowisk's approximation/model. Electrophoretic Light Scattering (ELS) is a technique used by the Zetasizer to measure the electrophoretic mobility of the particles in dispersion; this technique is based on the electrophoresis. In this research, the measurements were taken using the folded capillary cell (DTS1070) for both the size and the zeta potential, where cell contains two electrodes. Once the electrical field is applied to the electrodes, bubbles that have a net charge, or a zeta potential will travel towards the oppositely charged electrode and the velocity of this mobility/movement is measured based on the Laser Doppler Velocimetry (VDL) technique combined with M3-PALS technology. This method used the mixed-mode measuring techniques that allowed to measure the zeta potential without the influence of electrical osmosis. The mixed-mode measurement is the methods of changing the reversal cycle of the electric field, which is fast-field-reverse (FFR) and slow-field-reverse (SFR) [33]

All experiments were carefully conducted to avoid possible contamination. Before the bubble generation, water was tested for the presence of any nano-size material using the Zetasizer. Always the system was cleaned/washout before each test. In this research, DI water and different NaCl concentrations (0.001M, 0.01M, and 0.1M) were prepared.

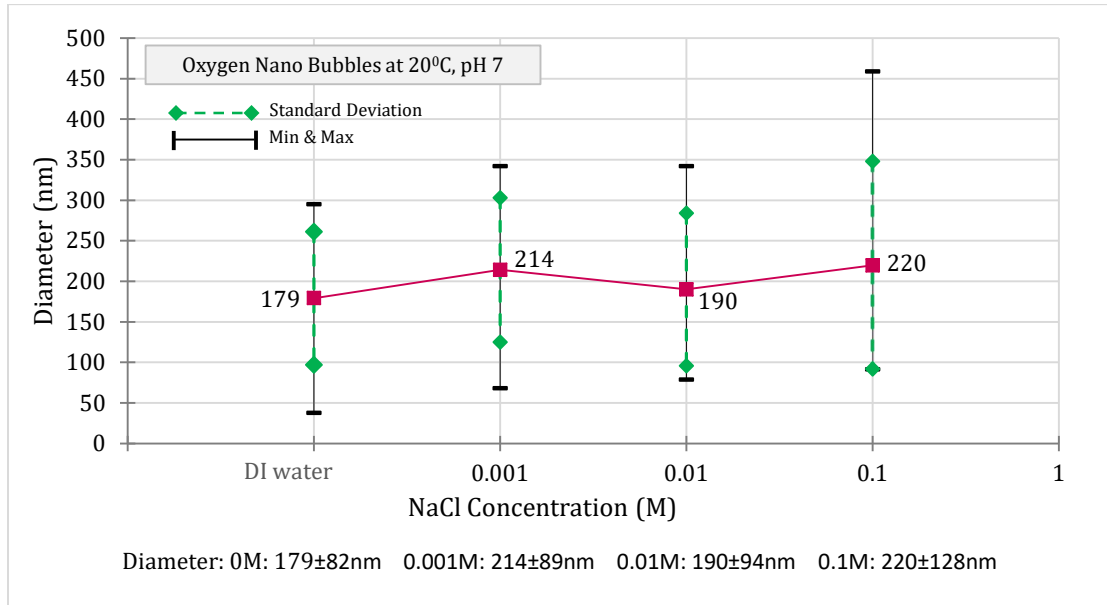
Freshly collected DI water was collected in a 100-liter tank and allowed to come to equilibrium with the atmospheric gases at the room temperature for 24 hours. Prior to the generation of nanobubbles, the gas concentrations in the bulk water in contact with air at 25<sup>0</sup>C were: Oxygen – 8.72mg/l (and at 22<sup>0</sup>C Oxygen – 9.2mg/l); Nitrogen – 13.34 mg/l; Carbon dioxide – 0.5mg/l; and negligible amounts of other gases in the air. For each test the same bulk liquid was used, the appropriate amount of salt was added, and allowed to be in equilibrium with air. Then these solutions were used to create oxygen nanobubbles. Generated nanobubbles were tested immediately after generation and 7 days after generation.

#### **4.4 Results and Discussion**

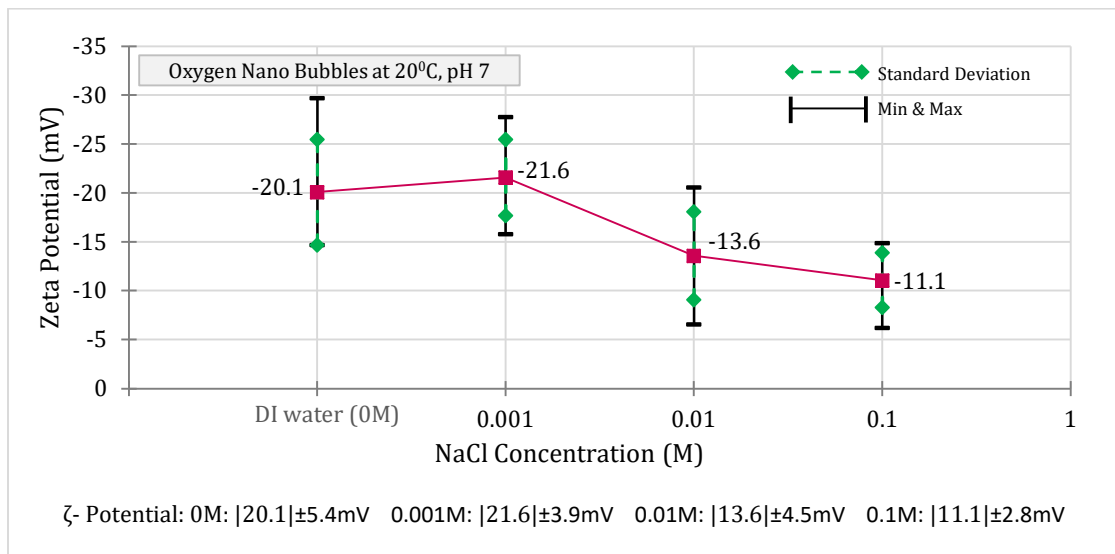
Figure 4.3(a) shows the variation of bubble sizes and 4.3(b) shows the variation of zeta potential values of the oxygen bubbles in different solutions of NaCl concentrations. Figure 4.4 shows the same test results just after the bubble generation (week 0) and after one week of generation (week1). The size/diameter results were recorded as the Number-Distribution data, where the peak values of the distribution curves are reported.

Reported test results in Figures 4.3 and 4.4 show the minimum, maximum and average values as well as the standard deviation values based on 6 measurements for each test with different salt concentrations. The results show that with the increase in NaCl concentration, bubble diameter slightly increased, and the magnitude of zeta potential decreased. All measured zeta potential values were negative. Hence, from here, onwards zeta potential values are reported without their sign. Figure 4.4(a) shows the variation of bubble diameter with time for different concentrations of NaCl solutions, where bubble diameter increased with time for all solutions. Figure 4.4(b) shows the variation of zeta

potential values with time for different concentrations of NaCl solutions, wherewith time zeta potential values decreased.

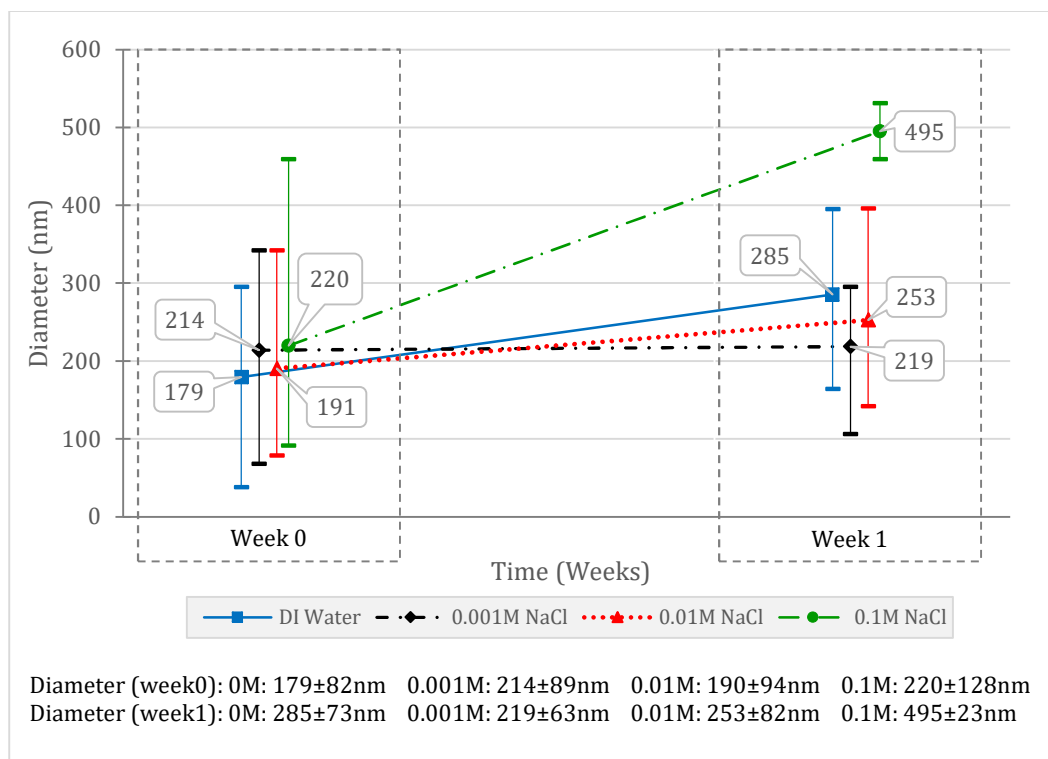


(a)

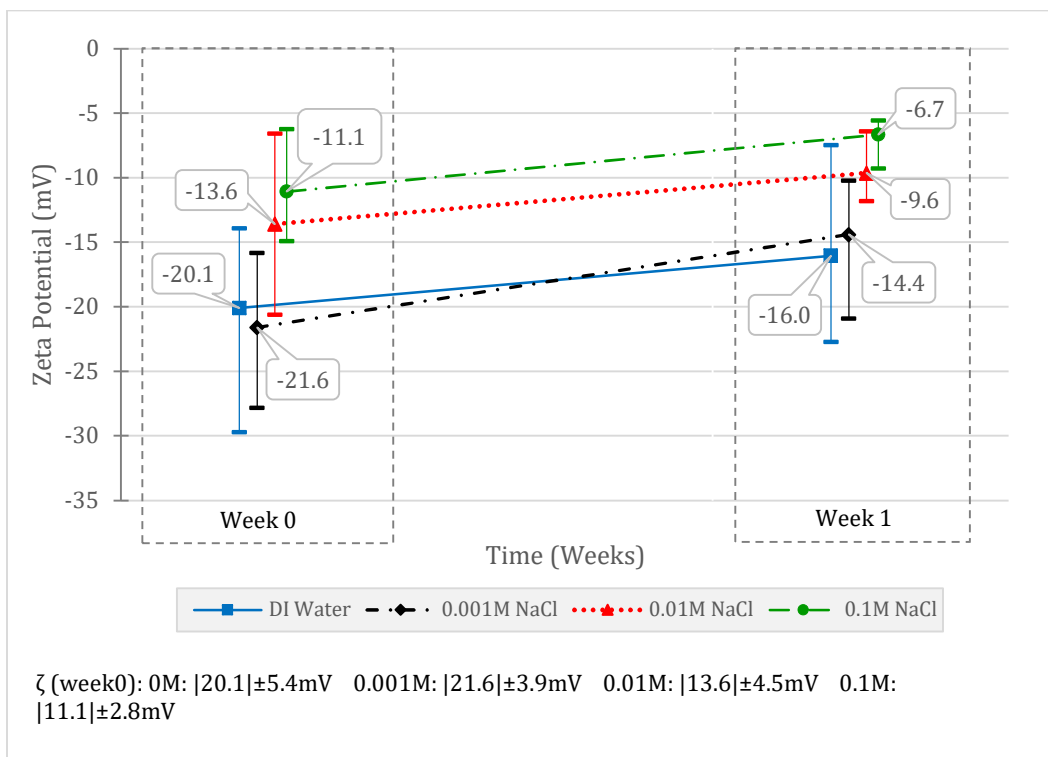


(b)

**Figure 4.3** Relationship between NaCl concentration and (a) bubble diameter, (b) zeta potential, for oxygen nanobubbles at 20°C and pH ≈ 7.



(a)



(b)

**Figure 4.4** Variation with time: (a) diameter, (b) zeta potential for oxygen nanobubbles in NaCl solution at 20°C and pH ≈ 7.



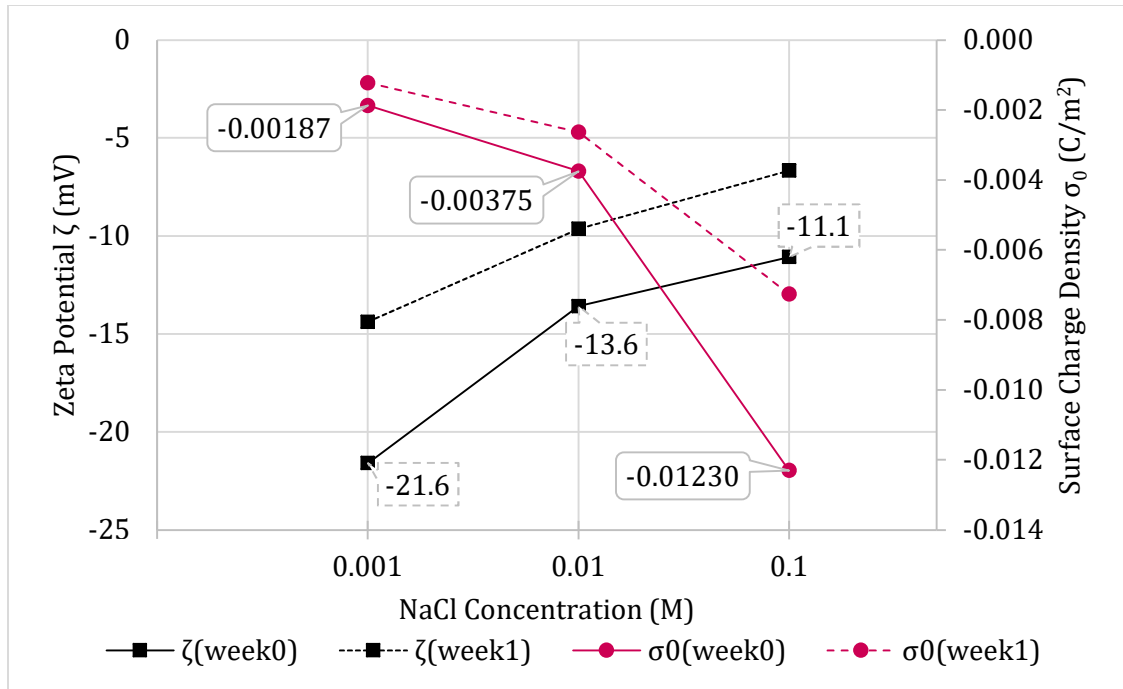
The measured data are used to compute the surface charge density, surface potential, double layer thickness, and internal gas pressure inside nanobubbles. Table 4.1 shows all the measured data as well as calculations for both week 0 and week 1. Columns 1, 2, and 3 show the NaCl concentration, bubble size, and zeta potential values, respectively. Column 4 shows the calculated double layer thickness ( $1/K$ ) based on Equation (4.11). For the DI water bubble solution, there is no stern layer without salts. Hence, double layer thickness was not computed for the DI water bubble solution. Column 5 shows the calculated surface charge density for each test. The calculated surface charge densities were based on the numerical and analytical solutions (obtained the same results) presented in Equations (4.20), (4.21), (4.22), and (4.23). Column 6 shows calculated surface potentials,  $\psi_0$  for each test. Surface potential values were calculated based on Equations (4.5) and (4.6). For the electrolyte solutions, the thickness of Stern potential ( $d$ ) was assumed as equal to the hydrated Na ion with an effective radius of 0.47 nm as previously explained. Column 7 shows the number of negative charges on the bubble surface (negative charge = (surface charge density\*surface area)/electron charge). Finally, Column 8 shows the calculated pressure difference across the fluid interface ( $\Delta P$ ) based on Equation (4.4).

Figure 4.4 and Table 4.1 illustrate that with the increase in NaCl concentration of the solution, bubble sizes slightly increased. Similarly, a week after the bubble generation, for all the solutions, bubble sizes increased. Furthermore, at week 0, zeta potential values decreased with the increase in NaCl concentration, and all the values (bubble size as well as zeta potential values) decreased after one week. For the 0.001M salt concentration, bubble size appears to be stable, with only a 2.3% increase in bubble size after one week.

However, the reduction in zeta potential was comparatively high. Also, with higher concentrations of NaCl (0.01M and 0.1M), the increase in bubble size and reduction in zeta potential values were significantly higher. The average surface charge densities and zeta potential values at week 0 and week 1 were plotted against concentrations of NaCl solutions and shown in Figure 4.5. Figure 4.5 shows that with increased NaCl concentrations, the zeta potential decreased, and the magnitude of surface charge density increased.

**Table 4.1** NaCl Solution Concentration with Average Size, Average Zeta Potential, the Calculated Double Layer Thickness, Surface Charge Density, Surface Potential, Number of Electrons, and the Pressure Difference Across the Fluid Interface.

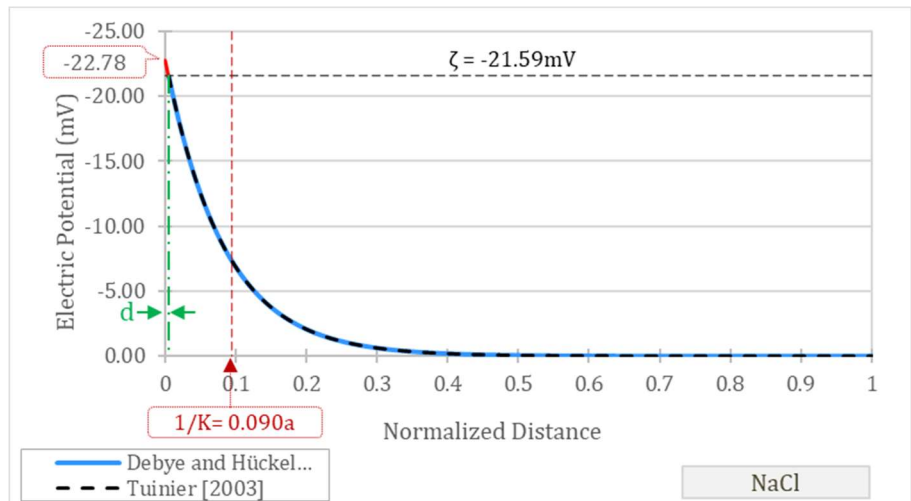
Col.1	Col. 2			Col. 3			Col. 4		Col. 5		Col. 6		Col. 7		Col. 8		
NaCl Concentration (M)	Size			Zeta Potential ( $\zeta$ )			Double Layer Thickness		Surface Charge Density ( $\sigma_0$ )		Surface Potential ( $\psi_0$ )		Number of Negative Charges		Average Pressure ( $\Delta P$ )		
	Diameter (nm)		% increase	$\zeta$ (mV)			(DLT/Radius)		(C/m <sup>2</sup> )		(mV)		#		(atm)		
	Week 0	Week 1		Week 0	Week 1	% reduction in magnitude	Week 0	Week 1	Week 0	Week 1	Week 0	Week 1	Week 0	Week 1	Week 0	Week 1	
0	179	285	59.2	-20.10	-16.00	20.4	N.D.	N.D.	N.D.	N.D.	N.D.	N.D.	N.D.	N.D.	N.D.	N.D.	ND
0.001	214	219	2.3	-21.59	-14.38	33.4	0.090	0.088	-0.0018	-0.0012	-22.78	-15.15	1605	1098	13.0	12.9	
0.01	190	253	33.2	-13.58	-9.63	29.1	0.032	0.024	-0.0033	-0.0023	-15.77	-11.16	2341	2900	14.0	10.8	
0.1	220	495	125.0	-11.07	-6.66	39.8	0.009	0.004	-0.0083	-0.0049	-16.57	-9.94	7873	23725	6.9	3.6	



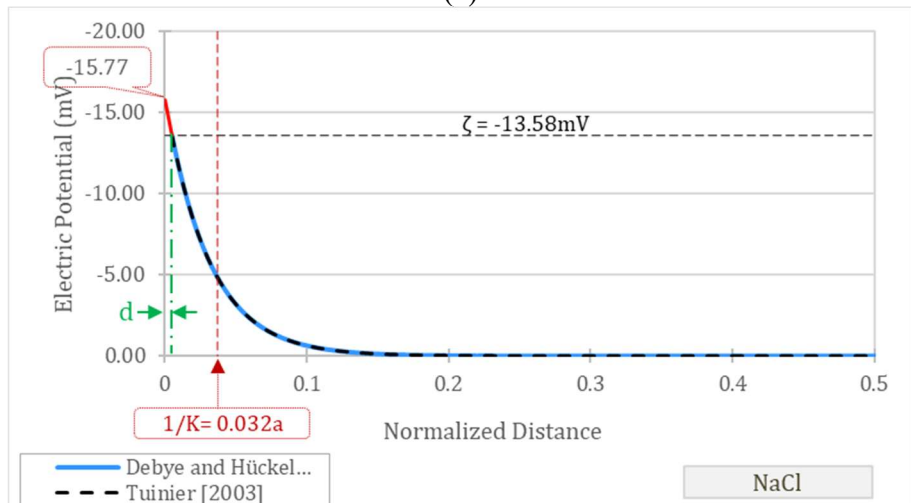
**Figure 4.5** Surface charge density for oxygen nanobubbles in NaCl solution at 20<sup>0</sup>C and pH  $\approx$  7.

Figure 4.6 shows the distribution of electric potential with the normalized distance against the bubble radius for four NaCl solutions. The corresponding double-layer thickness values correspond to the week 0 test results. It can be clearly observed from Figure 4.6 that the variation of electrical potential with distance had a steep rate of decline for solutions of higher NaCl concentrations and produced thinner double layer thickness values.

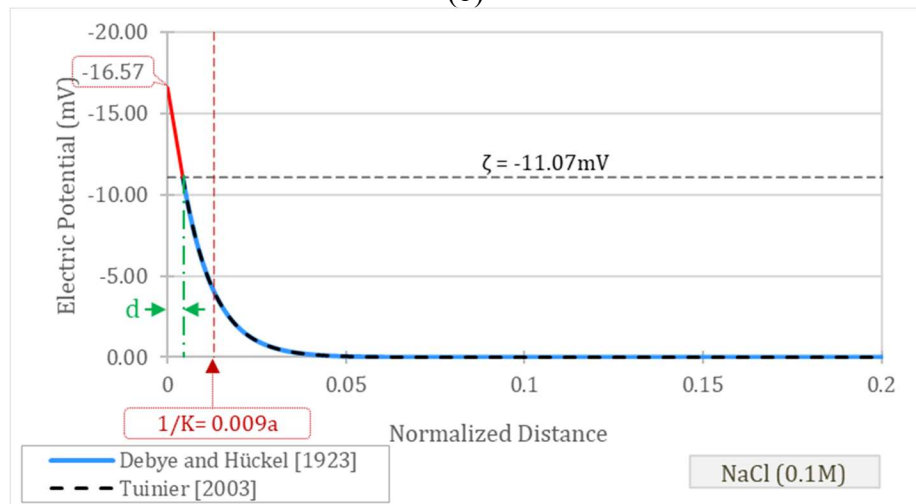
Figure 4.7 shows the total number of negative charges on the bubble surface for week 0 and week 1. It also shows the variation in double-layer thickness with increased NaCl solution concentrations for both week 0 and week 1. The double-layer thickness becomes thinner for all solutions after one week compared to those for week 0 (Table 4.1). The double-layer thickness declined with the increase in salt concentration.



(a)



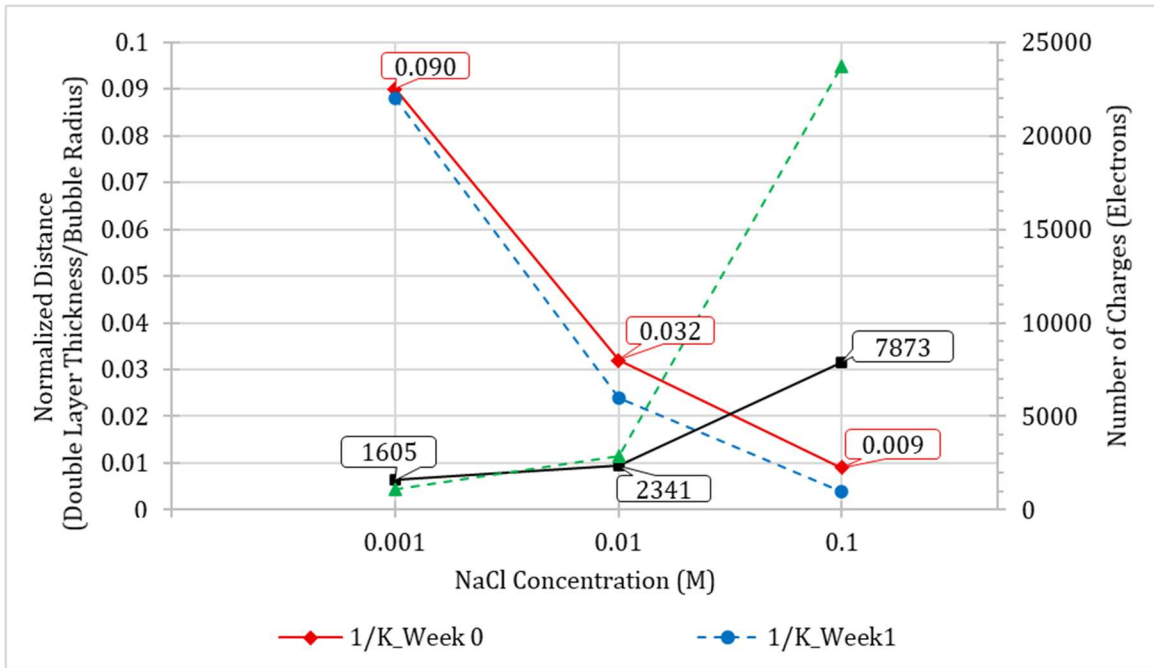
(b)



(c)

**Figure 4.6** Variation of electrical potential with distance for oxygen nanobubbles in NaCl solutions of varying concentrations (20°C and pH ≈ 7).

For bubble solutions with lower salt concentrations, there was no substantial change in the number of negative charges on bubble surfaces after 1 week. However, at high solution salt concentrations of 0.1M, the total number of surface charges increased to form large bubbles. To have such a high increase in the number of negative charges on the bubble surface, several bubbles should have merged to form larger bubbles. Hence, at high solution salt concentrations, nanobubbles seem to be much more vulnerable to coalescence due to the reduction in zeta potential and thinner double-layer thicknesses related.



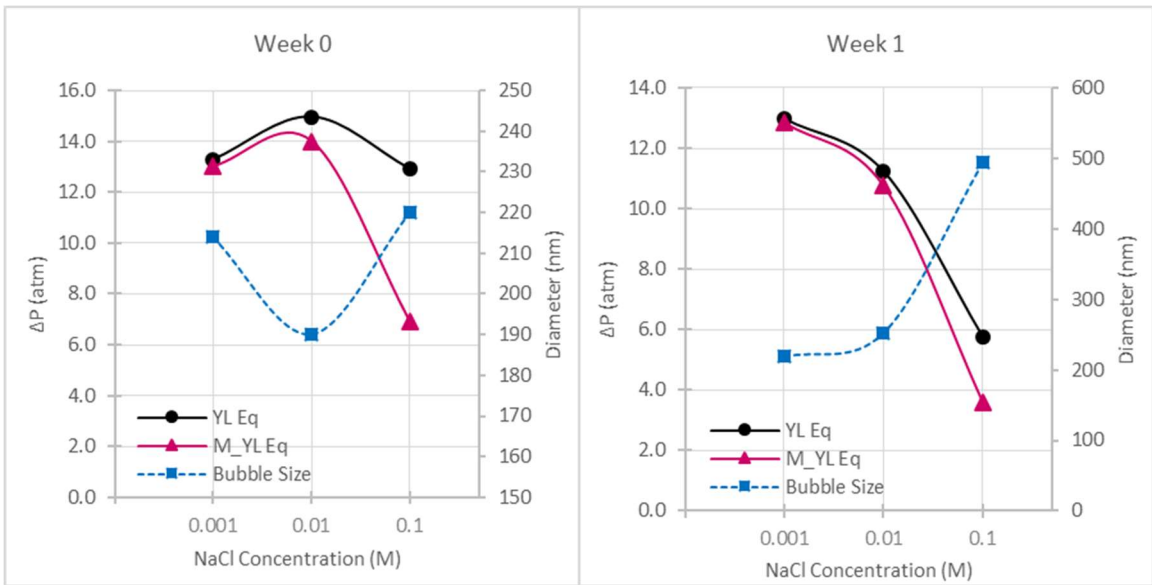
**Figure 4.7** The variation of the electric double layer thickness and number of electrons with NaCl concentration for oxygen nanobubbles at 20°C.

With the increase in ion concentration in the bulk solution, surface charge density increased while the absolute zeta potential/surface potential decreased due to the corresponding reduction in the diffuse layer thickness values of the nanobubbles. Even though, with the increase in NaCl concentration, decrease in zeta potential can be attributed to the thinning of the double layer thickness, the increase of negative charge density or the

total amount of negative charge is unexpected. With the hypothesis that the nanobubbles' negative charges are absorbed  $\text{OH}^-$  ions at the gas-liquid interface, especially for DI solution, this result suggests that the  $\text{OH}^-$  adsorption was stabilized by the added NaCl [9]. Higuchi et al. discussed a similar phenomenon for polymer material in water by considering the charge regulation mechanism [129]. By applying their finding to nanobubbles, when the two charged ions (i.e.,  $\text{OH}^-$ ) at the bubble surface approach each other, the surface charge density will be reduced to decrease the electrostatic repulsion either by absorption of the counterions and/or desorption or removal of surface charge. Therefore, it can be concluded that any increase in the ionic strength would favor the  $\text{OH}^-$  absorption as the reduction in electrostatic (repulsion) energy between absorbed  $\text{OH}^-$  ions. For lower NaCl concentration, zeta potential values did not significantly affect by the double layer thickness. For high concentration solutions (i.e., 0.01M and 0.1M), the negative charge density and the amount of negative charge increased, and this was confirmed by calculations as well. Even though absorbed  $\text{OH}^-$  density is high, with the high ionic strength the electrostatic repulsion between absorbed  $\text{OH}^-$  ions have to be weakened due to the increased amount of counterion concentration and the Debye length is sufficiently short and resulted in lowering the zeta potential. In such a situation, the charge regulation mechanism may become less effective compared to the weakened long-range repulsion causes the increase of the bubble coalescence.

The gas dissolution rates in a nanobubble would depend on inside gas pressure and with higher gas pressures causing higher diffusion rates. Column 8 of Table 4.1 shows the variation of average gas pressure in bubbles with different concentrations of the NaCl solutions based on Equation (4.4). Figure 4.8 shows the predicted gas pressures inside

nanobubbles for three salt solutions based on the Young Laplace and the Modified Young Laplace equation. Results show that, with increased salt concentration, pressure difference at the gas-liquid interface decreased; however, the bubble diameter did not significantly vary with the increased concentration of the NaCl solution. Even though it was expected that, with high surface charge densities, internal pressures inside the bubble would reduce, the results indicate that the contribution was minimal. Only with a high amount of NaCl (i.e., 0.1M), there was a considerable reduction in internal gas pressure. Table 4.1 shows that with the increase in surface charge density, there is minimal change in bubble characteristics as the inside gas pressure is still significantly high. Table 4.1 and Figure 4.8 shows that nanobubbles in 0.001M salt solution, the internal gas pressure did not significantly vary after one week.



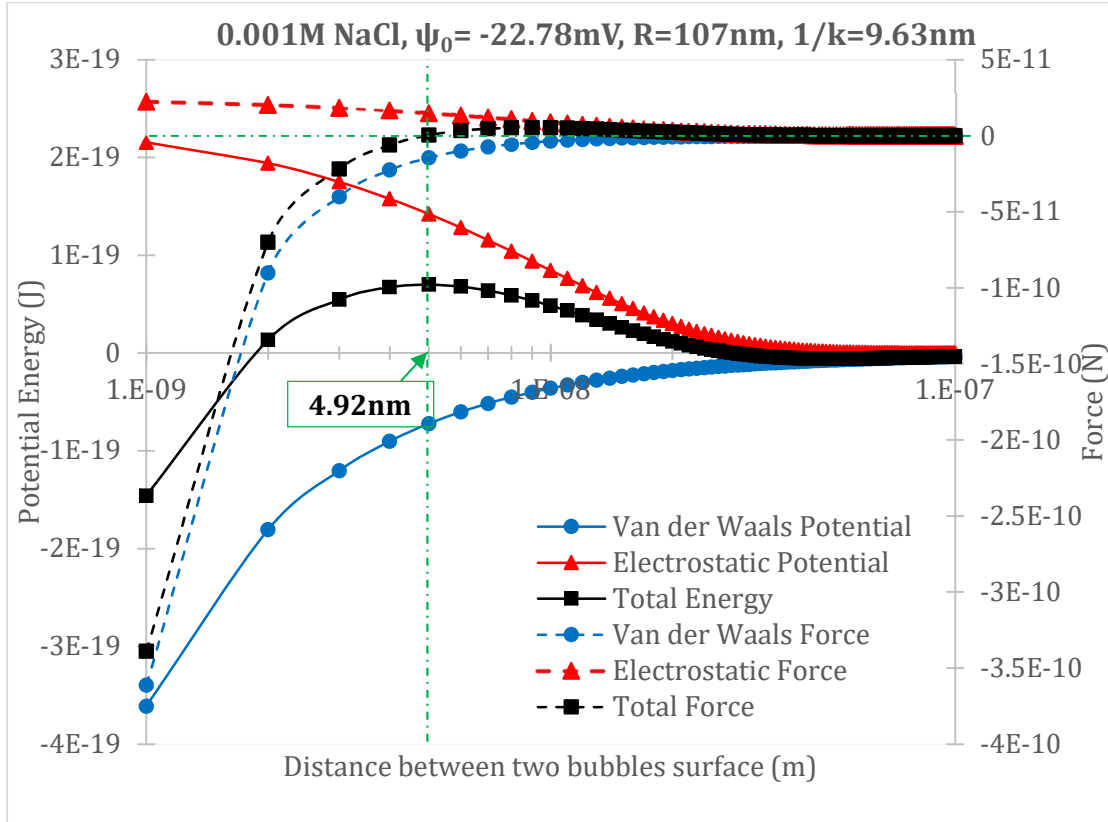
**Figure 4.8** Pressure difference across the fluid interface ( $\Delta P$ ) based on the Young- Laplace equation and Modified Young-Laplace equation.

Figure 4.9 shows that the van der Waals energy/force, electric double layer repulsion energy/force and the total energy/force for 0.001M, 0.01M and 0.1M NaCl concentrations. For the 0.001M NaCl solution, with higher the repulsive energy/forces a stable nanobubble solution was created as the bubble coalescence was prevented due to the neutralization of the van der Waals interactions. Based on Figure 4.9a, there is comparatively high electrostatic repulsion, and hence, the total interaction energy is positive for the intermediate separation distances. Also, there is a peak energy barrier of  $6.99 \times 10^{-20} \text{J}$  with zero net interaction force for a critical separation distance of 4.92nm. However, for higher NaCl concentration solutions (0.01M and 0.1M), results clearly indicated that the energy barrier disappeared, and total interaction energy and forces are dominated by the van der Waals attraction. This indicates that the net energy and force curves are always attractive with high potential for bubble coalescence (Figure 4.9b and 4.9c). The net negative energy and attractive force are shown in Figures 4.9b, and 4.9c indicate that the electrostatic repulsion is very sensitive to the ionic strength of the solution.

The higher concentration of ions in the solution reduces the double layer interaction between the charged surfaces resulting in the reduction in double layer thickness, and thereby reducing the magnitude of repulsive interaction. While the van der Waals attraction is insensitive to the electrolyte concentration. At the very smaller separation distance, the van der Waals force is always greater than the electrostatic force, because the van der Waals forces are based on the power law. This phenomenon can be seen in the Figure 8a as well, where the separation distance becomes smaller, and the net interaction energy is negative for separation distances less than 1nm, which can lead to bubble coalescence at smaller separation distances. Therefore, the above observations can be summarized as, for similarly

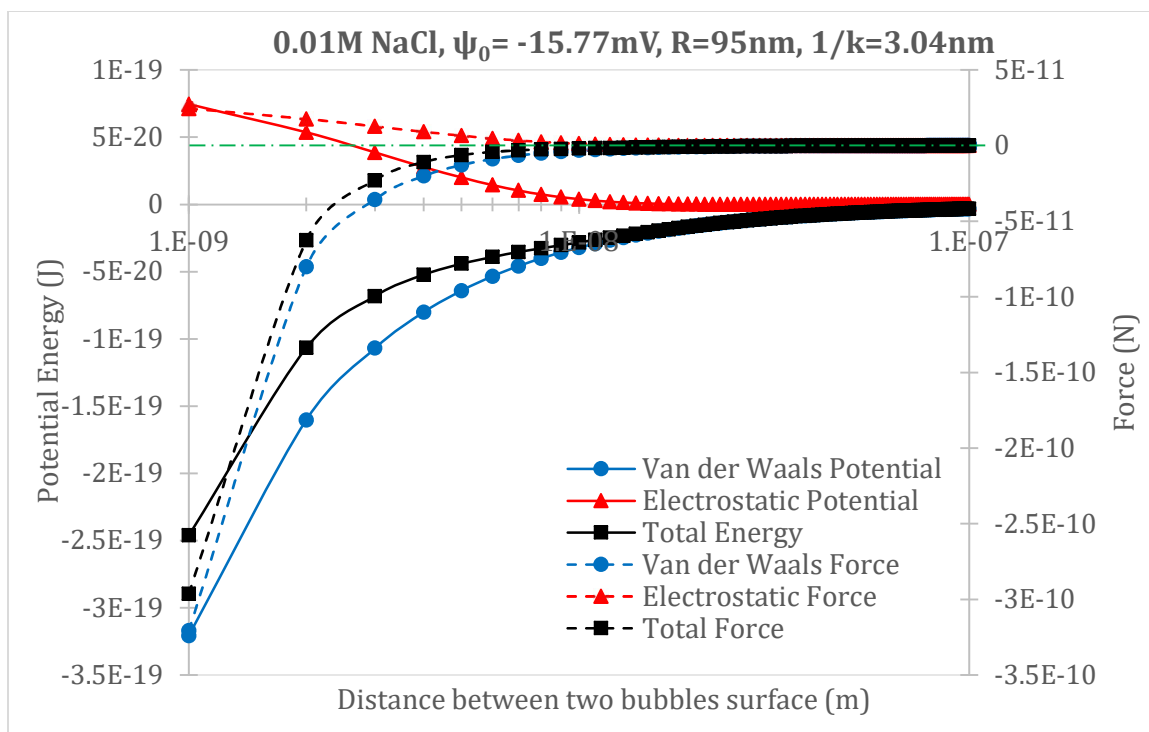


charged bubbles, at low NaCl concentration, there is high double-layer repulsion preventing bubble coalescence.

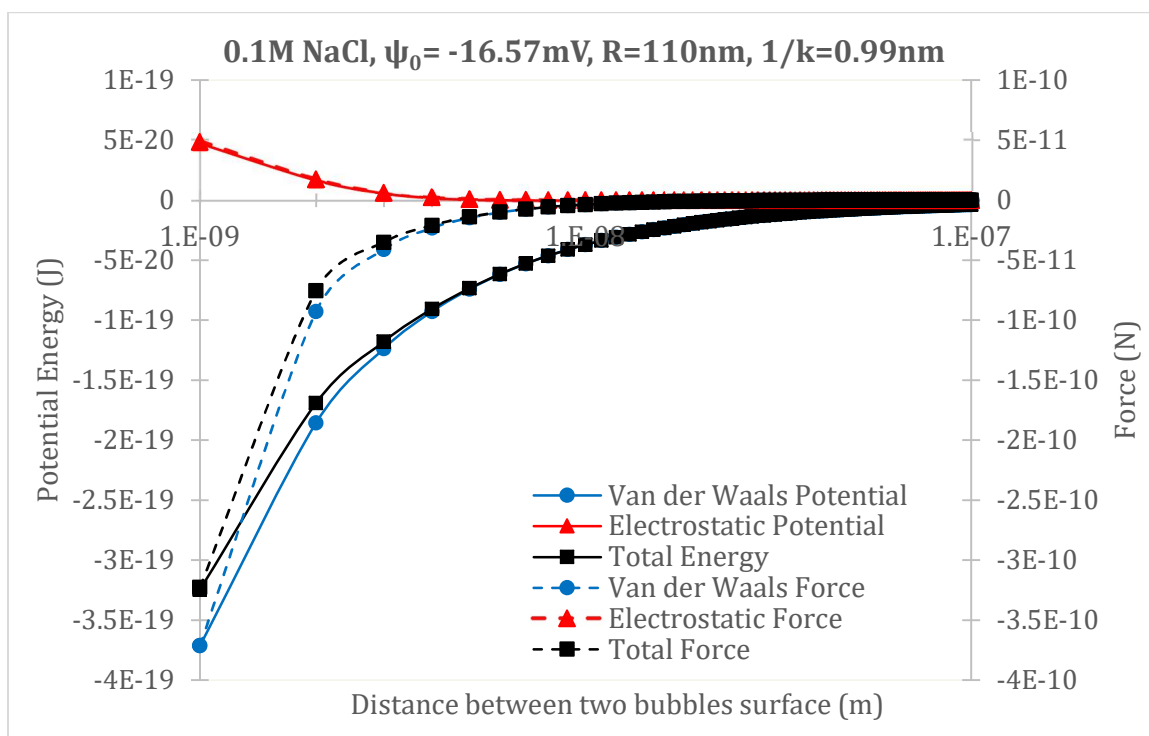


(a)

**Figure 4.9** Van der Waals, electrostatic and total energy and forces vs. separation distances for nanobubbles in NaCl solutions for varying concentrations (20<sup>0</sup>C, pH $\approx$ 7) (**Continued**).



(b)



(c)

**Figure 4.9 (Continued)** Van der Waals, electrostatic and total energy and forces vs. separation distances for nanobubbles in NaCl solutions for varying concentrations ( $20^\circ\text{C}$ ,  $\text{pH} \approx 7$ ).

Based on the above discussion, it can be stated that the most stable bubbles were obtained with 0.001M NaCl concentration and the least stability was recorded with the highest amount (0.1M) of NaCl concentration. Also, the experimental results showed that nanobubbles could be generated in DI water. This indicates that the stability of nanobubbles is a complex chemical and physical phenomenon. Therefore, there must be multiple factors contributing to the stability of nanobubbles as experimental data showed the existence of nanobubbles for long time periods. Hence, the mechanism behind the stability of nanobubbles is not just limited to smaller in size and having a high surface charge but a more complex phenomenon.

Dressaire et al. explained that bubble stability using a diffusion barrier because of ion accumulation (ions shielding) [99]. Uchida et al. used a transmission electron microscope to analyze nanobubbles and observed a thin film around the bubble surface [27]. They speculated that this thin layer consisted of impurities (including NaCl and NaCl-2H<sub>2</sub>O) and hypothesized that the Na<sup>+</sup> ion accumulation in the aqueous solution reduced the gas dissolution rate. Nakashima et al. [63] and Ohgaki et al. [19] reported that apparent stability of nanobubbles would strongly depend on the characteristics of the interfacial film and the interface of nanobubbles consisted of highly structured hydrogen bonds. Seddon et al. [58], Weijs et al. [1], and Uchida et al. [27] reported that bubble gas dissolution rate decreased as bubble solution become saturated with gas (diffusive shielding). Based on the bubbles suspended solution and bubble state (undersaturated, saturated or supersaturated), bubbles can either to grow or shrink.

The behavior of smaller nanobubbles is quite complex. This is because, in addition to saturation levels, the surface tension forces play a vital role. In order to achieve

thermodynamic equilibrium, the bubble system should be chemically and mechanically be in equilibrium. The bubble will be mechanically stable when the total outward pressure from inside the bubble at the gas-liquid interface equal to the total inward pressure at the gas bubble interface as expressed by Equation (4.4). The bubble will be chemically in equilibrium when partial pressures of each gas type in the bubbles are equal to their respective bulk liquid gas pressure described by Henry's law. However, if the bulk liquid is supersaturated relative to the bubble, then there is a bulk gas movement into the bubble. Also if the bulk medium is under-saturated, then there is bulk gas movement out of the bubble. If gas pressures are in equilibrium, bubble size will remain unchanged, and there will be no mass transfer between the bubble and the surrounding liquid [64]. In such conditions, bubbles are considered to be either thermodynamically stable (globally lowest total free energy) or thermodynamically metastable (locally lowest total free energy, but not globally minimum free energy) [64]. These metastable bubbles would eventually change to another metastable state or to a thermodynamical equilibrium state. Thus, nanobubble stability would also depend on the gas concentrations in the solution and inside the bubble. Therefore, there is an urgent need to develop methods to accurately determine the gas concentration/pressure inside nanobubbles.

If there are nanobubble coalescence, where bubbles grow in size by merging with adjacent nanobubbles, bubble merging can be caused due to different mechanisms. The coalescence of similar size bubbles may be due to the Brownian motion, while if the bubbles are of different sizes, they can be merged due to the Ostwald ripening effects. According to Henry's law and the Gibbs-Thomson equation, the smaller sized bubbles are a source of gas in the surrounding solution [27]. Consequently, a larger bubble grows as

the smaller bubble diffuses into larger bubbles. For the comprehensive investigation of nanobubbles stability, all the phenomena (i.e., surface charge, saturation level, diffusion rates, chemical potentials, surface tension, etc.) should be simultaneously considered. Such analysis is possible with the use of Molecular Dynamic simulations.

#### 4.5 Conclusions

In this present work, the ion distribution around the bubbles, and hence, the presence of a diffuse double layer theory was applied to nanobubbles in salt solutions of different concentrations. The surface charge density values on nanobubbles were computed using numerical simulations as well as previously developed analytical solutions. Then the double layer thicknesses, van der Waals attractive force, electrostatic repulsive force and the net interactive energies and forces were calculated. With the increase in NaCl concentration, bubble size increased, and zeta potential/surface potential decreased. With the reduction in zeta potential values, there was a corresponding reduction in double layer thickness. The literature confirmed that, with an increase of NaCl concentration, a reduction in negative zeta potential, and an increase in effective diameter [18,70,92]. Also, the surface charge density and total negative charge increased, which was explained as OH<sup>-</sup> absorption due to the added NaCl. Furthermore, interfacial forces calculation showed that, for the 0.001M NaCl solution, strong electrostatic repulsion with a positive energy barrier. With the increasing amount of NaCl concentration (i.e., 0.01M and 0.1M), there was the weakening of the electrostatic repulsion force. Uchida et al. [27] also showed a similar reduction in zeta potential with salts' addition. Furthermore, pressure calculation showed a reduction in the interfacial pressure difference with the increased NaCl concentration. Yet, the amount of reduction is insufficient to compensate for the pressure created due to the

surface tension. The experimental results reported in this study, and the diffused double layer application was limited to oxygen bubbles in different solutions of NaCl concentrations. The applicability of diffuse double layer theory for different solution chemistries should be investigated. Literature suggests bubble clustering to prevent gas diffusion. Also, there is a possibility of a reduction in surface tension of water due to salts' dissolution [130–132], which is not considered in this research. Finally, this research assumed that surface charge on bubbles consisted of  $\text{OH}^-$  but was not included in any calculations. However, there is a good possibility that those negative charges may be  $(\text{HCO}_3^-)$  ions due to dissolved  $\text{CO}_2$  in the air. All these need to be further studied to develop a comprehensive theory for nanobubbles behavior using molecular dynamics simulations.

## CHAPTER 5

### STABILITY OF NANOBUBBLES IN DIFFERENT SALTS SOLUTIONS

#### 5.1 Introduction

Bulk nanobubbles are gas-filled cavities suspended in aqueous solutions having diameters smaller than 200 nm [3,4,93]. The existence of these extremely small bubbles has been experimentally confirmed by different researchers [93,133]. These bubbles have attracted attention due to their extraordinary properties and characteristics, especially their long lifespans and electrically charged interfaces [5,6]. Nanobubbles are already used in a wide range of applications and areas, including drinking/wastewater/groundwater treatment [40,70,134,135], decontamination of sediments and soils [72–74,136], biomedical engineering [137–139], and the agricultural, fishing, and food industries [4,9,140,141]. Despite their widespread use, nanobubbles remain a poorly understood technology, especially relating to their long existence or stability, interfacial properties, and radical formation.

The stability and reactivity of nanobubbles depend on several factors, such as the bubble size, zeta potential, and interfacial characteristics [47,50,142–144]. Nanobubble characteristics also highly depend on solution properties, infilled gas type, and the energy provided to the system to generate nanobubbles [9]. Solution properties such as temperature, pressure, ion type, ion concentration, pH, presence of organic matters or impurities, presence of surfactants, and saturated gas concentration play an important role [26,47,145,146]. The infilled gas type and its solubility and reactivity can also impact the bubble properties [9,146,147]. Furthermore, the generation mechanism and energy

provided to the system (i.e., hydrodynamic method, ultrasound) are key factors that influence the bubble size, radical formation, and related chemical reactions [148–150].

Nanobubbles have an electrical charge interface which controls the ion distribution in aqueous solution near the bubble surface. The accumulation of ions near the gas-liquid interface influences the physical-chemical properties of the nanobubble. An application such as the flotation can be benefited by controlling the number of charges on nanobubbles. Hence, with the proper selection of electrolyte types and concentrations, the zeta potential of bubbles and the bubble stability can be controlled. The bubbles formed in the different electrolyte solutions can be used to further understand the nanobubble properties. Even though there are prior studies on nanobubbles formed in different electrolyte solutions, research findings and conclusions are only limited to the direct comparison of zeta potential values and specific adsorption with respect to the valency effect. Limited research has conducted on the application of DLVO theory for nanobubbles formed in multivalent electrolytes, as most of the prior research is limited to nanobubbles formed in symmetrical electrolytes. The present study provides experimental data on bubble sizes and zeta potential values for nanobubbles formed in different electrolyte solutions at both the generation and after one week to evaluate the long-term stability. The diffuse double layer theory was applied to calculate the potential distribution and ion distribution away from the bubble surface, and the DLVO theory applied for different electrolyte solutions by considering both the interactions of electrostatic repulsion and van der Waals attraction. The analyzed results were collectively considered to evaluate the properties and behavior of nanobubbles. Additionally, a literature review was conducted for nanobubbles in



different valency electrolytes to provide a meaningful comparison with respect to the work presented in this manuscript.

In this research, nanobubbles were generated in different electrolyte solutions under different ion valences and ionic strengths, namely deionized water and NaCl, Na<sub>2</sub>SO<sub>4</sub>, Na<sub>3</sub>PO<sub>4</sub>, CaCl<sub>2</sub>, and FeCl<sub>3</sub> in deionized water. The diffuse double layer theory was applied to nanobubbles in the monovalent electrolyte of NaCl for different concentrations and found stable nanobubbles were formed in low concentration (0.001M) solution [151]. Therefore, in this research, a concentration of 0.001M for the various electrolytes was used to generate nanobubbles to study the impact of different ion types on characteristics and behavior of nanobubbles.

## **5.2 Formation of Electric Double-Layer Around Nanobubbles**

Nanobubbles suspended in aqueous solutions carry electrical charges on the gas-liquid interface [9,145,151]. The nanobubble with an electrical charge interface accumulates counter charges in order to preserve electrical neutrality. For example, negatively charged surfaces are attracted to positively charged cations for electrostatic equilibrium. Simultaneously, due to ion diffusion, the cations move to the bulk solution, and the diffused layer is formed. At the diffused layer, the concentration of counterions is increased towards the bubble surface, and ion distribution primarily depends on the magnitude of the surface charge. In contrast, like charges (co-ions) are repelled away from the bubble surface, and there is a low concentration of co-ions at the interface. This diffuse ion distribution has been formulated by different models to evaluate the surface charge density and distribution of ions around the colloidal particles.

The Poisson-Boltzmann (PB) equation can be used to describe the distribution of ions around the charged particle and can calculate the electric potential,  $\psi(x)$ , around the surface. The non-linear second order PB equation can be solved subjected to the boundary conditions and then can be related to the surface charged density. No analytical solutions are available for the PB equation for the general case of spherical particles. However, there are a number of methods used to determine numerical solutions. In this analysis, due to the spherical colloidal condition along with asymmetric ionic valency conditions, the general nonlinear PB equation must be solved. Therefore, in this manuscript, we utilized the numerical simulation based on the network simulation method [152].

The network simulation method consists of modeling the governing equations by means of an electrical circuit. This network simulation method is useful as it avoids difficulties of mathematical analysis. The model consists of a graphical analogous representation of the physical process of the diffuse double layer to electrical circuit diagrams which are analyzed using an electric circuit simulation program. In this work, PSpice electric circuit simulation program was used for the analysis. The full details of the network model used in this manuscript can be found in [152].

### **5.3 The Bubbles Interaction Force and Energy**

The classical DLVO theory can be used to explain the interaction between nanobubbles suspended in an electrolyte solution. The stability of the bubble can be considered based on the energy or force balance between the attractive van der Waals interaction and the repulsive electric double layer interactions [120,121]. The relevant equations are given in the next section.

### 5.3.1 Equations for modeling

Consider the spherical nanobubble with radius  $a$ , stern layer thickness  $d$ , and zeta potential,  $\zeta$ . In this research, the zeta potential is assumed as equal to the Stern potential ( $\zeta \cong \psi_d$ ) and the justification for this assumption can be found in [151]. The Poisson–Boltzmann equation for a spherical charged particle immersed in an infinite electrolyte solution relates the electric potential  $\psi(r)$  to the charge density  $\rho(r)$  at any point of the diffuse electric double layer given by [152],

$$\frac{1}{r^2} \frac{d}{dr} \left[ r^2 \frac{d\psi(r)}{dr} \right] = -\frac{\rho(r)}{\varepsilon} = -\frac{1}{\varepsilon} \sum_{i=1}^N z_i e n_i^0 \exp\left(\frac{-z_i e \psi(r)}{kT}\right) \quad (5.1)$$

Here, we consider the boundary condition  $\psi(r = a + d) = \psi_{stern} = \zeta$  and  $\psi(r \rightarrow \infty) = 0$ , where,  $\varepsilon$  is the dielectric permittivity of the solution,  $z_i$  and  $n_i^0$  are valency and bulk concentrations ( $ions/m^3$ ) of the  $i^{\text{th}}$  ionic species respectively,  $e$  is an elementary charge ( $1.60217662 \times 10^{-19}$  C),  $k$  is Boltzmann constant ( $1.380649 \times 10^{-23}$  J·K<sup>-1</sup>), and T is temperature (K).

In order to simplify Equation (5.1), the dimensionless variables are needed as shown below,

$$y = \frac{e\psi(r)}{kT} \quad q = Kr \quad (5.2)$$

where the Debye length ( $K^{-1}$ ) or diffuse double layer characteristic length can be expressed as,

$$K^{-1} = \sqrt{\frac{\epsilon kT}{e^2 \sum_{i=1}^N z_i^2 n_i^0}} \quad (5.3)$$

Now Equation (5.1) can be updated,

$$\frac{1}{q^2} \frac{d}{dq} [q^2 l] = \bar{\rho}(y) \quad (5.4)$$

with

$$\bar{\rho}(y) = \frac{\sum_{i=1}^N z_i n_i^0 \exp(-z_i y)}{\sum_{i=1}^N z_i^2 n_i^0} \quad (5.5)$$

and

$$l = -\frac{dy}{dq} \quad (5.6)$$

The boundary condition for Equation (5.1) becomes,

$$y(q = q_{stern}) = y_{stern} \quad y(q \rightarrow \infty) = 0 \quad (5.7)$$

with

$$y_d = \frac{e\psi_{stern}}{kT} = \frac{e\zeta}{kT} \quad q_{stern} = K(a + d) \quad (5.8)$$

The surface charge density ( $\sigma_0$ ) and potential ( $\psi$ ) relationship can be expressed as,

$$\sigma_0 = -\epsilon \left( \frac{d\psi(r)}{dr} \right)_{r=(a+d)} \quad (5.9)$$

Thus, the surface potential ( $\psi_0$ ) can be calculated as,

$$\psi_0 = \psi_{stern}^{drop} + \zeta \quad (5.10)$$

The stern layer can be considered as a parallel concentric sphere capacitor, and therefore, the potential drop is linear within the stern layer. hence,  $\psi_{stern}^{drop}$  is,

$$\psi_{stern}^{drop} = \sigma_0 \left( \frac{d}{\epsilon} \right) \quad (5.11)$$

Once the potential distribution is solved, the ionic concentration at any point ( $n_i(r)$ ) of the double layer is given by the Boltzmann distribution of ions  $i$  at distance  $r$ ,

$$n_i(r) = n_i^0 \exp \left( \frac{z_i e \psi(r)}{kT} \right) \quad (5.12)$$

The ionic strength of the electrolyte solution is a measure of the concentration of ions in that solution, and given by,

$$I = \frac{1}{2} \sum_i n_i^0 z_i^2 \quad (m^{-1}) \quad (5.13)$$

Once the surface charge densities and surface potential calculations were obtained, the interaction between the particles can be found based on the DLVO theory by considering electrostatic repulsion and Van der Waals attraction.

For low surface potential, below about 25mV, for two spheres of radius, R with identical charges, the electrostatic interaction force F(D) and energy W(D) for separation distance D are given by [125],

$$F(D) \approx 2\pi R \epsilon K \psi_0^2 e^{-KD} = 2\pi R \sigma^2 e^{-KD} / K \epsilon \quad (N) \quad (5.14)$$

$$W(D) \approx 2\pi R \epsilon \psi_0^2 e^{-KD} = 2\pi R \sigma^2 e^{-KD} / K^2 \epsilon \quad (J) \quad (5.15)$$

The above equations, Equations (5.14) and (5.15) are valid for all the electrolytes (i.e., 1:1, 1:2, 2:2, 3:1, or mixtures) with appropriate Debye lengths.

The attractive van der Waals interaction for two spherical surfaces with radius,  $R$  for all the separation distances ( $D \ll R$ ) can be expressed as [120],

$$F(D) = -\frac{AR}{12D^2} \quad (N) \quad (5.16)$$

$$W(D) = -\frac{AR}{12D} \quad (J) \quad (5.17)$$

where  $A$  is the Hamaker's constant.

The van der Waals forces are effective at a short-range around a distance of 10nm. When the two bubbles approach, a thin-film is formed between them. As a result, excess surface salt in the thin film is higher than that on the bubble surface. It can reverse the direction of force at the bubble, which can weaken the van der Waals attraction force. Further, with significant salt concentration, the surface tension of the liquid film will increase, and concurrently will reduce the surface tension of the bulk fluid close to approaching bubbles. Likewise, the nanobubbles are believed to be stabilized by adsorbed impurities and ions at the gas-liquid interface. Therefore, to represent this weakened van der Waals forces, the Hamaker constant of  $2 \times 10^{-20} J$  was used [153] for the nanobubbles in electrolyte solutions, instead of the bubble-bubble interaction across pure water which has a Hamaker constant of  $3.7 \times 10^{-20} J$  [120]. However, the Hamaker constants used in van der Waals attractive force calculations in this manuscript do not explicitly depend on specific properties of salt ions [154].

One of the main features of nanobubbles is their estimated high internal pressure values. These high internal pressures and the long-term stability of nanobubbles are very debatable facts. One of the suggested rational for the stability of the nanobubble is associated with the surface charge at the gas/liquid interface, which introduces opposing forces to the surface tension that prevents the gas dissipation. Therefore, with the assumption that the nanobubble attains mechanical equilibrium, the nanobubbles pressure difference can be expressed using the Modified Young Laplace equation [151],

$$[P_{in} - P_{out}] = \frac{2\gamma}{R} - \frac{2\pi\sigma^2}{\varepsilon} \quad (5.18)$$

## 5.4 Experimental Procedure

### 5.4.1 Materials

Sodium Chloride (NaCl, 99+%), and Sodium Sulfate (Na<sub>2</sub>SO<sub>4</sub>, 99+%), from ACROS Organics and Sodium Phosphate Tribasic Dodecahydrate (Na<sub>3</sub>PO<sub>4</sub>·12H<sub>2</sub>O, 98 to 102%), Calcium Chloride Dihydrate (CaCl<sub>2</sub>·2H<sub>2</sub>O, 99.0 to 105.0%), Ferric Chloride Hexahydrate (FeCl<sub>3</sub>·6H<sub>2</sub>O, 97 to 102%), from Fisher Chemical, and Calcium Chloride Dihydrate (CaCl<sub>2</sub>·2H<sub>2</sub>O, 99+%), from Mallinckrodt, Inc were purchased. For all the experiments, de-ionized water (Millipore DIRECT-Q 3 UV system, Millipore Corporation) was used. The de-ionized water had an electrical conductance of 0.04 μS/cm, and fresh DI water was collected in a 100 L tank and allowed to reach equilibrium with the atmospheric gases at room temperature for 24 hours.

#### **5.4.2 Preparation of nanobubble**

To form nanobubbles in the electrolyte solution, the required amount of salt was measured and dissolved in 250 mL of DI water. Water was added to reach a total volume of 18 liters and the solution was placed in a 25 L chamber (e.g., for NaCl (99+%), 1.052g of NaCl dissolved in 18L of DI water to obtain 0.001M solution  $[(1/(58.44 \text{ g/mol})) \times 1.052 \text{ g} \times (1/18 \text{ L})]$ ). The nanobubbles were formed using the micro-nano nozzle (model BT-50FR, Riverforest Corporation, USA), which utilizes the hydrodynamic cavitation method. The solution was allowed to pass through the nano nozzle using a 55 psi water pump (model 4CUK6, Dayton, USA), where the pump ran for three minutes. All experiments were carefully performed to avoid possible contamination. Two separate experiments were performed for each salt type, and for each test, two samples were tested for bubble size, zeta potential and conductivity with each analyze having six readings (total of 24 records per solution). The solution conductivity was measured to confirm the accuracy of the salt concentration.

#### **5.4.3 Measurement of zeta-potential and nanobubble size**

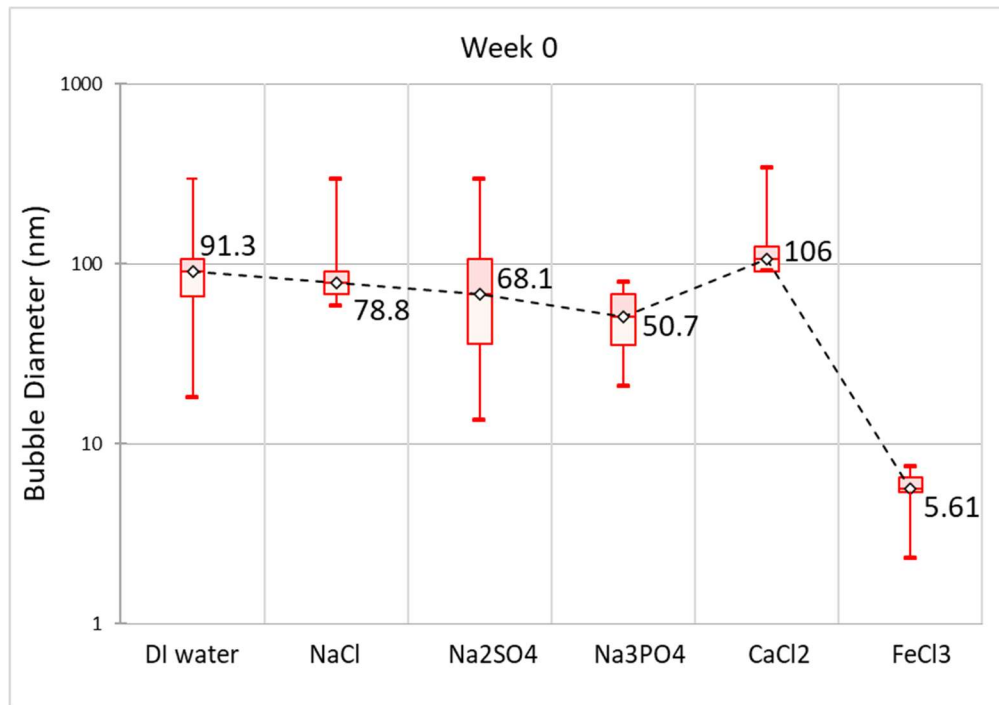
Immediately after the generation and one week after, the nanobubbles were tested for bubble size and  $\zeta$  potential value using the Malvern Zetasizer Nano ZS. The Zetasizer utilizes dynamic light scattering with Non-Invasive Backscatter (NIBS) optics for the size measurements and electrophoretic light scattering technique for the zeta potential measurements. Here, zeta potential was measured by determining the electrophoretic mobility of the particles and then applying Henry's equation based on the Smoluchowisk's approximation. All the tests were performed at room temperature, and the collected samples were stored in airtight flasks for one week for measurements.



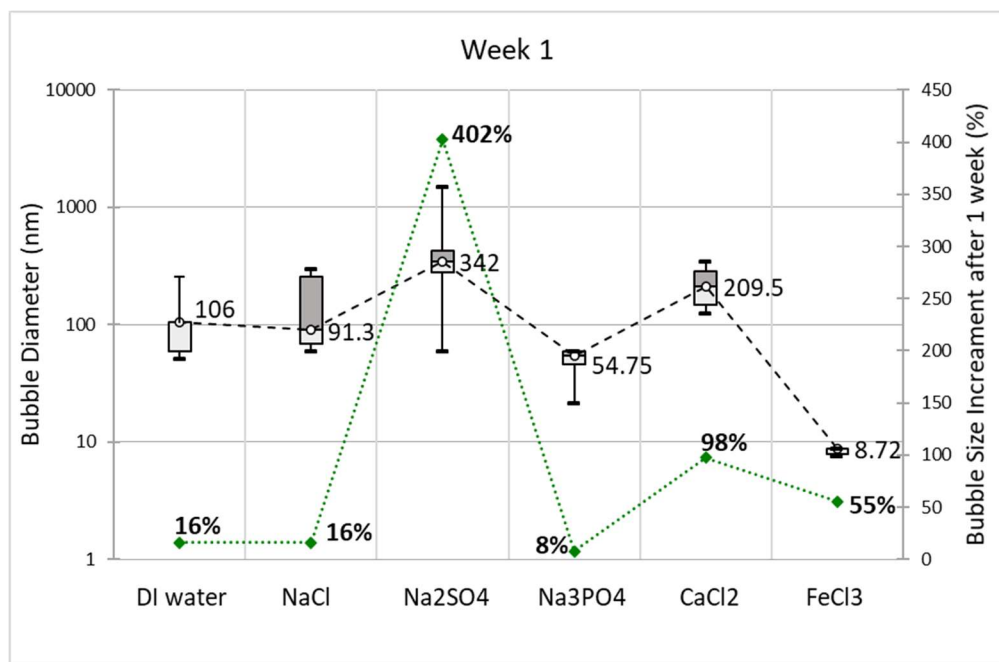
## 5.5 Results and Discussion

Table 5.1 shows solution parameters for the six samples used. It represents the solution type (Col. A), solution concentration (Col. B), molar mass of salt (Col. C), the charge density of cation (Col. D), ionic strength of the salt (Col. E), Debye length (Col. F), the average conductivity at week 0 and week 1 (Col. G,H), average pH at week 0 (Col. I) and average DO concentration at week 0 (Col. J). The dissolved oxygen (DO) concentrations are relatively high compared to ordinary conditions (above 6.5-8 mg/L). For all the samples, the DO concentration was relatively similar and were around  $33 \pm 0.89$  mg/L. Therefore, solution gas concentrations were considered to have reached supersaturation.

Figures 5.1a and 5.1b show the nanobubbles size variation for six aqueous solutions just after generation and after 1 week, respectively. At generation, the bubble size increase in order of  $\text{FeCl}_3 < \text{Na}_3\text{PO}_4 < \text{Na}_2\text{SO}_4 < \text{NaCl} < \text{DI water} < \text{CaCl}_2$  solutions. The percentage of bubble size growth over 1 week is shown in Figure 5.1b, and  $\text{Na}_3\text{PO}_4$  shows the smallest change ( $\sim 8\%$ ), and  $\text{Na}_2\text{SO}_4$  ( $\sim 400\%$ ) shows significant growth. However, all the solutions had stable bubbles with recorded diameters well below  $1 \mu\text{m}$ . The percentage of bubble growth increases in the order of  $\text{Na}_3\text{PO}_4 < \text{NaCl} = \text{DI water} < \text{FeCl}_3 < \text{CaCl}_2 < \text{Na}_2\text{SO}_4$  solutions.

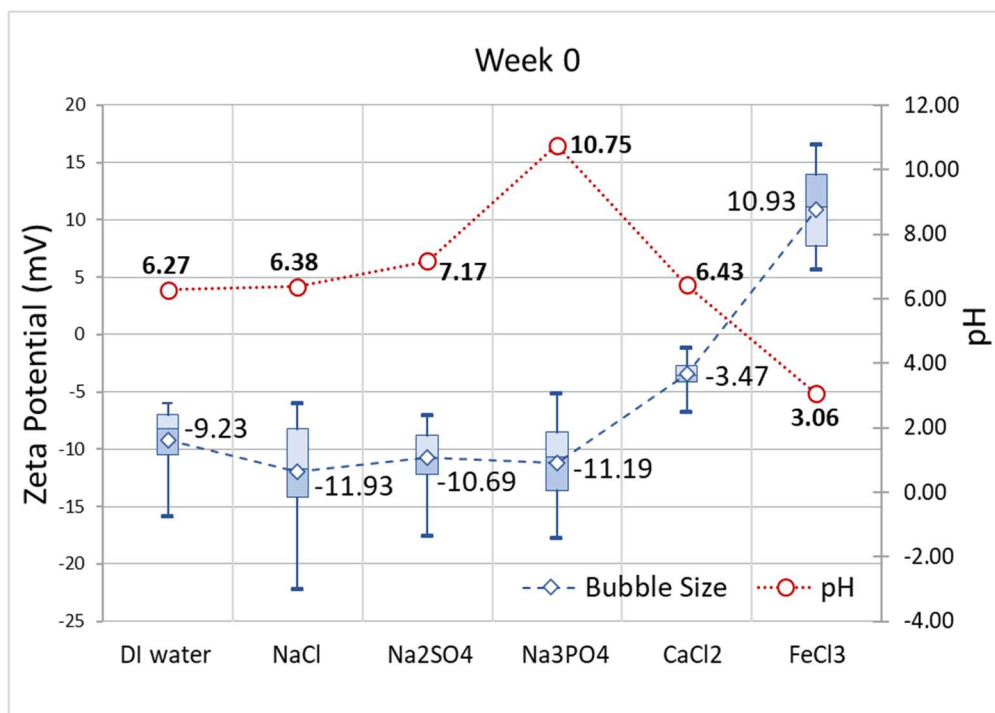


(a)

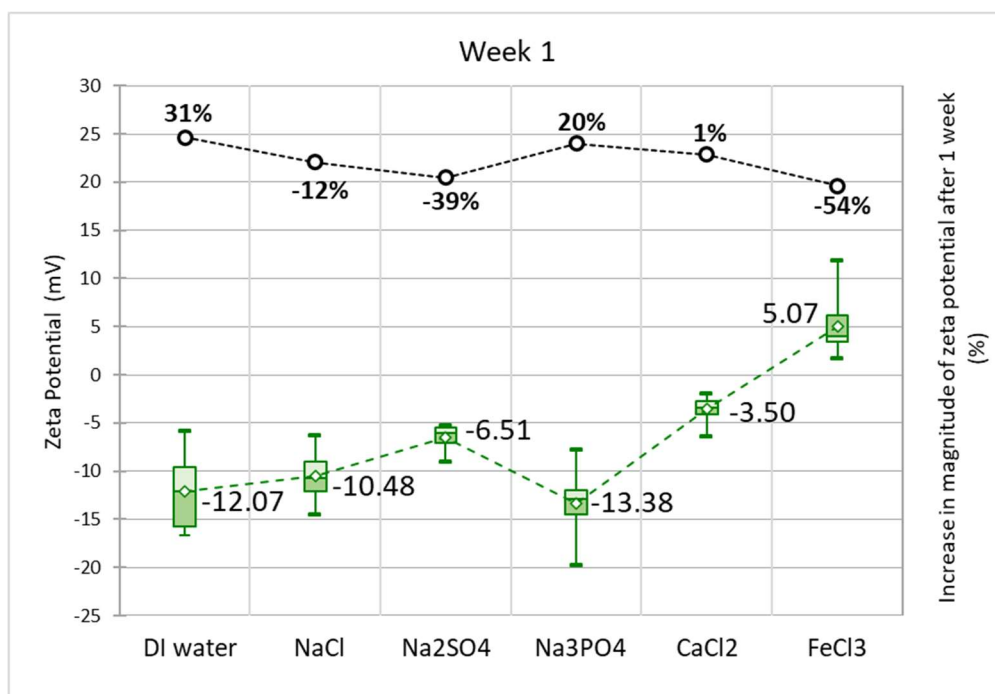


(b)

**Figure 5.1** The bubble size and zeta potential variation (a) bubble size at week 0, (b) bubble size and percentage change in size after 1 week (**Continued**).



(c)



(d)

**Figure 5.1 (Continued)** (c) zeta potential and pH of the solution in week 0, (d) zeta potential and percentage change in zeta potential after 1 week, for air bubbles at 25°C.

Figures 5.1c and 5.1d show the zeta potential just after generation and after 1 week, respectively. All the solutions had negative zeta potential values except for FeCl<sub>3</sub>, which had positive zeta potentials of 10.93 mV initially and 5.07 mV after 1 week. The magnitude of negative zeta potential increased for the other five samples as CaCl<sub>2</sub> < Na<sub>2</sub>SO<sub>4</sub> ≈ NaCl ≈ DI < Na<sub>3</sub>PO<sub>4</sub>. In addition, Figure 5.1c shows the pH variation for all six samples, and it shows the variation FeCl<sub>3</sub> < DI ≈ NaCl ≈ CaCl<sub>2</sub> ≤ Na<sub>2</sub>SO<sub>4</sub> < Na<sub>3</sub>PO<sub>4</sub>. Between six salts samples used, Na<sub>3</sub>PO<sub>4</sub> shows a strong alkaline condition, while FeCl<sub>3</sub> shows a strong acidic condition, which should result in highly negative zeta potential of Na<sub>3</sub>PO<sub>4</sub> and highly positive zeta potential of FeCl<sub>3</sub> apart from their ionic valence effect.

The size of a bubble depends on three factors, the bubble breakup mechanism due to applied energy to the system, the bubble coalescence effect, and the solution properties. The energy cost for the bubble formation depends on the interfacial area and is governed by the bubble's surface tension. Higher energy is required to form smaller bubbles but lowering the surface tension at the gas/liquid interface can lower the energy requirement. Zhang et al. (2020) stated that the free energy cost required ( $\Delta\Omega$ ) for the generation of bulk nanobubbles depends on three factors: (1) volume contribution, (2) interfacial energy, (3) electrostatic potential, and is given by,

$$\Delta\Omega = -[P_{in} - P_{out}]V + \gamma A + \frac{Q^2}{8\pi\epsilon R} \quad (5.19)$$

For all samples, the provided energy was identical, and condition states were similar except the salt type used, meaning the bubble size, zeta potential, and bubble concentration should wholly depend on the solution properties. In order to have a long lifespan, the bubbles

should be stable against dissolution, rising over, and coalescence. Therefore, bubbles should be smaller in size to prevent rapid rise to the surface, should have lower internal pressures to prevent fast diffusion and maintain the diffusion barrier, and should have high electrical charge potentials to stop coalescence.

Nanobubbles under neutral pH have negatively charged gas-liquid interfaces (Figure 5.1c and 5.1d), and the nanobubbles surface charges are believed to be a result of chemisorption of H<sub>2</sub>O, i.e., water splitting into H<sup>+</sup> and OH<sup>-</sup> during adsorption to form a hydroxylated surface [9,18,151]. OH<sup>-</sup> rather than H<sup>+</sup> is adsorbed at neutral pH conditions due to the difference in enthalpies of hydration. While the H<sup>+</sup> ions are likely to remain in the bulk aqueous phase (more likely hydrated), OH<sup>-</sup> stays at the bubble gas-water interface (less likely to hydrate) [18]. The liquid water interface has a strong affinity for the electrons, and therefore, nanobubbles are more likely to form in the alkaline solution. This might be the reason for stable bubbles in the Na<sub>3</sub>PO<sub>4</sub> solution which demonstrated high negative zeta potential and low percentage change in size over one week.

However, when the bubbles are formed in acidic electrolyte solutions, the positive counterions are adsorbed to the bubble interface. Adsorption of positively charged ions will cause a reduction in the negativity of the charged bubbles. This effect can be reflected in the measured zeta potential values (Figures 5.1c and 5.1d), where higher positively charged counterions adsorption causes smaller negative potentials. The CaCl<sub>2</sub> shows a lower negative potential of approximately 3.5 mV, and FeCl<sub>3</sub> shows a positive zeta potential value of approximately 10 mV. In the FeCl<sub>3</sub> solution, the low pH value of 3.06 and the adsorption of high positive charge density Fe<sup>3+</sup> ions (232 C/mm<sup>3</sup>) to the bubble surface causes the formation of positively charged ions. In contrast, the Na<sub>3</sub>PO<sub>4</sub> solution recorded

high negative zeta potentials which can be attributed to the high pH and the adsorption of  $\text{OH}^-$  ions at the interface. Further, with a similar positive monovalent ion,  $\text{Na}^+$ , and a similar pH range (between 6-7), the variation of zeta potential for NaCl and  $\text{Na}_2\text{SO}_4$  is influenced by the anion type, e.g.,  $\text{Cl}^-$  and  $\text{SO}_4^{2-}$ . The mobility of  $\text{Cl}^-$  is higher when compared to that for  $\text{SO}_4^{2-}$  and hence, the specific adsorption of  $\text{Cl}^-$  at the bubble interface may be higher for the NaCl solution producing higher negative zeta potential values when compared to bubbles in  $\text{Na}_2\text{SO}_4$  solution.

Table 5.2 shows the measured and calculated results for nanobubbles in six solutions. It represents the solution type (col. 1), average bubble diameter (col.2), average bubble  $\zeta$  potential (col.3), surface charge density (col. 4), surface potential (col. 5), ionic concentration at bubble surface (col. 6), and the pressure difference ( $\Delta P$ ) (col. 7).

Figure 5.2 shows the variation in surface charge density for five salt solutions, showing that magnitudes of surface charge density increase in the order of  $\text{CaCl}_2 < \text{Na}_2\text{SO}_4 < \text{Na}_3\text{PO}_4 = \text{NaCl} < \text{FeCl}_3$  at week 0 and after week 1, surface charge density decreased for all the samples except  $\text{Na}_3\text{PO}_4$ , where the surface charge density increased. As Table 5.1 (col E and F) shows, the ionic strength increased (and Debye length decrease) in the following order:  $\text{NaCl} < \text{Na}_2\text{SO}_4 = \text{CaCl}_2 < \text{Na}_3\text{PO}_4 = \text{FeCl}_3$ .

**Table 5.1** Solution Properties and Parameters

(A)	(B)	(C)	(D)	(E)	(F)	(G)	(H)	(I)	(J)
Solution	Concentration	Molar Mass	The charge density of cation	Ionic Strength	Debye length	Average Conductivity		Average pH	DO2 concentration
	(M)	(g/mol)	(C/mm <sup>3</sup> )	(mol/m <sup>3</sup> )	(nm)	Week 0	Week 1	Week 0	Week 0
						(mS/cm)	(mS/cm)	(-)	(mg/l)
H <sub>2</sub> O	10 <sup>-7</sup>					0.023	0.024	6.27	31.99
NaCl	10 <sup>-3</sup>	58.44	24	1.00	9.63	0.129	0.131	6.38	32.77
Na <sub>2</sub> SO <sub>4</sub>	10 <sup>-3</sup>	142.04	24	3.00	4.54	0.267	0.276	7.17	33.82
Na <sub>3</sub> PO <sub>4</sub>	10 <sup>-3</sup>	163.94	24	6.00	2.57	0.415	0.351	10.75	34.20
CaCl <sub>2</sub>	10 <sup>-3</sup>	110.98	52	3.00	4.54	0.253	0.257	6.43	33.74
FeCl <sub>3</sub>	10 <sup>-3</sup>	162.2	232	6.00	2.57	0.719	1.070	3.06	32.38

**Table 5.2** Nanobubbles Measured and Calculated Parameters

(1)	(2)		(3)		(4)		(5)		(6)						(7)	
Solution	Average Bubble Diameter		Average bubble ζ potential		surface charge density		Surface Potential		Ionic concentration at the bubble surface						Pressure Difference (ΔP)	
	W0	W1	W0	W1	W0	W1	W0	W1	Cation	Anions	Total	Cation	Anions	Total	W0	W1
Week	(nm)	(nm)	(mV)	(mV)	(C/m <sup>2</sup> )	(C/m <sup>2</sup> )	(mV)	(mV)	(M)	(M)	(M)	(M)	(M)	(M)	(atm)	(atm)
H <sub>2</sub> O	91.3	106.0	-9.23	-12.07												
NaCl	78.8	91.3	-11.93	-10.48	-0.0011	-0.0009	-12.49	-10.95	1.52E+02	6.59E-09	152.00	3.56E+01	2.81E-08	35.60	35.96	31.06
Na <sub>2</sub> SO <sub>4</sub>	68.1	342.0	-10.69	-6.51	-0.0010	-0.0005	-11.17	-6.77	8.78E+01	5.19E-13	87.80	1.34E+00	2.22E-09	1.34	41.66	8.29
Na <sub>3</sub> PO <sub>4</sub>	50.7	54.8	-11.19	-13.38	-0.0011	-0.0013	-11.73	-14.05	2.17E+02	2.64E-18	217.00	1.94E+03	3.71E-21	1940.00	55.96	51.72
CaCl <sub>2</sub>	106	209.5	-3.47	-3.50	-0.0003	-0.0003	-3.64	-3.66	1.03E+00	6.23E-05	1.03	1.10E+00	6.04E-05	1.10	26.81	13.56
FeCl <sub>3</sub>	5.6	8.7	+10.93	+5.07	0.0014	0.0006	12.73	5.78	5.76E-18	1.67E+02	167.00	2.47E-10	4.78E-01	0.48	507.38	326.68

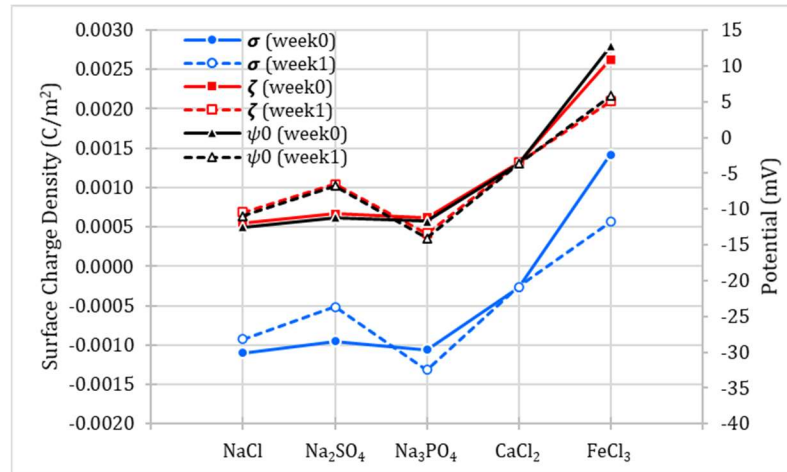
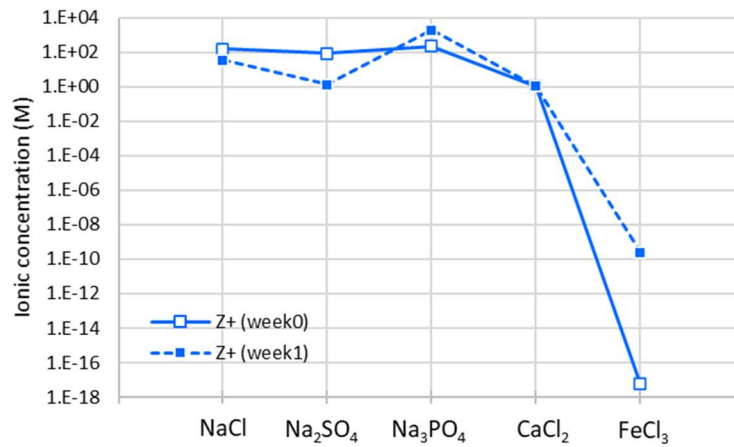
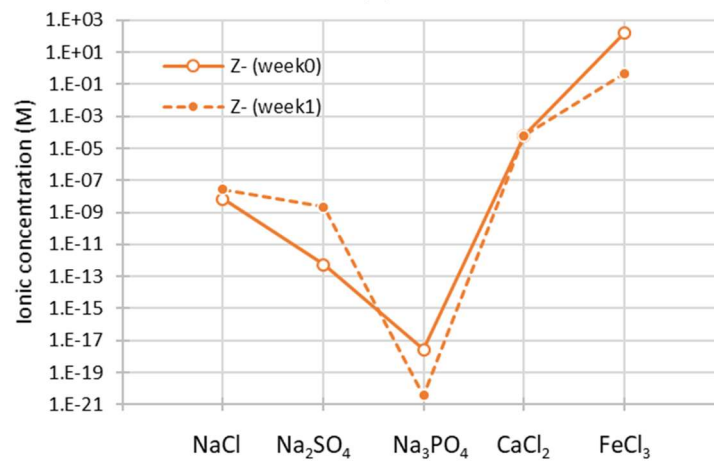


Figure 5.2 Surface charge density, zeta potential, surface potential at week0 and week1.



(a)



(b)

Figure 5.3 Ionic concentration at the bubble surface for different salts (a) cation (b) anions.

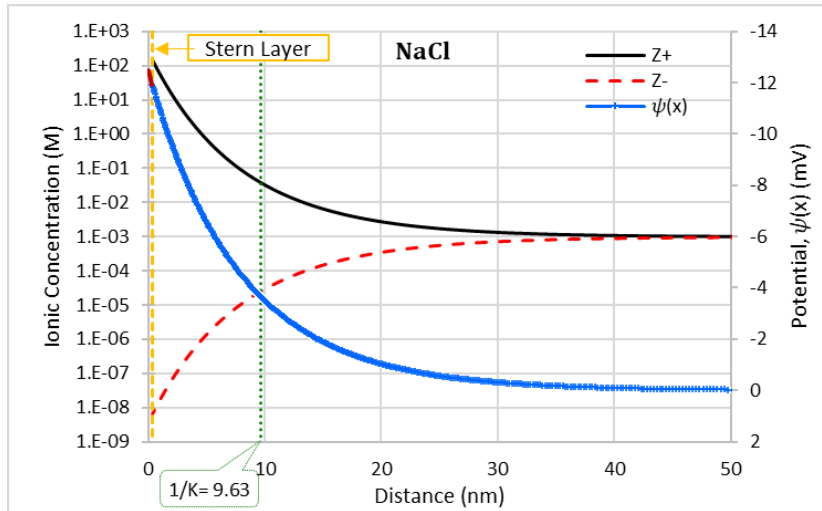


As shown in Figure 5.3, the ionic concentration of cations at the bubble surface increases in the following order:  $\text{FeCl}_3 (\text{Fe}^{3+}) < \text{CaCl}_2 (\text{Ca}^{2+}) < \text{Na}_2\text{SO}_4 (\text{Na}^+) < \text{NaCl} (\text{Na}^+) < \text{Na}_3\text{PO}_4 (\text{Na}^+)$  and cation concentrations were  $6\text{E}-15$ ,  $1\text{E}+03$ ,  $4\text{E}+04$ ,  $2\text{E}+05$  and  $7\text{E}+04$ , times the bulk cationic concentration, respectively at week 0. After one week, the  $\text{Na}_3\text{PO}_4$  sample had the highest cation concentration at the bubble surface. The contact concentration of anions was increased in the following order:  $\text{Na}_3\text{PO}_4 < \text{Na}_2\text{SO}_4 < \text{NaCl} < \text{CaCl}_2 < \text{FeCl}_3$  and the anion concentration was  $3\text{E}-15$ ,  $5\text{E}-10$ ,  $7\text{E}-06$ ,  $3\text{E}-02$ , and  $6\text{E}+04$  times the bulk anionic concentration, respectively.

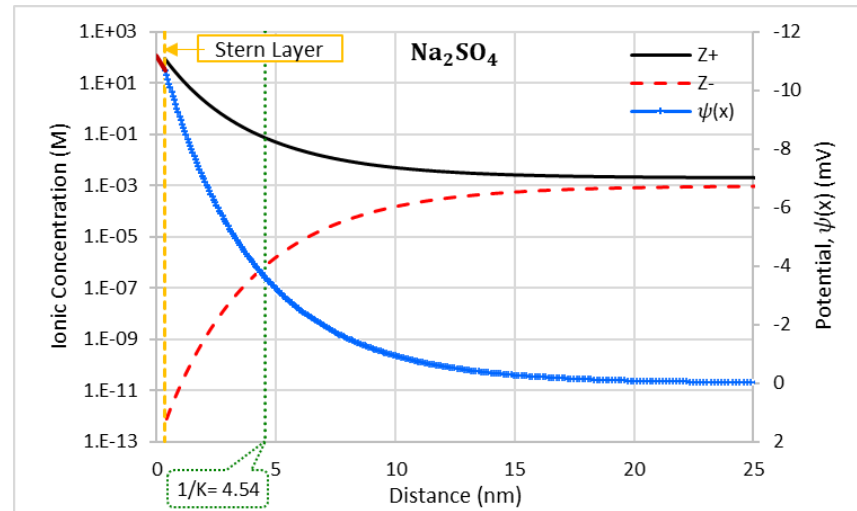
Figure 5.4 shows the variation of ion concentration with distance. Figures 5.4a, 5.4b, 5.4c, 5.4d, and 5.4e show the potential and ionic concentration distribution away from the charged bubble surface. Figure 5.4f shows the potential distribution profile for all the electrolytes solutions, and Figures 5.4g and 5.4h show the ion profile for cations and anions, respectively.

When monovalent  $\text{Na}^+$  counterion ions are compared in  $\text{NaCl}$ ,  $\text{Na}_2\text{SO}_4$ , and  $\text{Na}_3\text{PO}_4$  solutions, they had a similar range of values of surface potentials ( $\sim 11\text{mV}$ ) and counterion ion  $[\text{Na}^+]$  concentrations at the bubble surface were  $152\text{M}$ ,  $88\text{M}$ ,  $217\text{M}$ , respectively. However, the anions (co-ions) concentrations at the surface were  $7\text{E}-09\text{M}$ ,  $5\text{E}-13\text{M}$ , and  $3\text{E}-18\text{M}$  for  $\text{Cl}^-$ ,  $\text{SO}_4^{2-}$  and  $\text{PO}_4^{3-}$  ions, respectively and did not affect the zeta potential values. For these three samples, the potential distribution and the ion profile decayed away from the surface over the Debye length ( $1/K$ ).  $\text{NaCl}$  has the highest  $1/K$  of  $9.6\text{ nm}$ , followed by  $\text{Na}_2\text{SO}_4$  ( $4.5\text{ nm}$ ) and  $\text{Na}_3\text{PO}_4$  ( $2.6\text{ nm}$ ). The results of  $\text{NaCl}$ ,  $\text{CaCl}_2$ , and  $\text{FeCl}_3$  electrolyte solutions were compared to evaluate the impact of different valences of the counterions (cations). Here, as mentioned before, the potential distribution and ion profile

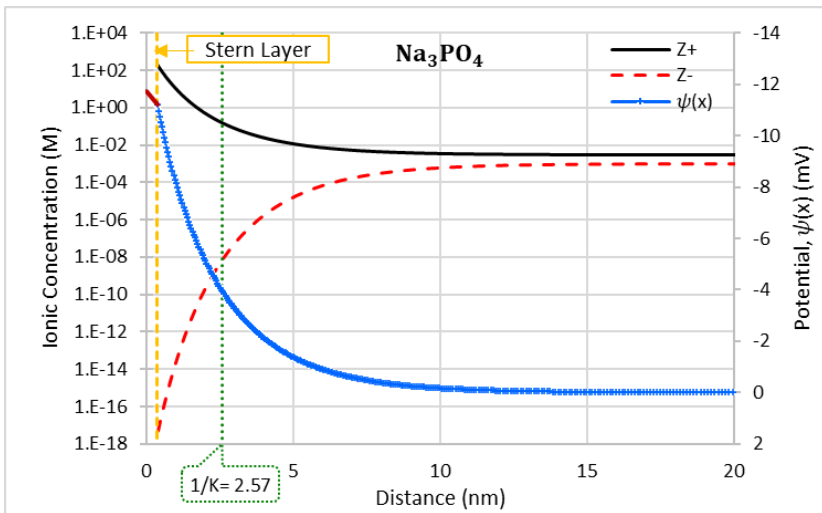
decayed with the Debye length. However, as the high valency cation adsorbed to the bubble surface, there was a charge reversal. When monovalent  $\text{Na}^+$  ions and divalent  $\text{Ca}^{2+}$  ions are compared,  $\text{NaCl}$  ( $-11.93\text{mV}$ ) has high negative surface potential while the  $\text{CaCl}_2$  ( $-3.47\text{mV}$ ) has a lower value. The ion profiles show that  $\text{NaCl}$  solution has a high concentration of  $\text{Na}^+$  ions at the surface when compared to  $\text{Ca}^{2+}$  ions at the surface of the  $\text{CaCl}_2$  solution. In both cases, the positive ion (counterion) concentration at the surface is higher than that of anions or co-ions concentration. When it comes to the  $\text{FeCl}_3$  solution, the surface potential has reversed to positive ( $\sim 10\text{mV}$ ). There was a very low concentration of adsorbed  $\text{Fe}^{3+}$  ions at the bubble interface ( $\sim 6\text{E-}18\text{M}$ ) compared to the anion concentration ( $\sim 167\text{M}$ ), confirming the complete charge reversal occurs when nanobubbles adsorb  $\text{Fe}^{3+}$  ions. When the high valency cations are bonded to the bubble surface, the negative charge on the bubble decreases. That tend to neutralize the surface charge ( $\sigma \rightarrow 0$ ,  $\psi_0 \rightarrow 0$ ). The presence of divalent ions ( $\text{Ca}^{2+}$ ), resulted in a lower magnitude negative zeta potential value around  $-3.5\text{ mV}$ . In the case of trivalent ions,  $\text{Fe}^{3+}$ , even with very low concentrations, the bubble surface can be neutralized, and above this minimum concentration, there is charge reversal wherein the cations continue to adsorb onto the bubble surface resulting in a net positive charge.



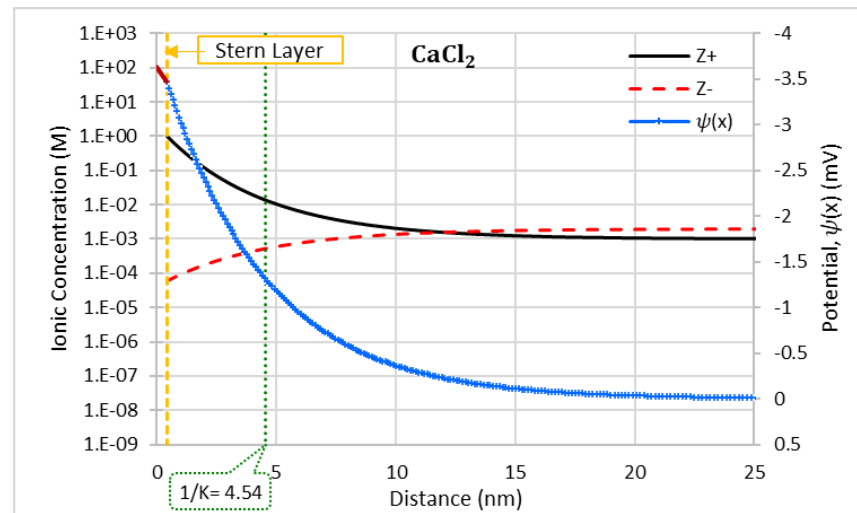
(a)



(b)

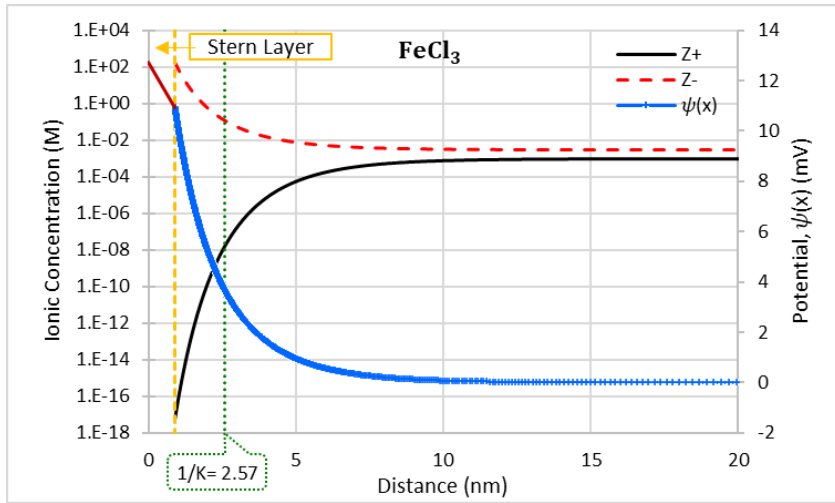


(c)

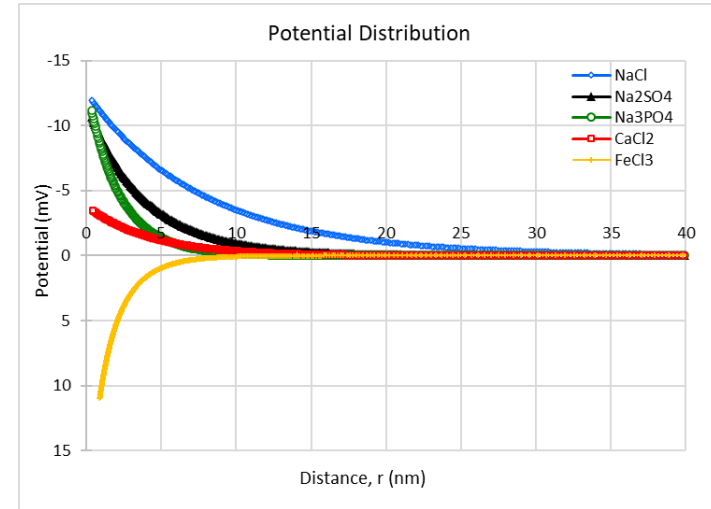


(d)

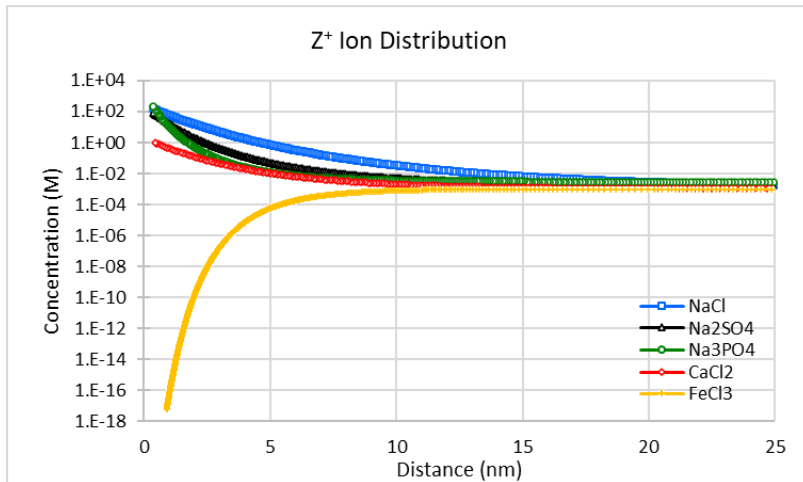
**Figure 5.4** The variation of ion concentration with distance (Continued).



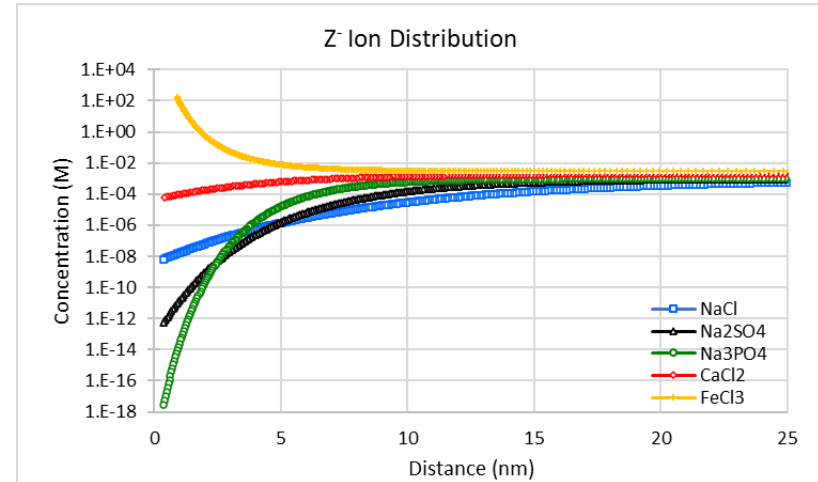
(e)



(f)



(g)



(h)

Figure 5.4 (Continued) The variation of ion concentration with distance.

The  $\text{FeCl}_3$  solution had positive charged surface due to the solution being acidic and the adsorption of  $\text{Fe}^{3+}$  ions to the bubble surface, yet the ionic concentration profile shows a very high concentration of  $\text{Cl}^-$  near the bubble surface, likely causing the smaller bubble sizes. Due to the increase in negatively-charged ions that benefit from the gas-liquid interface may lead to an increase of the electrostatic repulsion force between the nanobubbles and surface, resulting in a decrease in the average diameter of nanobubbles [155]. For five electrolyte solutions (excluding  $\text{FeCl}_3$ ), the surface charge density and the anion attraction were inversely proportional. This explains that the bubbles with high surface charge density (negatively charged bubble) tend to repel the like-charged anions away from the surface that resulted in a low concentration of anions at the surface. As the results indicate, at the gas-liquid interface, there was a high charge density of ions which can act as “structure-makers” in aqueous solution [27,156]. These ionic impurities form a diffusive shield to the outflux of gases making the bubbles more stable, and at the same time, lower the effective value of the liquid-gas surface tension [157]. Further, the ionic impurities are adsorbed at the gas-liquid interface resulting in mutual repulsion between the ions and also resulting change in surface tension will result in reducing the internal gas pressure and prevention the fast gas diffusion [157].

Inorganic ions can interact with the charged surface in either non-specific ion adsorption or specific ion adsorption. As all the graphs show, for all cases, ions are adsorbed onto the bubble surface, as their concentration is higher than the bulk concentration. It is therefore, assumed that one mode of nanobubble stability depends on the ion adsorption at the gas-liquid interface called the ionic shielding effect [27,99]. All the electrolyte solutions had the same low ionic bulk concentration of 0.001M, and the results

indicate that all the samples were relatively stable over time. This can be attributed to the presence of relatively high Debye length, and firmly adsorbed ions at the gas-liquid interface. This will result in reducing bubble coalescence as well as gas diffusion, thereby increasing the bubble stability.

Table 5.2 (col.7) shows the pressure difference calculated for each solution based on Equation (5.18). All the results were calculated with the assumption that surface tension values are equal to 0.072 N/m, the surface tension of the water at 20°C. Results indicated that the calculated pressure differences are very high and increase in the order of  $\text{CaCl}_2$  (26.81atm) <  $\text{NaCl}$  (35.96atm) <  $\text{Na}_2\text{SO}_4$  (41.66atm) <  $\text{Na}_3\text{PO}_4$  (55.96atm) <  $\text{FeCl}_3$  (507.38atm). At these high pressures, it is unlikely the bubble would be stable, suggesting that the actual surface tension may be significantly lower than that of water at 20°C. Hence, a change in the interfacial properties of the bubble likely have occurred, reducing the surface tension at the gas-liquid interface. This possibility of reduction in surface tension has been addressed by others. Ushida et al. [158] stated that solutions containing large concentrations of nanobubbles could reduce the surface tension by 15% and Attard [159] explained that surface tension reduces due to supersaturation and thus, reduces the pressure. Further Das et al. [157] and Uchida et al. [27] explained that the ion impurities act as a diffusion shield at the gas-liquid interface, increasing the stability against gas outflux and could lower the effective value of the gas-liquid surface tension.

The bulk electrolyte ion concentration has a significant contribution not only to the electrostatic potential but also to the forces between charged surfaces. DLVO theory explains that the stability of the colloidal system depends on the force or energy balance between the van der Waals attractive interaction and the electrical double layer interaction.

This theory explains that an energy barrier resulting from repulsive forces or energy would prevent the two particles from approaching each other and coalescing. Accordingly, Figure 5.5 presents the attractive, repulsive, and total interacting forces/energy diagrams for five electrolyte bubble solutions. Since the recorded results had very low electrical charges (low zeta potential values), the attractive van der Waals forces dominated. In the case of the NaCl solution, we can see an energy barrier of  $1.87 \times 10^{-20} J$  at a 5nm separation distance. For the samples of Na<sub>2</sub>SO<sub>4</sub>, Na<sub>3</sub>PO<sub>4</sub>, CaCl<sub>2</sub>, and FeCl<sub>3</sub>, there was no energy barrier to prevent bubble coalescence based on the DLVO calculations.

The above results indicate that the instability of the nanobubble systems for Na<sub>2</sub>SO<sub>4</sub>, Na<sub>3</sub>PO<sub>4</sub>, CaCl<sub>2</sub>, and FeCl<sub>3</sub> solutions based on the high net attractive forces compared to the repulsive forces. Figure 5.6 shows the comparison of electric double layer and van der Waals interaction potentials for two salt solutions of similar Debye lengths. Figure 5.6a shows the electric double layer repulsion force is higher for the Na<sub>2</sub>SO<sub>4</sub> (a=34nm,  $\zeta$ =-6.51mV,  $n_{total}(r = a + d)$ = 88M) when compared to that for CaCl<sub>2</sub> (a=53nm,  $\zeta$ =-3.50mV,  $n_{total}(r = a + d)$ = 1M). Also, van der Waals attraction potential is higher for CaCl<sub>2</sub> due to the large bubble size. Figure 5.6b shows that Na<sub>3</sub>PO<sub>4</sub> (a=25.35nm,  $\zeta$ =-11.19mV,  $n_{total}(r = a + d)$ =217M) has higher electrical repulsion potential compared to that for FeCl<sub>3</sub> (a=2.8nm,  $\zeta$ =+10.93mV,  $n_{total}(r = a + d)$ = 167M). However, since the bubbles in the FeCl<sub>3</sub> solution were much smaller, as it has a comparatively smaller van der Waals attraction potential. Therefore, with similar Debye lengths, the electric double layer repulsion potential of nanobubbles will depend on the surface/zeta potential and adsorbed ion type and ion concentration at the surface. Likewise, the monovalent ion adsorption will be beneficial towards the electrostatic repulsion and

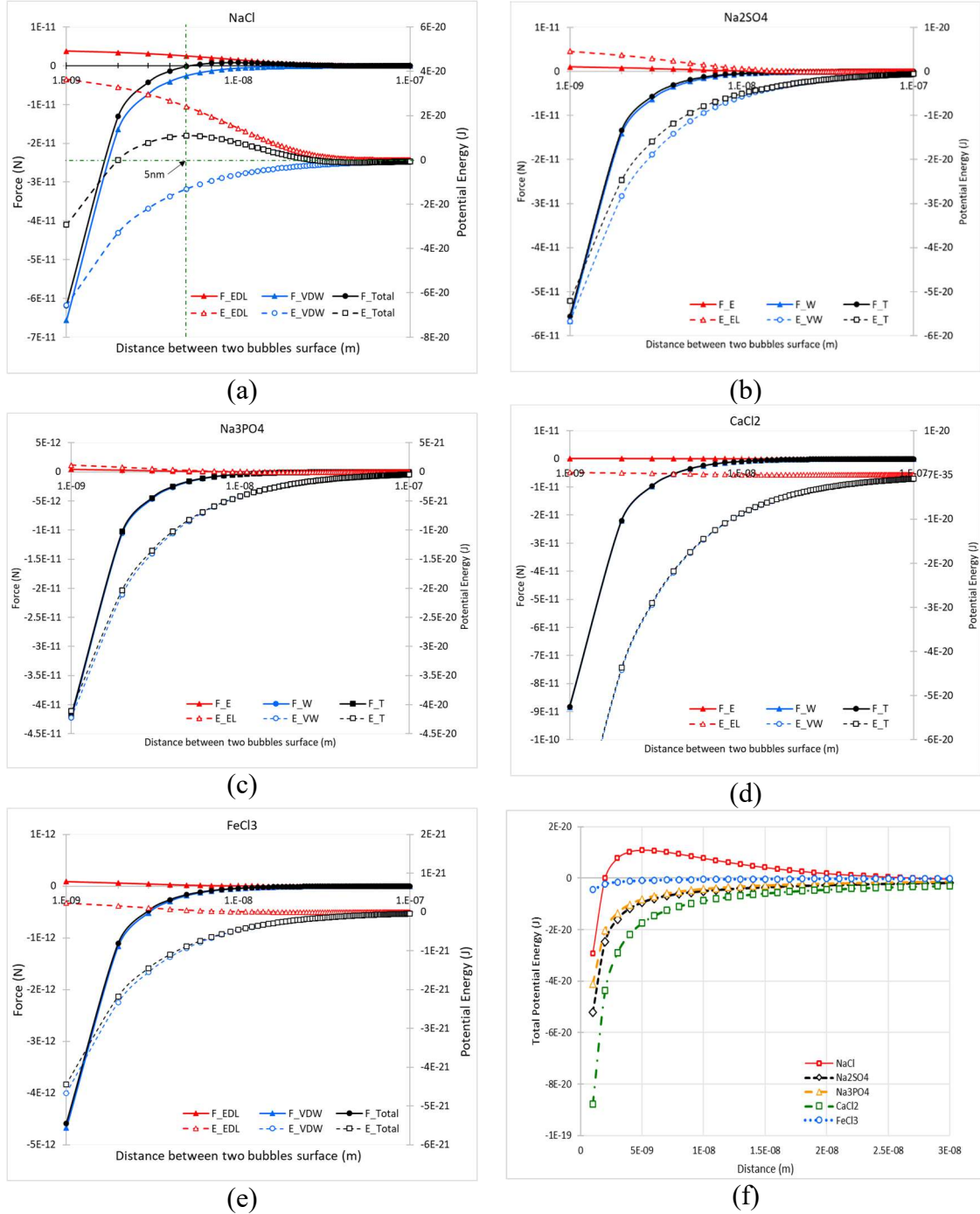
related bubble stability. Still, bubble size is a key factor when discussing the total interaction force/potential as larger bubbles' attractive forces are always impacted at smaller separation distances. For all the four samples shown in Figure 5.6, for separation distances smaller than the Debye length, the van der Waals attraction potential is very much higher, and thus, the total interaction potential is governed by the attractive force.

The experimental results indicated long term stability of these nanobubbles for all the five electrolytes solutions. One of the main concerns for deviation may be the Hamaker's constant used for the calculation of van der Waals forces. As we are still not certain of the exact properties of the bubble interface, values used for computation may be overestimated. Takahashi [18] explains that the  $H^+$  and  $OH^-$  ions have an exclusive effect on the gas-water interface electrical charge. These ions are essential for the hydrogen bond network at the gas-liquid interface, and the hydrogen bond structure at the interface differs from the bulk solution as do the density, viscosity, electrical conductivity, and dielectric permittivity.

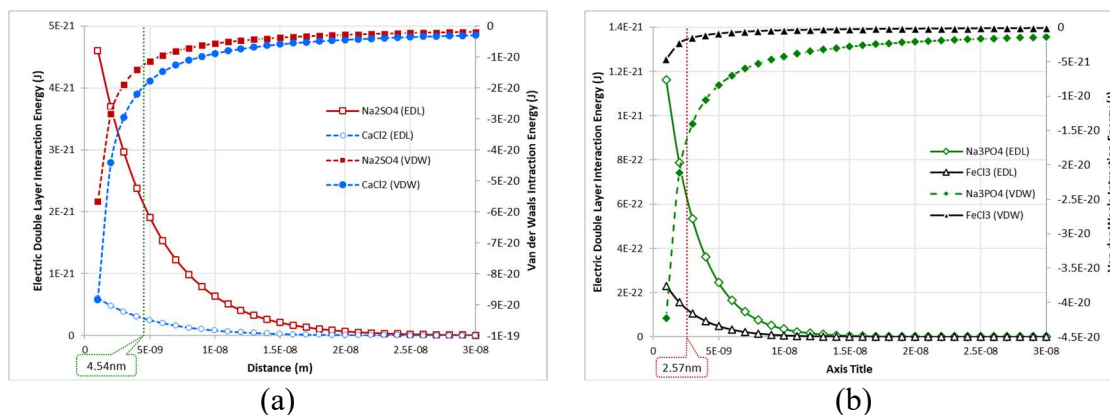
Ohgaki et al. [19] showed the possibility of highly structured hydrogen bonds at the gas-liquid interface of nanobubble that enhance bubble stability. Also, with the accumulation of ion impurities, a possible of “structure-maker” at the bubble interface can act as a shield [1,157]. In such a hard-interfacial structure, the assumed Hamaker constant might not be valid and may lead to erroneous conclusions. Further, it should be noted that, as two bubbles approach each other, the thin film between them has higher salt concentrations than that in the bulk fluid, and there may be weakened van der Waals forces, and thus, the calculation of Hamaker constants may require further modifications.



Depending on the ion type, both  $\sigma$  and  $\psi_0$  can change, leading to a substantial reduction in the repulsive double-layer forces.



**Figure 5.5** The attractive, repulsive, and total interacting forces/energy diagrams for five electrolyte bubble solutions.



**Figure 5.6** Comparison of results of salts solutions with similar Debye lengths (a)  $1/K = 4.54\text{nm}$   $\text{Na}_2\text{SO}_4$  and  $\text{CaCl}_2$ , (b)  $1/K = 2.57\text{nm}$   $\text{Na}_3\text{PO}_4$  and  $\text{FeCl}_3$ .

Table 5.3 summarizes findings for the nanobubble formation in different valency electrolytes. Those findings are consistent with the experimental results presented here. In summary, nanobubbles in pure water are negatively charged, and with increased concentration of electrolyte, the magnitude of the zeta potential decreases. Nanobubbles were negatively charged with the monovalent electrolytes, and with the increased cation valency, the zeta potential is neutralized or completely reversed. In literature, this phenomenon was explained with respect to the specific cation ion adsorption or, in high pH conditions, the adsorption of cation hydroxides on the gas-liquid interface of the bubble. However, the published literature does not discuss the long-term stability or application of DLVO theory to nanobubbles for multivalent electrolytes. Therefore, the present research attempts to fulfill this research gap.

## 5.6 Summary and Conclusions

All electrolytes solutions with 0.001M concentration produced stable bubbles over one week, with no significant deviation in either bubble size or zeta potential values. The difference between the bubble size and zeta potential can be attributed to the solution

properties and mainly dependent on solution pH and the cation valency, as nanobubbles under natural pH solutions tend to be negatively charged. Anions had minimal impact on the surface potential. The ion profiles revealed that cation concentrations at the bubble surface were higher than that of bulk liquid, confirming that the bubbles are negatively charged for neutral and high pH values ( $\geq 4$ ) for low valency cation adsorption. Low adsorption of high valency cations neutralized the charge on the bubble surface or completely reversed the charge. However, low ionic adsorptions at the gas-liquid interface produced stable nanobubbles due to the ion shielding effects. Also, with stable bubbles, the calculation of the attractive van der Waals forces produced unrealistic values suggesting that the Hamaker constant used for the calculation may not be valid at the nanobubble gas-liquid interface. Further, calculated pressure values were also unrealistically elevated and suggest that surface tension values should be lower than that of the surface tension of water. These results revealed that nanobubbles should contain exceptional interfacial properties that need to be carefully investigated and evaluated.

**Table 5.3** Summary of Findings for the Nanobubbles In Multivalent Electrolytes from the Published Literature (**Continued**)

#	Author (Year)	Bubble Generation Method	Gas Type	Electrolytes	Findings			
					Conclusions	Condition	Average bubble size at pH (5.5-7) & 25°C	Average, Zeta potential at pH (5.5-7) & 25°C
1	Nirmalkar et al (2018) [62]	hydrodynamic cavitation	Air	NaCl, CaI <sub>2</sub> , AlCl <sub>3</sub>	The addition of any salt leads to a reduction in bubble number density and a rise in the mean bubble diameter. The magnitude of the negative zeta potential decreases with added NaCl and CaI <sub>2</sub> , neutralizing the bubble charge while AlCl <sub>3</sub> reverses to a positive potential. Beyond the critical concentration of salts, the bubble system becomes unstable. The DLVO theory calculation for pure water shows the stable colloidal system for bulk nanobubbles.	NaCl (0.001M)	100	-28.0
						CaI <sub>2</sub> (0.001M)	150	-24.0
						AlCl <sub>3</sub> (0.001M)	125	-4.0
2	Sjogreen et al(2018) [160]	Injection of oxygen to a saline solution in a diffusive medium	O <sub>2</sub>	NaCl	The highest stability of nanobubbles obtained at the temperature T=4 °C with the diameter of the nanobubbles remains approximately constant with time, in the 0.9% NaCl concentration, irrespective of pH values.	NaCl (0.9%)	588	-13.1
3	Yurchenko et al (2016) [161]	optical (laser-Induced) breakdown	Air	KI, NaI, NaClO <sub>3</sub> , CaCl <sub>2</sub> , MaCl <sub>2</sub> , KBr, NaBr, KCl, NaCl, NaNO <sub>3</sub> , CsCl	They studied the bubstons, the stable bubble formation in electrolyte solutions with the ionic. They concluded nanobubbles stabilized by adsorption of chaotropic anions at the gas-liquid interface and the impact of cosmotropic cations is weak adsorption.	NaCl (0.1M)	250	-
						CaCl <sub>2</sub> (0.1M)	370	-
						Na <sub>2</sub> SO <sub>4</sub> (0.1M)	190	-
4	Jia et al (2013) [89]	bubble nucleation in a gas-supersaturated solution	Air	KCl	The pH of the solution greatly influences the bubbles zeta potential and should be well considered on the flotation process. The positive ions (H <sup>+</sup> ) favorably remain in the bulk aqueous phase allowing negative ions to be adsorbed at the gas-liquid interface. As pH decreases, OH <sup>-</sup> concentration decreases and potentially causing charge reversal and forming positively charged bubbles.	KCl (0.001M)	-	-5.8
5	Leroy et al. (2012) [105]	Theoretical work. Values used from the previous literature	Vapor	NaCl, KCl	They have developed the surface complex model for the gas/water interface by considering the negative surface sites and used to (I) determine the true values of zeta potential for H <sub>2</sub> bubbles in NaCl solution, (II) correct the electrophoretic mobility of H <sub>2</sub> bubbles from the retardation effect of surface conductivity, (III) predict the surface tension of the air/KCl solution interface.	NaCl (0.001M)	-	-32.5

**Table 5.3 (Continued)** Summary of Findings for the Nanobubbles In Multivalent Electrolytes from the Published Literature

#	Author (Year)	Bubble Generation Method	Gas Type	Electrolytes	Findings			
					Conclusions	Condition	Average bubble size at pH (5.5-7) and 25°C	Average, Zeta potential at pH (5.5-7) and 25°C
6	Bunkin et al (2012) [65]	Spontaneous gas cavities (bubstons)	Air	NaCl	Three independent techniques (phase microscopy, DLS, and polarimetric scatterometry) were used to claim the long-living gas nanobubble clusters in an aqueous salt solution with saturated dissolved gas.	-	-	-
7	Najafii et al (2007) [55]	Bubble nucleation	Air	NaCl, CaCl <sub>2</sub> , Al <sub>2</sub> (SO <sub>4</sub> ) <sub>3</sub>	Nanobubbles in an electrolyte solution, based on the valency of the cation and its concentration, the zeta potential reduced, neutralized, or even reverse the charge.	NaCl (0.001M) CaCl <sub>2</sub> (0.001M) Al <sub>2</sub> (SO <sub>4</sub> ) <sub>3</sub> (0.001M)	* Background 0.0001 M SDS solution	-70.7 -28.5 +3.6
8	Han et al. (2006) [162]	Electrochemical reaction	O <sub>2</sub> , H <sub>2</sub>	NaCl KCl MgCl <sub>2</sub> CaCl <sub>2</sub> AlCl <sub>3</sub>	The zeta potential was measured in various electrolyte solutions. Nanobubbles were negatively charged for Na <sup>+</sup> , K <sup>+</sup> and Ca <sup>2+</sup> at every concentration and pH range. However, the magnitude of the zeta potential decreased with an increase in concentration and a decrease in pH value. Positive nanobubbles were recorded for concentrations higher than the critical concentration of Mg <sup>2+</sup> for 10 <sup>-2</sup> M and Al <sup>3+</sup> for 10 <sup>-5</sup> M. They conclude that the generation of positively charged bubbles is attributed to both specific adsorptions of hydroxylated species and precipitation of metal hydroxides on the bubble interface.	NaCl (0.01M) KCl (0.01M) *MgCl <sub>2</sub> (0.001M) *CaCl <sub>2</sub> (0.001M) *AlCl <sub>3</sub> (0.001M)	*Background 0.01 NaCl	-30 -33 -20 -40 +25
9	Han et al. (2006) [163]	Electrochemical reaction	O <sub>2</sub> , H <sub>2</sub>	AlCl <sub>3</sub>	The positively charged bubbles were formed by controlling the aluminum concentration and pH. Bubbles zeta potentials were positive at pH 3–7 for both 10 <sup>-3</sup> and 10 <sup>-4</sup> M AlCl <sub>3</sub> solutions. The charge reversal of bubbles influenced by the hydrated precipitation of positively charged Al species, and Al <sup>3+</sup> , Al(OH) <sub>3</sub> (s), and Al(OH) <sub>4</sub> <sup>-</sup> was the predominant species.	*AlCl <sub>3</sub> (0.001M)	*Background 0.01 NaCl	+25
10	Takahashi (2005) [18]	Hydrodynamic cavitation	Air	NaCl MgCl <sub>2</sub>	For a wide range of pH conditions, microbubbles were negatively charged and positive under strongly acidic conditions. In the inorganic electrolytes solutions, zeta potential decreases by increasing the number of counterions within the slipping plane. OH <sup>-</sup> and H <sup>+</sup> ions dominate the charging mechanism of the gas-water interface, while other anions and cations have secondary effects. The force of the attraction depends on the valency of the counterions, and ions with high valency attract to the interface more strongly.	NaCl (0.001M) MgCl <sub>2</sub> (0.001M)	-	-23.0 -14.0

**Table 5.3 (Continued)** Summary of Findings for the Nanobubbles In Multivalent Electrolytes from the Published Literature

#	Author (Year)	Bubble Generation Method	Gas Type	Electrolytes	Findings			
					Conclusions	Condition	Average bubble size at pH (5.5-7) & 25°C	Average zeta potential at pH (5.5-7) & 25°C
11	Cho et al. (2005) [92]	Sonicated with a palladium electrode		NaCl, CaCl <sub>2</sub> , Na <sub>2</sub> SO <sub>4</sub>	The zeta-potentials of nanobubbles increase with salt concentrations. Generally, nanobubbles have negatively charged surface; hence, increase in electrolyte concentration allows more cation adsorption and compresses the electrical double layer thickness of a bubble. Compared to NaCl, with the presence of bivalent cations, Ca <sup>2+</sup> in CaCl <sub>2</sub> solution cause less negative zeta potential. Further suggesting that the bubble charge would be influenced by anion type between Cl <sup>-</sup> and SO <sub>4</sub> <sup>2-</sup> .	NaCl (0.001M) Na <sub>2</sub> SO <sub>4</sub> (0.001M) CaCl <sub>2</sub> (0.001M)	850 853 850	-14.5 -10.9 -7.5
12	Han et al. (2004) [164]	Electrochemical reaction	O <sub>2</sub> , H <sub>2</sub>	MgCl <sub>2</sub> CaCl <sub>2</sub>	The bubbles were negatively charged for CaCl <sub>2</sub> in all range of concentration and pH conditions, and the charge reversal of bubbles found in MgCl <sub>2</sub> in certain circumstances. Mg <sup>2+</sup> formed positively charged nanobubbles above 10 <sup>-2</sup> M concentration and above pH 9. The charge reversal explained as the combined mechanism of both specific adsorptions of hydroxylated species and the formation of hydroxide precipitates.	*MgCl <sub>2</sub> (0.001M) *CaCl <sub>2</sub> (0.001M)	*Background 0.01 NaCl	-20 -40
13	Karraker and Radke (2002) [165]	Porous-plate technique	Air	NaCl, KClO <sub>3</sub> , K <sub>2</sub> SO <sub>4</sub> , CaCl <sub>2</sub>	There is no influence of changing the electrolyte to NaCl or KClO <sub>3</sub> on the disjoining pressure isotherms. However, between CaCl <sub>2</sub> and K <sub>2</sub> SO <sub>4</sub> solutions with similar Debye length, the equilibrium film thickness is smaller for the CaCl <sub>2</sub> , suggesting that the gas-liquid interface is negatively charged and thus, the divalent Ca <sup>2+</sup> screen the charge more effectively compared to K <sup>+</sup> univalent ions.	NaCl (0.01M)	-	-38.0
14	Yang et al. (2001) [166]	electrophoresis	H <sub>2</sub>	NaCl, CaCl <sub>2</sub> , AlCl <sub>3</sub>	In univalent NaCl solutions, bubbles were negatively charged, but with the presence of multivalent metal ions magnitude of the zeta potential can be significantly changed, even reverse the bubble's charge polarity.	NaCl (0.001M) NaCl (0.01M) *CaCl <sub>2</sub> (0.001M) *AlCl <sub>3</sub> (0.001M)	*Background 0.01 NaCl	-35.0 -26.0 -5.5 +12.0

## CHAPTER 6

### MOLECULAR DYNAMICS SIMULATION OF BULK NANOBUBBLES

#### 6.1 Background Information

Bulk nanobubbles are a novel and emerging field of study. Nanobubbles are used in many scientific and technological fields in recent decades, and they have many commercial applications. Experimental results from numerous studies under various conditions have confirmed the existence of bubbles at the nanoscale. [4,93,133,167]. Ushikubo et al. 2010 confirmed the existence of nanobubbles using dynamic light scattering techniques. They reported that pure oxygen nanobubbles might exist for several days while air nanobubbles can only exist for 1 hr. Experiments demonstrated the nanobubble stability with the aid of a charged liquid-gas interface, which creates repulsive forces that prevent bubble coalescence and the high dissolved gas concentration present, creating a small concentration gradient between the interface and bulk liquid [6,9].

However, there are still many unanswered questions that confirm the theoretical existence of nanobubble. The main concern is the theoretical explanation of the recorded long-term stability and the high internal pressures calculated by the Young's Laplace equation ( $P = 2\gamma/R$ ), where  $\gamma$  is the interfacial tension, and  $R$  is the bubble radius. Experimentally recorded nanobubbles have often been found between the size range of 50 nm -500 nm. By assuming the surface tension ( $\gamma$ ) of water at 20 °C is 72.75 mN/m, the calculated pressure difference using the Young-Laplace equation at the gas-liquid interface for bubble radii 50nm and 100nm would be 28.74 atm and 14.34 atm, respectively. Because of such extremely high internal pressures, the nanobubbles' gas cannot be stable, as larger pressures create large chemical gradients. Consequently, in theory, nanobubbles should

rapidly diffuse/dissolve into the surrounding liquid (saturated environment) in less than a few microseconds [12,159,168]. Nevertheless, stable nanobubbles under favorable conditions were found over several weeks to months after generation [9].

Even though there is no universally accepted explanation for nanobubbles' extraordinary longevity, various theories have been proposed, including the existence of a diffusion barrier (i.e., ion/impurity accumulation), rigid hydrogen bond structures, gas supersaturation, bubble clustering effects, and dynamic stability.

Molecular dynamics (MD) simulations can be used as a virtual experiment to study nanobubble properties, bridging laboratory work with theoretical predictions. These simulations may hold the key to understand the long-term stability of bulk nanobubbles.

### **6.1.1 Literature survey of molecular dynamic simulations of bulk nanobubbles**

Many MD nanobubble stability studies have been performed, and some of the key findings are summarized below.

- Jain and Qiao [169] used the non-reactive MD simulations to heterogeneous systems to determine the water's surface tension as a function of the dissolved gaseous molecules (O<sub>2</sub>) concentration, which would help to predict the pressure inside the nanobubbles under supersaturation conditions. They performed the simulation using the LAMMPS code developed by Sandia National Lab consisting of three types of interactions 1) H<sub>2</sub>O-H<sub>2</sub>O interactions, 2) O<sub>2</sub>-O<sub>2</sub> interactions, and 3) H<sub>2</sub>O-O<sub>2</sub> interactions and based on water density at P=1 atm and T=300K. They showed surface tension of water was found to decrease with the increase in the amount of supersaturation or the dissolved O<sub>2</sub> gas molecules' concentration. Consequently, surface tension can play an important role in the stability of the nanobubbles. The internal pressure in nanobubbles is much smaller than what would have been predicted using the planar-interface surface tension value of water.
- Weijs et al. [1] used a quasi-2D MD simulation of binary mixtures of simple Lennard-Jones fluids. In doing so, they studied the nucleation, growth, and final sizes of bulk nanobubble clusters. It was shown that when nanobubbles are close enough, bubbles can supersaturate the liquid between bubbles with gas, protecting them from dissolution. A cluster also provides a mutual shielding effect that can protect from diffusion. Thus, bubbles' distance is an important factor of bubble stability [1,168].



- Hong et al. [168] used MD simulation with the canonical ensemble ( $N, V, T$  constant) to study the relationship between the maximum distance ( $L$ ) between bubbles and the bubble radius ( $R$ ) of a nanobubble cluster using the GROMACS program. Periodic cubic cells were equilibrated at 300 K, and water molecules used a modeled density of  $\sim 1000 \text{ kg/m}^3$ . Additionally, different cell sizes and initial bubble radii were used to simulate a nanobubble cluster. It was found that for a bubble to be stable, the maximum distance  $L^*$  between bubbles should be proportional to  $R^{4/3}$ , where  $R$  is the radius of the bubble.
- Yamamoto and Oshnishi [170] used MD simulation to study the dependence of the surface tension of helium nanobubbles on the radius of curvature. Simulations were performed using NAMD and used the SPC/F<sub>w</sub> flexible point-charge water model and Lennard-Jones helium parameters in a CHARMM force field. They demonstrated that surface tension could impact bubbles larger than 1 nm (critical radius). The surface tension can be modeled as a convex function of the inverse bubble radius up to 1 nm. However, the interface surface tension vanishes for bubbles smaller than the critical radius. This possibly indicates that helium nanobubbles with radii smaller than the critical radius are thermodynamically unstable.
- Matsumoto [171] used MD simulation with the canonical ensemble ( $N, T, V$  constant) of water molecules and TIP4P model interactions (a combination of Lennard-Jones type interaction and Coulombic ones) in a cubic cell to study differences in pressure between the interior and exterior of a nanobubble. They also studied surface tension and evaluated the Young-Laplace equations as applied to micro- and nanobubbles. They concluded that the bulk liquid surrounding the nanobubble has a large negative pressure and is highly stretched. Furthermore, surface tension is hardly dependent on bubble size and agrees with the bulk value (surface tension of the planar surface), confirming the validity of the Young-Laplace equation.

The main thrust of this research was to validate several critical hypotheses for nanobubble stability, using state-of-the-art molecular dynamics simulations. The goal is to model the stable nanobubbles, where molecules and atoms were allowed to interact for a known period of time under known laws of physics. Here, a single oxygen nanobubble of 10 nm diameter was simulated. The simulation results were then analyzed with respect to time, bubble dissolution, localized pressure, and interfacial tension to study the bubble stability. The MD simulation was performed using LAMMPS software running in the XSEDE using comet and stampede2 clusters.

## 6.2 Model and Simulation Details

### 6.2.1 Methodology

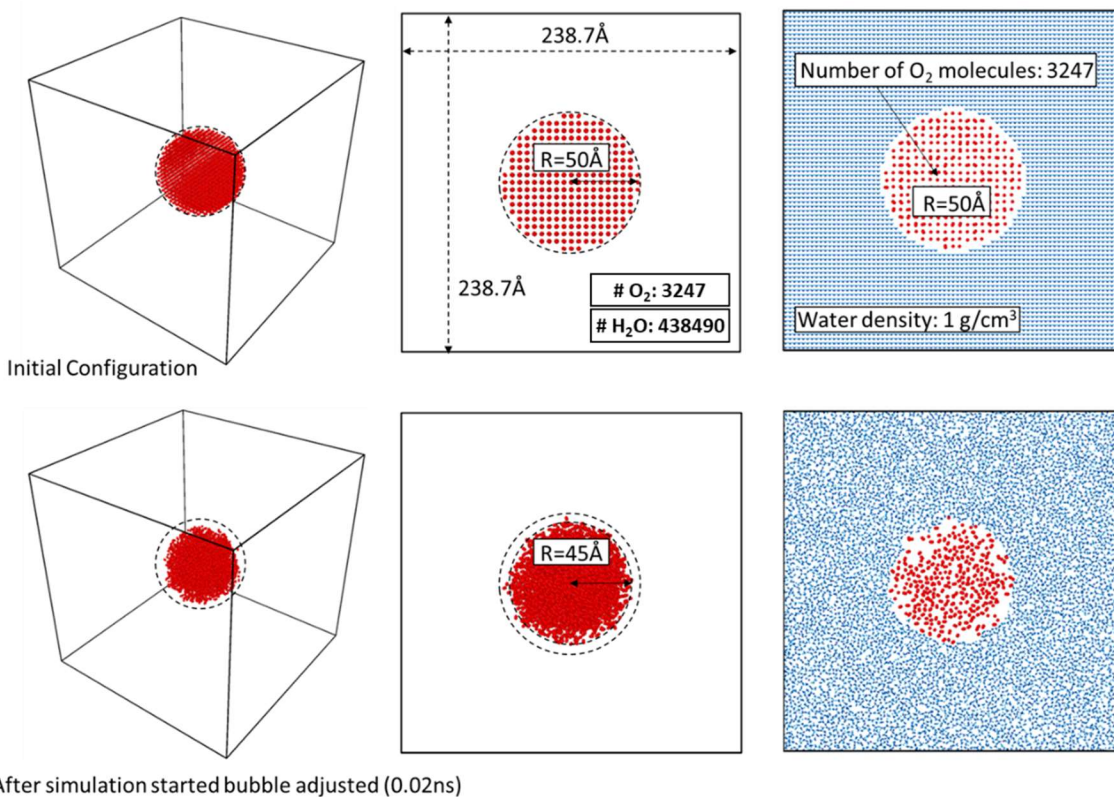
In this study, the LAMMPS molecular dynamic code was used to simulate bulk nanobubbles. LAMMPS is a classical molecular dynamics code developed by the Sandia National Laboratories, focusing on materials modeling. The abbreviation for LAMMPS is a Large-scale Atomic/Molecular Massively Parallel Simulator. Figure 6.1 shows the initial configuration of the O<sub>2</sub> nanobubble. The simulation was carried out in the NVT ensemble by using the Nose-Hoover thermostat. The temperature was maintained at 293.15K. SPC/E rigid water model with Lennard-Jones interactions was used for the simulation. Table 6.1 provides the L-J parameters used for the simulation [169]. Three types of atoms and interactions were introduced to the simulation (H<sub>2</sub>O molecule: H [type1], O [type2], and O<sub>2</sub> molecule: O [type 3]).

**Table 6.1** LJ Simulation Parameters

Atom type (i)	Atom type (j)	$\epsilon$ (kcal/mol)	$\sigma$ (Å)	Interaction between molecules H <sub>2</sub> O and O <sub>2</sub>
1	1	0	0	$\epsilon_{ij} = \sqrt{\epsilon_i \epsilon_j}$ $\sigma_{ij} = \frac{1}{2}(\sigma_i + \sigma_j)$
2	2	0.15535	3.166	
3	3	0.09538	3.094	

The initial simulation configuration was with a 238.7Å cube (periodic boundary) filled with water molecules having 1g/cm<sup>3</sup> density. Water molecules in a spherical volume of the radius of 50Å were deleted and replaced with O<sub>2</sub> gas molecules with a lattice length of 5.2, which ultimately required 3247 O<sub>2</sub> molecules to fill a 50 Å radius spherical volume, surrounded by 438490 H<sub>2</sub>O molecules. However, once the simulation proceeded, the

bubble size was reduced to 45 Å, and the simulation continued for 5ns, and necessary output data were created with specific time intervals.



**Figure 6.1** Simulation configuration.

## 6.3 Theory

### 6.3.1 Pressure and surface tension

For the nanobubble to be thermodynamically equilibrium, both the mechanical and chemical equilibrium should reach simultaneously. Mechanical equilibrium is related to the balance between opposing mechanical forces or the pressures within the system. Chemical equilibrium refers to the state of balance in the nonmechanical forces that drive specific chemical species from one region to another. The Young Laplace equation gives the pressure relationship. For the bubble system to be chemically in equilibrium, the partial

pressures of each of the gas constituents of the bubble should be equal to their respective pressures in the solution phase determined by Henry's law.

The Young Laplace equation gives:

$$P_{in} = P_{out} + \frac{2\gamma}{a} \quad (6.1)$$

Where,  $P_{in}$  is pressure inside the nanobubble,  $P_{out}$  is pressure outside the bubble,  $\gamma$  is surface tension at the gas-liquid interface of the bubble, and  $a$  is bubble radius.

By assuming the gas inside the bubble behave as an ideal gas, by applying the ideal gas law ( $PV = nRT$ ), Equation (6.2) will be modified,

$$\frac{nRT}{V} = P_{out} + \frac{2\gamma}{a} \quad (6.2)$$

If the bubble is chemically in equilibrium, then the equilibrium solution concentration near the bubble's surface should follow Henry's law. Therefore, the dissolved gas concentration is proportional to the corresponding partial pressure.

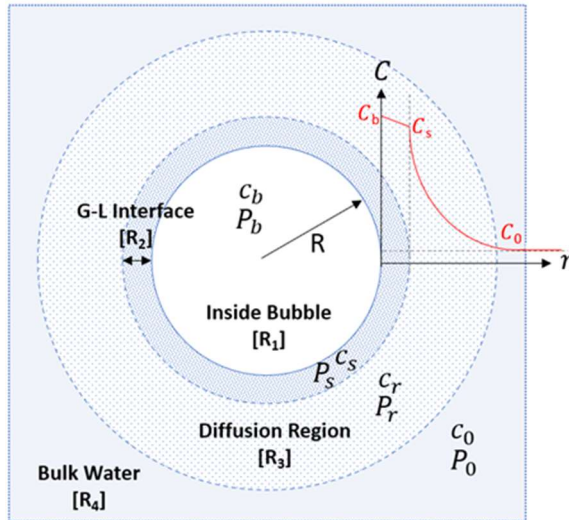
$$\frac{P_{in}}{P_{out}} = \frac{n_s}{n_{out}} \quad (6.3)$$

Where  $P_{in}$  is pressure inside the bubble,  $P_{out}$  is the external pressure after the system reached the chemical equilibrium,  $n_s$  is the equilibrium solution concentration at the gas-liquid interface, and  $n_{out}$  is the gas concentration in the bulk liquid.

Further, the LAMMPS simulation computes per-atom stress tensor for each atom in a group. Based on the stress/atom data, it is possible to plot the total pressure distribution profile with distance.

### 6.3.2 The diffusion of oxygen from the bubble

When a gas bubble is formed in a supersaturated solution, it obeys Henry's law. The systematic diagram of the gas concentration distribution around the nanobubble can be illustrated in Figure 6.2.



**Figure 6.2** The systematic diagram of the bulk nanobubble and gas-concentration profile.

**6.3.2.1 Diffusion coefficient based on a constant bubble size.** The steady-state solution for Fick's law of spherical diffusion can be used as shown in Equation (6.4) [172].

$$\frac{\partial c}{\partial t} = D \left( \frac{\partial^2 c}{\partial r^2} + \frac{2}{r} \cdot \frac{\partial c}{\partial r} \right) \quad (6.4)$$

Ng and Walkley 1969 derived a method to determine the diffusion coefficient when the gas bubble size is constant. The bubble radius maintained a constant radius of " $a$ ," the gas diffusion rate into the solution expressed by Equation (6.5) [172].

$$V = \frac{4\pi a C_0 D}{\rho} \cdot t \quad (6.5)$$

Where  $\rho$  is the density of the gas inside the bubble,  $a$  is bubble radius,  $C_0$  is equilibrium saturation concentration at the bubble interface,  $D$  is the diffusion coefficient,  $V$  is the volume of gas required to keep the bubble at a constant radius and the time,  $t$ .

**6.3.2.2 Diffusion coefficient based on molecular dynamic simulation.** The diffusion coefficients can be computed based on the mean square displacement (MSD) using the Einstein relationship [173],

$$D_{12} = \lim_{t \rightarrow \infty} \frac{\langle [r(t) - r(t_0)]^2 \rangle}{6t} \quad (6.6)$$

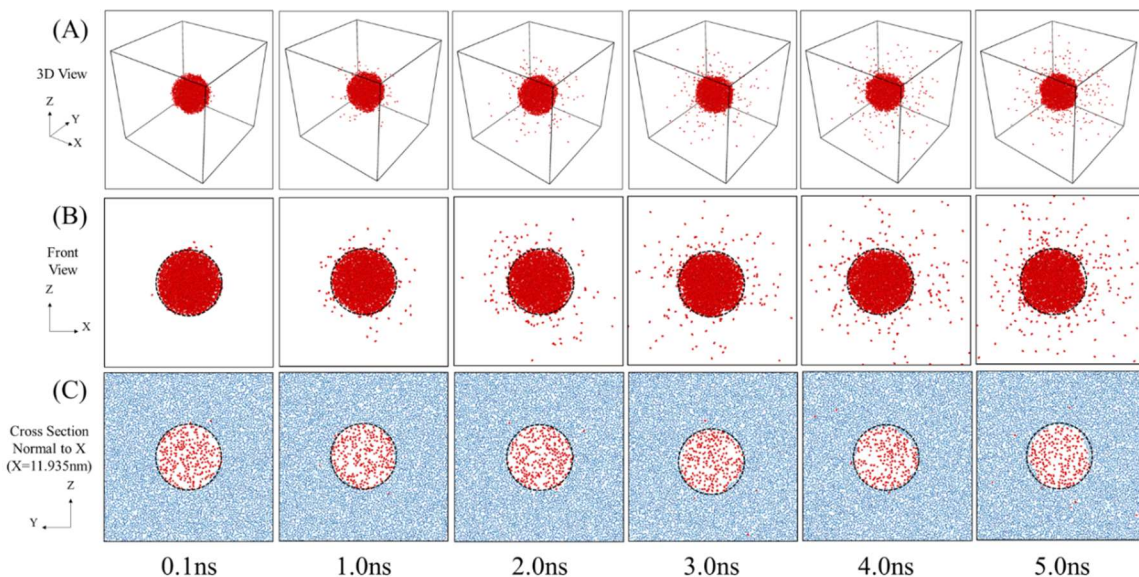
Where  $t$  is the elapsed time from the time origin  $t_0$ , and  $r$  is the position of a particle for each component. The slope of the linear  $MSD$  versus  $t$  plot gives the diffusion coefficient.

### 6.3 Simulation Results and Discussion

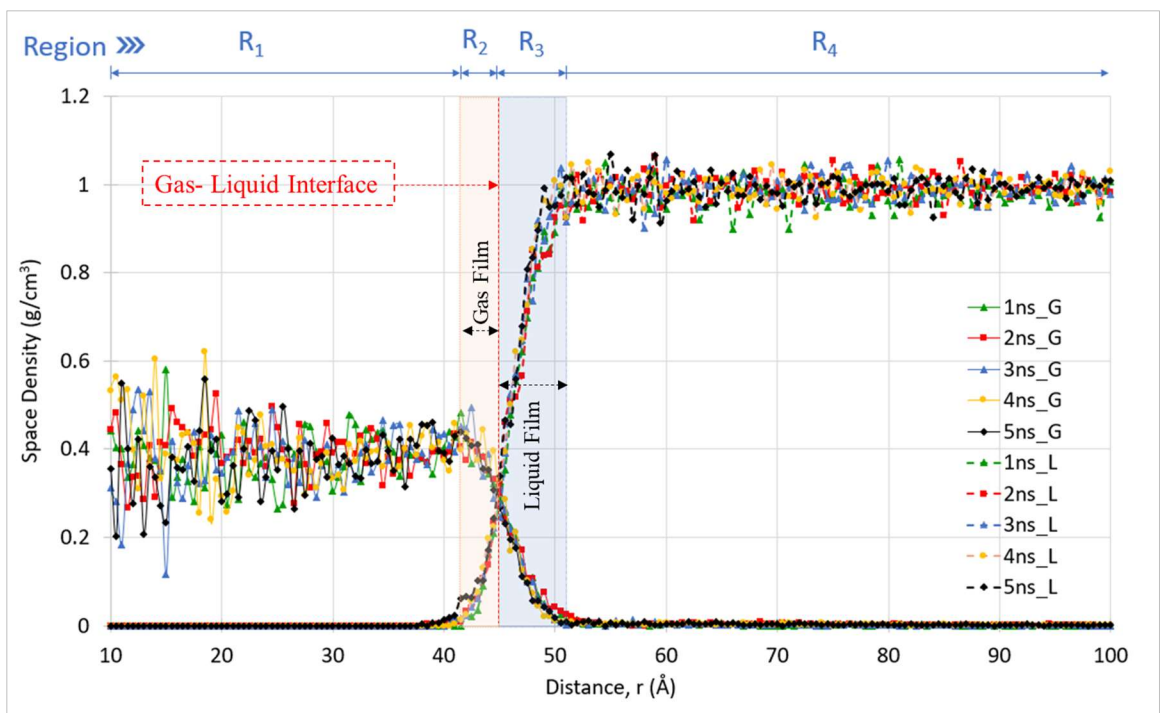
Figure 6.3 shows the snapshot of oxygen nanobubbles from 1 ns to 5 ns. During the 5 ns, gas molecules have diffuse into the bulk solution, yet the relative bubble size remained unchanged. Figure 6.4 shows the density profile for different time steps for both  $O_2$  and  $H_2O$  molecules. In order to plot the density profile, the center of the bubble was first

determined (bubble gently moved due to the Brownian motion), and then the number of molecules were counted. The density profile was then generated by considering the spherical shell of inner radius  $r$  and outer radius  $r + dr$  from the bubble's center. The density of each shell is calculated by counting the number of gas molecules in that shell. According to Figure 6.4, there were no significant changes to bubble size or gas-liquid interface thickness, or gas density profile over time, which indicated a stable bubble.

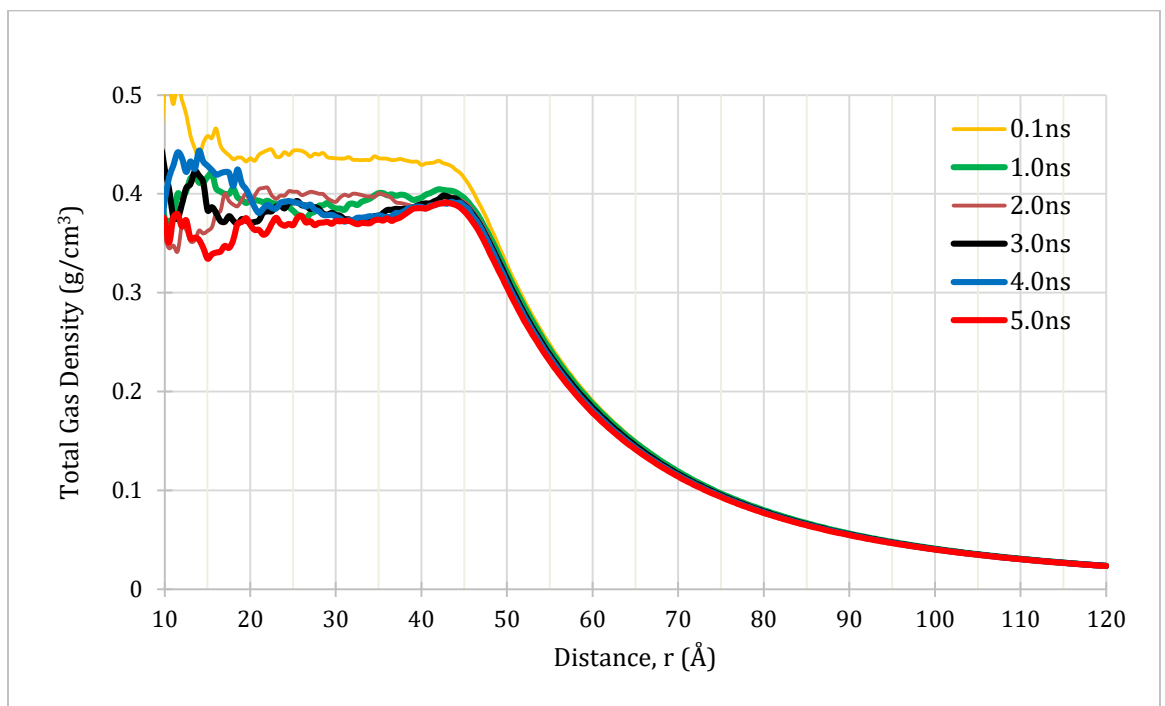
Figure 6.5 shows the total gas density with the distance, which is calculated by counting the total number of gas molecules in a given spherical volume from the distance  $r$  away from the center of the bubble. This graph looks at the reduction in total gas density inside the bubble over time and representing the constant bubble size over time.



**Figure 6.3** Snapshots of the bubble with time.

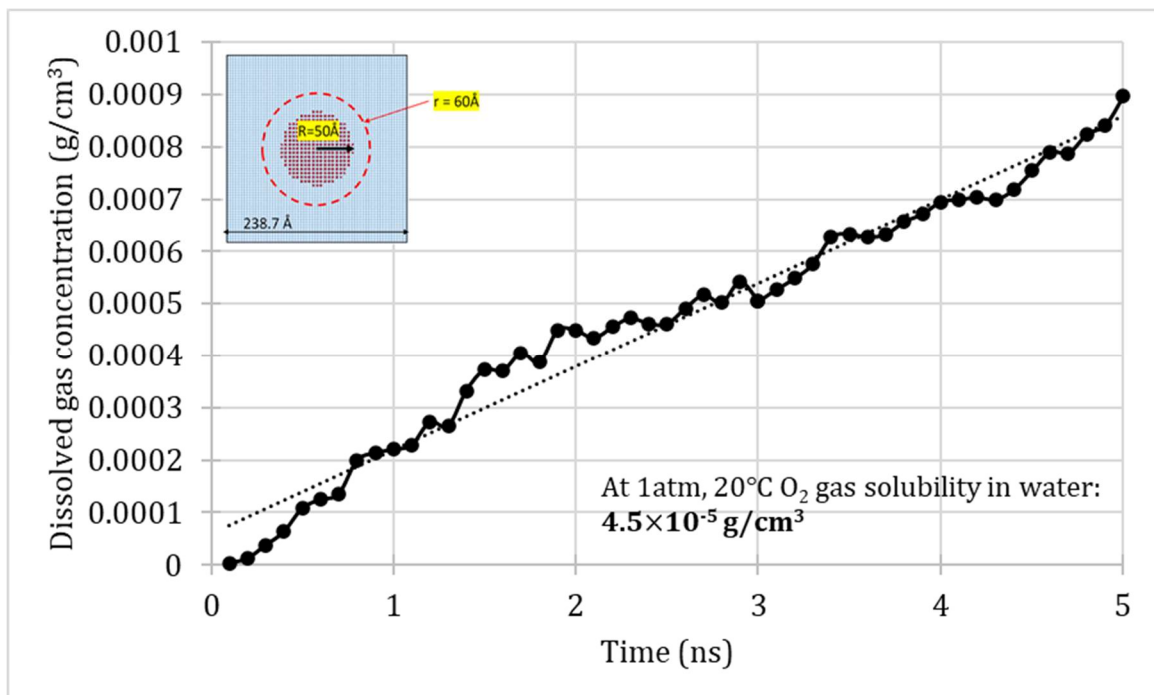


**Figure 6.4** Gas and liquid density profile.

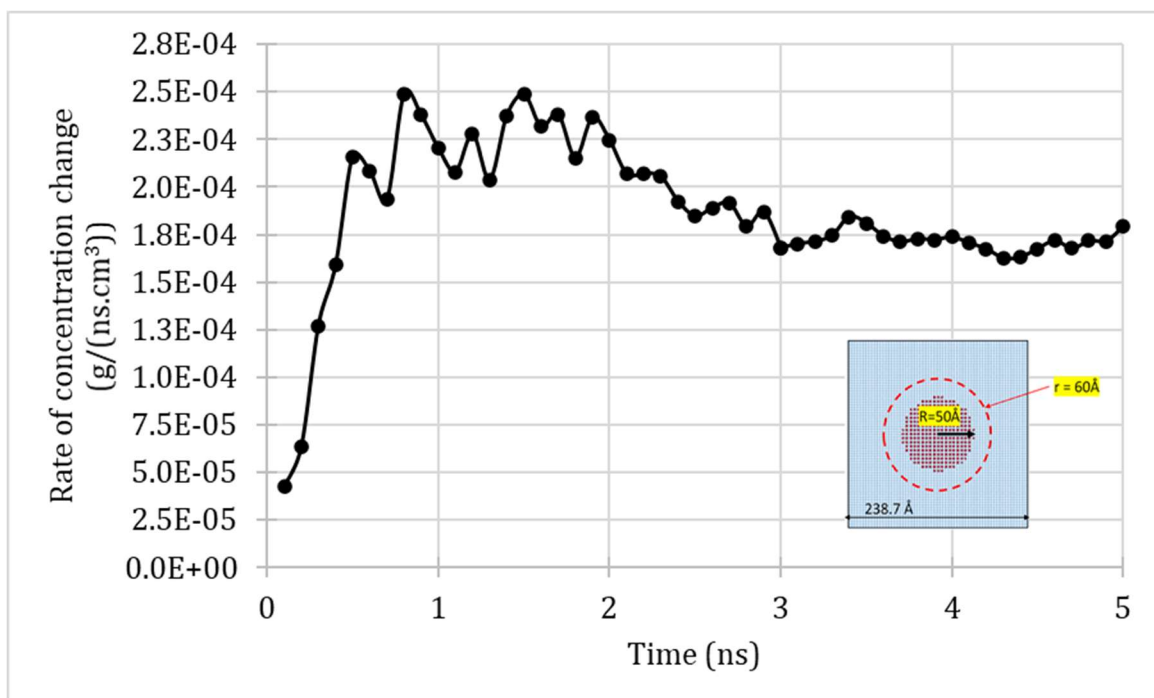


**Figure 6.5** The total gas density distribution.





**Figure 6.6** Dissolved gas concentration with time (outside distance  $r=60 \text{ \AA}$ ).

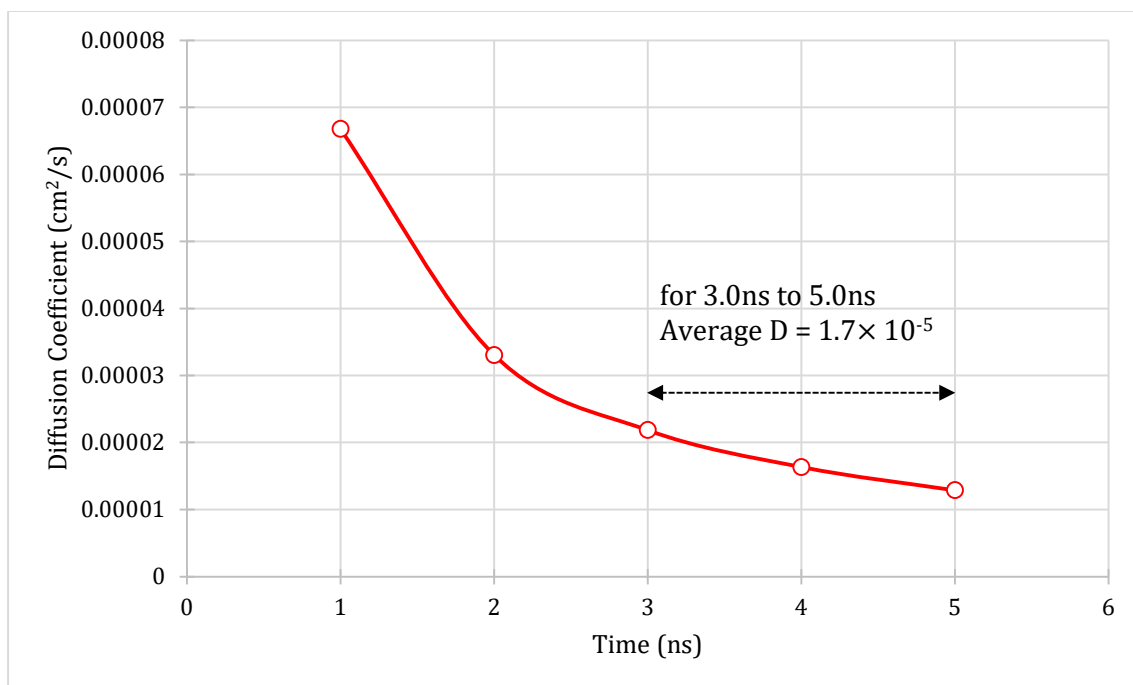


**Figure 6.7** The rate of change of dissolved gas concentration with time (outsider  $=60 \text{ \AA}$ ).

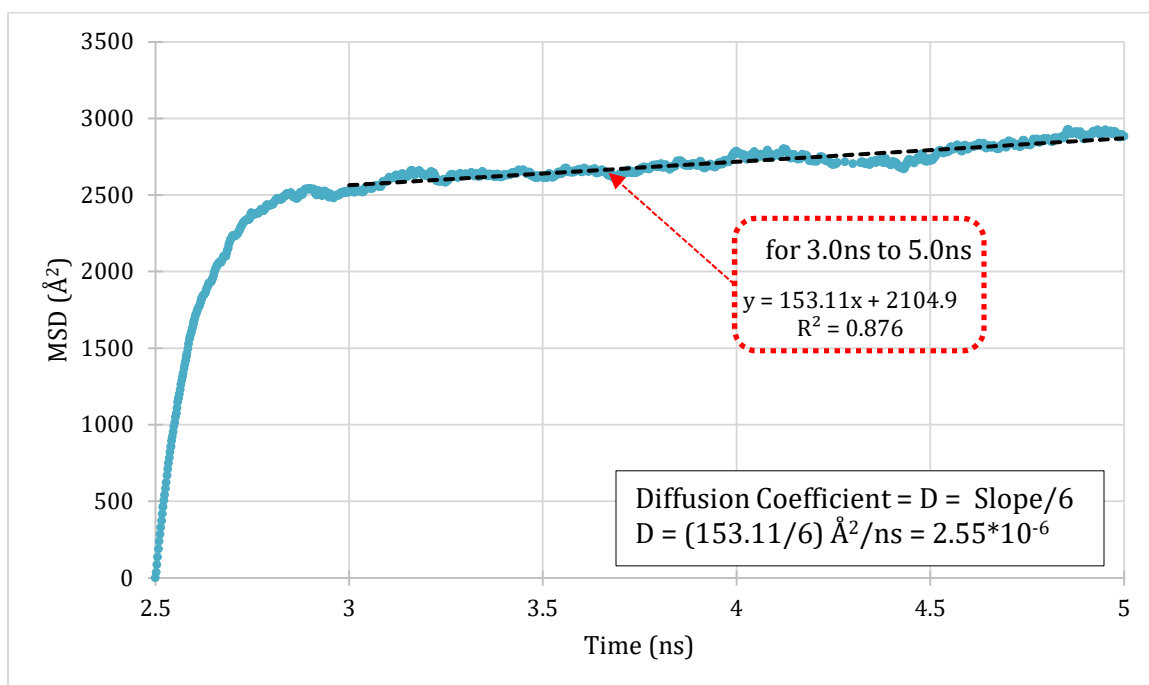
Figures 6.6 and 6.7 show the dissolved gas concentration and rate of gas concentration change outside a radial distance of 60 Å. Figure 6.6 shows that the dissolved gas concentration continuously increased with time, and the concentration of dissolved oxygen was far higher than the solubility at 1 atm and 20°C ( $4.5 \times 10^{-5}$  g/cm<sup>3</sup>). Hence, the system was at high supersaturation levels. Figure 6.7 shows that after 3ns, the gas concentration rate was approximately constant with time.

Figure 6.8 shows the calculated diffusion coefficient for different time steps based on the constant size bubble method (Ng and Walkley 1969). Figure 6.9 shows the variation in MSD value with time and calculated diffusion coefficient for different time steps based on MD simulation data. In Figure 6.8, the diffusion coefficient is calculated by taking the equilibrium concentration  $C_0$ , near the bubble surface at  $r \approx 44.5$  Å, as shown in Figure 6.4 for the gas-liquid interface.

When considering Figures 6.8 and 6.9, it is clear that initially, the bubble has diffused at a fast rate, and after 3ns for both cases, the diffusion coefficient reduced to a slower rate. After 3ns, the bubble diffusion coefficient is much smaller than the value of  $2.01 \times 10^{-5}$  cm<sup>2</sup>/s for 1 atm, and 20°C. These results match well with Figure 6.7 data as the dissolved gas concentration rate reached a stable value after 3ns, producing a smaller diffusion coefficient. Furthermore, there should be a slower gas diffusion rate to have stable gas bubbles, as a bubble should not lose gas by dissolution.



**Figure 6.8** The variation of the calculated diffusion coefficient based on Equation (6.5) with time.

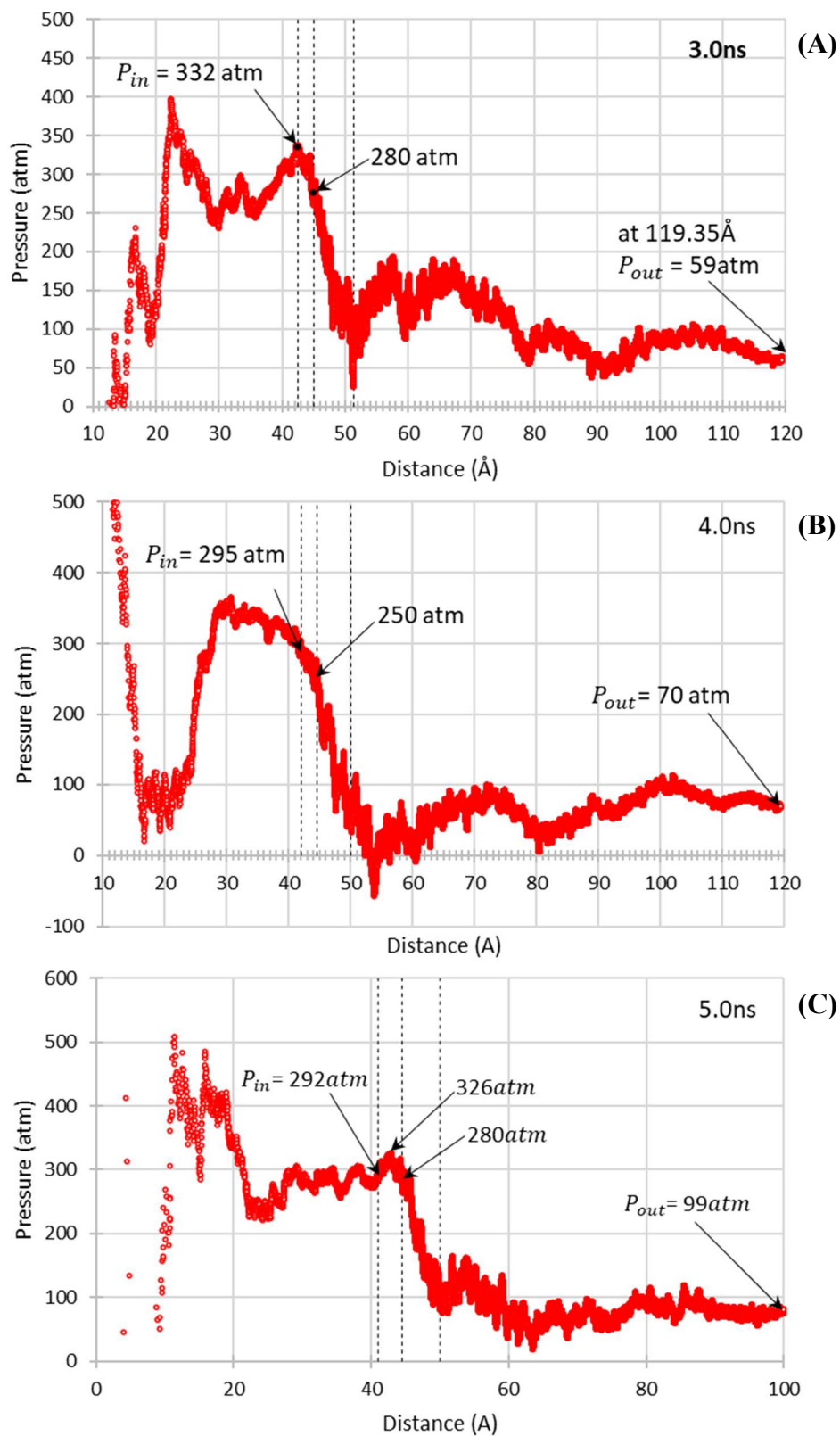


**Figure 6.9** The variation of the mean square displacement with time.

LAMMPS can compute the stress/atom data and saved it as a vector for each atom. Then this data was analyzed to obtain the variation in total pressure with distance. Inside the bubble, gas molecules move randomly and cause high or low-density spots, making the pressure and density fluctuate near the bubble's center. However, the purpose of this calculation was to determine the pressure at the bubble surface, gas-liquid interface, and at distances far from the bubble surface to obtain the outside pressure of the bubble. As the stable conditions were shown after 3ns, the pressure calculations were performed for 3, 4, and 5ns, and Figure 6.10 shows the total pressure variation with distance.

Furthermore, data from Figure 6.4 can be used to obtain the bubble size ( $r_b (=a)$ ) and the number of gas molecules inside the bubble and hence, calculate the inside pressure (using  $P_b = nRT/V$ ). Figure 6.10 can be used to obtain  $P_b$  (pressure inside the bubble),  $P_s$  (pressure at the gas-liquid interface), and  $P_o$  (outside pressure) values. Then surface tension can be back-calculated based on the Y-L equation, Equation (6.1). Table 6.2 shows the calculated values of pressures and surface tension with each consideration.

As per Table 6.2, the pressure calculated based on the number of molecules (c6) and the pressure plots (c7) are relatively closer with a small deviation. The difference in values is sensitive to the variation in pressure, as shown in Figure 6.10 (there is significant data variability within each  $0.02\text{\AA}$  distance). The results show that the total system pressure or the pressure at the far end from the center of the bubble increased with time. The partial gas pressures can explain this observation. With more gas molecules diffuse into the bulk solution, the bulk solution's partial gas pressure increases.



**Figure 6.10** The total pressure distribution calculated by stress/atom data obtained from MD simulation output data (A) 3ns, (B) 4ns, and (C) 5ns.

As indicated by the simulation results, when the surface tension is back-calculated using  $P_b$  and  $P_o = 1 \text{ atm}$ , the average surface tension value of  $0.0727 \text{ N/m}$  was obtained which is closer to the surface tension of  $0.0728 \text{ N/m}$  at  $1 \text{ atm}$  and  $20^\circ\text{C}$ . However, these values were cross-matched as this simulation was initiated with the outside pressure of  $1 \text{ atm}$ , surface tension value of  $0.0728 \text{ N/m}$ , and bubble radius  $50 \text{ \AA}$ . Hence, the required number of gas molecules was calculated based on the internal pressure. Based on simulation results, the system pressure is around  $100 \text{ atm}$  after  $5 \text{ ns}$ , and the relevant outside pressures values are reported in column 9 (c9) of Table 6.2 for each time step. Consequently, the back-calculated surface tension decreased with time, as shown in column 14 (c14) of Table 6.2 for the  $P_o$  values obtained from the simulation. This can be explained by the increased gas concentration outside the bubble with time. Several authors discussed this phenomenon as a reduction in surface tension with gas supersaturation [159,174–176]. As the output data, the current system pressure is around  $100 \text{ atm}$ ; and therefore, theoretically, which increases the gas solubility. Figure 6.6. show the gas solubility increase with time, and at  $5 \text{ ns}$ , it was around  $900 \text{ mg/L}$ . [177] showed that under high pressure, using a unique gas transfer reactor, it is possible to increase the dissolved oxygen gas concentration to  $10\text{-}300 \text{ mg/L}$ .

Based on simulation data, it is possible to comment on the validity of the Y-L equation for nanobubbles. As a classical thermodynamics theory, the Y-L equation considers the interface as the mathematical surface with no mass or volume and the density change across and function as a step-change in pressure across the interface [178]. German et al. 2016 confirmed the validity of the Y-L equation at the nanoscale with experimental data. However, when the density distribution profile in Figure 6.4 is observed, it is clear

that there is a finite thickness gas-liquid interface. Therefore, due to the high-density of O<sub>2</sub> molecules and reduced density of H<sub>2</sub>O (<1g/cm<sup>3</sup>) within the interfacial thickness would contribute to the reduced surface tension.

If the simulation box size was bigger than this current simulation cell size, while keeping same bubble size and gas mass, the gas would diffuse into the solution at a faster rate. Hence, when the simulation time of 3ns is reached, the gas concentration inside the bubble would be smaller than that shown in Figures 6.4 and 6.5. With lower gas concentration or density inside the nanobubble and thus, reduced inside gas pressure, the back calculated surface tension would be smaller than that shown in Table 6.2. Also, with a higher simulation volume high, the outside pressure will be smaller than that reported in in Table 6.2. consequently, the  $(P_{\text{out}} + 2\gamma/R)$  term will be smaller than the current simulation value make the  $P_{\text{in}}$  relatively higher, or else in other terms  $\Delta P$  would be higher, which means the bubble size should decrease (bubble shrink) with gas diffusion.

#### 6.4 Summary and Conclusions

High inner density oxygen gas nanobubble was simulated using the LAMMPS MD code. The simulation configuration includes 3,247 O<sub>2</sub> molecules embedded in 4.5nm radius spherical volume to represent bubble and surrounded by 438,490 H<sub>2</sub>O molecules, to form 1g/cm<sup>3</sup> density. The simulation ran for 5ns, and during the simulation, bubble size stayed constant around 4.5 nm. The gas and water molecules density profiles with distance did not significantly vary with time. Simulation results showed a smaller gas diffusion coefficient of  $\approx 2.55 \times 10^{-6}$  cm<sup>2</sup>/s than reported in the literature after 3ns. The pressure inside

the bubble decreased with time as the gas molecules diffused into the bulk solution while maintaining a constant bubble size.

However, the external pressure increased with time due to increased gas concentration with increased partial gas pressure outside the bubble. Surface tension values were back-calculated by considering the outside pressure obtained from the simulation and considering the 1 atm external pressure. In both cases, the calculated surface tensions were smaller than those reported in the literature for 20°C and 1atm. This reduction in surface tension would be attributed to the high-density profile of O<sub>2</sub> molecules and reduced H<sub>2</sub>O density (<1g/cm<sup>3</sup>) within the interfacial thickness. In classical thermodynamics, the Y-L equation would consider the interface with zero thickness and zero density. Still, the simulation results revealed the interface has a finite thickness and a density distribution, which would be the reason for these reduced surface tension values. With time the system still reached equilibrium (metastable), and gas diffused to the bulk solution at a slow rate with reduced surface tension values.

The stability of simulated nanobubble may be due to the bulk solution's supersaturation and high inner gas density. The gas concentration just outside the bubble was considerably high, causing a reduction in surface tension and increased external pressure. Therefore, the gas diffusion due to the internal bubble pressure is reduced or balanced and the bubble stability improved with slow diffusion. Hence, it can be concluded that supersaturation of gases in bulk solution and higher gas density inside the nanobubble are key parameters that would increase the bubble stability and control the diffusion.



**Table 6.2** Calculation of Possible Values for Internal Pressures and Surface Tension

(c1)	(c2)	(c3)	(c4)	(c5)	(c6)	(c7)	(c8)	(c9)	(c10)	(c11)	(c12)	(C13)	(c14)	(c15)	(c16)	(c17)
Time	$r_b$	$r_s$	$r_d$	$n$	$P = nRT/V$	From Figure 6.10			$\Delta P = 2\gamma/a$				$\gamma$			
						$P_b$	$P_s$	$P_o$	$P_b - P_o$	$P_b - 1$	$P_s - P_o$	$P_s - 1$	From			
														(c10)	(c11)	(c12)
(ns)		(Å)		(-)	(atm)	(atm)			(atm)				(N/m)			
3	42	44.5	50	2305	296.7	332	280	59	273	331	221	279	0.0581	0.0704	0.0470	0.0594
4	41.5	44.5	50	2189	292.1	295	250	70	225	294	180	249	0.0473	0.0618	0.0378	0.0524
5	41	44.5	50	2102	290.8	290	280	99	191	289	181	279	0.0397	0.0600	0.0376	0.0580

## CHAPTER 7

# IN-SITU REMEDIATION OF SEDIMENTS CONTAMINATED WITH ORGANIC POLLUTANTS USING ULTRASOUND AND OZONE NANOBUBBLES

### 7.1 Introduction

#### 7.1.1 Background

More than a century of industrial activity and discharges to the Passaic River, NJ, have resulted in high concentrations of legacy pollutants such as dioxin, polychlorinated biphenyls (PCBs), polycyclic aromatic hydrocarbons (PAHs), pesticides, and metals such as Cr and Pb in the river sediments, specifically in the Lower Passaic River and Newark Bay. The contamination of the river has caused poor water quality, banning of fish and shellfish consumption, loss of wetlands, and damaged wildlife habitats. Over one hundred industries have been identified as responsible for contaminating the Passaic River. Hence, the USEPA designated the Lower Passaic River as a Superfund site [179,180].

In April 2014, the USEPA announced a proposed cleanup plan for the Lower Passaic River Superfund Site. They proposed bank-to-bank dredging of contaminated sediments to a depth of 1m and placing an activated carbon cap to prevent the movement of contaminants to the river water from contaminated sediments below the depth of dredging. The above would cost \$1.38 billion to clean up the lower eight miles of the river. This would result in the secure disposal of 3.5 million cubic meters of contaminated sediments after dredging, dewatering, and transporting. This project is expected to be completed in five years, making it one of the longest cleanup projects proposed by the USEPA. The Lower Passaic River is a tidal river causing difficulty in transporting

dredged sediments in barges during high tides due to several bridges that cross the Passaic River. In addition, as one of the most congested regions in the country, the above plan has the potential to cause significant disruptions to its economic and social growth. Besides, finding and operating a large dewatering facility in densely populated Newark is a challenge. This will no doubt adversely impact the transfer of people, goods, and services in and out of the region. Cotillas et al. [181] suggested the need to search for novel treatment technologies that allow a complete and efficient abatement of these pollutants in sediments and in water in order to avoid their negative impacts on the environment.

Therefore, we have developed a cost-effective and environmentally sustainable in-situ remediation method based on chemical oxidation using ozone nanobubbles and ultrasound to treat the contaminated sediments. The proposed treatment method will be evaluated in four stages. This manuscript describes the first stage of evaluating the proposed method to decontaminate soil contaminated with Polycyclic Aromatic Hydrocarbons (PAHs) as a proof of concept evaluation. Concurrently, the decontamination of inorganic contaminants (the heavy metal chromium) and in the third stage, the combined contamination of both PAHs and one inorganic contaminant (chromium) in the same sediment will be tested to evaluate the technology. Finally, the actual Passaic River sediments will be tested before field implementation. If successful, this technology will eliminate most of the problems associated with the proposed USEPA cleanup proposal.

### **7.1.2 Research objectives**

The key aim of this research is to evaluate the performance of the developed method to remediate sediments contaminated with organic pollutants. Consequently, the synthetic sediments contaminated with a known quantity of p-terphenyl was used to evaluate the

treatment efficiency with different ultrasound and ozone nanobubbles conditions. Here, ultrasound provided the mechanical energy to desorb the contaminants from the sediments and ozone to oxidize the desorbed contaminants. The use of nanobubbles was to enhance the ozone concentration and ozone half-life in the solution. A comparison was performed between in-situ remediation using ultrasound technologies and results obtained from this research.

## **7.2 Remediation Method**

Although the ex-situ remediation methods are considered promising and have already been field implemented, their high treatment costs and socio-economic costs should not be neglected. Hence, in-situ treatment techniques have become attractive [182]. The most common in-situ sediment remediation technologies include but are not limited to, soil vapor extraction, solidification/stabilization, soil flushing, chemical oxidation, electrokinetic separation, bioventing, phytoremediation, monitored natural attenuation and thermal treatment technologies [183,184]. Because of the tidal action of the Passaic River, most of the above-mentioned methods are not applicable for sediments in a tidal river, leaving the chemical remediation as the only applicable method to treat the Passaic River sediments. Lemaire et al. [185] showed that with a proper oxidizer it is possible for chemical oxidation to remove most of organic contaminants. An oxidizer can destroy both high and low molecular weight hydrocarbons, thereby reducing the persistent, high-risk chemicals [186].

Over the past decades, the use of ozone to oxidize chemicals attached to soils has been investigated by many researchers, especially the removal of non-volatile organic compounds that are not easily removed by conventional methods such as soil venting [187]. The chemical oxidation can be combined with other processes to improve the effectiveness

of the chemical oxidation of organic contaminants that are strongly adsorbed to the organic and mineral constituents of the soil matrix [188]. Therefore, the ultrasound can be coupled with chemical oxidation to effectively degrade organic contaminants in the soil/sediments.

### **7.2.1 Ultrasound and ozone nanobubbles for remediation of sediments**

The ultrasound is considered a clean and green treatment method [189]. Ultrasound-assisted soil remediation relies on desorption and degradation in the treatment of organic pollutants. With the application of ultrasound, sediment will be kept in suspension, and contaminants will be sheared and desorbed from the soil particles due to sono-physical effects such as microstreaming, shockwave, and microjets. Theoretically, for hydrocarbon contaminated soil, the energy required for desorption of pollutants from the soil depends on the change in Gibbs energy of the system that is required to remove the hydrocarbons molecules from the soil surface [190,191]. This change in Gibbs energy can be provided by the concentrated energy and the cavitation produced by ultrasound, which facilitates the desorption of organic compounds from the soil surface.

Besides the sono-physical effects of ultrasound on the desorption of contaminants from the soil surface, sonochemical effects facilitate the degradation of organic contaminants due to cavitation. Hoffmann et al. [192] explained ultrasound-assisted degradation occurs through three pathways: sono-lysis by free radicals, pyrolysis with extremely high pressures and temperatures, and supercritical water oxidation. Hence, with ultrasound, the long carbon chains or aromatic hydrocarbons with complex structures and high molecular weights can be broken down into simpler hydrocarbons [191].

There are several factors that determine the treatment efficiency of ultrasonic sediment remediation: sediment size, ultrasound frequency, power, and intensity, irradiation time,

etc. Particle size is a sediment property that determines how strongly the contaminants are attached to the sediment particles. Among the sediment types, clay has the highest chemical and physical affinity; therefore, the applicability of any remediation effort would depend on the clay content. Clays have high sorption of water, organic compounds, and cations due to high specific surface area, cation exchange capacity, and unsatisfied bonds at the edges of clay structure [193,194].

Low-frequency ultrasound produces a small number of large bubbles due to cavitation, which then collapse due to microstreaming, hence, strong sono-physical effects. In contrast, high-frequency ultrasound produces a high number of much smaller bubbles due to cavitation. This increases both the •OH radical production and diffusion of gas and volatile compounds into bubbles [195]. Elevated power or power intensity (power/surface area of the ultrasonic transducer) causes higher acoustic pressure (amplitude of vibration), greater cavitation and more violent collapse of bubbles. Due to the bubble shielding effect, there is optimum power intensity for the highest reaction rate [196,197]. Sonication time and the mode of sonication, pulsed or continued mode, were found to be key factors that determine the success of remediation. In general, for longer treatment time, pulsed mode of sonication increases the treatment efficiency [197].

Many oxidizing agents with high oxidizing potential are used in a multitude of industries. A few of the most common oxidizers are ozone (O<sub>3</sub>), hydrogen peroxide (H<sub>2</sub>O<sub>2</sub>), fluorine (F<sub>2</sub>), and potassium permanganate (KMnO<sub>4</sub>). Among the most powerful oxidizing agents for in-situ treatment, fluorine and potassium permanganate would require special methods to remove oxidation byproducts. The use of hydrogen peroxide requires special handling with respect to storage and is expensive to generate [198]. Furthermore, the ozone

is a strong oxidant with a much higher oxidation potential than hydrogen peroxide [199]. Ozone has an oxidation potential of 2.07 V, which is only lower than the common oxidation agents such as Fluorine (F<sub>2</sub>), hydroxyl radicals ( $\bullet$ OH), and atomic oxygen (O), with oxidation potentials of 3.03 V, 2.80 V, and 2.42 V respectively [200]. Ozonolysis includes not only direct oxidation but also the indirect reaction of secondary oxidizers such as the formation of  $\bullet$ OH radicals due to ozone decomposition, and further increases the oxidation potential of ozone [40,201–205]. The hydroxyl radical can non-selectively attack both organic and inorganic compounds with high reaction rates [206,207]. Once a hydroxyl radical is formed, it attacks nearly all the organic complexes and leads to a complete breakdown of the organic compound [206]. Therefore, in the organic compound destruction process, the indirect ozone reactions are often responsible. Theoretically, the organic compound (R-H) react with  $\bullet$ OH radicals, and it takes away a hydrogen atom causing the formation of organic radicals ( $\bullet$ R) ( $\text{R-H} + \bullet\text{OH} \rightarrow \text{H}_2\text{O} + \bullet\text{R}$ ). These reactions continue through a series of radical chain reactions to form several products and by-products or the complete mineralization to form carbon dioxide and water [206]. Furthermore, most of the ozone remediation are free of chemical residuals and leave behind O<sub>2</sub> after the reaction. Unlike other AOPs, ozone does not produce chemical residuals and leave behind O<sub>2</sub> after the reaction. However, water-soluble harmful byproducts can be formed during ozone treatment and hence, requires careful monitoring for complete oxidation.

The capital and operational costs of ozone-based treatment are high and energy-intensive [206,207]. However, with high remediation efficiencies and comparing to other AOPs, the overall costs of ozone-based AOP treatment is preferable [208]. One of the main

drawbacks of the conventional ozone treatment is the low water solubility of ozone and loss of ozone in the treatment. If this wastage can be minimized, it can considerably reduce the cost of ozone treatment.

As stated before, nanobubbles are gas cavities in an aqueous solution with diameters smaller than 1 $\mu$ m that are filled with different gases. Nanobubbles have remarkable properties, which the ordinary bubbles do not have. Nanobubbles are very small in size; this leads to smaller buoyancy force and hence, very slow rising velocity and are impacted by Brownian motion [9,10,93], which ultimately increases the bubble residence time in the solution. Yet, the long residence time alone would not increase the reactivity and need to control the dissolution. There are believed to be many factors contributing to the dissolution/diffusion of gas, such as diffusion barrier [27] (i.e., ion shielding/ accumulation of impurities), rigid interfacial properties (i.e., hard hydrogen bond structure [19]), cluster formation [1,65] and gas supersaturation [1,27,58].

In addition to the long residence time of nanobubbles in aqueous solutions, nanobubbles have large specific surface areas when compared to macro bubbles. When surface areas of macro, micro, and nanobubbles are compared, nanobubbles with higher specific surface areas have a higher probability of reacting with pollutants. The large surface area will also enhance gas diffusion into water. In order to calculate the diffusion of ozone in water,  $R$ , Equation (7.1) can be used [209].

$$R = 2S(C' - C_0) \sqrt{\frac{DT}{\pi}} \quad (7.1)$$



where  $S$  is the surface area of the gas bubble,  $C'$  is the concentration of  $O_3$  in the gas-liquid interface and assumed as  $3.90 \times 10^3 \text{ atm}$  for ozone [210],  $C_0$  is the initial concentration of the gas, and  $D$  is diffusivity of ozone given as  $1.76 \times 10^{-9} \text{ m}^2 \text{ s}^{-2}$  [209]. Calculations based on the same volume of a macro-bubble and the total nanobubble volume (equal volumes of gases) show the diffusivity of nanobubbles and micro-bubbles as  $4.42 \times 10^{-8} \text{ m}^2 \text{ s}^{-1}$  and  $4.42 \times 10^{-16} \text{ m}^2 \text{ s}^{-1}$ , respectively, showing that the gas diffusion for nanobubbles is much higher than that for macro-bubbles. Therefore, nanobubbles can deliver higher ozone concentrations to the water due to its size and high retention time. Hence, nano ozone reduces the ozone wastage and increases reaction rates with contaminants.

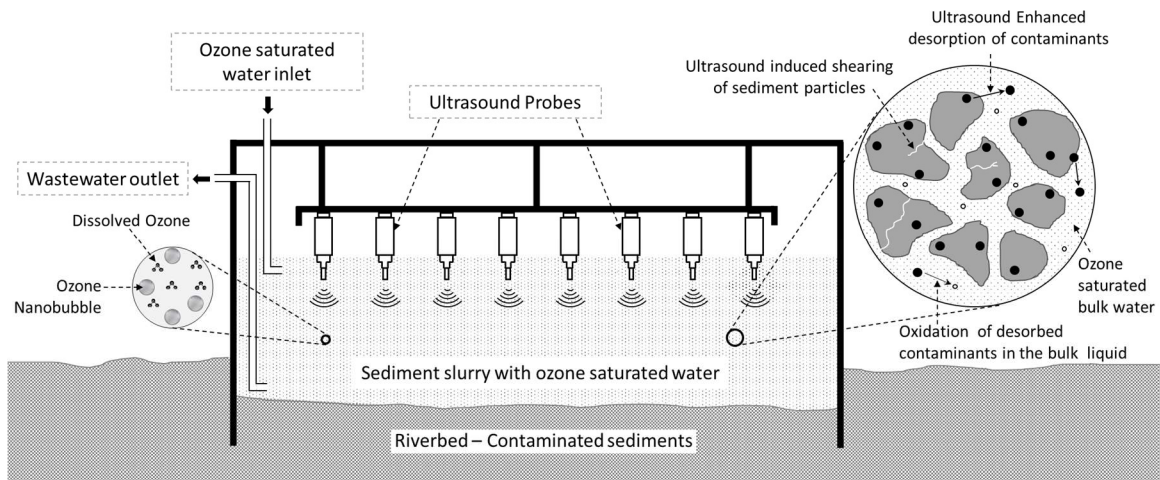
### **7.2.1 Proposed in-situ remediation technology**

For the field implementation, ultrasound transducers will be housed in a containment chamber, which is made of anti-corrosive material. The chamber will include an ozone nanobubble delivery system and a wastewater removal system. The wastewater removed will be treated, filtered, and returned to the chamber with additional ozone nanobubbles. The sediment treatment will be performed inside the containment chamber. A sketch of the proposed containment chamber is shown in Figure. 7.1.

The proposed containment chamber will be  $3.5\text{m} \times 3.5\text{m} \times 1.5\text{m}$  ( $L \times W \times D$ ), made out of anti-corrosive material. Probe type ultrasound transducers will be arranged in a grid of 0.3m intervals to maximize the impact of the sonication. The chamber in a barge will be lowered to sediments in the river bottom, allowing it to sink into the contaminated sediments. The containment chamber will be filled with ozone nanobubble saturated water, while ultrasound is applied to the contaminated sediments. Desorbed contaminants from the sediment due to ultrasound will be oxidized by the water saturated with ozone

nanobubbles. During the sonication, river sediments will be mixed with water containing ozone nanobubbles to form a slurry. After ultrasound treatment, cleaned sediments inside the chamber are allowed to settle, and the wastewater above the settled sediments will be extracted and treated on a barge. The extracted contaminants are to be oxidized before recirculating the treated water back into the containment chamber. This treatment can be repeated in another section of the river by dividing the river into a 3.5mx3.5m grid [211].

This experimental study is one in a larger investigation to support the development of a proposed technology. The proposed ultrasound and ozone nanobubbles coupled sediment remediation method is designed as first the desorption of contaminants from the sediment and then oxidize the contaminants present in the extract. The ultrasound was used to desorb the contaminants from the sediment due to the sono-physical effects such as micro streaming and turbulence forces [212]. Then the extracted contaminants degraded utilizing direct and indirect ozone reactions and free radicals formed by sonochemical effects of ultrasound.



**Figure 7.1** A sketch of the containment chamber was used for the proposed remediation.

## 7.3 Materials and Methods

### 7.3.1 Sediment sample preparation

The sediments recovered from the Passaic River contain various organic and metal contaminants, and hence, not suitable for laboratory batch scale experiments to evaluate the proof of concept. This is due to the variation in the contaminant types, concentration, and distribution within the sediment matrix. Therefore, for the bench-scale testing, a synthetic sediment was prepared to match the size distribution of the actual Passaic River sediments and the soil was artificially mixed with the known quantity of selected contaminant [73]. The laboratory-prepared synthetic sediment sample was a mixture of kaolin, rock flour, silt, and fine sand with  $\text{pH} \approx 7$ , 3.6% moisture content and negligible organic carbon content (additional details on synthetic sediment can be found in the supporting materials). A major fraction of this sediment consisted of silt and clay sizes, which have the highest capacity to adsorb organic contaminants. The clay content was 15%, and silt content was 62%, so the total fine fraction was 77%.

### 7.3.2 Sediment contamination

The prepared synthetic sediment was artificially contaminated with p-terphenyl (CAS No. 92-94-4) (the selected organic compound to represent PAHs). The reason for this selection was because most of the commonly found PAHs in the river are very hazardous and highly toxic to handle under laboratory conditions, and there are risks to the health and safety of laboratory staff. The p-terphenyl is analogous to regularly encountered PAHs due to its high MW and its physical-chemical properties such as low solubility and low volatility, but comparatively less toxic and less hazardous. Hence, p-terphenyl was selected in this research (MW:228.29  $\text{g mol}^{-1}$ , VP: $4.9 \times 10^{-6}$  Pa, MP:213°C, BP: 448.0°C, water

solubility:  $0.018 \text{ gm}^{-3}$ , octanol/water partition constant ( $\log K_{ow}$ ): 6.03, Henry's law constant:  $2.9 \times 10^{-1} \text{ mol. m}^{-3} \cdot \text{Pa}^{-1}$ , ionization potential:  $7.83 \text{ eV}$ ). The justification for the selection of p-terphenyl to represent PAH is given in the supporting materials.

A 0.15g of p-terphenyl (p-Terphenyl, 99+%, pure, Acros Organics) was mixed with 50 ml of acetone (Certified ACS Reagent Grade with  $\geq 99.5\%$  purity) until all the p-terphenyl flakes dissolve in acetone. Then 80g of synthetic sediment mixed with the p-terphenyl in acetone for 2 hours until the acetone evaporated from the sediment sample, leaving the p-terphenyl absorbed onto the sediment matrix. The resulting mixture was further mixed for another 2 hours to ensure the homogeneous distribution of p-terphenyl in the sediment and air-dried for 24 hours prior to use.

### **7.3.3 Ozone nanobubble generation**

Industrial grade ozone was produced by passing the oxygen through Ozonator (Model T Series, Welsbach Ozone System Corporation, USA & A2Z Ozone Inc. Model MP-3000). Ozone Nanobubbles were generated using the micro-nano bubble nozzle (Model BT-50FR, Riverforest Corporation, USA), which uses the hydrodynamic cavitation. A pump (Model 4CUK6, Dayton, USA) maintained at a constant running pressure of 0.38 MPa was used to recirculate nano ozone mixture [73]. In this experimental setup, ozone nanobubbles generated in a chamber with a capacity of 25 liters filled up to 21 liters, and the generation system was operated for 6 minutes to obtain the maximum ozone concentrations in water.

### **7.3.4 Ultrasound generation**

In this study, the sonication was carried out using the ultrasonic processor (Sonics & Materials, Inc., Model vibracell VC-1500, 240 Volts, Power 1500 Watts), which operates

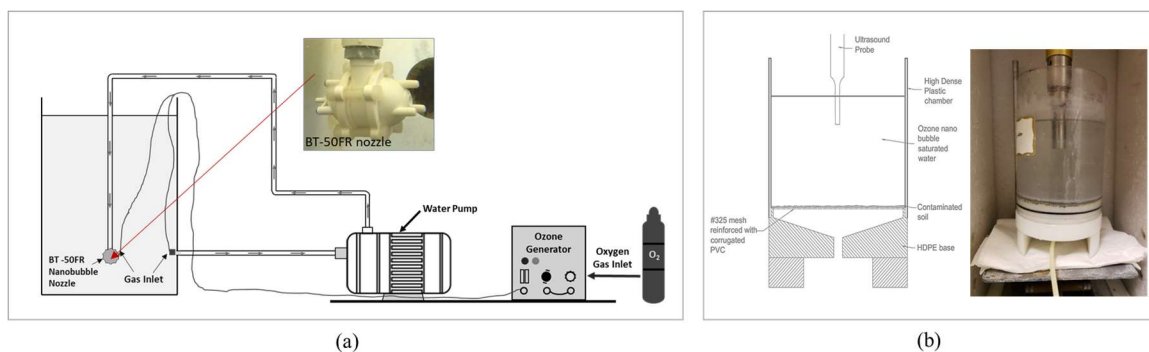
at 20 kHz frequency. The generator was a horn-type (19mm tip diameter and 127mm length).

### **7.3.5 Sediment remediation**

The contaminated sediment prepared in the lab was placed in a sediment treatment chamber. The chamber consisted of a high-density polycarbonate (transparent) shell and a high-density polyethylene base. The 80g of the contaminated sediment sample was placed on top of the US number 325 mesh (mesh aperture of 0.044mm).

After 6 minutes of ozone nanobubble generation, 2000ml of ozone gas saturated water was pumped into the sediment treatment chamber to form a sediment slurry with a solvent ratio of 4% (w/w as %). Then the probe was dipped 7cm into the sediment-water slurry, and ultrasound applied for 2 minutes. The sonication was initiated immediately after adding the ozonated water into the sediment chamber to minimize the depletion of ozone in the solution. The experimental setup for nanobubbles generation and treatment chamber is shown in Figure 7.2. In this experiment, the ultrasound power and the ultrasound dwell time were varied to determine the impact of each parameter on the removal efficiency. After each sonication trial (2 minutes of ultrasound), sediments were allowed to settle, and the wastewater drained out from the chamber. This treatment cycle was repeated until the desired total sonication time was achieved.

After completion of treatment trials, water in the sample was drained out of the chamber, and collected sediment was dried at 60<sup>0</sup>C for 72 hours in a temperature-controlled oven. These sediment samples were brought back to room temperature and were air-dried for another 24 hours. Then, the treated sediment samples were subjected to the next phase of analysis to determine the removal efficiency.



**Figure 7.2** Experimental setup (a) nanobubble generation setup, (b) the sediment treatment chamber.

### 7.3.6 Chemical analysis

The EPA method 3550B was used to extract p-terphenyl from the treated synthetic contaminated sediments. The treated and untreated synthetic sediments were extracted using solvent extraction enhanced by ultrasound. A 20g of the representative sediment sample was extracted from the treated sediment and was placed in a 250ml beaker with 100ml of acetone. The acetone and sediment solution was subjected to sonication under the horn type 475W ultrasound generator (Virtis Virsonic 475 Sonicator). Sonication was applied to the sample in short bursts for around five seconds. These short bursts are carried with a gap of 10 minutes between each sonication burst to prevent temperature rise, to avoid any change to the chemical composition of the organic materials in the liquid. After completion of 10 ultrasound bursts cycles, the sample was filtered using filter paper and collected into a 250ml flask. Then another 100ml of acetone added to the sediment sample, and the process was repeated to ensure the complete extraction of all the organic material from the sediment. After the extraction with the ultrasonic probe, the collected acetone samples were concentrated using Kuderna-Danish (K-D) method to 10 ml. The (K-D) column was washed to prevent the loss of organic contaminants during concentration. The

concentrated contaminated sample was analyzed using a gas chromatograph with mass spectrometry (GC/MS).

### **7.3.7 Other measurements**

*Temperature:* A Fluke 53II B thermometer (with an accuracy of 0.05% + 0.3°C) was used for the investigation to collect continuous real-time temperature.

*Ozone concentration:* The dissolved ozone was tested using the 4500-O<sub>3</sub> indigo Colorimetric method (APHA et al. 1992). A Thermo Scientific™ Evolution 201 and 220 UV-V spectrophotometers were used during the 4500-O<sub>3</sub> ozone analysis.

*Nanobubble Size and Zeta potential:* The Malvern Nano Zetasizer with Folded Capillary Zeta Cells (model DTS1070) was used for the analysis of nanobubbles size and their zeta potential values.

## **7.4 Results and Discussion**

### **7.4.1 Ozone nanobubbles**

Figures 7.3a and 7.3b show the nanobubble size distribution and zeta potential respectively for three different temperatures (15, 20, and 25°C). Figure 7.3c shows the variation of ozone concentration with time for two different solutions: ozone nanobubbles solution and regular ozone bubbles (dissolve ozone using a regular diffuser), for three different temperature settings 10,15, and 20°C.

On average, the size of ozone nanobubbles was in the range of 100-300 nm, and the negative zeta potential values were in the range of 14 -25mV in magnitude. The increased temperature caused nanobubble sizes to increase and the magnitude of zeta potential to decrease. Figure 7.3c, test results showed that ozone concentration in the

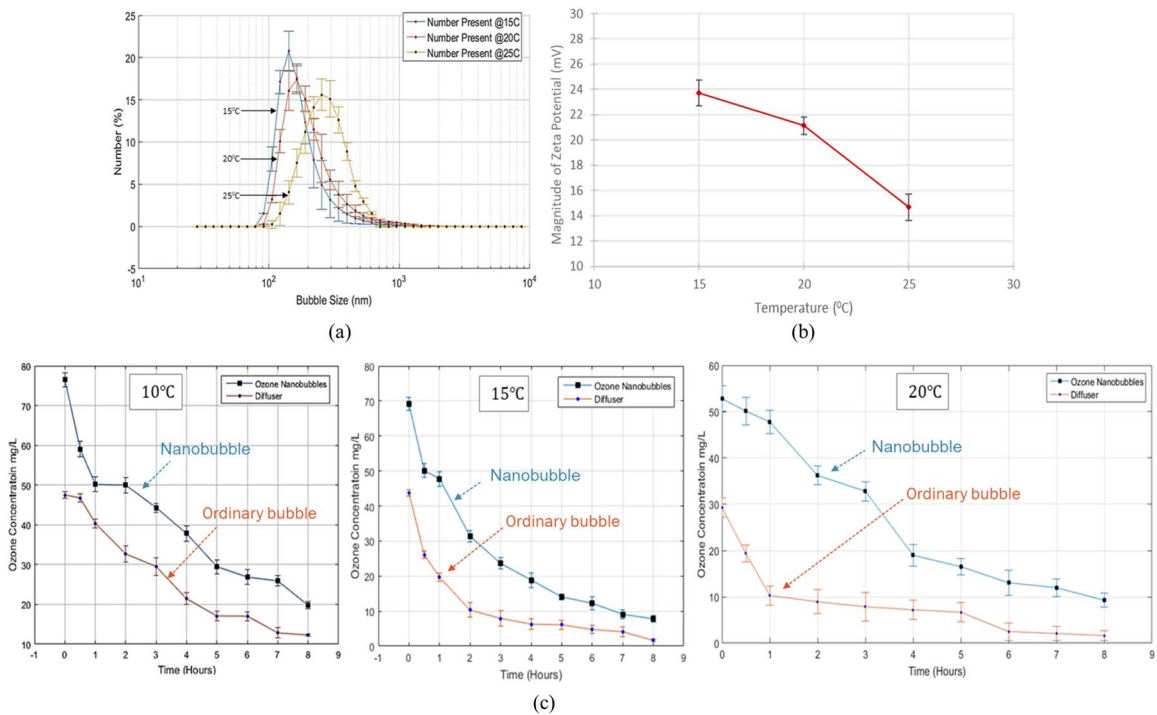
nanobubble solutions is much higher than that without nanobubbles (or with the use of the regular diffuser). Likewise, the concentration of ozone in the solution was high at low temperatures. Also, the rate of decrease in the ozone concentration over time shows a gradual reduction for the nanobubble solution when compared to that for the ozone solution made from the regular diffuser, where ozone concentration depleted rapidly with time. Hence, the use of ozone nanobubbles could deliver a much higher dose of ozone to water and can maintain those high ozone concentrations for prolonged periods allowing time for further oxidation of contaminants.

Bubble size and zeta potential are key factors that determine the stability of nanobubbles in aqueous solutions. The ozone nanobubbles stability directly impacts the dissolved ozone concentration and, thus, the treatment efficiency. Smaller bubbles with higher magnitudes of zeta potentials produce the desired long-term stability of these bubbles and increased gas mass transfer rates of ozone [9]. Similarly, smaller bubbles have high specific surface areas and also low rising velocities due to low buoyancy forces, which ultimately increases the possibility of reaction between ozone and the contaminants [40,73]. The zeta potential is one factor that increases the bubble stability against coalescence. Higher the magnitude of zeta potential ensures lesser coalescence probability by increasing the repulsion forces between the bubbles [213]. The temperature-dependent zeta potentials of nanobubbles zeta potential are good indicators of the number of adsorbed ions at the gas-liquid interface at different temperatures. Under neutral conditions, nanobubbles are found to be negatively charged, and this mechanism is believed to be mainly due to adsorbed  $\text{OH}^-$  ions at the interface. The decreased zeta potential or decrease in surface charge density may be due to decreased  $\text{OH}^-$  ion concentration on the bubble



surface. With increased temperature, mobility of the ions in the solution is higher and, thus, decreased  $\text{OH}^-$  ion absorption onto the bubble surface [9].

Therefore, the low temperature improves the dissolved ozone gas concentration and ozone retention time in the solution. The average temperature in the river sediments is below  $20^\circ\text{C}$ . However, with the application of ultrasound, the water temperature would increase. Hence,  $20^\circ\text{C}$  was selected for all treatment tests, which would be an average temperature during actual implementation. This was easily accomplished by adding ice into the nanobubble generation system.



**Figure 7.3** Variation (a) diameter/bubble size distribution and (b) zeta potential for ozone nanobubbles with the temperature at  $\text{pH} \approx 7$ , and (c) ozone concentration with time for regular bubbles and nanobubbles at different temperatures and  $\text{pH} \approx 7$  (a)  $10^\circ\text{C}$ , (b)  $15^\circ\text{C}$ , and (c)  $20^\circ\text{C}$ .

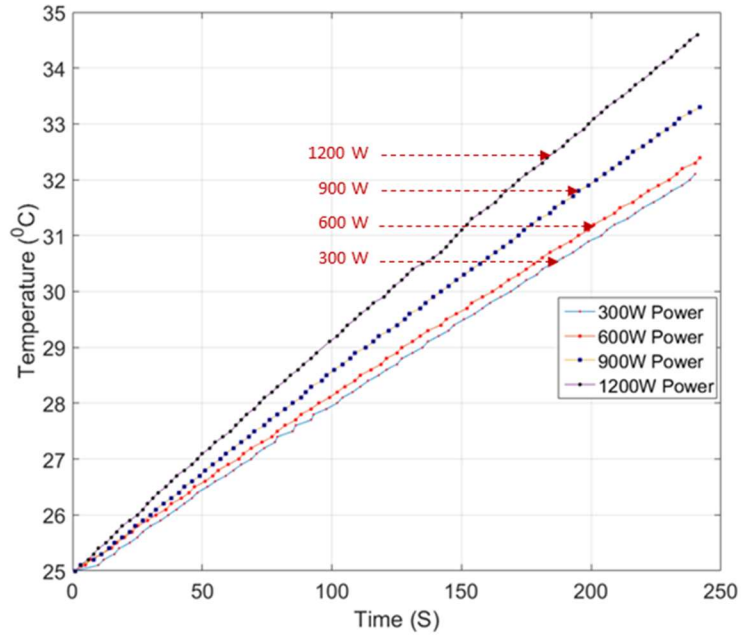
Source: Batagoda [211], Aluthgun Hewage et.al [72].

#### 7.4.2 Impact of ultrasound on solution properties

The application of high-intensity ultrasound can change the solution properties, which will affect treatment efficiency. Hence, changes in solution temperatures, dissolved ozone gas concentration, and particle size distribution due to the application of ultrasound were investigated.

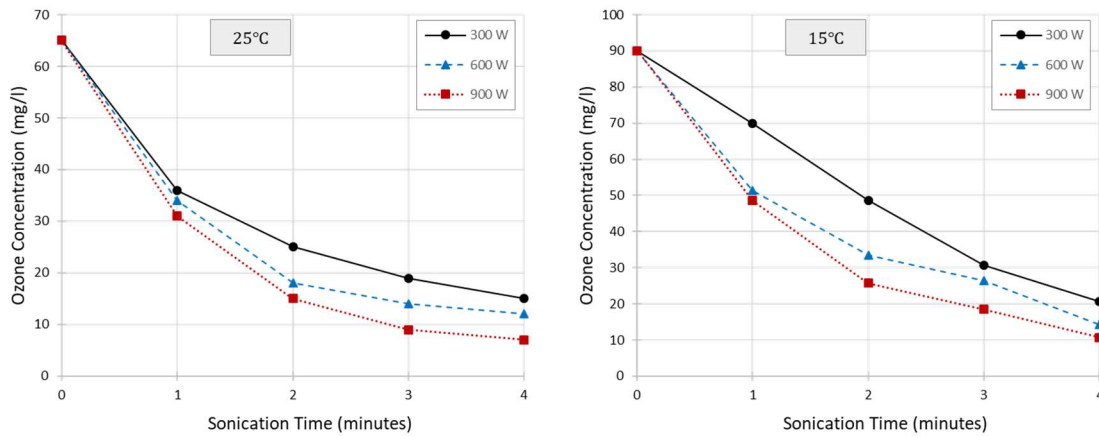
Several tests were conducted to study the variation in temperature and dissolved ozone concentration with the sonication for different power intensities. For that, deionized water was allowed to come to equilibrium with air for 24 hours before the experiments. The sonication performed in a 1000 ml glass beaker for different power levels. Figure 7.4 shows the variation in temperature with sonication time for four different power levels 300, 600, 900, and 1200W. Results showed that an increase in sonication power caused increased rate of change in temperatures. For the highest power level of 1200W test results showed the rate of change in temperature was  $0.04^{\circ}\text{C sec}^{-1}$ . Increased temperature is not beneficial to the selected treatment of using ozone nanobubbles. Also, elevated temperatures are an indication of energy loss during the sonication. However, on the other hand, the elevated temperature will be beneficial for the desorption of contaminants from sediments with increased internal energy of adsorbed contaminant molecules.

Figure 7.5 shows the change in ozone concentration with sonication time for three different power levels 300W, 600W, and 900W for two different time settings at 15°C and 25°C. The results indicated that ozone concentration decreases with increased sonication time and higher power levels. The reduction in ozone concentration is affected by both the elevated temperature and increased microstreaming associated with higher power level ultrasound.



Power (W)	Energy Density ( $W/cm^3$ )	Rate of change in temperature ( $^{\circ}C/s$ )
300	0.3	0.0299
600	0.6	0.0306
900	0.9	0.0347
1200	1.2	0.0399

**Figure 7.4** Temperature variation in water to different ultrasonic power. Source: Batagoda [211], Aluthgun Hewage et.al [72].

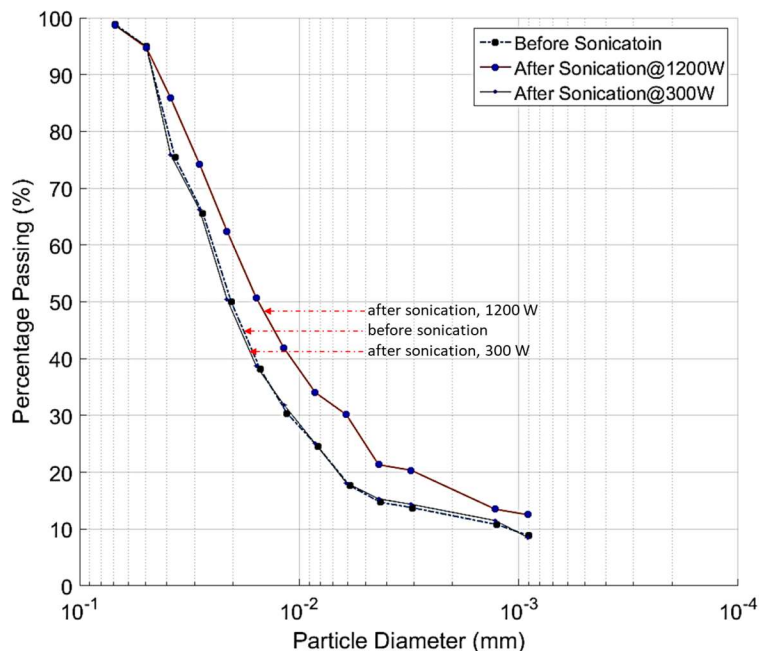


**Figure 7.5** Ozone concentration variation with time for different sonication power levels. Source: Batagoda [211], Aluthgun Hewage et.al [72].

Increment of temperature and reduction in ozone concentrations are the significant facts that should be taken into account when implementing this treatment method because ozone concentration in the solution directly impacts the treatment efficiency. Therefore, optimum treatment conditions required, which would effectively desorb contaminants from sediments and maintain sufficient ozone concentration for effective oxidization. The use of pulse sonication can reduce the increase in temperature or loss of ozone.

#### **7.4.3 Change in the particle size distribution of sediments due to sonication**

The micro-streaming produced during the application of ultrasound is capable of breaking the bonds between sediment and the contaminant, and the same can also shear sediment particles. Hence, the micro-streaming can change the particle size distribution as well as the surface texture of sediment particles. The 80g of sediment sonicated for 100 minutes with 4 minutes pulses and test performed for both the 300W and 1200W power levels in 1000 ml of sediment slurry. Figure 7.6 shows the particle size distribution (based on the hydrometer test) before and after sonication for 300W and 1200W. Figure 7.6 shows that high-intensity ultrasound increases the shearing effects, which explain that the high-power levels would increase the desorption of contaminants from the sediment surface. However, increased power levels cause sediment particles to be sheared and become finer, which can be considered as one limiting factor of the high-power ultrasound in sediment remediation. Finer sediments would take extended time to settle causing delay in overall treatment time of Passaic River.



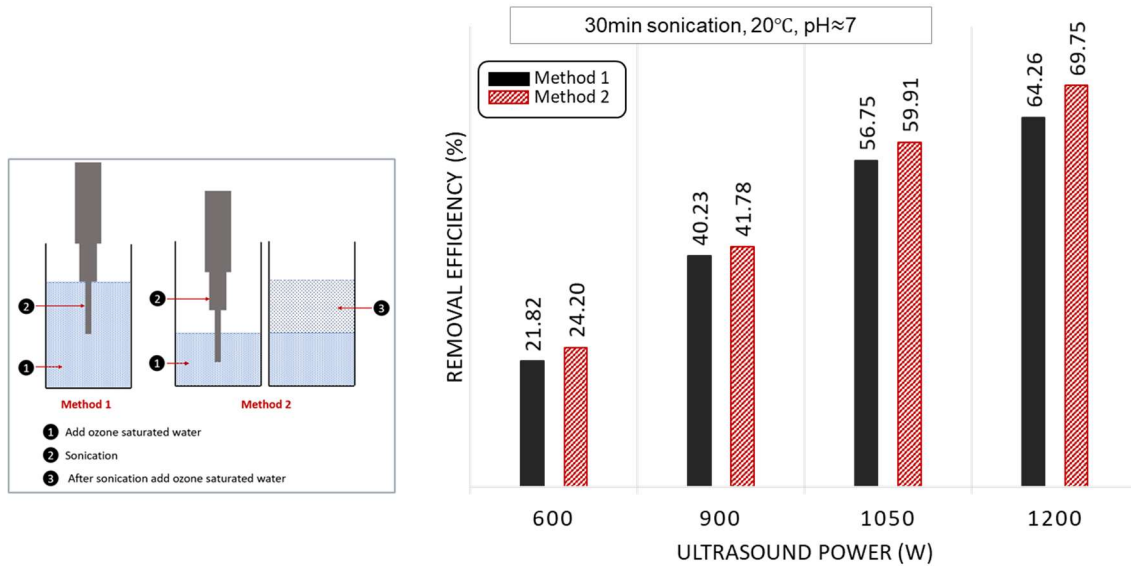
**Figure 7.6** Particle size distribution of sediments with and without sonication. Source: Batagoda [211], Aluthgun Hewage et.al [72].

#### 7.4.4 Remediation of sediment using ultrasound and ozone nanobubbles

Table 7.1 shows the experimental results for two different experiments (Method 1 and Method 2). In Method 1, the treatment chamber filled with 2000ml of ozone nanobubble saturated water and then sonicated. In Method 2, ozone was added to the treatment chamber in two steps. In the first step, 1000 ml ozone water was added, and sonicated (solvent ratio doubled). Then immediately after the sonication, another 1000 ml added. Table 7.1 shows the treatment efficiency for the initial concentration of  $1875 \text{ mgkg}^{-1}$  p-terphenyl contaminated sediments after 30-minute of sonication for four power levels 600 W, 900 W, 1050 W, and 1200 W. Each experiment was repeated to check for repeatability of results. There was a slight variation in the removal efficiency of approximately 0.73% with the same ultrasound power. Figure 7.7 summarizes the obtained average removal efficiencies for different power levels for both Method 1 and Method 2.

**Table 7.1** Impact of Ultrasound Power and Ozone Delivery Method on Treatment Efficiency

Method	Sonication			Concentration (contaminant/sediment)		Removal Efficiency (%)
	Total duration	Power	Power density	Initial	After treatment	
	(minutes)	(W)	(W/cm <sup>3</sup> )	(mg/kg)	(mg/kg)	
1	30	600	0.3	1875	1469.63	21.62
		600	0.3		1462.31	22.01
		900	0.45		1146.38	38.86
		900	0.45		1095.19	41.59
		1050	0.525		801.94	57.23
		1050	0.525		820.13	56.26
		1200	0.6		663.38	64.62
		1200	0.6		677.06	63.89
2	30	600	0.6	1875	1457.81	22.25
		600	0.6		1384.88	26.14
		900	0.9		1102.69	41.19
		900	0.9		1080.75	42.36
		1050	1.05		765.94	59.15
		1050	1.05		737.63	60.66
		1200	1.2		586.69	68.71
		1200	1.2		547.69	70.79

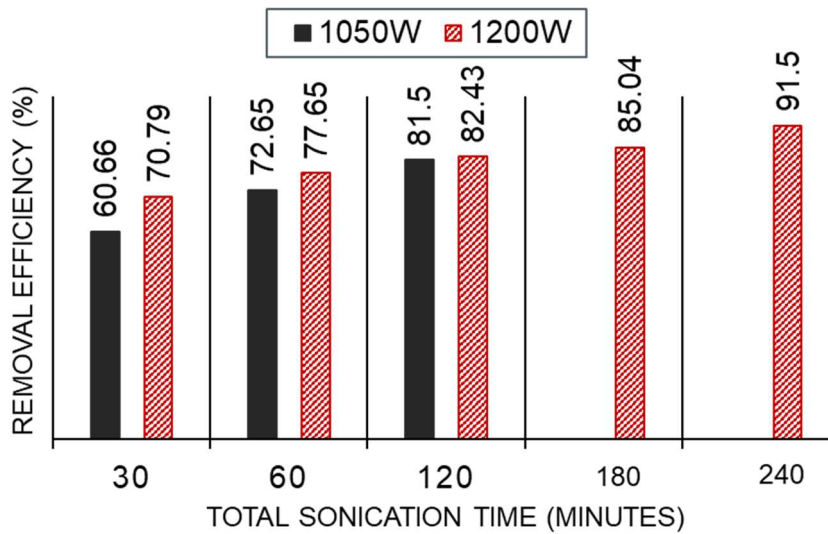


**Figure 7.7** Variation of removal efficiency for different ultrasound power levels.

Table 7.2 shows the contaminant removal efficiency for ultrasound with 1050W and 1200W power for different treatment durations and Figure 7.8. summarizes those results. For all the tests results reported in Table 7.2, ozone was added to the system in two stages (Method 2).

**Table 7.2** Removal Efficiency of P-Terphenyl by Varying the Treatment Duration

Power (W)	Ultrasound		Average ozone concentration (mg/l)	Concentration (contaminant/sediment)		Removal efficiency (%)
	Duration per cycle	Total sonication time		Initial	After treatment	
	(min)	(min)		(mg/kg)	(mg/kg)	
1050	2	30	66.73	1875	737.63	60.66
		60			512.81	72.65
		120			346.88	81.5
1200	2	30	69.2	1875	547.69	70.79
		60			419.06	77.65
		120			329.44	82.43
		180			280.5	85.04
		240			159.38	91.5



**Figure 7.8** Removal efficiency of p-terphenyl by varying the treatment duration.

The prolonged ultrasound treatment substantially reduced the p-terphenyl concentration in the sediment. However, with the longer treatment time, there was breakage of sediment particles, observed through the change in gradation of sediment after treatment. The lengthy treatment time with high ultrasound power also increased the degradation of p-terphenyl in the sediments.

The GC/MS analysis for the treated sediment samples shows the residual p-terphenyl in the treated sediment, and hardly recorded very low concentration (ppb levels) of daughter products. The ultrasound coupled ozone has been fully mineralized the organic p-terphenyl to carbon dioxide and water. According to the GC/MS records, in the wastewater, no p-terphenyl detected and there were tracer concentration of daughter products. The GC/MS results for by-product for treated sediments and for wastewater are included in the supporting materials. The test results indicated that ultrasound application and direct and indirect ozone reactions caused complete oxidation of p-terphenyl molecules. It appears that the broken benzene rings in the p-terphenyl allowed ozone to further oxidize degraded compounds at a faster rate. Hence, exposing contaminated sediments to intense sonication power and ozone nanobubbles for many remediation cycles can remove organic pollutants attached to sediment particles.

The high-power ultrasound produces very high destructive forces that effectively break the bond between sediments and contaminants and allows the pollutants to come into the solution. The ultrasound irradiation to water produces cavitation that can cause contaminant degradation due to both the sono-chemical (radical formation) as well as sono-physical (pyrolysis) effects. Ozone is known to attack the C=C double bond, and the indirect reaction of  $\cdot\text{OH}$  radicals non-selectively attack the organic compound with very



high reaction rates. The ultrasound will cause a reduction in nanobubble concentration and dissolved ozone concentration over time in the solution, however the mass transfer of ozone to water should be increased during ultrasonic irradiation [198].

To investigate the contribution of the use of ozone nanobubbles on removal efficiency, an additional experiment was conducted with only ultrasound and without ozone. Therefore, 80g of p-terphenyl contaminated synthetic sediment sample was placed in the reaction chamber and filled to 2000ml of water (not nano ozone saturated water), and 1200 W of ultrasound applied as 2-minute pulses for 240 minutes of sonication. During all the sonication trials, temperature maintained at 20-30°C by providing enough time to cool the sample and by placing the sediment chamber inside a cold-water bath. After completion of treatment, the chemical analysis showed 76.7% removal efficiency. This is comparatively good treatment efficiency. However, with 91.5% removal efficiency, the proposed method of ultrasound coupled with ozone nanobubbles is a promising technology for sediment remediation.

The removal efficiencies obtained from this research were compared with other studies found in the literature and are summarized in Table 7.3. Table 7.3 shows that when ultrasound combined with other oxidation technologies such as Fenton solution or electrokinetic remediation, comparable removal efficiencies can be obtained. However, if such technologies listed in Table 7.3 are to be implemented as in-situ treatment, they would not be as cost-effective as the proposed technology. The tests reported in this research uses sediment with high contamination concentrations ( $1875 \text{ mgkg}^{-1}$ ) and high fine content (71%). In this research, no chemicals other than ozone (will also revert to  $\text{O}_2$  upon oxidation) was used to achieve a very high treatment efficiency value of 91.7%.

The aged chemicals in soil and sediments would impact biodegradability and Extractability. Organic compounds become increasingly difficult to desorb from soil and sediment over time with chemical aging [214,215]. Therefore, it is very important to evaluate this treatment method to determine the removal efficiency of river sediments obtained from the Lower Passaic River.

### **7.5 Summary and conclusions**

This paper is one of a series of papers that will provide supporting evidence towards the development of an in-situ remediation technology to remediate the heavily contaminated Passaic River sediments using ultrasound and ozone nanobubbles. This study evaluated the performance of the proposed method to remediate the organic pollutants in the sediments. The application of ultrasound kept the sediment in suspension, and it provided the mechanical energy to breaks the bonds between the sediment and the contaminants and release them to the bulk solution. The role of ozone was to degrade the desorbed organic contaminants to intermediate products that are more soluble and benign in the aqueous phase and removed by subsequent treatment and filtration. The ozone gas is to be delivered as nanobubbles to increase the ozone gas dissolution in water and to maintain high ozone concentration in the liquid phase for a long time. A set of laboratory-scale experiments were performed using simulated dredged sediments to identify the impact of sonication time and sonication power with nano ozone in oxidizing PAHs. First, tests were performed to determine the enhancement in ozone delivery to water as nanobubbles. It found that the ozone nanobubbles can deliver higher ozone concentrations to water and can maintain those high ozone concentrations for long periods. Then after the impact of ultrasound on the sediment slurry evaluated, it was found that with the application of ultrasound solution

temperature increased and also under high power levels, sediments became finer. The treatment efficiency ultrasound without nano ozone was 76.7%. The next sets of experiments were performed by applying ultrasound with ozone nanobubbles. In these experiments varying ultrasound power levels and sonication time were applied. Continuous application of ultrasound heated the solution, reducing the amount of ozone available for remediation. Hence, the treatment was performed in 2-minute treatment cycles until the desired sonication time was achieved. Also, treatment efficiency was improved by adding ozone to the system in two stages; before and after sonication. The batch-scale experiments were conducted for different ultrasound power levels and different sonication times to evaluate the removal efficiencies. With the prolonged application of ultrasound with ozone nanobubbles, it was possible to achieve a contaminant removal efficiency of 91.5% for PAH contaminated sediment after a total sonication time of 240 minutes.

**Table 7.3** Review of Different Research Findings: Ultrasound to Remediate Organic Pollutants in Sediment (**Continued**)

#	Condition	Contaminant	Soil type	Sediment weight (g)	Slurry volume (ml)	Sediment/water ratio	Frequency (kHz)	Power (W)	Probe, $\Phi$ (mm)	Treatment time (min)	Treatment efficiency	Reference
1	Ultrasound stand alone	<b>(PAHs):</b> P-terphenyl, 1875mg/kg	Fine: 71% (Clay 26% Silt:45%)	80	2000	1:25	20	1200	191	240	76.7%	<b>This paper</b>
	Ultrasound + Ozone nanobubble											
2	ultrasound + vacuum pressure (15psi) + Surfactant	<b>(PAHs):</b> P-terphenyl, (1875mg/kg)	Sand 2.6% Silt: 4.62% Rock flour: 20.24% Kaolin: 1.45% Rock flour <75 $\mu$ m: 71.09%	-	-	1:15	20	900	-	9min	Coarse Fraction: 99%	Meegoda & Veerawat [216]
			1:50			1200		90min		Fine Fraction: (without surfactant): 55%		
			1:50			1200		60 min		Fine Fraction: (0.1% surfactant concentration) : 89%		
3	Ultrasound Stand alone	<b>(POPs):</b> hexachlorobenzene (HCB), 500mg/kg + phenanthrene (PHE), 500mg/kg	<b>Kaolin</b> Sand:3.9% Silt:20.2% Clay:75.9%	100	300	1:3	30	100	-	60	HCB:29%, PHE:53%	Shrestha et al. [217]
			<b>Synthetic clay</b> Sand:6.8% Silt:62.7% Clay:30.6%					140		60	HCB:10%, PHE:45%	
			<b>Natural clay</b> Sand:39.0% Silt:54.6% Clay:6.3%	100	300	1:3	30	100	60	HCB:48%, PHE:68%		
			140	60	HCB:38%, PHE:65%							
			100	60	HCB:55%, PHE:71%							
				100	300	1:3	30	140	-	60	HCB:43%, PHE:60%	

**Table 7.3 (Continued)** Review of Different Research Findings: Ultrasound to Remediate Organic Pollutants in Sediment

#	Condition	Contaminant	Soil type	Sediment weight (g)	Slurry volume (ml)	Sediment/water ratio	Frequency (kHz)	Power (W)	Probe, $\phi$ (mm)	Treatment time (min)	Treatment efficiency	Reference
4	Ultrasound + Fenton's reaction (H <sub>2</sub> O <sub>2</sub> )	Petroleum hydrocarbons (PHC) in oily sludge	-	1	25	1:25	20	60	-	5	43.1%	Zhang et al. [218]
5	Ultrasound stand alone	Petroleum hydrocarbons (PHC) in sediment	Sediment A: Sand:100% Silt:0% Clay:0%	5	30	1:6	20	600	-	10	22	Li et al. [219]
			Sediment B: Sand:72.4% Silt: 15.9% Clay: 11.7%	5	30	1:6	20	600	-	10	61	
			Sediment C: Sand: 44.7% Silt: 31.8% Clay: 23.5%	5	30	1:6	20	600	-	10	49	
5	Ultrasound stand alone	Total petroleum hydrocarbon (THP), 14362.455 mg/kg	Gravel:5.2% Sand:15.81% Silt:45.46% Clay:33.53%	300	900	1:3	28	220	Plate Transducers	10	55.61	Wulandari & Effendi [220]
							48	220		10	67.09	
6	Ultrasound stand alone	PCB 1260	Sand	-	30	2:3	not mentioned	150	12.5	60	85%	Collings et al. [221]
		PAH	Riverine sediment	-	30	2:3	(assume 20-30)	150	12.5	10	≈49%	
				-	-	2:3		1500	38	5	≈77%	
				-	-	2:3		4000	-	5	≈81%	

**Table 7.3 (Continued)** Review of Different Research Findings: Ultrasound to Remediate Organic Pollutants in Sediment

#	Condition	Contaminant	Soil type	Sediment weight (g)	Slurry volume (ml)	Sediment/water ratio	Frequency (kHz)	Power (W)	Probe, $\Phi$ (mm)	Treatment time (min)	Treatment efficiency	Reference
7	Ultrasound stand-alone (sediment-flushing tests)  (hydraulic gradient: 1.6)	Non-aqueous phase liquid (NAPL) hydrocarbon  (Crisco Pure Vegetable Oil)	<b>Ottawa Sand (USCS-SP)</b> Max particle size: 0.8mm Cu:1.85 D10:0.27mm D50:0.45mm e = 0.67	-	-	-	20	50	-	-	37	Kim & Wang [222]
								100	-	-	45	
								140	-	-	43	
8	Ultrasound stand alone	DDT (250ppm)	In Sand	200	200	1:1	20	170	12.5	10	70%	Mason et al. [223]
		PCB (250 ppm)								30	74%	
		PAH (250 ppm)								25	70%	
		PAH (250 ppm)								60	85%	
9	Ultrasound + Fenton-type catalyst (FeSO <sub>4</sub> ) + H <sub>2</sub> O <sub>2</sub> (10 wt.%)	Toluene + Xylenes	Sediment	20	40	1:2	47	147	Ultrasonic bath	10	Toluene: 96% Xylenes: 80%	Flores et al. [224]
10	Electrokinetic (EK) + Ultrasound (sediment flushing tests) (hydraulic gradient: 0)	<b>heavy metal + (PAH)</b>  Pb (500 mg/kg) + phenanthrene (500mg/kg)	<b>Natural clay</b> finer #200 sieve < 90%  (USCS - CL)	-	-	-	30	<b>US: 200W</b>  electric current: <b>50mA</b> for EK test	-	<b>360 hr.</b>	<b>For Pb:</b> EK: 88% EK+US:91%  <b>For PAH:</b> EK: 85% EK+US:90%	Chung & Kamon [225]

## CHAPTER 8

# REMEDIATION OF CONTAMINATED SEDIMENTS CONTAINING BOTH ORGANIC AND INORGANIC CHEMICALS USING ULTRASOUND AND OZONE NANOBUBBLES

### 8.1 Introduction

#### 8.1.1 Background

Most river and lake sediments worldwide are contaminated by organic and inorganic pollutants [226]. River sediments act as a sink or reservoir for industrial, agricultural, or other sources of waste releases and are subject to sediment contamination [227]. The United States Environmental Protection Agency (USEPA) stated that sediments are a common cause of contamination of freshwater bodies, and these contaminated sediments cause environmental damage accounting for over \$16 billion per year [228].

The lower Passaic River, NJ, USA, has been identified as being heavily contaminated with organic and inorganic chemicals due to a century of industrial activity and development [229]. Sediments were found to contain dioxins and furans, polychlorinated biphenyls (PCBs), DDT, dieldrin, polycyclic aromatic hydrocarbons (PAHs), and heavy metals such as lead, mercury, copper, and chromium [229]. Those contaminants can cause public and environmental health risks for communities along the river. The USEPA has declared the lower Passaic River as a Superfund site [230]. In 2014, the USEPA proposed an ex-situ remediation plan consisting of mechanical dredging, dewatering, and secure disposal for the lower Passaic River's contaminated soils.

There is limited research on remediation methods to treat soils/sediments contaminated with both organic and inorganic contaminants. Mostly, evaluation of soil/sediment treatment methods has addressed individual contaminants and not both types.

Due to the significant difference between the environmental, chemical, and physical behavior of heavy metals and organic pollutants in sediments, finding an alternative remediation method for treating both types of contaminants poses a significant challenge. The USEPA has summarized the in-situ treatment technologies applications for contaminant classes and it shows the effectiveness of different treatment methods for different independent contaminant types [183] but not for combined organic and inorganic contaminants.

This research develops an alternative, novel, and emerging in situ remediation method that can remediate heavily contaminated sediments by the combined effects of ultrasound, ozone, and nanobubbles. This manuscript presents the third stage of the experiment series. In the first two stages, the treatment method was evaluated for a single contaminant in the sediment [72,73].

### **8.1.2 Hypothesis**

The ex-situ treatment methods are not always feasible, requiring the low-cost in-situ treatment alternatives that can remediate the contaminated sediments. Sediments are found to be contaminated by various chemical compounds that require viable treatment methods with the capacity to treat both the organic and inorganic compounds simultaneously. There are fewer studies on sediment remediation for the mixture of organic and inorganic contaminants than single contaminant types (organic or inorganic). It is hypothesized that the treatment of sediments containing both organic and inorganic contaminants would not substantially reduced compared to the treatment efficiencies of organic or inorganic contaminants due to interactions.



### **8.1.3 Research objectives**

The sediment contaminated by organic p-terphenyl and inorganic chromium used to evaluate the proposed treatment method. Therefore, the prepared contaminated sediment was treated with ultrasound and ozone nanobubbles under different operating conditions to obtain optimal treatment efficiency under laboratory conditions.

## **8.2 The Development of The Treatment Method**

A contamination treatment is expected to destroy, remove, immobilize, isolate, or detoxify the contaminants [231]. The treatment methods can be divided into two categories, in-situ and ex-situ treatment techniques. In general, in-situ treatment methods have significant cost benefits compared to ex-situ methods, but ex-situ treatment methods have higher treatment efficiency. However, for larger contaminated sites, in-situ remediation methods are more viable concerning cost and socioeconomic impact on the region [232].

### **8.2.1 In-situ treatment technologies**

Although many treatment methods are available for in-situ soil treatment, selecting a suitable treatment method depends on site characteristics, treatment cost, specific objectives, required levels of treatment, and external environmental impacts. In-situ treatment can be mainly divided into five categories [183,232]; (1) physical, (2) chemical, (3) biological, (4) thermal, and (5) combined. For the lower Passaic River, a sediment treatment method at the bottom of the river is needed. Hence, most of the above treatments are inapplicable, leaving chemical oxidation as the only feasible option. Consequently, an appropriate oxidizer should be selected that can treat both organic and inorganic contaminants.

**8.2.1.1 Selection of an oxidizing agent.** Chemical oxidation is one of the promising treatment methods that has been utilized to treat both organic and inorganic pollutants. It has the capability of not only destroying contaminants but also reducing their toxicity. However, depending on the chemical condition, the toxicity can increase or decrease with chemical oxidation [233]. The most commonly used oxidizing agents are ozone, hydrogen peroxide, hypo-chlorites, chlorine, permanganate, and chlorine dioxide [234,235]. Also, advanced oxidation processes (AOPs) which involve the use of hydroxyl radicals  $OH^\bullet$  (oxidation potential, 2.80 V) have been widely investigated by researchers in recent years as an effective oxidizing agent.

For this research, ozone is selected as the oxidizing agent because it has many advantages over other oxidizers. Most of the oxidizers listed earlier are either too costly, localized, have a very short half-life, or are new technologies that are not well established. Moreover, ozonation can also be considered as an AOP in soil treatment processes as it involves the formation of  $OH^\bullet$  radicals due to the indirect reactions formed by the degradation of ozone.

**8.2.1.2 Ozone as an oxidizer.** Ozone reacts readily with organic and inorganic substances [236]. It is a powerful oxidant that has been used in the chemical industry. Ozone has one of the highest oxidation potentials of any substance (2.07 V), exceeded only by fluorine (2.87 V), hydroxyl radicals (2.86 V), and oxygen atoms (2.34 V) [237]. Ozone treatment includes direct and indirect reactions [238,239]. Indirect oxidation is due to the disintegration of ozone in water to  $OH^\bullet$  radicals [40]. With the formation of  $OH^\bullet$  radicals, successive reaction chains are created that yield  $H_2O_2$  and  $OH^\bullet$ , among other radicals [40,206]. Many factors control the stability and half-life of aqueous ozone. They include ozone concentration, temperature, pH, hydroxyl radicals, motion or dynamics of the liquid,

and the availability of organic and inorganic substances [40]. The stability (i.e., contact time), ozone concentration, and hydroxyl radical formation are essential factors that control the oxidation's efficiency. The solubility of ozone in water is relatively low, so ozone delivery to the aqueous solution can be improved using ozone nanobubbles [70].

**8.2.1.3 Application of nanobubbles.** In general, bubbles are defined based on their size (diameter); macro-bubbles ( $>100\ \mu\text{m}$ ), micro-bubbles ( $1\ \mu\text{m}$  to  $100\ \mu\text{m}$ ), and nanobubbles ( $<1\ \mu\text{m}$ ) [2]. Nanobubbles have a diameter smaller than  $200\ \text{nm}$  [3,4,9]. The industrial application of nanobubble technology has exponentially increased over the past two decades due to their long-term stability and reactivity [5,6]. Due to their extremely small size, high internal pressures, high specific area, and long stagnation times, they have improved the mass transport from gases to liquids. Nanobubbles have an electrically charged interface and facilitate the physical adsorption, expediting the chemical reactions at the gas-liquid interface compared to ordinary and microbubbles [9,70]. Further, the surface charges reduce bubble coalescence and improve bubble stability due to electrostatic repulsion [151,167].

However, in order to have contact between the soil contaminant and the ozone nanobubbles, the soil needs to be in a suspension, and contaminants must be desorbed from the sediments. The ultrasound can produce such desorption of contaminants from the sediments and maintain the sediment in suspension.

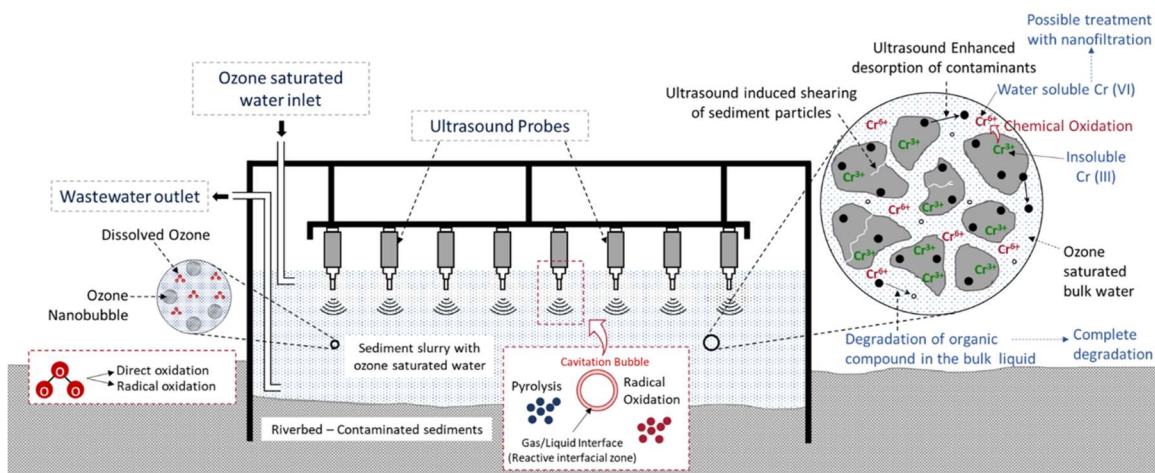
**8.2.1.4 Application of ultrasound.** In this research, the ultrasound's primary purpose is to agitate the soil, keep the soil in suspension, and desorb the sediments' contaminant. Depending on the applied ultrasound's power and frequency, it can break the bonds between the soil and the contaminants via shearing. This shearing force is developed by a

phenomenon known as acoustic cavitation. During the cavitation process, the bubble obtains an ample amount of potential energy from the sound wave. This energy concentrates as kinetic energy when a bubble implosion can erode solids, initiate chemical reactions, and produce radicals [39]. Therefore, the sonication is a combination of sonochemical and sonophysical effects. The chemical effects occur due to the localized high temperatures and pressures at the cavity implosion. This results in the thermolysis of chemicals and the formation of radicals such as  $OH^\bullet$  and  $H^\bullet$  [240]. The sono-physical effects, such as shock waves produced by the bubbles' cavitation, result in turbulent fluid movements and a higher microscale velocity gradient in the cavitation vicinity [241]. The shock waves can break particles and macromolecules; for macromolecules, this is referred to as shear degradation by ultrasound.

The yield of sonication treatment of soil depends on ultrasonic waves, soil, and contaminant properties. The power and frequency control the applied ultrasonic waves. A higher power intensity leads to higher acoustic pressures (amplitude and vibration), more significant cavitation, and violent cavitation collapses. Compared to higher frequencies of ultrasound, low-frequency ultrasound has a lower number of bubbles, larger resonant bubble size, and more violent bubble collapse [241]. Typically, low-frequency ultrasound has strong sono-physical effects compared to high-frequency ultrasound. High-frequency ultrasound promotes more sonochemical reactions due to increased cavitation bubble events and the associated formation of  $OH^\bullet$  radicals.

The purpose of ultrasound in this research is to aid the mechanical agitation and desorption of contaminants from the soil particles. Accordingly, low frequency (20kHz) ultrasound with optimum power levels was selected for this treatment process.

**8.2.1.5 In-situ treatment method.** Details of the proposed in-situ treatment method are explained in previous publications [72–74]. The proposed in-situ treatment device is depicted in Figure 8.1 for field implementation.



**Figure 8.1** Sketch of the sediment treatment chamber for field implementation.

### 8.3 Materials and Methods

#### 8.3.1 Soil preparation and contamination

The sediments from the Passaic River contain many different organic and inorganic contaminants. To evaluate the treatment process and to optimize, a controlled environment is needed. Therefore, it was decided to use synthetic sediments contaminated with one organic and one inorganic compound.

##### 8.3.1.1 Preparation of synthetic soil.

The synthetic soil was prepared based on the actual size distribution of Passaic River sediments. The particle size distribution of synthetic soil and the dredged river sediment sample can be found [72,73,211]. Based on the Passaic River sediments' average size distribution, there was 15% clay and 62% silt

content, yielding a total fine fraction of 77%. A laboratory soil mixture consisting of kaolin, silt, rock flour, and fine sand was used to prepare the synthetic soil.

**8.3.1.2 Organic contaminant.** P-terphenyl ( $C_{18}H_{14}$ ) was selected to represent the organic contaminant. This compound was selected to mimic the properties of PAH contamination as it has lower toxicity and less hazardous, a consideration that ensured the safety of the research environment. The appropriateness of the selection of p-terphenyl to represent PAH has been explained [72]. The p-terphenyl is a white or light-yellow compound that appears in the form of needles. It has a molecular weight of 230.31 g/mol, a melting point of 213 °C, a boiling point of 376 °C, and is insoluble in water. When compared, PAHs have molecular weights of 152.21-276.34 g/mol, melting points of 93-278 °C, and boiling points of 270-496 °C.

**8.3.1.3 Inorganic contaminant (heavy metal).** Chromium was selected as a representative heavy metal contaminant as it is one of the most challenging metal contaminants to decontaminate. Lin and Chen showed the ability to adsorb heavy metals into sediments increased in the order  $Zn < Pb < Cu < Cr$ , and adsorbed Chromium in sediments were much higher than that of the other metals [242]. Hence, Chromium facilitates the understanding of the applicability of the proposed technology and to extrapolate the possibility of removing other metal contaminants, which are comparatively easier to remove than chromium.

Chromium is present in many forms, yet there are two primary stable chromium forms: trivalent and hexavalent chromium. It should also be noted that trivalent chromium is not water-soluble, while hexavalent chromium is water-soluble over the full range of pH

values [243]. Even though the trivalent chromium is not water-soluble, its sorption properties cause it to seep into the soil and contaminate [243].

Hence, in this research, trivalent chromium was used to represent heavy metal contaminants. The treatment protocol proceeds as follows. The desorption of contaminants from the soil occurs due to the application of ultrasound. The ozone oxidized the contaminant in the solution, allowing the trivalent chromium to become hexavalent, thereby becoming soluble in water and easier to remove from the soil water mixture with nanofiltration. However, Chromium (VI) has to be carefully handled as it is 100 times more toxic than Chromium (III). Chromium (VI) is included in the list of class "A" human carcinogens by the USEPA [244–246]. It was also found that chromium in clay is immobile and stable, which requires substantial energy for decontamination [212].

### **8.3.2 Preparation of contaminated sediments**

In order to prepare contaminated sediments, 80 g of synthetic soil was mixed with 1g of  $CrCl_3 \cdot 6H_2O$ . Later on, the chromium-contaminated dry soil was mixed with 0.15 g of p-terphenyl. The following section described soil preparation.

A 1.0 g of  $CrCl_3 \cdot 6H_2O$  was dissolved in 50 ml of deionized (DI) water. This solution was then mixed with the 80 g of synthetic soil for one hour using a mechanical mixer. The sample was placed in an oven at 40 °C for 24 hours to evaporate water. This sample was then kept in a high-temperature oven at 800 °C for three hours under an oxygen-free environment (under the nitrogen gas supply) to create adsorption of the proper bond between soil and the chromium. The oxygen-free environment was maintained to ensure that the chromium would not become oxidized during heating. After 3 hours, the oven was

turned off, but the nitrogen gas supply was maintained until the samples reached room temperature.

The chromium contaminated soil is then mixed with p-terphenyl. In order to do so, 0.15 g of p-terphenyl was measured and dissolved in 50 ml of acetone (certified ACS reagent grade with  $\geq 99.5\%$  purity) for two hours to ensure complete dissolution. The previously prepared 80 g of chromium-contaminated soil was then mixed with the p-terphenyl solution for another 2 hours until the acetone evaporated and p-terphenyl was absorbed into the soil matrix. This sample was then further mixed to ensure the even distribution of contaminants. The thoroughly contaminated soil was air-dried for 24 hours before use.

According to the previous tests with the single contaminant condition [72,73], most of the suspended ozone was utilized. Therefore, theoretically, with two contaminants in the soil, the ozone concentration demand will be doubled. However, with the solubility limit of ozone nanobubbles, such ozone concentration demand might not be possible. Then, for selected experiments, contaminant concentration was reduced to 1/2 or 1/3 of the values mentioned above (1 g of Chromium and 0.15 g of p-terphenyl in 80 g of soil).

#### **8.4 Experimental Setup**

The main experimental setup can be classified into six stages: (1) preparation of synthetic sediment, (2) sediment contamination, (3) ozone nanobubble generation, (4) soil treatment using ozone nanobubbles and ultrasound, (5) chemical analysis, and (6) data processing to calculate the removal efficiencies. This treatment process adopted in this research is shown in Figure 8.2.



### 8.4.1 Generation of ozone nanobubbles

Nanobubbles were generated in a 25 L container filled up to 18 L. Hydrodynamic cavitation method used to generate ozone nanobubbles. The BT-50FR micro-nano-sized nozzle was used to form nanobubbles, and a 55 psi water pump circulating the water through the nozzle. In the nozzle, water was pumped into the nozzle in a tangential direction to form a swirled flow inside the vessel. This generated a flume of micro and nanobubbles in water. Nanobubbles were generated for 6 minutes, while ozone gas was supplied. Ozone gas was produced by passing the oxygen gas (provided by the compressed gas cylinders with regulators) through an Ozonator (A2Z Ozone MP - 3000 Multipurpose Ozone Generator). The nanobubble generation setup details can be found [72,73].

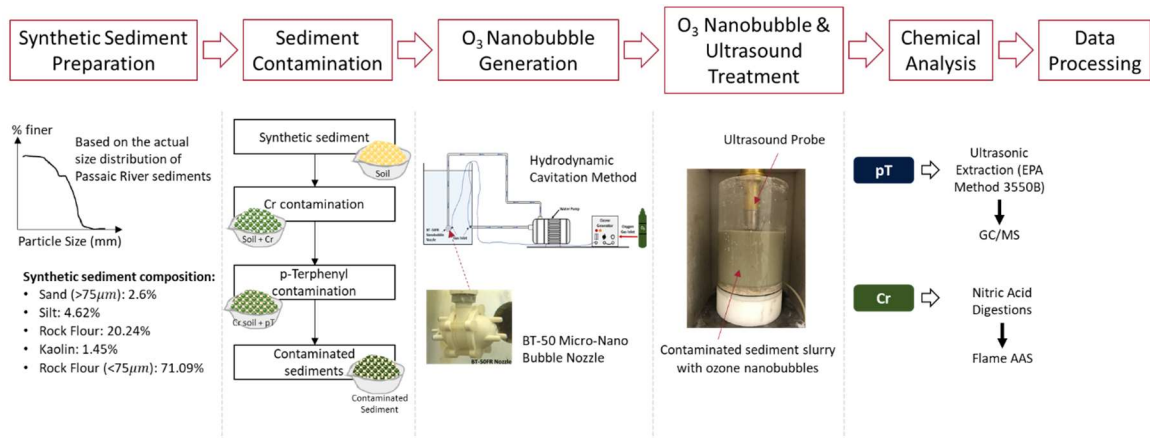
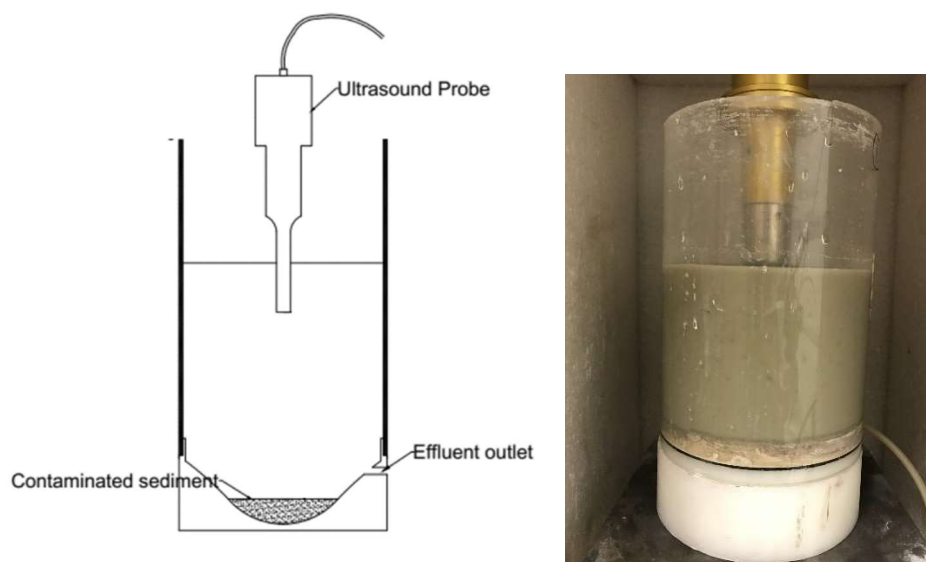


Figure 8.2 Schematic flow diagram of the experimental procedure.

### 8.4.2 Treatment of sediments using ozone nanobubbles and ultrasound

The prepared contaminated sediments were placed in the treatment chamber. The chamber was constructed using high-density polycarbonate (transparent) shell walls and a high-density polyethylene base, as shown in Figure 8.3. The total volume of the chamber was

3.5 L. The base of the chamber was designed in a cone shape to enable the sediments to settle and accumulate at the bottom of the chamber. The outlet for the effluent wastewater was placed at a height above the level of accumulated soil. This minimized the probability of losing sediments. However, the effluent water was collected into another bucket and allowed to settle for 24 hours before disposal. This ensured that any soil swept into the effluent stream could be returned to the treatment chamber.



**Figure 8.3** Contaminated sediment treatment chamber.

After placing the contaminated soil in the treatment chamber, the nanobubble water was filled to half of the chamber's height. The ultrasound was then applied for the specified time (i.e., 2min, 3min, or 4min, depending on the selected experiment). The probe-typed ultrasound source used in this research had a 1.91 cm tip diameter (Sonic & Materials, Inc., Model Vibracell VC-1500, 240 V, Power 1500 W, and Frequency 20 kHz). Based on the previous experience with optimum power levels, 1200 W was selected for all experiments conducted in this research. At the end of the ultrasound application, the chamber's full height is filled with nanobubble-saturated water.

The stepwise application of nanobubbles was utilized because high temperatures caused by the application of ultrasound led to faster ozone depletion, and the higher speed of stirring/movement in the ozone solution resulted in faster decomposition. Thus, both these factors caused a reduction in the efficiency of the oxidation. Therefore, the addition of ozone nanobubbles water to the treatment chamber was carried out in two stages. The first half involved the filling of the chamber and the application of ultrasound to suspend the soil and to desorb contaminants. The second half involved the addition of ozone nanobubbles to facilitate oxidation. Then, the soil was allowed to settle, and the effluent was drained from the treatment chamber. This treatment scheme was repeated until the desired time of ultrasound application, and ozonation was achieved.

At the end of the treatment, sediments were collected in a porcelain container and placed in a temperature-controlled oven at 40 °C until the soil to be completely dried. The soil was then allowed to reach room temperature and air-dried for another 24 hours before chemical analyses were performed to determine the removal efficiency.

### **8.4.3 Chemical analysis**

The soil's chemical analysis was a two-step procedure as soil treatment was conducted for organic and inorganic contaminants.

**8.4.3.1 Chemical analysis of p-terphenyl.** The USEPA method 3550B [247] was used to extract p-terphenyl. Solvent extraction was used to isolate contaminants using enhanced ultrasound in acetone. Accordingly, 20 g of the treated sediment and 100 mL of acetone were mixed in a 250mL beaker. Sonication was performed in short, 5-second bursts using a 300 W horn-type ultrasound transducer. Short bursts protected the sample from changing in chemical composition, and sudden temperature increases. After 10 cycles of sonication,

the sample was filtered and collected in a clean 200 mL flask. Then, another cycle of extraction was performed using another 100 mL of acetone to ensure the complete extraction of contaminants, and the resulting slurry was added to the previously collected sample. The collected 200 mL sample was concentrated using a Kuderna-Danish triple ball concentration column to a volume of 10 mL. The resulting concentrated organic material and acetone were analyzed using gas chromatography with mass spectrometry (GC/MS - Agilent 5973N) to obtain the contaminant concentration and compute the removal efficiency.

**8.4.3.2 Chemical analysis of chromium.** The heavy metal (Cr) was extracted from 1.0 g of treated dry sediment for the chemical analysis. The 1.0 g sample was digested with 10 mL of trace metal-grade nitric acid (67% to 70% w/w). The acid-soil mixture was then heated to 80 °C until the soil sample was completely dissolved in the acid. Then, by adding 990 mL of DI water, this acid-soil solution was diluted. The diluted solutions were tested using flame atomic absorption spectrometry (AAS - Perkin Elmer AAnalyst 400) to determine the total element chromium concentration and treatment efficiency.

## **8.5 Results and Discussion**

### **8.5.1 Size of ozone nanobubbles, zeta potential, and dissolved gas concentration**

The determination of chemical and physical characteristics is essential for the successful application of ozone nanobubbles. Consequently, the generated ozone nanobubbles were tested for size distribution and the zeta potential values. Figure 8.4 shows the (a) size distribution and (b) zeta potential values of 48 nanobubble samples obtained over 24 different bubble generations with two duplicates. Those measurements were taken 20

minutes after nanobubble generation. During the bubble generation, the bubble solution's temperature was increased by an average of  $3.06 \pm 0.34$  °C, where the initial was 20 °C.

Figure 8.4(a) shows a positively skewed cumulative average size distribution graph, indicating that 75% of the generated bubbles were smaller than 122 nm in diameter. The median of the distribution was 68.1nm. In general, the size distribution of the bubbles was recorded between 30-300 nm. Treatment efficiency is directly related to the amount of ozone delivered to the system and the ozone solution's half-life. Based on these factors, the size of the bubble plays a vital role. Smaller bubbles have increased stability by experiencing a lower buoyancy force, which prevents faster upward movements. Furthermore, smaller bubbles have a higher specific surface area and a larger contact area to react with the pollutants. The nanobubbles have high internal gas pressures, which increases gas diffusion and ozone concentrations at the bubble-liquid interface.

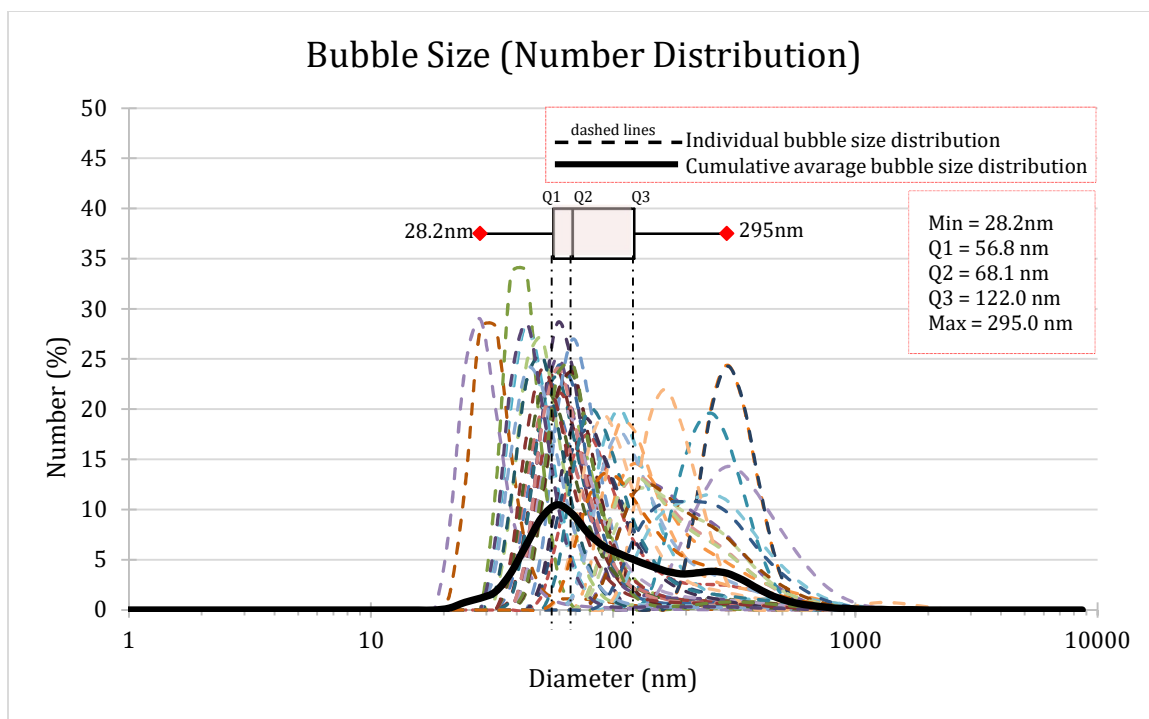
Another critical factor that influences the stability of the nanobubbles is zeta potential. Nanobubbles with high zeta potentials values prevent the bubbles from merging due to repulsive electrostatic forces. Figure 8.4(b) shows the measured zeta potential values and the average zeta potential, recorded as -22.77 mV. Higher zeta potential would reduce the internal gas pressure to balance the surface tension and increase the nanobubbles' life span [151].

### **8.5.2 Treatment efficiencies of contaminated sediments**

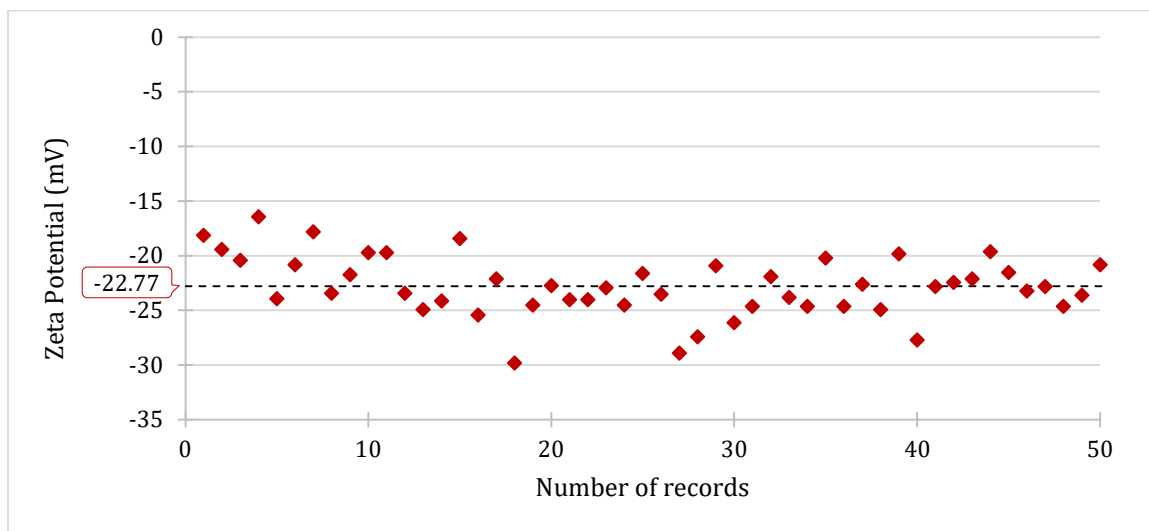
Table 7.1 describes the experimental parameters and the obtained removal efficiencies. Test IDs O<sub>1</sub> and O<sub>2</sub> show the optimum test results from a previous study where removal efficiencies of 91.5% and 97.5% were obtained for p-terphenyl and chromium, respectively, when there was a single contaminant. Test IDs from N<sub>1</sub> to N<sub>13</sub> were performed

with combined chromium and p-terphenyl and tested under different experimental conditions. For each experiment, samples were analyzed 2 times for p-terphenyl using GC/MS and 3 times for chromium using AAS. The relative errors in measurements were minimal, as shown in Table 7.1, with standard deviation for chromium was  $\pm 1$  mg/kg and for p-terphenyl was  $\pm 4$  mg/kg. The recovery of p-terphenyl extracted from sediment was  $86 \pm 1\%$ , and for chromium, it was  $93 \pm 1\%$ .

Figure 8.5a and 8.5b show Test ID  $N_1$  to  $N_{13}$  tests conditions and treatment efficiencies. Figure 8.5a shows the initial chromium and p-terphenyl concentration and removal efficiencies for each test. Further, it shows the relative contamination levels compared to each test performed in  $N_1$  to  $N_{13}$ . Figure 8.5b shows removal efficiencies for both chromium and p-terphenyl and the average for Test  $O_1$ ,  $O_2$ , and  $N_1$  to  $N_{13}$ . It also indicates ultrasound energy densities for each test and the number of treatment cycles performed.



(a)



(b)

**Figure 8.4** The characteristics of ozone nanobubbles generated at 20 °C and pH≈7 (a) size distribution, (b) zeta potential (48 nanobubble samples obtained over 24 different bubble generations with two duplicates).

**Table 8.1 Summary of Results (Continued)**

Test #	Sonication Parameters (20kHz, 1200W)					Amount of Total Ozone water used (L)	Contaminant Type	Concentration (contaminant/soil)			Removal Efficiency	
	Time duration		Total (Min)	Volume/ cycle (L)	Energy Density (J/ml)			Initial (mg/kg)	Residual (mg/kg)	Removal (mg/kg)	For Individual Contaminant (%)	Total Average (%)
	Per cycle (Min)	No of cycle #										
O <sub>1</sub>	1	-	240	2	72	300	Cr	-	-	-	-	91.5
	2	120										
	3	-										
	4	-										
	<b>Total</b>	<b>120</b>										
O <sub>2</sub>	1	-	240	2	72	300	Cr	3253	81	3172	97.5	97.5
	2	120										
	3	-										
	4	-										
	<b>Total</b>	<b>120</b>										
N <sub>1</sub>	1	-	240	2.5	57.6	300	Cr	4211	1242±20	2969	70.5	61.65
	2	120										
	3	-										
	4	-										
	<b>Total</b>	<b>120</b>										
N <sub>2</sub>	1	-	240	2.5	57.6	300	Cr	4211	1209±30	3002	71.3	61.75
	2	120										
	3	-										
	4	-										
	<b>Total</b>	<b>120</b>										
N <sub>3</sub>	1	-	240	2	72	300	Cr	4211	1284±12	2927	69.5	70.9
	2	120										
	3	-										
	4	-										
	<b>Total</b>	<b>120</b>										
	1	-	240	2	72	300	P-terphenyl	1875	159	1716	91.5	91.5
	2	120										
	3	-										
	4	-										
	<b>Total</b>	<b>120</b>										



**Table 8.1 (Continued)** Summary of Results

Test #	Sonication Parameters (20kHz, 1200W)					Amount of Total Ozone water used (L)	Contaminant Type	Concentration (contaminant/soil)			Removal Efficiency	
	Time duration			Volume/ cycle (L)	Energy Density (J/ml)			Initial (mg/kg)	Residual (mg/kg)	Removal (mg/kg)	For Individual Contaminant (%)	Total Average (%)
	Per cycle (Min)	No of cycle #	Total (Min)									
N <sub>4</sub>	1	-	424	2	127.2	300	Cr	4211	1108±22	3103	73.7	78.2
	2	-										
	3	56					P-terphenyl	1875	324	1551	82.7	
	4	64										
	<b>Total</b>	<b>120</b>										
N <sub>5</sub>	1	20	320	2	96	300	Cr	2106	495±11	1610	76.5	75.05
	2	-										
	3	100					P-terphenyl	937.5	238±10	699.5	74.7	
	4	-										
	<b>Total</b>	<b>120</b>										
N <sub>6</sub>	1	53	262	2	78.75	320	Cr	1840	354±9	1486	80.8	73
	2	25										
	3	23					P-terphenyl	937.5	326	611.5	65.2	
	4	27										
	<b>Total</b>	<b>128</b>										
N <sub>7</sub>	1	53	262	2	78.75	320	Cr	1227	157±14	1070	87.2	69.25
	2	25										
	3	23					P-terphenyl	625	304	321	51.3	
	4	27										
	<b>Total</b>	<b>128</b>										
N <sub>8</sub>	1	0	300	2.5	57.6	375	Cr	4211	965±34	3246	77.1	75.2
	2	150										
	3	0					P-terphenyl	1875	492±4	1383	73.8	
	4	0										
	<b>Total</b>	<b>150</b>										

**Table 8.1 (Continued)** Summary of Results

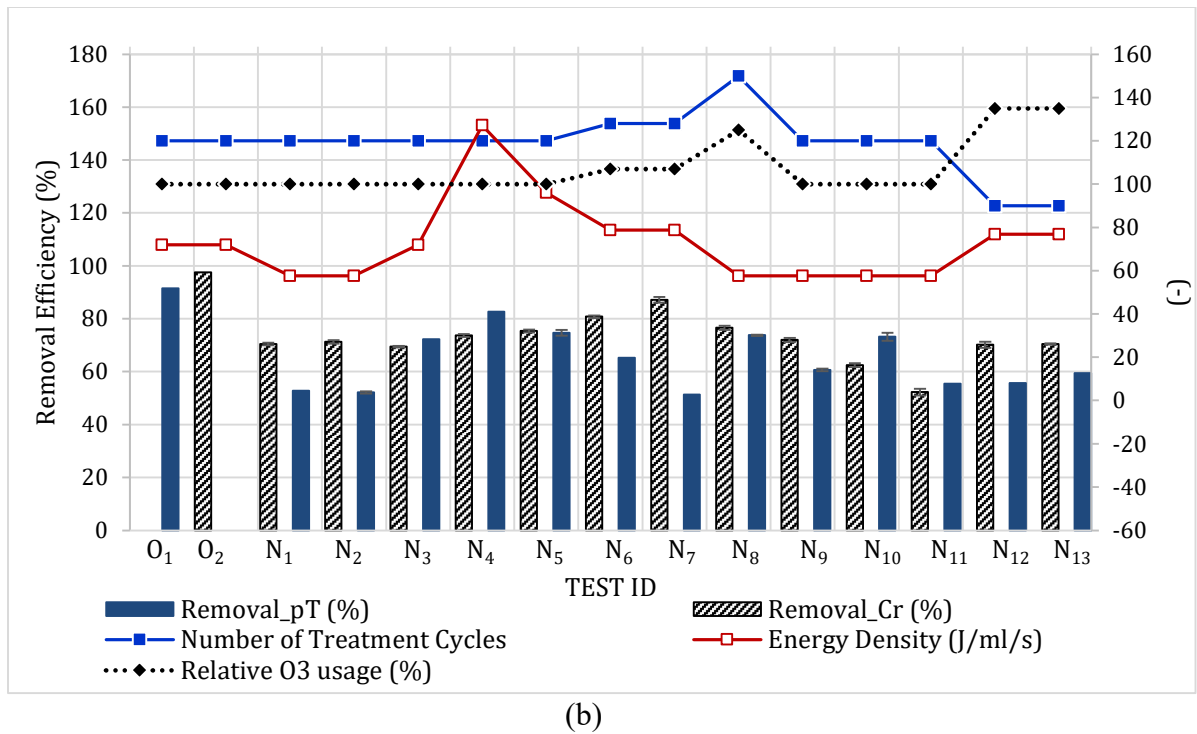
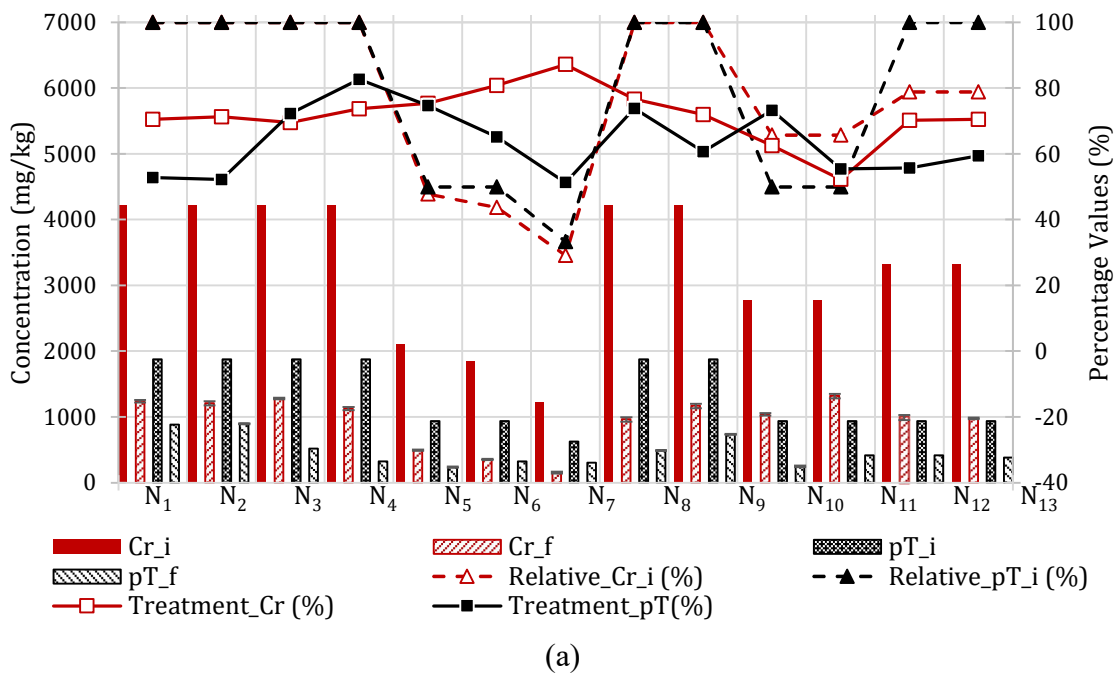
Test #	Sonication Parameters (20kHz, 1200W)					Amount of Total Ozone water used (L)	Contaminant Type	Concentration (contaminant/soil)			Removal Efficiency	
	Time duration			Volume/ cycle (L)	Energy Density (J/ml)			Initial (mg/kg)	Residual (mg/kg)	Removal (mg/kg)	For Individual Contaminant (%)	Total Average (%)
	Per cycle (Min)	No of cycle #	Total (Min)									
N <sub>9</sub>	1	0	240	2.5	57.6	300	Cr	4211	1168±33	3032	72.0	66.35
	2	120										
	3	0					P-terphenyl	1875	737±9	1138	60.7	
	4	0										
	<b>Total</b>	<b>120</b>										
N <sub>10</sub>	1	0	240	2.5	57.6	300	Cr	2770	1040±19	1730	62.5	67.85
	2	120										
	3	0					P-terphenyl	937.5	251±14	686.5	73.2	
	4	0										
	<b>Total</b>	<b>120</b>										
N <sub>11</sub>	1	0	240	2.5	57.6	300	Cr	2770	1320±34	1450	52.3	53.85
	2	120										
	3	0					P-terphenyl	937.5	418.5	519	55.4	
	4	0										
	<b>Total</b>	<b>120</b>										
N <sub>12</sub>	1	0	240	2.5	76.8	405	Cr	3323	991±38	2332	70.2	62.95
	2	60										
	3	0					P-terphenyl	1875	830	1045	55.7	
	4	30										
	<b>Total</b>	<b>90</b>										
N <sub>13</sub>	1	0	240	2.5	76.8	405	Cr	3323	980±10	2343	70.5	64.95
	2	60										
	3	0					P-terphenyl	1875	761	1114	59.4	
	4	30										
	<b>Total</b>	<b>90</b>										

Figure 8.6 illustrates selected tests with a similar contaminant concentration. It shows that higher ultrasound energy density and the number of treatment cycles improves the overall treatment efficiency. However, it is very clear from Figure 8.6 that p-terphenyl removal efficiencies are highly dependent on the sonication energy. It shows that the highest removal efficiency of p-terphenyl was 82.7% with 127.2 J/ml energy density. Simultaneously, for Tests N<sub>1</sub>, N<sub>2</sub>, and N<sub>9</sub>, all had similar conditions ( $E_v$ : 57.6 J/ml, No. of cycles: 120, and relative ozone usage 100%), yet Test N<sub>9</sub> shows relatively better performance. This improved performance can be attributed to the direct impact of the ultrasound probe with the sediments caused by moving the sediment chamber throughout the sonication cycles. For the chromium removal efficiency, the increased energy density had minimal impact, but the increased number of treatment cycles and ozone usage did improve the treatment of chromium.

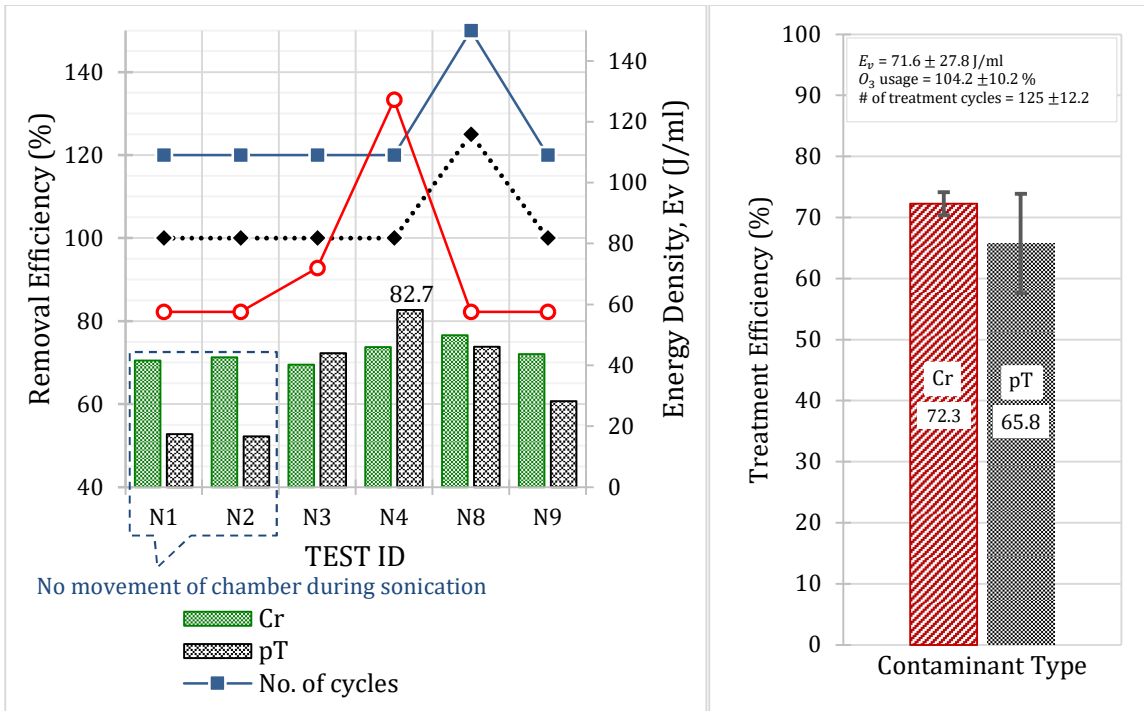
Figure 8.7 shows the comparison between the test results for different initial contaminant concentrations. Chromium removal efficiencies decrease with increasing concentration of chromium. However, p-terphenyl treatment efficiency shows unexpected results as the decrease in initial p-terphenyl concentration resulted in low removal efficiencies. It can be related to the pyrolysis of p-terphenyl with ultrasound application. When the ultrasound causes the cavitation bubbles to collapse, the chemicals near the collapse site can get pyrolyzed. As the p-terphenyl concentration is reduced in the solution, the probability of p-terphenyl contaminated sediment particles reaching the cavitation/reaction zone is reduced, explaining the reduction in the treatment efficiency. Therefore, in the experimental laboratory setup, the p-terphenyl removal efficiencies highly depend on how proper the sediment chamber moved during the sonication. If the

system is adequately mixed, it allows the sediment particles to reach the reaction zone and detached or pyrolyze the contaminants. During the sonication, the sediment chamber movement may explain the difference between Test N<sub>10</sub> and N<sub>11</sub> results, while all the other parameters are identical. In practical applications, this factor should be carefully addressed so that ultrasound energy is uniformly and effectively distributed in the system.

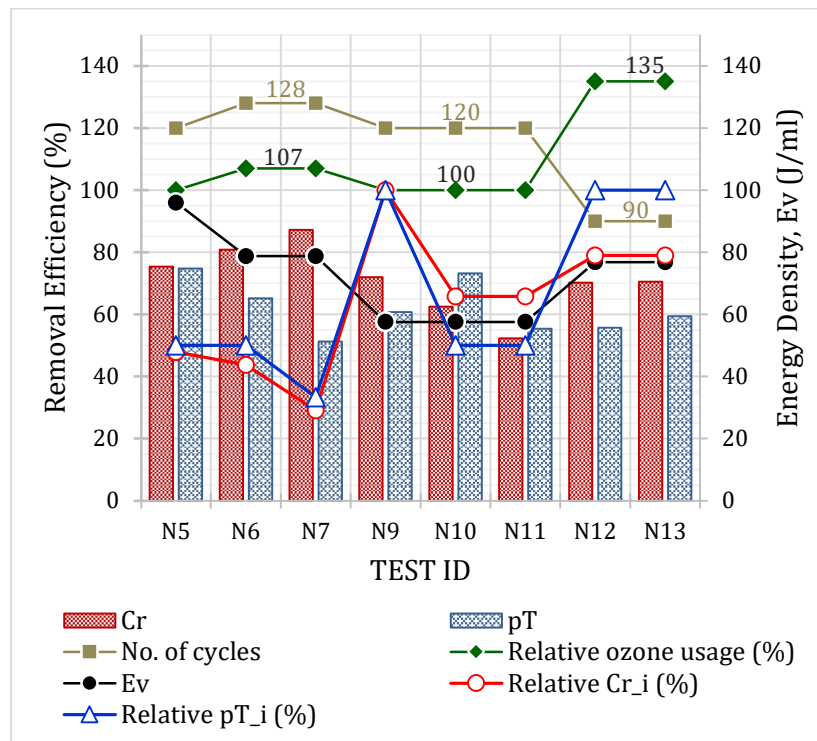
In Tests N<sub>12</sub> and N<sub>13</sub>, additional amounts of ozone saturated water volume were added compared to other experiments. These tests also had a relatively high energy density of 76.8 J/ml, and sonication was performed for 240 minutes in only 90 cycles (2min pulse for 60 cycles and 4 min pulse of 30 cycles). Although the additional amount of ozone was added to the system, the reduction in treatment cycles profoundly impacted the removal efficiency of p-terphenyl. Tests N<sub>12</sub> and N<sub>13</sub> indicate that the importance of washing cycles on treatment efficiency. To summarize, the p-terphenyl removal efficiency increased with an increased amount of ozone availability but was mainly impacted by the ultrasound energy and the number of treatment cycles. By selecting higher energy densities and increasing the number of treatment cycles, p-terphenyl degradation can be optimized.



**Figure 8.5** Summary of the calculated values for each test performed (a) Part A, (b) (Part B).



**Figure 8.6** Test results for similar contamination concentration (chromium: 4211 mg/kg and p-terphenyl: 1875 mg/kg).



**Figure 8.7** Effect of the initial concentration of contaminants.

When the overall experimental results were considered for all the tests, chromium removal efficiencies were held nearly constant, around 71%, showing no impact from the increase in ultrasound energy. Because the currently applied ultrasound energies contribute to chromium removal's best possible impact, no additional increment causes any further improvements but can reduce removal competence as higher ultrasound power can reduce the solution's ozone concentration. Results indicate that the available ozone directly impacts chromium removal efficiency. Consequently, to improve the chromium removal efficiency, the number of treatment cycles, and the ozone concentration in the solution should be increased while desired ultrasound power levels are maintained.

Based on the above observations, chromium removal is directly influenced by the chemical oxidation and sonication for chromium detachments. P-terphenyl degradation is more likely influenced by the combined effects of oxidation and ultrasound-assisted pyrolysis.

Heavy metals are not degradable pollutants. Thus, to complete the removal of cr, it needs to be extracted from the sediment-water mixture. Hence, in this process, as the chromium(III) is firmly bonded onto sediment particles, it needs complete oxidation into chromium(VI) of the water-soluble phase, where it is then extracted out by several cycles of washing out with ozonated water.

Other researchers have reported that the degradability of organic contaminants decreased with heavy metals in the sediments. The organic pollutant biodegradability and their biodegradation rate decreased with heavy metals in the environment and, therefore, doubled the environmental pollution [248].

The sorption process influences organic contaminants' interaction with sediments [249]. The sediment and organic pollutant sorption process are driven by van der Waals interactions, electrostatic interactions,  $\pi$ -bonding, hydrogen bonding, ligand exchange reactions, dipole-dipole interaction, and chemisorption [226]. The hydrophobic effect of pollutants mainly drives the organic contaminant sorption into the sediment. Further, sediments organic fraction and the clay mineral fraction significantly influence the sorption process.

Heavy metals in the soil/sediments in nature are mainly in immobile forms and primarily bond with the silicate minerals and secondarily to clay minerals [226]. When the heavy metal contaminates the soil due to external sources, the contaminants are not always be attached to silica bonds or clay minerals in sediments, and weakly bond and thus, environmentally available and toxic, impacting humans and natural habitats. There are five types of heavy metal binding to accumulate metals in sediments: 1) adsorptive and exchangeable, 2) bound to carbonates, 3) bound to organic matter and sulfides, 4) bound to Fe and Mn oxides, and 5) residual metals [242].

With combined contamination of organic and inorganic contaminants, the overall response may differ from that for each contaminant acting independently. Results showed that sediments mixed with p-terphenyl and chromium had increased the overall bonds with sediments and increased removal resistance. Therefore, p-terphenyl degradability and chromium extractability has been reduced with combined contamination causing the recorded low removal efficiencies compared to the treatment soil/sediment contaminated with an individual contaminant.



The next step of this research would be to evaluate the treatment technology to remediate actual sediments from the lower Passaic River and develop an in situ treatment device [40,72,74] for field implementation. Concurrently, the authors explore the feasibility of high and low-frequency ultrasound to remediate lower Passaic River sediments without using ozone nanobubbles [250].

### **8.6 Summary and Conclusions**

This research evaluated an in-situ sediment remediation method using ultrasound and ozone nanobubbles to remediate both organic and inorganic chemicals in contaminated sediments to be applied to remediate lower Passaic River sediments. Sediment contaminated with both chromium and p-terphenyl were tested subjected to different experimental conditions. This proposed treatment method shows significant remediation success with removing these combined contaminants, on average, 64% and 71% for p-terphenyl and chromium, respectively. According to the obtained results, the chromium removal is directly influenced by the chemical oxidation and sonication for chromium detachments. While p-terphenyl degradation is more likely influenced by the combined effects of chemical oxidation and ultrasound-assisted pyrolysis. These contaminant removal rates can be improved by increasing the amount of ozone added to the system and increasing the treatment cycles to washout the sediments. The increase in sonication time can also improve treatment efficiency but would increase energy costs. Further, this method may be evaluated by combining with proper catalysis and using different ultrasound frequencies or multiple ultrasound sources. The chemical oxidation improvement through increasing the hydroxyl radical in the system would benefit the proposed method. Hence, research will continue to evaluate the methods to improve the

oxidation agent. This treatment method's initial concept seems promising but requires additional investigation to improve and optimize the treatment to lower energy cost and time.

## CHAPTER 9

### SUMMARY, CONCLUSIONS AND FUTURE RECOMMENDATIONS

#### 9.1 Summary and Conclusions

##### 9.1.1 Experimental investigation: nanobubble stability based on infilled gas type and effect of solution chemistry

The impacts of gases inside nanobubbles on their properties and behavior were investigated. Oxygen, air, nitrogen, and ozone gas bubbles were generated and measured size and zeta potential values immediately after generation and one week after generation. The results revealed that nanobubbles' size and zeta potential were a function of the gas type, specifically the gas solubility. Smaller bubble sizes were associated with lower gas solubility. Hence, smallest bubble size was for the lowest soluble gas, N<sub>2</sub> gas, and the largest size was for highest soluble gas, ozone. As the same DI water was used for all bubbles, the differences in zeta potential values could be correlated to the gas diffusivity, solubility, and potential contribution to form the OH<sup>-</sup> at the bubble's gas-liquid interface. Based on test results, ozone had the highest negative zeta potential value, followed by oxygen, air, and nitrogen.

Then the effect of solution chemistry on nanobubbles was investigated by varying the solution pH, temperature, and NaCl concentration. The surface negativity of the bubble increased with increased solution pH. Also, in higher pH values, smaller bubbles were formed. The bubbles formed in acidic solutions were relatively large and unstable. Hence, smaller diameter and higher negatively charged stable bubbles were formed in high pH solutions. This supports the hypothesis that OH<sup>-</sup> ions adsorption at the gas-liquid interface controls the surface charge and stability of nanobubbles.

The impact of temperature on bubble size was not clear from the results, yet the zeta potential values decreased with increased solution temperature. The reduction in negative charge could be related to the change in  $\text{OH}^-$  ion concentration on the bubble surface. The mobility of ions increased with elevated temperatures and reduced the adsorbed  $\text{OH}^-$  concentration on the bubble surface.

With increased NaCl concentration, zeta potential values decreased while the bubble diameter increased. A decrease in zeta potential can be attributed to the adsorbed positive  $\text{Na}^+$  ions at the bubble interface that reduces the negativity of bubbles. These results were further investigated with the applied diffused double layer theory.

Irrespective of gas type, stable bubbles with high negative zeta potential values can be generated by providing sufficient energy or pressure under controlled gas flow rates. Also, bubble stability can be increased by providing a favorable environment that can generate higher  $\text{OH}^-$  ions concentration on the bubble surface.

### **9.1.2 Application of the diffused double layer theory to nanobubbles**

Nanobubbles have an electrically charged surface, and hence, a diffuse double layer is formed around the nanobubble. Nanobubbles were formed in different concentrations (0, 0.001 M, 0.01 M, and 0.1 M) of NaCl solutions, and size and zeta potentials were measured. Then the diffuse double layer theory was applied to explain the stability of bubbles. The diffused double layer theory is used to calculate the surface potential, surface charge density, potential distribution, and internal gas pressure. The surface charge density values on nanobubbles were computed using numerical simulations and previously developed analytical solutions. The double-layer thicknesses, van der Waals attractive force,

electrostatic repulsive force, and the net interactive energies and forces were also calculated.

With the increase in NaCl concentration, bubble size increased, and zeta potential/surface potential decreased. With the reduction in zeta potential values, there was a corresponding reduction in double-layer thickness. The literature confirmed that, with an increase of NaCl concentration, a reduction in negative zeta potential, and an increase in effective diameter [18,70,92]. The surface charge density and total negative surface charge increased due to the added NaCl, which was explained as OH<sup>-</sup> absorption. Furthermore, calculation of interfacial forces showed that for the 0.001M NaCl solution, strong electrostatic repulsion with a positive energy barrier. With increasing NaCl concentration (i.e., 0.01M and 0.1M), the electrostatic repulsion force weakened. Uchida et al. [27] also showed a similar reduction in zeta potential values with the addition of salts. The pressure calculations showed a reduction in the interfacial pressure difference with the increased NaCl concentration. Yet, the amount of reduction is insufficient to compensate for the pressure created due to the surface tension.

### **9.1.3 The stability of nanobubbles in different electrolyte solutions**

The stability of nanobubbles in electrolyte solutions with different ion types was studied using deionized water, NaCl, Na<sub>2</sub>SO<sub>4</sub>, Na<sub>3</sub>PO<sub>4</sub>, CaCl<sub>2</sub>, and FeCl<sub>3</sub> solutions. The size and zeta potential measurements were taken just after the bubble generation and after one week. The diffuse double layer theory was applied to explain the bubble behavior. The nonlinear Poisson Boltzman equation was solved using a numerical simulation based on the network simulation method [34] for the spherical colloidal and asymmetric ions.

All electrolyte solutions with 0.001M salt concentration produced stable bubbles over one week, with no significant change in either bubble size or zeta potential values. The difference between the bubble size and zeta potential can be attributed to the solution properties and mainly dependent on solution pH and the cation valency, as nanobubbles under natural pH solutions tend to be negatively charged. Anions had minimal impact on the surface potential. The ion distribution profiles revealed that cation concentrations at the bubble surface were higher than that in the bulk liquid, confirming that the bubbles formed in neutral and high pH values ( $\geq 4$ ) are negatively charged due to low valency cation adsorption. Low adsorption of high valency cations neutralized the charge on the bubble surface or completely reversed the charge. However, low ionic adsorptions at the gas-liquid interface produced stable nanobubbles due to the ion shielding effects. Also, for stable bubbles, the attractive van der Waals forces were unrealistic suggesting that the selected Hamaker constant for the calculation may not be valid for gas-liquid interfaces of nanobubbles. Further, calculated pressure values were also unrealistically high and suggesting that surface tension values should be lower than the surface tension ( $\gamma$ ) value of 72.75mN/m for water at 20<sup>0</sup>C and 1atm. These results revealed that nanobubbles should contain exceptional interfacial properties that need to be carefully investigated and evaluated.

#### **9.1.4 Molecular dynamic simulation of oxygen gas nanobubble**

High inner density oxygen gas nanobubble was simulated using the LAMMPS MD code. The simulation configuration includes 3,247 O<sub>2</sub> molecules embedded in 4.5nm radius spherical volume to represent bubble and surrounded by 438,490 H<sub>2</sub>O molecules, to form 1g/cm<sup>3</sup> density. The simulation ran for 5ns, and during the simulation, bubble size stayed

constant around 4.5 nm. The gas and water molecules density profiles with distance did not significantly vary with time. Simulation results showed a smaller gas diffusion coefficient of  $\approx 2.55 \times 10^{-6} \text{ cm}^2/\text{s}$  that is reported in the literature after 3ns. The pressure inside the bubble decreased with time as the gas molecules diffused into the bulk solution while maintaining a constant bubble size. However, the external pressure increased with time due to increased gas concentration with increased partial gas pressure outside the bubble. Surface tension values were back calculated by considering the outside pressure obtained from the simulation and considering the 1 atm external pressure. In both cases, the calculated surface tensions were smaller than that reported in the literature for 20°C and 1atm. This reduction in surface tension would be attributed to the high-density profile of O<sub>2</sub> molecules and reduced H<sub>2</sub>O density ( $< 1 \text{ g/cm}^3$ ) within the interfacial thickness. In classical thermodynamics, the Y-L equation would consider the interface with zero thickness and zero density. Still, the simulation results revealed the interface has a finite thickness and a density distribution, which would be the reason for this reduced surface tension values. With time the system still reached equilibrium (metastable) and gas diffused to the bulk solution at a slow rate with reduced the surface tension values.

The stability of simulated nanobubble may be due to the supersaturation of the bulk solution and high inner gas density. The gas concentration just outside the bubble was considerably high, causing a reduction in surface tension and increased external pressure. Therefore, the gas diffusion due to the internal bubble pressure is reduced or balanced and the bubble stability improved with slow diffusion. Hence, it can be concluded that supersaturation of gases in bulk solution and higher gas density inside the nanobubble are key parameters that would increase the bubble stability and control the diffusion.

### **9.1.5 Application of ozone nanobubbles coupled with ultrasound to treat contaminated sediments**

This research evaluated the feasibility of in-situ sediment remediation of contaminated sediments using ultrasound and ozone nanobubbles to be applied for lower Passaic River, NJ. The application of ultrasound kept the sediment in suspension and provided mechanical energy to desorb contaminants from sediments and release them to the bulk solution. The ozone was used to oxidize or degrade the desorbed contaminants to intermediate products that are more soluble and benign in the aqueous phase and remove by subsequent treatment filtration. The ozone was delivered as nanobubbles to increase the ozone gas dissolution in water and to maintain high ozone concentration in the liquid phase. A set of laboratory-scale experiments were performed using simulated dredged sediments to identify the impact of sonication time and sonication power with nano ozone.

**9.1.5.1 Treatment of organic contaminant (p-terphenyl).** This study evaluated the performance of the proposed method to remediate the organic pollutants in the sediments. A set of laboratory-scale experiments were performed using simulated dredged sediments to identify the impact of sonication time and sonication power with nano ozone in oxidizing PAHs. First, tests were performed to determine the enhancement in ozone delivery to water as nanobubbles. The ozone nanobubbles can deliver higher ozone concentrations to water and maintain those high ozone concentrations for long periods. Then the impact of ultrasound on the sediment slurry was evaluated. It was found that with the application of ultrasound, the temperature increased, and sediments became finer under high power levels. The treatment efficiency ultrasound without nano ozone was 76.7%. The next sets of experiments were performed by applying ultrasound with ozone nanobubbles where varying ultrasound power levels and sonication time were applied. Continuous application



of ultrasound heated the solution, reducing the amount of ozone available for remediation. Hence, the treatment was performed in 2-minute treatment cycles until the desired sonication time was achieved. Also, treatment efficiency improved by adding ozone to the system in two stages; before and after sonication. With the prolonged application of ultrasound with ozone nanobubbles, it was possible to achieve a contaminant removal efficiency of 91.5% for PAH contaminated sediment after a total sonication time of 240 minutes.

#### **9.1.5.2 Treatment of combined contaminant of organic and inorganic (p-terphenyl and chromium).**

Sediment contaminated with both chromium and p-terphenyl were tested subjected to different ultrasound power and dwell times. Test results showed significant remediation success with removing these combined contaminants, on average, 64% and 71% for p-terphenyl and chromium, respectively. Based on test results, the chromium removal is directly influenced by the chemical oxidation due to ozone and chromium detachments due to sonication. While p-terphenyl degradation is more likely influenced by the combined effects of chemical oxidation and ultrasound-assisted pyrolysis. These contaminant removal rates can be improved by increasing the amount of ozone added to the system and increasing the treatment cycles. The increase in sonication time can also improve treatment efficiency but would increase energy costs. Further, this method may further be improved by adding catalysis and using different ultrasound frequencies or multiple ultrasound sources. The improved chemical oxidation due to the hydroxyl radical generated from ultrasound would benefit the proposed technology. Hence, research will continue to evaluate the methods to improve oxidation agents. This treatment

method and initial results are promising but require additional investigation to improve and optimize the treatment to lower energy cost and time.

## **9.2 Future Recommendations**

### **9.2.1 Experimental and theoretical study on nanobubble stability**

1. The experiments with the different valency salts were limited to 0.001M salt concentration. It would be beneficial to conduct additional tests with nanobubble solutions having the same debye length to investigate the bubble stability using diffused double layer and DLVO theory.
2. Results showed that the used Hamaker constant for the Van der Waals interactions made unrealistic results. Therefore, it is required to evaluate the accurate method to determine nanobubbles' interaction energy or modified Hamaker constant that is valid at the nanobubbles' gas-liquid interface.
3. The laboratory measurements of nanobubbles were limited to bubble size and zeta potentials. A complete evaluation of nanobubbles requires to measure the concentration of nanobubbles and their decay with time. Thus, it requires additional investigation of bubbles with different solution chemistries and gas types to study bubble sizes, zeta potential values, and bubble concentrations.
4. This research did not evaluate one of the critical features of nanobubbles, the radical formation. Future research should evaluate the radical formation and factors that influence the radical concentration.
5. The most common method of zeta potential measurements of nanobubbles was limited to electrophoretic mobility measurements and the application of Smoluchowski's equation. However, several publications questioned the application of Smoluchowski's model for gas bubbles and liquid droplets with mobile interfaces. Hence, the nanobubble research community should investigate the validity of the use of electrophoretic mobility measurements and the application of Smoluchowski's equation.

### **9.2.2 Molecular dynamic simulation**

1. Present work was limited to a single O<sub>2</sub> nanobubble simulation with high gas density and simulated for a short period of 5ns. The simulation should continue for a longer time. Further, simulation should be repeated for other gas types and different volumes of the bulk solution for comparison and to provide more meaningful information.

2. In this study, the simulation was limited to nonreactive force field molecular dynamics simulation. The simulation should be extended with reactive force field parameters to investigate the bubble charging mechanism and the adsorption of opposing charged ions at the bubble interfaces.
3. This work was limited to a single nanobubble; it requires evaluating the bubble interaction. Hence, the simulation needs to be extended at least to evaluate the interactions of two bubbles.
4. In the present work, the surface tension was not directly calculated based on the MD simulation local pressure data. That will be a good approach to evaluating the surface tension based on simulation data for accuracy and cross-check, which will also help validate the reduction in surface tension.

### **9.2.3 Application of nanobubbles for sediment treatment**

1. The treatment method should be validated by testing sediments from the Passaic River before the field implementation.
2. The treatment method should explore ways to increase ozone concentration and nanobubbles, as the ozone seems to be the limiting factor of the performed treatment efficiencies.
3. In this presented work, nanobubbles were utilized as added ozone nanobubbles to oxidized the contaminant. However, research should investigate the use of high-frequency ultrasound to generate nanobubbles and free radicals to oxidate contaminants.

**APPENDIX A**  
**SYNTHETIC SEDIMENT COMPOSITION**

Table A.1 shows the synthetic dredge sediment composition based on the Passaic River actual sediment particle size distribution.

**Table A.1** Composition of Synthetic Dredge Sediment

Soil Type	Percent of Soil	Other Properties
Sand ( $>75\mu m$ )	2.60	
Silt	4.62	Water Content = 3.6%
Rock Flour	20.24	pH $\approx$ 7 and negligible organic carbon content
Kaolin	1.45	
Rock Flour ( $<75\mu m$ )	71.09	
Total	100.00	

## APPENDIX B

### DETAILS FOR THE TEST OF DISSOLVED OZONE CONCENTRATION USING A REGULAR DIFFUSER

The advantage of using ozone nanobubbles to dissolve ozone into the water was investigated in this study. The ozone concentration in the water was measured for 8 hours. The nanobubble generation tank was filled with 20 liters of filtered water. In the test without nanobubbles, the tank was aerated using a 20mm diameter fish tank air diffuser for 3 minutes, and the nanobubble generation was also done for the same duration. The test samples were prepared at 10<sup>0</sup>C, 15<sup>0</sup>C, and 20<sup>0</sup>C to examine the impact of the temperature on ozone concentrations with and without nanobubbles. The ozone was delivered at a rate of 3 liters per minute with 6.9 kPa pressure. The two prepared samples in 800ml containers were kept inside a constant temperature bath, as shown in Figure B.1. The containers were vented to prevent ozone buildup inside the container.



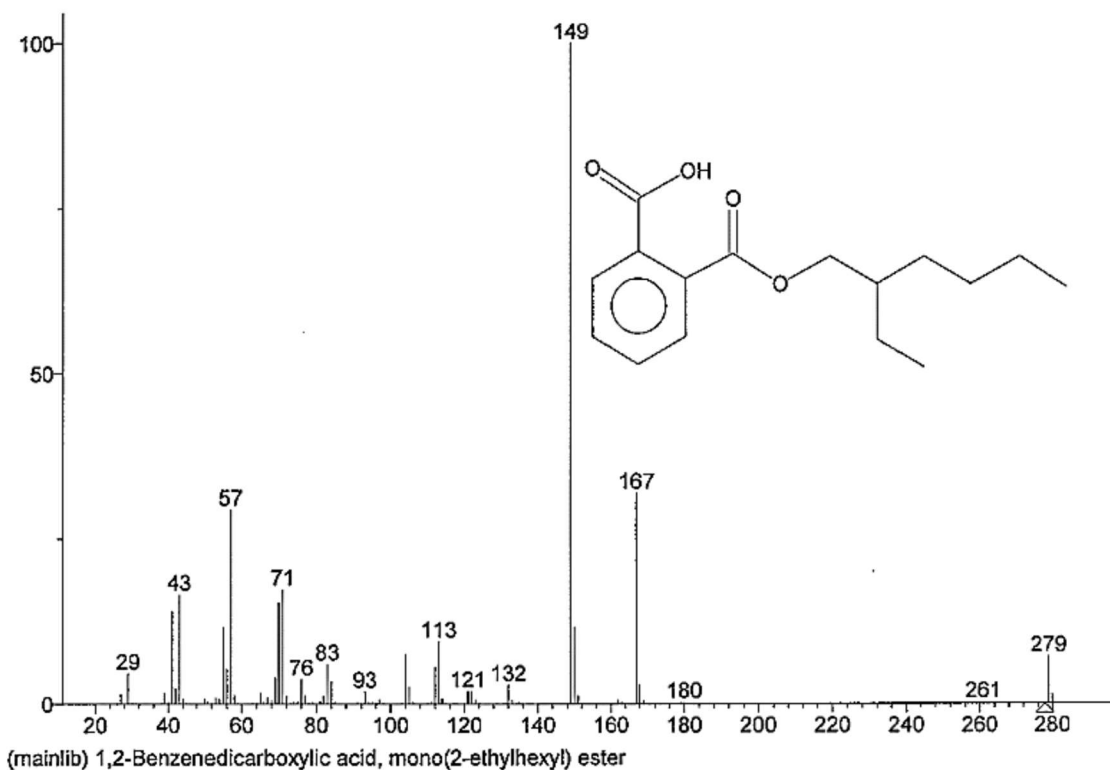
**Figure B.1** Diffuser used for ozonation and the constant temperature baths.

## APPENDIX C

### GS/MS ANALYSIS DATA

#### C.1 GS/MS Analysis Data for Sampled Collected from Sediments

During the GC/MS analysis, it was observed that ozone is reacting with the benzene ring of the *p*-terphenyl. The GC/MS results indicated the broken bonds that contained oxygen molecules, and the evidence of the broken benzene rings, as shown in Figure C.1.

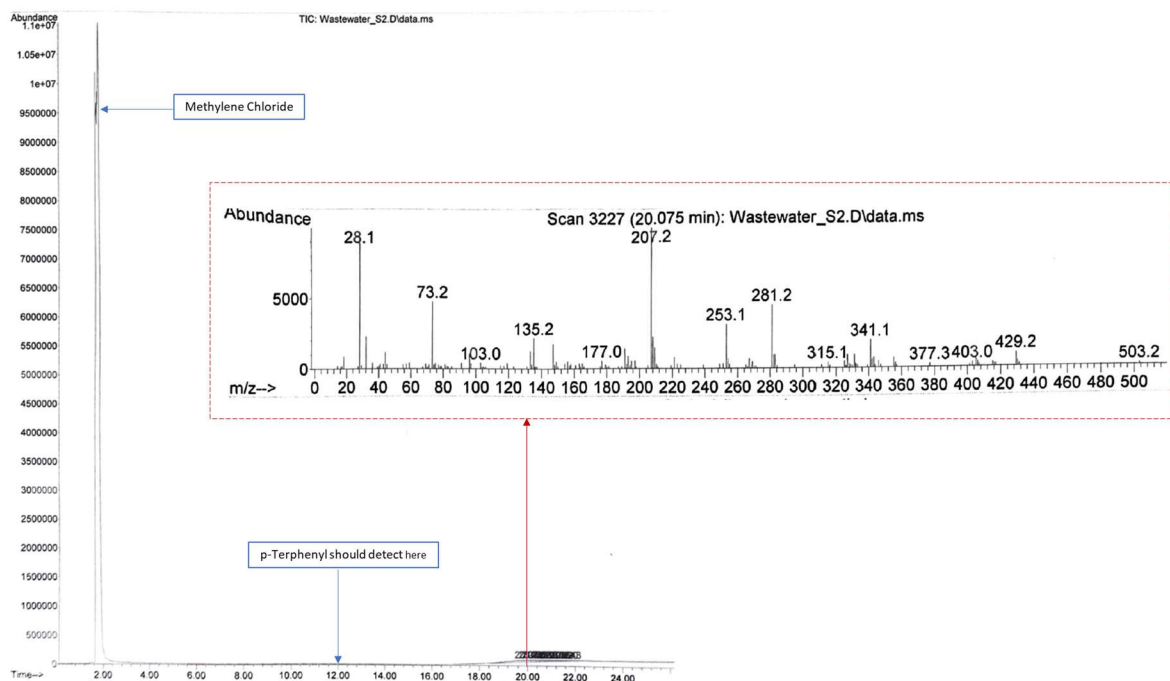


**Figure C.1** Formation of esters from broken *p*-terphenyl benzene rings.

Source: Batagoda, 2018 [211].

## C.2 GS/MS Analysis Data for Sampled Collected from Wastewater

The ultrasound coupled ozone has been fully mineralized the organic p-terphenyl to carbon dioxide and water. According to the GC/MS records, in the wastewater, no p-terphenyl detected, and there was tracer concentration of daughter products. The relevant GC/MS chromatogram and a mass spectrum are given in Figure C.2.



**Figure C.2** GC/MS chromatogram and a mass spectrum for wastewater.


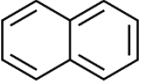
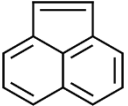
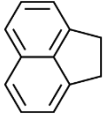
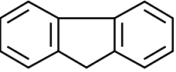
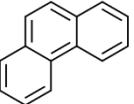
## **APPENDIX D**

### **COMPARISON OF P-TERPHENYL WITH 16 US-EPA PAHS**

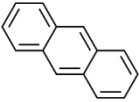
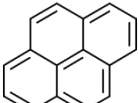
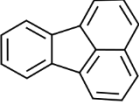
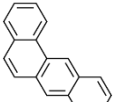
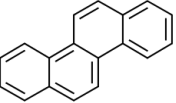
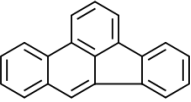
Tables A.1 and A.2 show the Properties and Laboratory chemical safety of p-Terphenyl compared to 16 US-EPA PAHs, respectively.



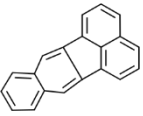
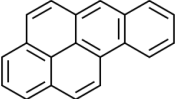
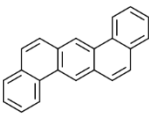
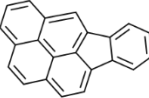
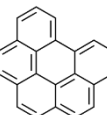
**Table D.1** Comparison of Properties of P-Terphenyl with 16 US-EPA PAHs (**Continued**)

Name	Formular	CAS No.	Structure	Number of rings	Molecular weight	Boiling Point	Melting Point	Aqueous solubility	Vapor press.	Log K <sub>ow</sub>	Henry's Law Constant	Hydroxyl Radicals Reaction	Soil Adsorption Coefficient (Log K <sub>oc</sub> )
					(g/mol)	(°C)	(°C)	(mg/l)	(Pa)	(-)	(atm-m <sup>3</sup> /mole)	(× 10 <sup>-12</sup> ) (cm <sup>3</sup> /mole-cule-sec)	(-)
p-Terphenyl	C <sub>18</sub> H <sub>14</sub>	92-94-4		3	230	376	210.1	0.0179	4.9×10 <sup>-6</sup>	6.03	4.83E-07	9.2	5.37
Naphthalene	C <sub>10</sub> H <sub>8</sub>	91-20-3		2	128	217.9	80.2	31	1.0×10 <sup>2</sup>	3.37	4.80E-05	21.6	3.26
Acenaphthylene	C <sub>12</sub> H <sub>8</sub>	208-96-8		3	152	280	92.5	16	9.0×10 <sup>-1</sup>	4	1.01E-04	75.5	3.79
Acenaphthene	C <sub>12</sub> H <sub>10</sub>	83-32-9		3	154	279	93.4	3.8	3.0×10 <sup>-1</sup>	3.92	1.03E-04	66.9	3.79
Fluorene	C <sub>13</sub> H <sub>10</sub>	86-73-7		3	166	295	114.8	1.9	9.0×10 <sup>-2</sup>	4.18	5.39E-05	8.9	4.05
Phenanthrene	C <sub>14</sub> H <sub>10</sub>	85-01-8		3	178	340	99.2	1.1	2.0×10 <sup>-2</sup>	4.57	1.50E-05	13.0	4.32


















**Table D.1 (Continued)** Comparison of Properties of P-Terphenyl with 16 US-EPA PAHs

Name	Formular	CAS No.	Structure	Number of rings	Molecular weight	Boiling Point	Melting Point	Aqueous solubility	Vapor press.	Log $K_{ow}$	Henry's Law Constant	Hydroxyl Radicals Reaction	Soil Adsorption Coefficient (Log $K_{oc}$ )
					(g/mol)	(°C)	(°C)	(mg/l)	(Pa)	(-)	(atm-m <sup>3</sup> /mole)	( $\times 10^{-12}$ ) (cm <sup>3</sup> /mole-cule-sec)	(-)
Anthracene	C <sub>14</sub> H <sub>10</sub>	120-12-7		3	178	339.9	215	0.045	1.0x10 <sup>-3</sup>	4.54	7.37E-07	40.0	4.31
Pyrene	C <sub>16</sub> H <sub>10</sub>	129-00-0		4	202	404	151.2	0.13	6.0x10 <sup>-4</sup>	5.18	4.07E-07	50.0	4.84
Fluoranthene	C <sub>16</sub> H <sub>10</sub>	206-44-0		4	202	384	107.8	0.26	1.2x10 <sup>-3</sup>	5.22	6.42E-06	29.2	4.85
Benzo[a]anthracene	C <sub>18</sub> H <sub>12</sub>	56-55-3		4	228	437.6	162	0.011	2.8x10 <sup>-5</sup>	5.91	2.81E-06	50.0	5.36
Chrysene	C <sub>18</sub> H <sub>12</sub>	218-01-9		4	228	448	258.2	0.006	5.7x10 <sup>-7</sup>	5.91	1.78E-08	50.0	5.37
Benzo[b]fluoranthene	C <sub>20</sub> H <sub>12</sub>	205-99-2		5	252	481	168	0.0015	-	5.8	4.00E-07	18.6	5.91










**Table D.1 (Continued)** Comparison of Properties of P-Terphenyl with 16 US-EPA PAHs

Name	Formular	CAS No.	Structure	Number of rings	Molecular weight	Boiling Point	Melting Point	Aqueous solubility	Vapor press.	Log K <sub>ow</sub>	Henry's Law Constant	Hydroxyl Radicals Reaction	Soil Adsorption Coefficient (Log K <sub>oc</sub> )
					(g/mol)	(°C)	(°C)	(mg/l)	(Pa)	(-)	(atm-m <sup>3</sup> /mole)	(× 10 <sup>-12</sup> ) (cm <sup>3</sup> /mole cule-sec)	(-)
Benzo[k]fluoranthene	C <sub>20</sub> H <sub>12</sub>	207-08-9		5	252	480	217	0.0008	5.2x10 <sup>-8</sup>	6	2.42E-08	53.6	5.90
Benzo[a]pyrene	C <sub>20</sub> H <sub>12</sub>	50-32-8		5	252	495	176.5	0.0038	7.0x10 <sup>-7</sup>	5.91	4.65E-06	384.8	5.40
Dibenzo[a,h]anthracene	C <sub>22</sub> H <sub>14</sub>	53-70-3		6	278	524	266	0.0006	3.7x10 <sup>-10</sup>	6.75	1.54E-09	50.0	6.42
Indeno[1,2,3-cd]pyrene	C <sub>22</sub> H <sub>12</sub>	193-39-5		6	276	536	163.6	0.00019	-	6.5	3.46E-06	446.5	5.78
Benzo[ghi]perylene	C <sub>22</sub> H <sub>12</sub>	191-24-2		6	276	550	278	0.00026	1.4x10 <sup>-8</sup>	6.5	1.28E-07	50.0	6.43

**Table D.2** Comparison of Laboratory Chemical Safety of P-Terphenyl with 16 US-EPA PAHs (PubChem Database) (**Continued**)

Name Formular CAS No.	Pictogram(s)	Signal	GHS Hazard Statements
<b>p-Terphenyl</b> C <sub>18</sub> H <sub>14</sub> 92-94-4	  Irritant Environmental Hazard	Warning	H315 (97.96%): Causes skin irritation [Warning Skin corrosion/irritation] H319 (97.96%): Causes serious eye irritation [Warning Serious eye damage/eye irritation] H335 (93.88%): May cause respiratory irritation [Warning Specific target organ toxicity, single exposure; Respiratory tract irritation] H400 (85.71%): Very toxic to aquatic life [Warning Hazardous to the aquatic environment, acute hazard]
Naphthalene C <sub>10</sub> H <sub>8</sub> 91-20-3	   Irritant Health Hazard Environmental Hazard	Warning	H302: Harmful if swallowed [Warning Acute toxicity, oral] H351: Suspected of causing cancer [Warning Carcinogenicity] H400: Very toxic to aquatic life [Warning Hazardous to the aquatic environment, acute hazard] H410: Very toxic to aquatic life with long lasting effects [Warning Hazardous to the aquatic environment, long-term hazard]
Acenaphthylene C <sub>12</sub> H <sub>8</sub> 208-96-8	  Acute Toxic Irritant	Danger	H302 (60%): Harmful if swallowed [Warning Acute toxicity, oral] H310 (40%): Fatal in contact with skin [Danger Acute toxicity, dermal] H315 (60%): Causes skin irritation [Warning Skin corrosion/irritation] H319 (60%): Causes serious eye irritation [Warning Serious eye damage/eye irritation] H330 (40%): Fatal if inhaled [Danger Acute toxicity, inhalation] H335 (40%): May cause respiratory irritation [Warning Specific target organ toxicity, single exposure; Respiratory tract irritation]
Acenaphthene C <sub>12</sub> H <sub>10</sub> 83-32-9	  Irritant Environmental Hazard	Warning	H319 (85.71%): Causes serious eye irritation [Warning Serious eye damage/eye irritation] H400 (90.48%): Very toxic to aquatic life [Warning Hazardous to the aquatic environment, acute hazard] H410 (90.48%): Very toxic to aquatic life with long lasting effects [Warning Hazardous to the aquatic environment, long-term hazard]
Fluorene C <sub>13</sub> H <sub>10</sub> 86-73-7	  Irritant Environmental Hazard	Warning	H315 (11.11%): Causes skin irritation [Warning Skin corrosion/irritation] H319 (11.11%): Causes serious eye irritation [Warning Serious eye damage/eye irritation] H335 (11.11%): May cause respiratory irritation [Warning Specific target organ toxicity, single exposure; Respiratory tract irritation] H400 (83.33%): Very toxic to aquatic life [Warning Hazardous to the aquatic environment, acute hazard] H410 (61.11%): Very toxic to aquatic life with long lasting effects [Warning Hazardous to the aquatic environment, long-term hazard]
Phenanthrene C <sub>14</sub> H <sub>10</sub> 85-01-8	  Irritant Environmental Hazard	Warning	H302 (99.63%): Harmful if swallowed [Warning Acute toxicity, oral] H400 (16.48%): Very toxic to aquatic life [Warning Hazardous to the aquatic environment, acute hazard] H410 (15.73%): Very toxic to aquatic life with long lasting effects [Warning Hazardous to the aquatic environment, long-term hazard]
Anthracene C <sub>14</sub> H <sub>10</sub> 120-12-7	  Irritant Health Hazard	Danger	H304 (33.33%): May be fatal if swallowed and enters airways [Danger Aspiration hazard] H315 (66.67%): Causes skin irritation [Warning Skin corrosion/irritation] H317 (66.67%): May cause an allergic skin reaction [Warning Sensitization, Skin] H350 (33.33%): May cause cancer [Danger Carcinogenicity] H361 (66.67%): Suspected of damaging fertility or the unborn child [Warning Reproductive toxicity] H412 (66.67%): Harmful to aquatic life with long lasting effects [Hazardous to the aquatic environment, long-term hazard]
Pyrene C <sub>16</sub> H <sub>10</sub> 129-00-0	  Irritant Environmental Hazard	Warning	H315 (68.93%): Causes skin irritation [Warning Skin corrosion/irritation] H319 (68.93%): Causes serious eye irritation [Warning Serious eye damage/eye irritation] H335 (68.93%): May cause respiratory irritation [Warning Specific target organ toxicity, single exposure; Respiratory tract irritation] H400 (88.35%): Very toxic to aquatic life [Warning Hazardous to the aquatic environment, acute hazard] H410 (96.12%): Very toxic to aquatic life with long lasting effects [Warning Hazardous to the aquatic environment, long-term hazard]

**Table D.2 (Continued)** Comparison of Laboratory Chemical Safety of P-Terphenyl with 16 US-EPA PAHs (PubChem Database)

Name Formular CAS No.	Pictogram(s)	Signal	GHS Hazard Statements
Fluoranthene C <sub>16</sub> H <sub>10</sub> 206-44-0		Warning	H302 (97.59%): Harmful if swallowed [Warning Acute toxicity, oral] H400 (73.49%): Very toxic to aquatic life [Warning Hazardous to the aquatic environment, acute hazard] H410 (72.29%): Very toxic to aquatic life with long lasting effects [Warning Hazardous to the aquatic environment, long-term hazard]
Benzo[a]anthracene C <sub>18</sub> H <sub>12</sub> 56-55-3		Danger	H350: May cause cancer [Danger Carcinogenicity] H400: Very toxic to aquatic life [Warning Hazardous to the aquatic environment, acute hazard] H410: Very toxic to aquatic life with long lasting effects [Warning Hazardous to the aquatic environment, long-term hazard]
Chrysene C <sub>18</sub> H <sub>12</sub> 218-01-9		Danger	H341: Suspected of causing genetic defects [Warning Germ cell mutagenicity] H350: May cause cancer [Danger Carcinogenicity] H400: Very toxic to aquatic life [Warning Hazardous to the aquatic environment, acute hazard] H410: Very toxic to aquatic life with long lasting effects [Warning Hazardous to the aquatic environment, long-term hazard]
Benzo[b]fluoranthene C <sub>20</sub> H <sub>12</sub> 205-99-2		Danger	H350: May cause cancer [Danger Carcinogenicity] H400: Very toxic to aquatic life [Warning Hazardous to the aquatic environment, acute hazard] H410: Very toxic to aquatic life with long lasting effects [Warning Hazardous to the aquatic environment, long-term hazard]
Benzo[k]fluoranthene C <sub>20</sub> H <sub>12</sub> 207-08-9		Danger	H350: May cause cancer [Danger Carcinogenicity] H400: Very toxic to aquatic life [Warning Hazardous to the aquatic environment, acute hazard] H410: Very toxic to aquatic life with long lasting effects [Warning Hazardous to the aquatic environment, long-term hazard]
Benzo[a]pyrene C <sub>20</sub> H <sub>12</sub> 50-32-8		Danger	H317: May cause an allergic skin reaction [Warning Sensitization, Skin] H340: May cause genetic defects [Danger Germ cell mutagenicity] H350: May cause cancer [Danger Carcinogenicity] H360FD: May damage fertility; May damage the unborn child [Danger Reproductive toxicity] H400: Very toxic to aquatic life [Warning Hazardous to the aquatic environment, acute hazard] H410: Very toxic to aquatic life with long lasting effects [Warning Hazardous to the aquatic environment, long-term hazard]
Dibenzo[a,h]anthracene C <sub>22</sub> H <sub>14</sub> 53-70-3		Danger	H350: May cause cancer [Danger Carcinogenicity] H400: Very toxic to aquatic life [Warning Hazardous to the aquatic environment, acute hazard] H410: Very toxic to aquatic life with long lasting effects [Warning Hazardous to the aquatic environment, long-term hazard]
Indeno[1,2,3-cd]pyrene C <sub>22</sub> H <sub>12</sub> 193-39-5		Warning	H351 (100%): Suspected of causing cancer [Warning Carcinogenicity]
Benzo[ghi]perylene C <sub>22</sub> H <sub>12</sub> 191-24-2		Warning	H400 (100%): Very toxic to aquatic life [Warning Hazardous to the aquatic environment, acute hazard] H410 (66.67%): Very toxic to aquatic life with long lasting effects [Warning Hazardous to the aquatic environment, long-term hazard] H413 (33.33%): May cause long lasting harmful effects to aquatic life [Hazardous to the aquatic environment, long-term hazard]

## REFERENCES

- [1] Weijjs, J.H., Seddon, J.R.T. and Lohse, D. (2012) Diffusive shielding stabilizes bulk nanobubble clusters. *ChemPhysChem*, **13**, 2197–2204.  
<https://doi.org/10.1002/cphc.201100807>
- [2] Chaplin, M. (2019) Water Structure and Science: Nanobubbles (ultrafine bubbles). Retrieved November 30, 2020, from,  
<http://www1.lsbu.ac.uk/water/nanobubble.html>
- [3] Agarwal, A., Ng, W.J. and Liu, Y. (2011) Principle and applications of microbubble and nanobubble technology for water treatment. *Chemosphere*, **84**, 1175–1180.  
<https://doi.org/10.1016/j.chemosphere.2011.05.054>
- [4] Ebina, K., Shi, K., Hirao, M., Hashimoto, J., Kawato, Y., Kaneshiro, S. et al. (2013) Oxygen and air nanobubble water solution promote the growth of plants, fishes, and mice. *PLoS ONE*, **8**. <https://doi.org/10.1371/journal.pone.0065339>
- [5] Liu, S., Kawagoe, Y., Makino, Y. and Oshita, S. (2013) Effects of nanobubbles on the physicochemical properties of water: The basis for peculiar properties of water containing nanobubbles. *Chemical Engineering Science*, **93**, 250–256.  
<https://doi.org/10.1016/j.ces.2013.02.004>
- [6] Ushikubo, F.Y., Furukawa, T., Nakagawa, R., Enari, M., Makino, Y., Kawagoe, Y. et al. (2010) Evidence of the existence and the stability of nano-bubbles in water. *Colloids and Surfaces A: Physicochemical and Engineering Aspects*, **361**, 31–37.  
<https://doi.org/10.1016/j.colsurfa.2010.03.005>
- [7] Soutter, W. (2013) What are nanobubbles? AZoNano. Retrieved November 30, 2020, from, <https://www.azonano.com/article.aspx?ArticleID=3151>
- [8] IDEC Corporation. (2020) What are ultrafine bubbles? Retrieved November 30, 2020, from, <http://www.idec.com/home/finebubble/bubble01.html>
- [9] Meegoda, J.N., Aluthgun Hewage, S. and Batagoda, J.H. (2018) Stability of nanobubbles. *Environmental Engineering Science*, **35**, 1216–1227.  
<https://doi.org/10.1089/ees.2018.0203>
- [10] Azevedo, A., Etchepare, R., Calgaroto, S. and Rubio, J. (2016) Aqueous dispersions of nanobubbles: Generation, properties and features. *Minerals Engineering*, **94**, 29–37. <https://doi.org/10.1016/j.mineng.2016.05.001>
- [11] Seung-Uk, L. (2016) Onsite algae harvesting using micro and nano (sub-micron) bubbles. [Presentation]. *7th International Conference on Flotation for Water and Wastewater Systems*, Toulouse, France.  
<https://www.pdfFiller.com/425438528--Multifunctional-bubble-treatment-ship->

- [12] Demangeat, J.-L.L. (2015) Gas nanobubbles and aqueous nanostructures: The crucial role of dynamization. *Homeopathy*, **104**, 101–115. <https://doi.org/10.1016/j.homp.2015.02.001>
- [13] ISO. (2014) The Fine Bubble Breakthrough. Int. Organ. Stand. International Organization for Standardization. Retrieved November 30, 2020, from, <https://www.iso.org/news/2014/05/Ref1844.html>
- [14] Alheshibri, M., Qian, J., Jehannin, M. and Craig, V.S.J. (2016) A History of nanobubbles. *Langmuir*, **32**, 11086–11100. <https://doi.org/10.1021/acs.langmuir.6b02489>
- [15] Epstein, P.S. and Plesset, M.S. (1950) On the stability of gas bubbles in liquid-gas solutions. *The Journal of Chemical Physics*, **18**, 1505–1509. <https://doi.org/10.1063/1.1747520>
- [16] Ishida, N., Inoue, T., Miyahara, M. and Higashitani, K. (2000) Nano bubbles on a hydrophobic surface in water observed by tapping-mode atomic force microscopy. *Langmuir*, **16**, 6377–6380. <https://doi.org/10.1021/la000219r>
- [17] Lou, S.-T., Ouyang, Z.-Q., Zhang, Y., Li, X.-J., Hu, J., Li, M.-Q. et al. (2000) Nanobubbles on solid surface imaged by atomic force microscopy. *Journal of Vacuum Science & Technology B: Microelectronics and Nanometer Structures*, **18**, 2573. <https://doi.org/10.1116/1.1289925>
- [18] Takahashi, M. (2005)  $\zeta$  Potential of microbubbles in aqueous solutions: Electrical properties of the gas - Water interface. *Journal of Physical Chemistry B*, **109**, 21858–21864. <https://doi.org/10.1021/jp0445270>
- [19] Ohgaki, K., Khanh, N.Q., Joden, Y., Tsuji, A. and Nakagawa, T. (2010) Physicochemical approach to nanobubble solutions. *Chemical Engineering Science*, **65**, 1296–1300. <https://doi.org/10.1016/j.ces.2009.10.003>
- [20] Yasui, K., Tuziuti, T., Kanematsu, W. and Kato, K. (2016) Dynamic equilibrium model for a bulk nanobubble and a microbubble partly covered with hydrophobic material. *Langmuir*, **32**, 11101-11110. <https://doi.org/10.1021/acs.langmuir.5b04703>
- [21] Serizawa, A. (2017) Fundamentals and applications of micro/nano bubbles. *1st International Symposium on Application of High Voltage, Plasmas & Micro/Nano Bubbles to Agriculture and Aquaculture (ISHPMNB 2017)*, Lanna Chiang Mai, Thailand.
- [22] Oh, S.H., Han, J.G. and Kim, J.M. (2015) Long-term stability of hydrogen nanobubble fuel. *Fuel*, **158**, 399–404. <https://doi.org/10.1016/j.fuel.2015.05.072>

- [23] Takahashi, M., Chiba, K. and Li, P. (2007) Free-radical generation from collapsing microbubbles in the absence of a dynamic stimulus. *Journal of Physical Chemistry B*, **111**, 1343–1347. <https://doi.org/10.1021/jp0669254>
- [24] Liu, S., Oshita, S., Makino, Y., Wang, Q., Kawagoe, Y. and Uchida, T. (2016) Oxidative capacity of nanobubbles and its effect on seed germination. *ACS Sustainable Chemistry and Engineering*, **4**, 1347–1353. <https://doi.org/10.1021/acssuschemeng.5b01368>
- [25] Yasui, K., Tuziuti, T. and Kanematsu, W. (2018) Mysteries of bulk nanobubbles (ultrafine bubbles); stability and radical formation. *Ultrasonics Sonochemistry*, **48**, 259-266. <https://doi.org/10.1016/j.ultsonch.2018.05.038>
- [26] Ahmed, A.K.A., Sun, C., Hua, L., Zhang, Z., Zhang, Y., Marhaba, T. et al. (2018) Colloidal properties of air, oxygen, and nitrogen nanobubbles in water: effects of ionic strength, natural organic matters, and surfactants. *Environmental Engineering Science*, **35**, 720–727. <https://doi.org/10.1089/ees.2017.0377>
- [27] Uchida, T., Liu, S., Enari, M., Oshita, S., Yamazaki, K. and Gohara, K. (2016) Effect of NaCl on the lifetime of micro- and nanobubbles. *Nanomaterials*, **6**, 31. <https://doi.org/10.3390/nano6020031>
- [28] Japanese Industrial Standards Committee. (2013) ISO/TS/P 234 – Fine bubble technology Proposal Submitted to International Organization for Standardization. Retrieved November 30, 2020, from, [https://www.jisc.go.jp/international/nwip/tsp234\\_Fine%20bubble%20technology.pdf](https://www.jisc.go.jp/international/nwip/tsp234_Fine%20bubble%20technology.pdf)
- [29] Acniti LLC. (2017) The world agrees: ISO International Standardization fine bubbles. Retrieved November 30, 2020, from, <https://www.acniti.com/technology/iso-fine-bubbles/>
- [30] Pecora, R. (2000) Dynamic light scattering measurement of nanometer particles in liquids. *Journal of Nanoparticle Research*, **2**, 123–131. <https://doi.org/10.1023/A:1010067107182>
- [31] Bhattacharjee, S. (2016) DLS and zeta potential - What they are and what they are not? *Journal of Controlled Release*, **235**, 337–351. <https://doi.org/10.1016/j.jconrel.2016.06.017>
- [32] IDEC Corporation. (2020) How are Ultrafine Bubbles measured? Retrieved November 30, 2020, from, <http://www.idec.com/home/finebubble/bubble04.html>
- [33] Tsuge, H. (2014) Micro- and nanobubbles - fundamentals and applications. *Micro-nanobubbles*. <https://doi.org/10.4032/9789814463119>



- [34] Malvern Panalytical Ltd. (2017) Resonance mass measurement (RMM). Retrieved November 30, 2020, from, <https://www.malvernpanalytical.com/en/support/product-support/archimedes#manuals>
- [35] Otsuka LTD. (2020) Zeta-potential & Particle size Analyzer ELSZ-2000 series. Retrieved November 30, 2020, from, <https://www.otsukael.com/product/detail/productid/1/category1id/2/category2id/1/category3id/29>
- [36] Padilla-Martinez, J.P., Berrospe-Rodriguez, C., Aguilar, G., Ramirez-San-Juan, J.C. and Ramos-Garcia, R. (2014) Optic cavitation with CW lasers: A review. *Physics of Fluids*, **26**, 122007. <https://doi.org/10.1063/1.4904718>
- [37] Maoming, F.A.N., Daniel, T.A.O., Honaker, R. and Zhenfu, L.U.O. (2010) Nanobubble generation and its application in froth flotation (part I): nanobubble generation and its effects on properties of microbubble and millimeter scale bubble solutions. *Mining Science and Technology (China)*, **20**, 1–19.
- [38] Ozonek, J. (2012) Application of hydrodynamic cavitation in environmental engineering. London: CRC Press. <https://doi.org/10.1201/b11825>
- [39] Batagoda, J.H., Hewage, S.D.A. and Meegoda, J.N. (2018) Nano-ozone bubbles for drinking water treatment. *Journal of Environmental Engineering and Science*, ICE Publishing. **14**, 57–66. <https://doi.org/10.1680/jenes.18.00015>
- [40] Young, F.R. (1999) Cavitation. Imperial College Press. <https://doi.org/10.1142/p172>
- [41] OHR Co. (2020) Comparison of a conventional static mixer with the OHR MIXER. Retrieved November 30, 2020, from, <http://ohr-labo.com/en/mixer-mechanism-comparison/>
- [42] Li, H., Hu, L. and Xia, Z. (2013) Impact of groundwater salinity on bioremediation enhanced by micro-nano bubbles. *Materials*, **6**, 3676–3687. <https://doi.org/10.3390/ma6093676>
- [43] Xiong, Y. and Peng, F. (2015) Optimization of cavitation venturi tube design for pico and nano bubbles generation. *International Journal of Mining Science and Technology*, **25**, 523-529. <https://doi.org/10.1016/j.ijmst.2015.05.002>
- [44] Abbas, S., Hayat, K., Karangwa, E., Bashari, M. and Zhang, X. (2013) An overview of ultrasound-assisted food-grade nanoemulsions. *Food Engineering Reviews*, **5**, 139–157. <https://doi.org/10.1007/s12393-013-9066-3>

- [45] Lauterborn, W. (1978) Optic Cavitation. *Journal de Physique Colloque*, **40**, C8-273 - C8-278. <https://doi.org/10.1051/jphyscol:1979847>
- [46] Poulain, S., Guenoun, G., Gart, S., Crowe, W. and Jung, S. (2015) Particle motion induced by bubble cavitation. *Physical Review Letters*, **114**, 214501. <https://doi.org/10.1103/PhysRevLett.114.214501>
- [47] Temesgen, T., Bui, T.T., Han, M., Kim, T. il and Park, H. (2017) Micro and nanobubble technologies as a new horizon for water-treatment techniques: A review. *Advances in Colloid and Interface Science*. **246**, 40–51. <https://doi.org/10.1016/j.cis.2017.06.011>
- [48] Ushikubo, F.Y., Enari, M., Furukawa, T., Nakagawa, R., Makino, Y., Kawagoe, Y. et al. (2010) Zeta-potential of micro- and/or nano-bubbles in water produced by some kinds of gases. *IFAC Proceedings Volumes (IFAC-PapersOnline)*, **3**, 283–288. <https://doi.org/10.3182/20101206-3-jp-3009.00050>
- [49] Kim, J.Y., Song, M.G. and Kim, J.D. (2000) Zeta potential of nanobubbles generated by ultrasonication in aqueous alkyl polyglycoside solutions. *Journal of Colloid and Interface Science*, **223**, 285–291. <https://doi.org/10.1006/jcis.1999.6663>
- [50] Calgaroto, S., Wilberg, K.Q.Q. and Rubio, J. (2014) On the nanobubbles interfacial properties and future applications in flotation. *Minerals Engineering*, **60**, 33–40. <https://doi.org/10.1016/j.mineng.2014.02.002>
- [51] Salgin, S., Salgin, U. and Bahadir, S. (2012) Zeta potentials and isoelectric points of biomolecules: The effects of ion types and ionic strengths. *International Journal of Electrochemical Science*, **7**, 12404 - 12414. <http://www.electrochemsci.org/papers/vol7/71212404.pdf>
- [52] Graciaa, A., Morel, G., Saulner, P., Lachaise, J. and Schechter, R.S. (1995) The  $\zeta$ -potential of gas bubbles. *Journal of Colloid And Interface Science*, **172**, 131–136. <https://doi.org/10.1006/jcis.1995.1234>
- [53] Wu, C., Nasset, K., Masliyah, J. and Xu, Z. (2012) Generation and characterization of submicron size bubbles. *Advances in Colloid and Interface Science*, **179-182**, 123-132. <https://doi.org/10.1016/j.cis.2012.06.012>
- [54] Brandon, N.P. and Kelsall, G.H. (1985) Growth kinetics of bubbles electrogenerated at microelectrodes. *Journal of Applied Electrochemistry*, **15**, 475–484. <https://doi.org/10.1007/BF01059288>
- [55] Najafi, A.S., Drelich, J., Yeung, A., Xu, Z. and Masliyah, J. (2007) A novel method of measuring electrophoretic mobility of gas bubbles. *Journal of Colloid and Interface Science*, **308**, 344–350. <https://doi.org/10.1016/j.jcis.2007.01.014>

- [56] Kelsall, G.H., Tang, S., Yurdakul, S. and Smith, A.L. (1996) Electrophoretic behaviour of bubbles in aqueous electrolytes. *Journal of the Chemical Society - Faraday Transactions*, **92**, 3887–3893. <https://doi.org/10.1039/ft9969203887>
- [57] Matsumoto, M. and Tanaka, K. (2008) Nano bubble-Size dependence of surface tension and inside pressure. *Fluid Dynamics Research*, **40**, 546–553. <https://doi.org/10.1016/j.fluiddyn.2007.12.006>
- [58] Seddon, J.R.T.T., Lohse, D., Ducker, W.A. and Craig, V.S.J.J. (2012) A Deliberation on nanobubbles at surfaces and in bulk. *ChemPhysChem*, **13**, 2179–2187. <https://doi.org/10.1002/cphc.201100900>
- [59] Bunkin, N.F. and Shkirin, A. V. (2012) Nanobubble clusters of dissolved gas in aqueous solutions of electrolyte. II. Theoretical interpretation. *Journal of Chemical Physics*, **137**. <https://doi.org/10.1063/1.4739530>
- [60] Zimmerman, W.B., Tesař, V. and Bandulasena, H.C.H. (2011) Towards energy efficient nanobubble generation with fluidic oscillation. *Current Opinion in Colloid & Interface Science*, **16**, 350-356. <https://doi.org/10.1016/j.cocis.2011.01.010>
- [61] Ducker, W.A. (2009) Contact angle and stability of interfacial nanobubbles. *Langmuir*, **25**, 8907–10. <https://doi.org/10.1021/la902011v>
- [62] Nirmalkar, N., Pacek, A.W. and Barigou, M. (2018) Interpreting the interfacial and colloidal stability of bulk nanobubbles. *Soft Matter*, **14**, 9643–9656. <https://doi.org/10.1039/c8sm01949e>
- [63] Nakashima, S. (2004) Physicochemistry of water in geological and biological systems: structures and properties of thin aqueous films. *Proceedings of the International Symposium on Physicochemistry of Water and Dynamics of Materials and the Earth--structures and Behaviors of the Thin Film Water*, Universal Academy Press. Tokyo, Japan.
- [64] Goldman, S., Solano-Altamirano, J.M. and Ledez, K.M. (2018) Driving force of gas-bubble growth and dissolution. *Gas Bubble Dynamics in the Human Body*, Elsevier. p. 49–62. <https://doi.org/10.1016/B978-0-12-810519-1.00002-6>
- [65] Bunkin, N.F., Shkirin, A. V., Ignatiev, P.S., Chaikov, L.L., Burkhanov, I.S. and Starosvetskij, A. V. (2012) Nanobubble clusters of dissolved gas in aqueous solutions of electrolyte. I. Experimental proof. *Journal of Chemical Physics*, **137**, 054706. <https://doi.org/10.1063/1.4739528>
- [66] Riesz, P., Berdahl, D. and Christman, C.L. (1985) Free radical generation by ultrasound in aqueous and nonaqueous solutions. *Environmental Health Perspectives*, **64**, 233–252. <https://doi.org/10.1289/ehp.8564233>

- [67] Gogate, P.R., Shirgaonkar, I.Z., Sivakumar, M., Senthilkumar, P., Vichare, N.P. and Pandit, A.B. (2001) Cavitation reactors: Efficiency assessment using a model reaction. *American Institute of Chemical Engineers Journals*, **47**, 2526–2538. <https://doi.org/10.1002/aic.690471115>
- [68] Krishnan, J.S., Dwivedi, P. and Moholkar, V.S. (2006) Numerical investigation into the chemistry induced by hydrodynamic cavitation. *Industrial and Engineering Chemistry Research*, **45**, 1493–1504. <https://doi.org/10.1021/ie050839t>
- [69] Tada, K., Maeda, M., Nishiuchi, Y., Nagahara, J., Hata, T., Zhuowei, Z. et al. (2014) ESR measurement of hydroxyl radicals in micro-nanobubble water. *Chemistry Letters*, **43**, 1907-1908. <https://doi.org/10.1246/cl.140691>
- [70] Hu, L. and Xia, Z. (2018) Application of ozone micro-nano-bubbles to groundwater remediation. *Journal of Hazardous Materials*, **342**, 446–453. <https://doi.org/10.1016/j.jhazmat.2017.08.030>
- [71] Meegoda, J.N. (2016) Remediation of Contaminated Sediments with Ultrasound and Ozone Nano-bubbles [Abstract]. Retrieved November 30, 2020, from, [https://www.nsf.gov/awardsearch/showAward?AWD\\_ID=1634857&HistoricalAwards=false](https://www.nsf.gov/awardsearch/showAward?AWD_ID=1634857&HistoricalAwards=false)
- [72] Aluthgun Hewage, S., Batagoda, J.H. and Meegoda, J.N. (2020) In situ remediation of sediments contaminated with organic pollutants using ultrasound and ozone nanobubbles. *Environmental Engineering Science*, **37**, 521–534. <https://doi.org/10.1089/ees.2019.0497>
- [73] Batagoda, J.H., Hewage, S.D.A. and Meegoda, J.N. (2019) Remediation of heavy-metal-contaminated sediments in USA using ultrasound and ozone nanobubbles. *Journal of Environmental Engineering and Science*, **14**, 130–138. <https://doi.org/10.1680/jenes.18.00012>
- [74] Meegoda, J.N., Batagoda, J.H. and Aluthgun-Hewage, S. (2017) Briefing: In situ decontamination of sediments using ozone nanobubbles and ultrasound. *Journal of Environmental Engineering and Science*, **12**, 1–3. <https://doi.org/10.1680/jenes.17.00006>
- [75] Hu, L., Wu, X., Liu, Y., Meegoda, J.N. and Gao, S. (2010) Physical modeling of air flow during air sparging remediation. *Environmental Science and Technology*, **44**, 3883–3888. <https://doi.org/10.1021/es903853v>
- [76] Hu, L., Meegoda, J.N., Du, J., Gao, S. and Wu, X. (2011) Centrifugal study of zone of influence during air-sparging. *Journal of Environmental Monitoring*, **13**, 2443–2449. <https://doi.org/10.1039/c0em00594k>

- [77] Hu, L., Meegoda, J.N., Li, H., Du, J. and Gao, S. (2015) Study of flow transitions during air sparging using the geotechnical centrifuge. *Journal of Environmental Engineering*, **141**, 04014048. [https://doi.org/10.1061/\(asce\)ee.1943-7870.0000877](https://doi.org/10.1061/(asce)ee.1943-7870.0000877)
- [78] NIH. (2016) Nanobubbles generated by pulsed laser identify & destroy cancer cells. Retrieved November 30, 2020, from, <https://www.nibib.nih.gov/news-events/newsroom/nanobubbles-generated-pulsed-laser-identify-destroy-cancer-cells>
- [79] Narayan, D. (2014) Development and application of nanobubbles. Retrieved November 30, 2020, from, <https://www.biotecharticles.com/Nanotechnology-Article/Development-and-Applications-of-Nanobubbles-3129.html>
- [80] Bauer Nanobubbles. (2020) Nanobubbles applications. Retrieved November 30, 2020, from, <http://www.nanobubbles.com/what-are-nanobubbles/nanobubbles-applications/#.WWexoYjyvIU>
- [81] Bauer, W.J. (2015.) Nanobubble-containing liquid solutions. Retrieved November 30, 2020, from, <https://patents.google.com/patent/CA2888661A1/en>
- [82] Nanobubble Systems. (2020) Nanobubble systems applications: dissolved air flotation (DAF). Retrieved November 30, 2020, from, <https://www.nanobubblesystems.com/aquaculture>
- [83] Nanobubble Systems. (2020) Nanobubble systems applications: cleaning processes. Retrieved November 30, 2020, from, <https://www.nanobubblesystems.com/cleaning-processes>
- [84] Nanobubble Systems. (2020) Nanobubble systems applications: aquaculture. Retrieved November 30, 2020, from, <https://www.nanobubblesystems.com/aquaculture>
- [85] Ozone Solutions. (2020) Ozone solubility in water. Retrieved November 30, 2020, from, <https://ozonesolutions.com/blog/ozone-solubility-in-water/>
- [86] Wang, L.K., Shammass, N.K., Selke, W.A. and Aulenbach, D.B. (2010) Gas dissolution, Release, and Bubble Formation in Flotation Systems. *Flotation Technology*, **12**, 49-83. [https://doi.org/10.1007/978-1-60327-133-2\\_2](https://doi.org/10.1007/978-1-60327-133-2_2)
- [87] Hasegawa, H., Kataoka, H. and Asano, K. (2009) Effect of electrical potential of microbubbles on ozone dissolution. *Journal of Physics: Conference Series*, **147** 012024. <https://doi.org/10.1088/1742-6596/147/1/012024>

- [88] Zheng, T., Wang, Q., Zhang, T., Shi, Z., Tian, Y., Shi, S. et al. (2015) Microbubble enhanced ozonation process for advanced treatment of wastewater produced in acrylic fiber manufacturing industry. *Journal of Hazardous Materials*, **287**, 412-420. <https://doi.org/10.1016/j.jhazmat.2015.01.069>
- [89] Jia, W., Ren, S. and Hu, B. (2013) Effect of water chemistry on zeta potential of air bubbles. *International Journal of Electrochemical Science*, **8**, 5828–5837.
- [90] Liu, H. and Cao, G. (2016) Effectiveness of the Young-Laplace equation at nanoscale. *Scientific Reports*, **6**, 23936. <https://doi.org/10.1038/srep23936>
- [91] Eagleton, J. (1999) Ozone in drinking water treatment. Retrieved November 30, 2020, from, <https://www.ozonotech.com/sites/default/files2/pdf/Ozone-in-Drinking-Water-Treatment-A-brief-overview.pdf>
- [92] Cho, S.H., Kim, J.Y.D., Chun, J.H. and Kim, J.Y.D. (2005) Ultrasonic formation of nanobubbles and their zeta-potentials in aqueous electrolyte and surfactant solutions. *Colloids and Surfaces A: Physicochemical and Engineering Aspects*, **269**, 28–34. <https://doi.org/10.1016/j.colsurfa.2005.06.063>
- [93] Nirmalkar, N., Pacek, A.W. and Barigou, M. (2018) On the existence and stability of bulk nanobubbles. *Langmuir*, **37**, 10964-10973. <https://doi.org/10.1021/acs.langmuir.8b01163>
- [94] Oh, S.H. and Kim, J.-M. (2017) Generation and stability of bulk nanobubbles. *Langmuir*, **33**, 3818–23. <https://doi.org/10.1021/acs.langmuir.7b00510>
- [95] Sekiguchi, T., Kawaguchi, T., Saito, T. and Satoh, I. (2011) Investigation of brownian motion of micro- and nano-bubble [abstract]. *Transactions of The Japan Society of Mechanical Engineers Series B*, **77**, 2316–2327.
- [96] Ljunggren, S. and Eriksson, J.C. (1997) The lifetime of a colloid-sized gas bubble in water and the cause of the hydrophobic attraction. *Colloids and Surfaces A: Physicochemical and Engineering Aspects*, **129–130**, 151–155. [https://doi.org/10.1016/S0927-7757\(97\)00033-2](https://doi.org/10.1016/S0927-7757(97)00033-2)
- [97] German, S.R., Chen, Q., Edwards, M.A. and White, H.S. (2016) Electrochemical measurement of hydrogen and nitrogen nanobubble lifetimes at Pt nanoelectrodes. *Journal of The Electrochemical Society*, **163**, H3160–3166. <https://doi.org/10.1149/2.0221604jes>
- [98] Bunkin, N.F., Yurchenko, S.O., Suyazov, N. V. and Shkirin, A. V. (2012) Structure of the nanobubble clusters of dissolved air in liquid media. *Journal of Biological Physics*, **38**, 121–152. <https://doi.org/10.1007/s10867-011-9242-8>

- [99] Dressaire, E., Bee, R., Bell, D.C., Lips, A. and Stone, H.A. (2008) Interfacial polygonal nanopatterning of stable microbubbles. *Science*, **320**, 1198–1201. <https://doi.org/10.1126/science.1154601>
- [100] Liu, X., Ding, W., Tian, R., Du, W. and Li, H. (2017) Position of shear plane at the clay-water interface: strong polarization effects of counterions. *Soil Science Society of America Journal*, **81**, 268–276. <https://doi.org/10.2136/sssaj2016.08.0261>
- [101] Ding, W., Liu, X., Song, L., Li, Q., Zhu, Q., Zhu, H. et al. (2015) An approach to estimate the position of the shear plane for colloidal particles in an electrophoresis experiment. *Surface Science*, **632**, 50–59. <https://doi.org/10.1016/j.susc.2014.08.024>
- [102] Li, H., Wei, S., Qing, C. and Yang, J. (2003) Discussion on the position of the shear plane. *Journal of Colloid and Interface Science*, **258**, 40–44. [https://doi.org/10.1016/S0021-9797\(02\)00077-2](https://doi.org/10.1016/S0021-9797(02)00077-2)
- [103] Sainath, K. and Ghosh, P. (2014) Electrical properties of silicone oil-water interface in the presence of ionic surfactants and salt: importance in the stability of oil-in-water emulsions. *Chemical Engineering Communications*, **201**, 1645–1663. <https://doi.org/10.1080/00986445.2013.823543>
- [104] Delgado, A.V., González-Caballero, F., Hunter, R.J., Koopal, L.K. and Lyklema, J. (2007) Measurement and interpretation of electrokinetic phenomena. *Journal of Colloid and Interface Science*, **309**, 194–224. <https://doi.org/10.1016/j.jcis.2006.12.075>
- [105] Leroy, P., Jougnot, D., Revil, A., Lassin, A. and Azaroual, M. (2012) A double layer model of the gas bubble/water interface. *Journal of Colloid and Interface Science*, **388**, 243–256. <https://doi.org/10.1016/j.jcis.2012.07.029>
- [106] Verwey, E.J.W., Overbeek, J.T.G. and Overbeek, J.T.G. (1999) *Theory of the Stability of Lyophobic Colloids* [Internet]. Dover Publications.
- [107] Tripathy, S., Bag, R. and Thomas, H.R. (2014) Effect of Stern-layer on the compressibility behaviour of bentonites. *Acta Geotechnica*, **9**, 1097–1099. <https://doi.org/10.1007/s11440-013-0222-y>
- [108] Shang, J.Q., Lo, K.Y. and Quigley, R.M. (1994) Quantitative determination of potential distribution in Stern–Gouy double-layer model. *Canadian Geotechnical Journal*, **31**, 624–636. <https://doi.org/10.1139/t94-075>
- [109] Sridharan, A. (1996) Potential-distance relationships of clay-water systems considering the stern theory. *Clays and Clay Minerals*, **44**, 479–484. <https://doi.org/10.1346/CCMN.1996.0440405>

- [110] Brown, M.A., Abbas, Z., Kleibert, A., Green, R.G., Goel, A., May, S. et al. (2016) Determination of surface potential and electrical double-layer structure at the aqueous electrolyte-nanoparticle interface. *Physical Review X*, **6**, 011007. <https://doi.org/10.1103/PhysRevX.6.011007>
- [111] Herbowski, L., Gurgul, H. and Staron, W. (2009) Experimental determination of the Stern layer thickness at the interface of the human arachnoid membrane and the cerebrospinal fluid. *Zeitschrift Für Medizinische Physik*, **19**, 189–192. <https://doi.org/10.1016/j.zemedi.2009.06.007>
- [112] Allison, S., Rasmusson, M. and Wall, S. (2003) The primary electroviscous effect, free solution electrophoretic mobility, and diffusion of dilute prolate ellipsoid particles (minor axis = 3 nm) in monovalent salt solution. *Journal of Colloid and Interface Science*, **258**, 289–297. [https://doi.org/10.1016/S0021-9797\(02\)00215-1](https://doi.org/10.1016/S0021-9797(02)00215-1)
- [113] Lim, J., Whitcomb, J., Boyd, J. and Varghese, J. (2007) Transient finite element analysis of electric double layer using Nernst–Planck–Poisson equations with a modified Stern layer. *Journal of Colloid and Interface Science*, **305**, 159–174. <https://doi.org/10.1016/j.jcis.2006.08.049>
- [114] Brown, M.A., Goel, A. and Abbas, Z. (2016) Effect of electrolyte concentration on the stern layer thickness at a charged interface. *Angewandte Chemie International Edition*, **55**, 3790–3794. <https://doi.org/10.1002/anie.201512025>
- [115] Kielland, J. (1937) Individual activity coefficients of ions in aqueous solutions. *Journal of the American Chemical Society*, **59**, 1675–1678. <https://doi.org/10.1021/ja01288a032>
- [116] Debye, P. and Hückel, E. (1923) The theory of electrolytes. I. Lowering of freezing point and related phenomena. *Physikalische Zeitschrift*.
- [117] Tuinier, R. (2003) Approximate solutions to the Poisson–Boltzmann equation in spherical and cylindrical geometry. *Journal of Colloid and Interface Science*, **258**, 45–49. [https://doi.org/10.1016/S0021-9797\(02\)00142-X](https://doi.org/10.1016/S0021-9797(02)00142-X)
- [118] Ohshima, H., Healy, T.W. and White, L.R. (1982) Accurate analytic expressions for the surface charge density/surface potential relationship and double-layer potential distribution for a spherical colloidal particle. *Journal of Colloid and Interface Science*, **90**, 17–26. [https://doi.org/10.1016/0021-9797\(82\)90393-9](https://doi.org/10.1016/0021-9797(82)90393-9)
- [119] Loeb, A.L., Overbeek, J.T.G. and Wiersema, P.H. (1961) The electrical double layer around a spherical colloidal particle. *Journal of The Electrochemical Society*, **108**, 269C-269C.



- [120] Leite, F.L., Bueno, C.C., Da Róz, A.L., Ziemath, E.C. and Oliveira, O.N. (2012) Theoretical models for surface forces and adhesion and their measurement using atomic force microscopy. *International Journal of Molecular Sciences*, **13**, 12773–12856. <https://doi.org/10.3390/ijms131012773>
- [121] Uskoković, V. (2012) Dynamic light scattering based microelectrophoresis: main prospects and limitations. *Journal of Dispersion Science and Technology*, **33**, 1762–1786. <https://doi.org/10.1080/01932691.2011.625523>
- [122] Xie, L., Shi, C., Cui, X., Huang, J., Wang, J., Liu, Q. et al. (2018) Probing the interaction mechanism between air bubbles and bitumen surfaces in aqueous media using bubble probe atomic force microscopy. *Langmuir*, **34**, 729–738. <https://doi.org/10.1021/acs.langmuir.7b02693>
- [123] Xie, L., Shi, C., Cui, X. and Zeng, H. (2017) Surface forces and interaction mechanisms of emulsion drops and gas bubbles in complex fluids. *Langmuir*, **33**, 3911–3925. <https://doi.org/10.1021/acs.langmuir.6b04669>
- [124] Chen, A., Li, S.-W., Sang, F.-N., Zeng, H.-B. and Xu, J.-H. (2018) Interactions between micro-scale oil droplets in aqueous surfactant solution determined using optical tweezers. *Journal of Colloid and Interface Science*, **532**, 128–135. <https://doi.org/10.1016/j.jcis.2018.07.116>
- [125] Israelachvili, J.N. (2011) Electrostatic forces between surfaces in liquids. *Intermolecular and Surface Forces*, p. 291–340. <https://doi.org/10.1016/b978-0-12-375182-9.10014-4>
- [126] Hamaker, H.C. (1937) The London—van der Waals attraction between spherical particles. *Physica*, **4**, 1058–1072. [https://doi.org/10.1016/S0031-8914\(37\)80203-7](https://doi.org/10.1016/S0031-8914(37)80203-7)
- [127] Nörtemann, K., Hilland, J. and Kaatze, U. (1997) Dielectric properties of aqueous NaCl solutions at microwave frequencies. *The Journal of Physical Chemistry A*, **101**, 6864–6869. <https://doi.org/10.1021/jp971623a>
- [128] Schnitzer, O., Frankel, I. and Yariv, E. (2014) Electrophoresis of bubbles. *Journal of Fluid Mechanics*, **753**, 49–79. <https://doi.org/10.1017/jfm.2014.350>
- [129] Higuchi, S. and Satoh, M. (2017) Effects of NaCl, NaOH, and HCl concentration on the cloud point of poly(vinyl methyl ether) in water—electrostatic interactions are inevitably involved in the hydrophobic interaction. *Colloid and Polymer Science*, **295**, 1511–20. <https://doi.org/10.1007/s00396-017-4130-9>
- [130] Jones, G. and Ray, W.A. (1937) The surface tension of solutions of electrolytes as a function of the concentration. I. A differential method for measuring relative surface tension. *Journal of the American Chemical Society*, **59**, 187–198. <https://doi.org/10.1021/ja01280a048>

- [131] Jones, G. and Ray, W.A. (1941) The surface tension of solutions of electrolytes as a function of the concentration  $\Pi^*$ . *Journal of the American Chemical Society*, **63**, 288–294. <https://doi.org/10.1021/ja01846a070>
- [132] Duignan, T., Baer, M. and Mundy, C. (2017) Surfactant impurities can explain the Jones-Ray effect. *Surfactant Impurities Can Explain the Jones-Ray Effect*, <https://doi.org/10.26434/chemrxiv.5732976>
- [133] Jadhav, A.J. and Barigou, M. (2020) Bulk nanobubbles or not nanobubbles: that is the question. *Langmuir*, **36**, 1699–1708. <https://doi.org/10.1021/acs.langmuir.9b03532>
- [134] Li, H., Hu, L., Song, D. and Lin, F. (2015) Characteristics of micro-nano bubbles and potential application in groundwater bioremediation. *Water Environment Research*, **86**, 844–851. <https://doi.org/10.2175/106143014x14062131177953>
- [135] Xia, Z. and Hu, L. (2018) Treatment of organics contaminated wastewater by ozone micro-nano-bubbles. *Water (Switzerland)*, **11**. <https://doi.org/10.3390/w11010055>
- [136] Batagoda, J.H., Meegoda, J.N. and Hewage, S.A. (2018) In situ remediation of Passaic River sediments using ultrasound and ozone nanobubbles. *World Environmental and Water Resources Congress 2018: Groundwater, Sustainability, and Hydro-Climate/Climate Change - Selected Papers from the World Environmental and Water Resources Congress 2018*, American Society of Civil Engineers, Reston, VA. 49–63. <https://doi.org/10.1061/9780784481417.005>
- [137] Gao, Y., Hernandez, C., Yuan, H.X., Lilly, J., Kota, P., Zhou, H. et al. (2017) Ultrasound molecular imaging of ovarian cancer with CA-125 targeted nanobubble contrast agents. *Nanomedicine: Nanotechnology, Biology, and Medicine*, **13**, 2159–2168. <https://doi.org/10.1016/j.nano.2017.06.001>
- [138] Lukianova-Hleb, E.Y., Ren, X., Sawant, R.R., Wu, X., Torchilin, V.P. and Lapotko, D.O. (2014) On-demand intracellular amplification of chemoradiation with cancer-specific plasmonic nanobubbles. *Nature Medicine*, **20**, 778–784. <https://doi.org/10.1038/nm.3484>
- [139] Thakur, S.S., Chen, Y.S., Houston, Z.H., Fletcher, N., Barnett, N.L., Thurecht, K.J. et al. (2019) Ultrasound-responsive nanobubbles for enhanced intravitreal drug migration: An ex vivo evaluation. *European Journal of Pharmaceutics and Biopharmaceutics*, **136**, 102–107. <https://doi.org/10.1016/j.ejpb.2019.01.014>
- [140] Azevedo, A., Oliveira, H. and Rubio, J. (2019) Bulk nanobubbles in the mineral and environmental areas: Updating research and applications. *Advances in Colloid and Interface Science*, **271**, 101992. <https://doi.org/10.1016/j.cis.2019.101992>

- [141] Sang, H.H., Jiao, X.Y., Wang, S.F., Guo, W.H., Salahou, M.K. and Liu, K.H. (2018) Effects of micro-nano bubble aerated irrigation and nitrogen fertilizer level on tillering, nitrogen uptake and utilization of early rice. *Plant, Soil and Environment*, **64**, 297–302. <https://doi.org/10.17221/240/2018-PSE>
- [142] Zhang, X. yu, Wang, Q. shuai, Wu, Z. xian and Tao, D. ping. (2020) An experimental study on size distribution and zeta potential of bulk cavitation nanobubbles. *International Journal of Minerals, Metallurgy and Materials*, **27**, 152–161. <https://doi.org/10.1007/s12613-019-1936-0>
- [143] Chen, C., Li, J. and Zhang, X. (2020) The existence and stability of bulk nanobubbles: a long-standing dispute on the experimentally observed mesoscopic inhomogeneities in aqueous solutions. *Communications in Theoretical Physics*, **72**, 037601. <https://doi.org/10.1088/1572-9494/ab6183>
- [144] Sun, Y., Xie, G., Peng, Y., Xia, W. and Sha, J. (2016) Stability theories of nanobubbles at solid-liquid interface: A review. *Colloids and Surfaces A: Physicochemical and Engineering Aspects*, **495**, 176-186. <https://doi.org/10.1016/j.colsurfa.2016.01.050>
- [145] Bui, T.T., Nguyen, D.C. and Han, M. (2019) Average size and zeta potential of nanobubbles in different reagent solutions. *Journal of Nanoparticle Research*, **21**. <https://doi.org/10.1007/s11051-019-4618-y>
- [146] Guo, Z., Wang, X., Wang, H., Hu, B., Lei, Z., Kobayashi, M. et al. (2019) Effects of nanobubble water on the growth of: *Lactobacillus acidophilus* 1028 and its lactic acid production. *RSC Advances*, **9**, 30760–30767. <https://doi.org/10.1039/c9ra05868k>
- [147] Jadhav, A.J. and Barigou, M. (2020) Proving and interpreting the spontaneous formation of bulk nanobubbles in aqueous organic solvent solutions: Effects of solvent type and content. *Soft Matter*, **16**, 4502–4511. <https://doi.org/10.1039/d0sm00111b>
- [148] Yasuda, K., Matsushima, H. and Asakura, Y. (2019) Generation and reduction of bulk nanobubbles by ultrasonic irradiation. *Chemical Engineering Science*, **195**, 455–461. <https://doi.org/10.1016/j.ces.2018.09.044>
- [149] Min, S.H. and Berkowitz, M.L. (2019) Bubbles in water under stretch-induced cavitation. *Journal of Chemical Physics*, **150**, 054501. <https://doi.org/10.1063/1.5079735>
- [150] Kim, S., Kim, H., Han, M. and Kim, T. (2019) Generation of sub-micron (Nano) bubbles and characterization of their fundamental properties. *Environmental Engineering Research*, **24**, 382–388. <https://doi.org/10.4491/EER.2018.210>

- [151] N. Meegoda, J., Aluthgun Hewage, S., H. Batagoda, J., Meegoda, J.N., Hewage, S.A. and Batagoda, J.H. (2019) Application of the Diffused Double Layer Theory to Nanobubbles. *Langmuir*, **35**, 12100–12112. <https://doi.org/10.1021/acs.langmuir.9b01443>
- [152] López-García, J.J., Moya, A.A., Horno, J., Delgado, A. and González-Caballero, F. (1996) A network model of the electrical double layer around a colloid particle. *Journal of Colloid and Interface Science*, **183**, 124–30. <https://doi.org/10.1006/jcis.1996.0525>
- [153] Prince, M.J. and Blanch, H.W. (1990) Transition electrolyte concentrations for bubble coalescence. *American Institute of Chemical Engineers Journals*, **36**, 1425–1429. <https://doi.org/10.1002/aic.690360915>
- [154] Firouzi, M., Howes, T. and Nguyen, A. V. (2015) A quantitative review of the transition salt concentration for inhibiting bubble coalescence. *Advances in Colloid and Interface Science*, **222**, 305–318. <https://doi.org/10.1016/j.cis.2014.07.005>
- [155] Bhushan, B., Pan, Y. and Daniels, S. (2013) AFM characterization of nanobubble formation and slip condition in oxygenated and electrokinetically altered fluids. *Journal of Colloid and Interface Science*, **392**, 105–116. <https://doi.org/10.1016/j.jcis.2012.09.077>
- [156] Corridoni, T., Mancinelli, R., Ricci, M.A. and Bruni, F. (2011) Viscosity of aqueous solutions and local microscopic structure. *Journal of Physical Chemistry B*, **115**, 14008–1413. <https://doi.org/10.1021/jp202755u>
- [157] Das, S., Snoeijer, J.H. and Lohse, D. (2010) Effect of impurities in description of surface nanobubbles. *Physical Review E - Statistical, Nonlinear, and Soft Matter Physics*, **82**, 056310. <https://doi.org/10.1103/PhysRevE.82.056310>
- [158] Ushida, A., Hasegawa, T., Narumi, T. and Nakajima, T. (2013) Flow properties of nanobubble mixtures passing through micro-orifices. *International Journal of Heat and Fluid Flow*, **40**, 106–115. <https://doi.org/10.1016/j.ijheatfluidflow.2013.01.013>
- [159] Attard, P. (2013) The stability of nanobubbles. *The European Physical Journal Special Topics*. <https://doi.org/10.1140/epjst/e2013-01817-0>
- [160] Sjøgreen, C.A., Landínez Téllez, D.A., Rosas Pérez, J.E., Plazas Hurtado, P.C. and Roa-Rojas, J. (2018) Experimental study of nanobubbles in salt solutions. *Revista de La Academia Colombiana de Ciencias Exactas, Físicas y Naturales*, **42**, 41. <https://doi.org/10.18257/raccefyn.543>

- [161] Yurchenko, S.O., Shkirin, A. V., Ninham, B.W., Sychev, A.A., Babenko, V.A., Penkov, N. V. et al. (2016) Ion-specific and thermal effects in the stabilization of the gas nanobubble phase in bulk aqueous electrolyte solutions. *Langmuir*, **32**, 11245–11255. <https://doi.org/10.1021/acs.langmuir.6b01644>
- [162] Han, M.Y., Kim, M.K. and Shin, M.S. (2006) Generation of a positively charged bubble and its possible mechanism of formation. *Journal of Water Supply: Research and Technology - AQUA*, **55**, 471–478. <https://doi.org/10.2166/aqua.2006.055>
- [163] Han, M.Y., Kim, M.K. and Ahn, H.J. (2006) Effects of surface charge, micro-bubble size and particle size on removal efficiency of electro-flotation. *Water Science and Technology*, **53**, 127–132. <https://doi.org/10.2166/wst.2006.216>
- [164] Han, M.Y., Ahn, H.J., Shin, M.S. and Kim, S.R. (2004) The effect of divalent metal ions on the zeta potential of bubbles. *Water Science and Technology*, **50**, 49–56. <https://doi.org/10.2166/wst.2004.0486>
- [165] Karraker, K.A. and Radke, C.J. (2002) Disjoining pressures, zeta potentials and surface tensions of aqueous non-ionic surfactant/electrolyte solutions: Theory and comparison to experiment. *Advances in Colloid and Interface Science*, **96**, 231–264. [https://doi.org/10.1016/S0001-8686\(01\)00083-5](https://doi.org/10.1016/S0001-8686(01)00083-5)
- [166] Yang, C., Dabros, T., Li, D., Czarnecki, J. and Masliyah, J.H. (2001) Measurement of the zeta potential of gas bubbles in aqueous solutions by microelectrophoresis method. *Journal of Colloid and Interface Science*, **243**, 128–135. <https://doi.org/10.1006/jcis.2001.7842>
- [167] Hewage, S.A., Kewalramani, J. and Meegoda, J.N.J.N. (2021) Stability of nanobubbles in different salts solutions. *Colloids and Surfaces A: Physicochemical and Engineering Aspects*, **609**, 125669. <https://doi.org/10.1016/j.colsurfa.2020.125669>
- [168] Hong, S.-N., Choe, S.-H., Jong, U.-G., Pak, M.-S. and Yu, C.-J. (2019) The maximum interbubble distance in relation to the radius of spherical stable nanobubble in liquid water: A molecular dynamics study. *Fluid Phase Equilibria*, **487**, 45–51. <https://doi.org/https://doi.org/10.1016/j.fluid.2019.01.014>
- [169] Jain, S. and Qiao, L. (2017) Molecular dynamics simulations of the surface tension of oxygen-supersaturated water. *AIP Advances*, American Institute of Physics. **7**, 45001. <https://doi.org/10.1063/1.4979662>
- [170] Yamamoto, T. and Ohnishi, S. (2011) Molecular dynamics study on helium nanobubbles in water. *Physical Chemistry Chemical Physics*, **13**, 16142–16145. <https://doi.org/10.1039/c1cp22018g>

- [171] Matsumoto, M. (2008) Surface tension and stability of a nanobubble in water: molecular simulation. *Journal of Fluid Science and Technology*, **3**, 922–929. <https://doi.org/10.1299/jfst.3.922>
- [172] Ng, W.Y. and Walkley, J. (1969) Diffusion of gases in liquids: the constant size bubble method. *Canadian Journal of Chemistry*, **47**, 1075-1077. <https://doi.org/10.1139/v69-170>
- [173] Vaz, R. V., Gomes, J.R.B. and Silva, C.M. (2016) Molecular dynamics simulation of diffusion coefficients and structural properties of ketones in supercritical CO<sub>2</sub> at infinite dilution. *Journal of Supercritical Fluids*, **107**, 630-638. <https://doi.org/10.1016/j.supflu.2015.07.025>
- [174] Moody, M.P. and Attard, P. (2004) Monte Carlo simulation methodology of the ghost interface theory for the planar surface tension. *The Journal of Chemical Physics*, **120**, 1892–1904. <https://doi.org/10.1063/1.1635801>
- [175] He, S. and Attard, P. (2005) Surface tension of a Lennard-Jones liquid under supersaturation. *Physical Chemistry Chemical Physics*, **7**, 2928. <https://doi.org/10.1039/b507106b>
- [176] Lee, J. Il, Yim, B.-S. and Kim, J.-M. (2020) Effect of dissolved-gas concentration on bulk nanobubbles generation using ultrasonication. *Scientific Reports*, **10**, 18816. <https://doi.org/10.1038/s41598-020-75818-8>
- [177] Speece, R.E. (2007) Superoxygenation: Facts and myths. Retrieved November 30, 2020, from, <http://www.eco2tech.com/wp-content/uploads/2016/01/Superoxygenation-Facts-and-Myths.pdf%0A>
- [178] German, S.R., Edwards, M.A., Chen, Q. and White, H.S. (2016) Laplace pressure of individual H<sub>2</sub> nanobubbles from pressure–addition electrochemistry. *Nano Letters*, **16**, 6691–6694. <https://doi.org/10.1021/acs.nanolett.6b03590>
- [179] USEPA. (2016) Record of decision: Lower 8.3 Miles of the lower Passaic river part of the Diamond Alkali Superfund site Essex and Hudson Counties, New Jersey. *United States Environmental Protection Agency*. Retrieved November 30, 2020, from, <https://semspub.epa.gov/work/02/396055.pdf>
- [180] USEPA. (2017) Community involvement plan for the Lower Passaic River. *United States Environmental Protection Agency*. Retrieved November 30, 2020, from, <https://semspub.epa.gov/work/02/538469.pdf>

- [181] Cotillas, S., Lacasa, E., Herraiz-Carboné, M., Sáez, C., Cañizares, P. and Rodrigo, M.A. (2020) Innovative photoelectrochemical cell for the removal of CHCs from soil washing wastes. *Separation and Purification Technology*, **230**, 115876. <https://doi.org/10.1016/j.seppur.2019.115876>
- [182] Falciglia, P.P., Mancuso, G., Scandura, P. and Vagliasindi, F.G.A. (2015) Effective decontamination of low dielectric hydrocarbon-polluted soils using microwave heating: Experimental investigation and modelling for in situ treatment. *Separation and Purification Technology*, **156**, 480–488. <https://doi.org/10.1016/j.seppur.2015.10.038>
- [183] U.S. EPA. (2006) In situ treatment technologies for contaminated soil. Retrieved November 30, 2020, <https://clu-in.org/download/remed/542f06013.pdf>
- [184] Rocha, I.M.V., Silva, K.N.O., Silva, D.R., Martínez-Huitle, C.A. and Santos, E. V. (2019) Coupling electrokinetic remediation with phytoremediation for depolluting soil with petroleum and the use of electrochemical technologies for treating the effluent generated. *Separation and Purification Technology*, **208**, 194–200. <https://doi.org/10.1016/j.seppur.2018.03.012>
- [185] Lemaire, J., Buès, M., Kabeche, T., Hanna, K. and Simonnot, M.O. (2013) Oxidant selection to treat an aged PAH contaminated soil by in situ chemical oxidation. *Journal of Environmental Chemical Engineering*, **1**, 1261–1268. <https://doi.org/10.1016/j.jece.2013.09.018>
- [186] Peters, C.A., Knightes, C.D. and Brown, D.G. (1999) Long-term composition dynamics of PAH-containing NAPLs and implications for risk assessment. *Environmental Science and Technology*, **33**, 4499–4507. <https://doi.org/10.1021/es981203e>
- [187] O’Mahony, M.M., Dobson, A.D.W., Barnes, J.D. and Singleton, I. (2006) The use of ozone in the remediation of polycyclic aromatic hydrocarbon contaminated soil. *Chemosphere*, **63**, 307–314. <https://doi.org/10.1016/j.chemosphere.2005.07.018>
- [188] Goi, A. and Viisimaa, M. (2015) Integration of ozonation and sonication with hydrogen peroxide and persulfate oxidation for polychlorinated biphenyls-contaminated soil treatment. *Journal of Environmental Chemical Engineering*, **3**, 2839–2847. <https://doi.org/10.1016/j.jece.2015.09.025>
- [189] Tiwari, B.K. (2015) Ultrasound: A clean, green extraction technology. *TrAC - Trends in Analytical Chemistry*, **71**, 100–109. <https://doi.org/10.1016/j.trac.2015.04.013>
- [190] Feng, D. and Aldrich, C. (2000) Sonochemical treatment of simulated soil contaminated with diesel. *Advances in Environmental Research*, **4**, 103–112. [https://doi.org/10.1016/S1093-0191\(00\)00008-3](https://doi.org/10.1016/S1093-0191(00)00008-3)

- [191] Effendi, A.J., Wulandari, M. and Setiadi, T. (2019) Ultrasonic application in contaminated soil remediation. *Current Opinion in Environmental Science and Health*, **12**, 66–71. <https://doi.org/10.1016/j.coesh.2019.09.009>
- [192] Hoffmann, M.R., Hua, I. and Höchemer, R. (1996) Application of ultrasonic irradiation for the degradation of chemical contaminants in water. *Ultrasonics Sonochemistry*, **3**, S163–172. [https://doi.org/10.1016/S1350-4177\(96\)00022-3](https://doi.org/10.1016/S1350-4177(96)00022-3)
- [193] Conklin, A. (1995) Secrets of clay: Why is it most stubborn and difficult soil type to clean up? *Soil & Groundwater Cleanup*, 38-41.
- [194] Meegoda, J.N. and Martin, L. (2019) In-situ determination of specific surface area of clays. *Geotechnical and Geological Engineering*, **37**, 465–474. <https://doi.org/10.1007/s10706-018-0623-7>
- [195] Hung, H.M. and Hoffmann, M.R. (1999) Kinetics and mechanism of the sonolytic degradation of chlorinated hydrocarbons: Frequency effects. *Journal of Physical Chemistry A*, **103**, 2734–9. <https://doi.org/10.1021/jp9845930>
- [196] Hatanaka, S.I., Yasui, K., Kozuka, T., Tuziuti, T. and Mitome, H. (2002) Influence of bubble clustering on multibubble sonoluminescence. *Ultrasonics*, **40**, 655–660. [https://doi.org/10.1016/S0041-624X\(02\)00193-2](https://doi.org/10.1016/S0041-624X(02)00193-2)
- [197] Chen, D. (2011) Applications of ultrasound in water and wastewater treatment. *Handbook on Applications of Ultrasound: Sonochemistry for Sustainability*, CRC Press. p. 373–405. <https://doi.org/10.1201/b11012-16>
- [198] Dietrich, M., Andaluri, G., Smith, R.C. and Suri, R. (2017) Combined ozone and ultrasound for the removal of 1,4-Dioxane from drinking water. *Ozone: Science and Engineering*, **39**, 244–254. <https://doi.org/10.1080/01919512.2017.1321981>
- [199] Speight, J.G. (2018) Redox transformations. *Reaction Mechanisms in Environmental Engineering*, p. 231–267. <https://doi.org/10.1016/b978-0-12-804422-3.00007-9>
- [200] Son, Y. (2015) Advanced oxidation processes using ultrasound technology for water and wastewater treatment. In: Ashokkumar M, editor. *Handbook of Ultrasonics and Sonochemistry*, Springer Singapore, Singapore. p. 1–22. [https://doi.org/10.1007/978-981-287-470-2\\_53-1](https://doi.org/10.1007/978-981-287-470-2_53-1)
- [201] Staehelin, J. and Holgné, J. (1982) Decomposition of ozone in water: Rate of initiation by hydroxide ions and hydrogen peroxide. *Environmental Science and Technology*, **16**, 676–681. <https://doi.org/10.1021/es00104a009>



- [202] Hoigné, J. and Bader, H. (1983) Rate constants of reactions of ozone with organic and inorganic compounds in water-I. Non-dissociating organic compounds. *Water Research*, **17**, 173–183. [https://doi.org/10.1016/0043-1354\(83\)90098-2](https://doi.org/10.1016/0043-1354(83)90098-2)
- [203] Glaze, W.H., Kang, J.W. and Chapin, D.H. (1987) The chemistry of water treatment processes involving ozone, hydrogen peroxide and ultraviolet radiation. *Ozone: Science & Engineering*, **9**, 335–352. <https://doi.org/10.1080/01919518708552148>
- [204] Jürg, H. (1992) Comparison of ozone and hydroxyl radical-induced oxidation of chlorinated hydrocarbons in water. *Ozone: Science & Engineering*, **14**, 197–214. <https://doi.org/10.1080/01919519208552475>
- [205] Westerhoff, P., Song, R., Amy, G. and Minear, R. (1997) Applications of ozone decomposition models. *Ozone: Science and Engineering*, **19**, 55–73. <https://doi.org/10.1080/01919519708547318>
- [206] Krishnan, S., Rawindran, H., Sinnathambi, C.M. and Lim, J.W. (2017) Comparison of various advanced oxidation processes used in remediation of industrial wastewater laden with recalcitrant pollutants. *IOP Conference Series: Materials Science and Engineering*. <https://doi.org/10.1088/1757-899X/206/1/012089>
- [207] Ameta, S.C. and Ameta, R. (2018) Advanced oxidation processes for wastewater treatment: Emerging green chemical technology. <https://doi.org/10.1016/C2016-0-00384-4>
- [208] Andreozzi, R., Caprio, V., Insola, A. and Marotta, R. (1999) Advanced oxidation processes (AOP) for water purification and recovery. *Catalysis Today*, **53**, 51–59. [https://doi.org/10.1016/S0920-5861\(99\)00102-9](https://doi.org/10.1016/S0920-5861(99)00102-9)
- [209] Johnson, P.N. and Davis, R.A. (1996) Diffusivity of ozone in water. *Journal of Chemical and Engineering Data*, **41**, 1485–1487. <https://doi.org/10.1021/jc9602125>
- [210] Kavanaugh, M.C. and Trussell, R.R. (1980) Design of aeration towers to strip volatile contaminants from drinking water. *Journal / American Water Works Association*, **72**, 684–692. <https://doi.org/10.1002/j.1551-8833.1980.tb04613.x>
- [211] Hewa Batagoda, J. (2018) Decontamination of the Passaic River sediments using ultrasound with ozone nano-bubble [Dissertation]. New Jersey Institute of Technology. <https://digitalcommons.njit.edu/dissertations/1368>
- [212] Meegoda, J.N. and Perera, R. (2001) Ultrasound to decontaminate heavy metals in dredged sediments. *Journal of Hazardous Materials*, **85**, 73–89. [https://doi.org/10.1016/S0304-3894\(01\)00222-9](https://doi.org/10.1016/S0304-3894(01)00222-9)

- [213] Meegoda, J., Aluthgun Hewage, S. and H. Batagoda, J. (2019) Application of the diffused double layer theory to nanobubbles. *Langmuir*, **35**, 12100–12112. <https://doi.org/10.1021/acs.langmuir.9b01443>
- [214] Pavlostathls, S.G. and Mathavan, G.N. (1992) Desorption kinetics of selected volatile organic compounds from field contaminated soils. *Environmental Science and Technology*, **26**, 532–538. <https://doi.org/10.1021/es00027a014>
- [215] Hatzinger, P.B. and Alexander, M. (1995) Effect of aging of chemicals in soil on their biodegradability and extiactability. *Environmental Science and Technology*, **29**, 537–545. <https://doi.org/10.1021/es00002a033>
- [216] Meegoda, J.N. and Veerawat, K. (2002) Ultrasound to decontaminate organics in dredged sediments. *Soil and Sediment Contamination*, **11**, 91–116. <https://doi.org/10.1080/20025891106718>
- [217] Shrestha, R.A., Pham, T.D. and Sillanpää, M. (2009) Effect of ultrasound on removal of persistent organic pollutants (POPs) from different types of soils. *Journal of Hazardous Materials*, **170**, 871–875. <https://doi.org/10.1016/j.jhazmat.2009.05.048>
- [218] Zhang, J., Li, J., Thring, R. and Liu, L. (2013) Application of ultrasound and Fenton’s reaction process for the treatment of oily sludge. *Procedia Environmental Sciences*, **18**, 686–693. <https://doi.org/10.1016/j.proenv.2013.04.093>
- [219] Li, J., Song, X., Hu, G. and Thring, R.W. (2013) Ultrasonic desorption of petroleum hydrocarbons from crude oil contaminated soils. *Journal of Environmental Science and Health - Part A Toxic/Hazardous Substances and Environmental Engineering*, **48**, 1378–1389. <https://doi.org/10.1080/10934529.2013.781885>
- [220] Wulandari, M. and Effendi, A.J. (2018) Effect of frequency and ratio solid liquid on ultrasonic remediation of petroleum contaminated soil. *AIP Conference Proceedings*, p. 020120. <https://doi.org/10.1063/1.5054524>
- [221] Collings, A.F., Farmer, A.D., Gwan, P.B., Pintos, A.P.S. and Leo, C.J. (2006) Processing contaminated soils and sediments by high power ultrasound. *Minerals Engineering*, **19**, 450–453. <https://doi.org/10.1016/j.mineng.2005.07.014>
- [222] Kim, Y.U. and Wang, M.C. (2003) Effect of ultrasound on oil removal from soils. *Ultrasonics*, **41**, 539–542. [https://doi.org/10.1016/S0041-624X\(03\)00168-9](https://doi.org/10.1016/S0041-624X(03)00168-9)
- [223] Mason, T.J., Collings, A. and Sumel, A. (2004) Sonic and ultrasonic removal of chemical contaminants from soil in the laboratory and on a large scale. *Ultrasonics Sonochemistry*, **11**, 205–210. <https://doi.org/10.1016/j.ultsonch.2004.01.025>

- [224] Flores, R., Blass, G. and Domínguez, V. (2007) Soil remediation by an advanced oxidative method assisted with ultrasonic energy. *Journal of Hazardous Materials*, **140**, 399–402. <https://doi.org/10.1016/j.jhazmat.2006.09.044>
- [225] Chung, H.I. and Kamon, M. (2005) Ultrasonically enhanced electrokinetic remediation for removal of Pb and phenanthrene in contaminated soils. *Engineering Geology*, **77**, 233–420. <https://doi.org/10.1016/j.enggeo.2004.07.014>
- [226] Wuana, R. a, Okieimen, F.E. and Vesuwe, R.N. (2014) Mixed contaminant interactions in soil: Implications for bioavailability , risk assessment and remediation. *African Journal of Environmental Science and Technology*, **8**, 691–706.
- [227] Yong, R.N. (1995) Fate of toxic pollutants in contaminated sediments. *ASTM Special Technical Publication*, ASTM International, 100 Barr Harbor Drive, PO Box C700, West Conshohocken, PA 19428-2959. p. 13-13–27. <https://doi.org/10.1520/STP15989S>
- [228] U.S.EPA. (2019) What is sediment pollution? *Mid-America Regional Council*, Kansas City, Missouri. 1–2.
- [229] USEPA. (2014) Fact Sheets: The Passaic River’s Polluted Past. *United States Environmental Protection Agency*.
- [230] USEPA. (2014) Memorandum to Diane Salkie, Remedial Project Manager, Region 2. CSTAG Recommendations on the Lower Passaic River Study Area, 17 Mile Remedial Investigation/Feasibility Study and Proposed Interim Remedial Action. *United States Environmental Protection Agency*. <https://semspub.epa.gov/work/HQ/100001369.pdf>
- [231] Agency, U.S.E.P. (1991) Handbook - Remediation of Contaminated Sediments [Internet]. EPA, Cincinnati, OH. <https://semspub.epa.gov/work/HQ/189668.pdf>
- [232] Thomé, A., Reginatto, C., Vanzetto, G. and Braun, A.B. (2019) Remediation technologies applied in polluted soils: New perspectives in this field. *Environmental Science and Engineering*, p. 186–203. [https://doi.org/10.1007/978-981-13-2221-1\\_11](https://doi.org/10.1007/978-981-13-2221-1_11)
- [233] Sharma, A., Ahmad, J. and Flora, S.J.S. (2018) Application of advanced oxidation processes and toxicity assessment of transformation products. *Environmental Research*, **167**, 223–233. <https://doi.org/10.1016/j.envres.2018.07.010>
- [234] Kuppusamy, S., Palanisami, T., Megharaj, M., Venkateswarlu, K. and Naidu, R. (2016) Ex-situ remediation technologies for environmental pollutants: A critical perspective. *Reviews of Environmental Contamination and Toxicology*, p. 117–192. [https://doi.org/10.1007/978-3-319-20013-2\\_2](https://doi.org/10.1007/978-3-319-20013-2_2)

- [235] Teefy, D.A. (1997) Remediation technologies screening matrix and reference guide: Version III. Remediation. <https://doi.org/10.1002/rem.3440080111>
- [236] Loeb, B.L., Thompson, C.M., Drago, J., Takahara, H. and Baig, S. (2012) Worldwide Ozone Capacity for Treatment of Drinking Water and Wastewater: A Review. *Ozone: Science and Engineering*, **34**, 64–77. <https://doi.org/10.1080/01919512.2012.640251>
- [237] Yang, G. and Zhu, J.J. (2016) Sonoelectrochemical synthesis and characterization of nanomaterials #10. *Handbook of Ultrasonics and Sonochemistry*, Springer Singapore, Singapore. p. 295–324. [https://doi.org/10.1007/978-981-287-278-4\\_11](https://doi.org/10.1007/978-981-287-278-4_11)
- [238] Eriksson, M. (2005) Ozone chemistry in aqueous solution - Ozone decomposition and stabilisation. *Technology*, Retrieved November 30, 2020, from, <http://kth.diva-portal.org/smash/record.jsf?pid=diva2%3A87778&dswid=1810>
- [239] Rasalingam, S., Peng, R. and Koodali, R.T. (2014) Removal of hazardous pollutants from wastewaters: Applications of TiO<sub>2</sub>-SiO<sub>2</sub> mixed oxide materials. *Journal of Nanomaterials*, **2014**, 1–42. <https://doi.org/10.1155/2014/617405>
- [240] Flint, E.B. and Suslick, K.S. (1991) The temperature of cavitation. *Science*, **253**, 1397–1399. <https://doi.org/10.1126/science.253.5026.1397>
- [241] Chen, D., Sharma, S.K. and Mudhoo, A., editors. (2011) Handbook on Applications of Ultrasound. CRC Press. <https://doi.org/10.1201/b11012>
- [242] Lin, J.G. and Chen, S.Y. (1998) The relationship between adsorption of heavy metal and organic matter in river sediments. *Environment International*, **24**, 345–52. [https://doi.org/10.1016/S0160-4120\(98\)00012-9](https://doi.org/10.1016/S0160-4120(98)00012-9)
- [243] Kamolpornwijit, W., Meegoda, J.N. and Batagoda, J.H. (2015) Engineering properties of chromium contaminated soils. *Geotechnical Engineering*, **46**, 8–15.
- [244] Meegoda, J.N., Kamolpornwijit, W. and Batagoda, J.H. (2017) A Detailed Laboratory Scale Feasibility Study of Recovering Metallic Iron and Chromium from Chromium Contaminated Soils. *Indian Geotechnical Journal*, **47**, 437–444. <https://doi.org/10.1007/s40098-016-0208-4>
- [245] Kamolpornwijit, W., Batagoda, J.H. and Meegoda, J.N. (2018) Optimisation of metal extraction from chromium ore processing residue in New Jersey, USA. *Journal of Environmental Engineering and Science*, **13**, 98–107. <https://doi.org/10.1680/jenes.18.00009>
- [246] Richard, F.C. and Bourg, A.C.M. (1991) Aqueous geochemistry of chromium: A review. *Water Research*, **25**, 807–816. [https://doi.org/10.1016/0043-1354\(91\)90160-R](https://doi.org/10.1016/0043-1354(91)90160-R)

- [247] Environmental Protection Agency. (2007) Ultrasonic Extraction. *EPA Method 3550C*, 1–17.
- [248] Masindi, V. and Muedi, K.L. (2018) Environmental Contamination by Heavy Metals. *Heavy Metals*, InTech. <https://doi.org/10.5772/intechopen.76082>
- [249] Karickhoff, S.W., Brown, D.S. and Scott, T.A. (1979) Sorption of hydrophobic pollutants on natural sediments. *Water Research*, **13**, 241–248. [https://doi.org/10.1016/0043-1354\(79\)90201-X](https://doi.org/10.1016/0043-1354(79)90201-X)
- [250] Meegoda, J.N. and Kewalramani, J. (2020.) Coupled High and Low Frequency Ultrasonic for Destruction of Organics. US Provisional Patent Filed.